Micro- and Macro-mechanical Testing of Grain Boundary Sliding in a Sn-Bi Alloy

Junnan Jiang

Hertford College

Department of Materials

Supervisors: Prof. Angus J. Wilkinson & Prof. Richard I. Todd

A thesis submitted for the degree of

Doctor of Philosophy

Trinity Term 2017

Preface

This doctoral thesis presents the work carried out by the author at the Department of Materials, University of Oxford from October 2013 to October 2017, under the supervision of Prof. Angus J. Wilkinson and Prof. Richard I. Todd. All the research for this thesis is original. Where the work of others is included, it has been referenced and acknowledged in the text. The references are listed at the end of the thesis.

No part of this thesis has been previously submitted for a degree at this or any other university. Some of the work in this thesis has been reported at the following conferences:

- The 12th International Conference on Superplasticity in Advanced Materials (ICSAM 2015), Tokyo, Japan – Micro- and Macro-mechanical Testing of Grain Boundary Sliding, September 2015.
- The 12th International Conference on the Mechanical Behaviour of Materials (ICM12), Karlsruhe, Germany – Micro- and Macro-mechanical Testing of Grain Boundary Sliding, May 2015.
- The National Student Conference in Metallic Materials, Sheffield, UK – Micro- and Macro-mechanical Testing of Grain Boundary Sliding, June 2014.

Abstract

This project explores the fundamental mechanisms of grain boundary sliding (GBS) with an emphasis on its role in superplasticity, using both micro- and macro-mechanical testing methods. GBS plays an important role in the deformation of polycrystalline materials, especially at high homologous temperatures (above half of the melting point). Classical models for GBS (Rachinger sliding and Lifshitz sliding) assume that all grains and grain boundaries undergo the same process, but recent research has shown this is not true [1]. Individual grain boundaries differ in their ability to participate in sliding and diffusion. Therefore, it is important to investigate the response of individual grain boundaries to stress. This project uses microcantilevers, loaded using a nanoindenter, to investigate the response to stress of individual grain boundaries in Sn-1%Bi, which is expected to exhibit GBS at room temperature. The response of individual grain boundaries are correlated with grain boundary characters determined using electron backscattered diffraction (EBSD). On the macroscopic scale, both in-situ and ex-situ shear tests are conducted to investigate the superplastic behaviour of this material. The strain rate sensitivity index of the material with a grain size of 8.5 μm is found to be around 0.45. Surface marker lines have quantitatively revealed grain boundary sliding. The investigation from surface studies is expanded to the interior of bulk material in 3D by conducting an in-situ tensile test coupled with diffraction contrast tomography (DCT) at a synchrotron facility.

The microcantilever tests enable grain boundary sliding and diffusion creep to be investigated separately by varying the normal and shear stresses on the grain boundary plane. GBS is dependent on grain boundary structure (misorientation angle, rotation axis and grain boundary plane orientation). The microcantilever size is similar to the grain size used in the macro-mechanical tests. It is demonstrated that the shear stress for steady-state GBS is comparable in micro- and macro-tests. Grain neighbour switching events have been identified in the interior of bulk material in 3D for the first time.

Acknowledgements

I would like to thank my supervisors, Prof Angus Wilkinson and Prof Richard Todd for their support and guidance throughout this project. Regular discussions with both supervisors have always been helpful and inspiring. Their enthusiasm for this project and patient guidance have made me enjoy the last four years of research very much.

I am very grateful for the help and advice from my collaborators for the diffraction contrast tomography (DCT) experiment — Dr Wolfgang Ludwig at the ESRF and Dr Samuel McDonald at the University of Manchester. The DCT data analysis was successfully conducted by the collaborators with their expertise in DCT. The experiment has obtained exciting out-comings and their contribution is much appreciated. My thanks are also given to Prof James Marrow, who provided access to software on digital image correlation (LaVision DaVis) and 3D visualisation (Avizo). I would like to thank Dr Enrique Alabort, who kindly helped me conduct the in-situ SEM mechanical tests. Thanks are also given to Oxford Solid Mechanics Group for providing access to the SEM and in-situ testing device.

The Oxford Micromechanics group has always been a wonderful place to work in. All the group members have always been extremely friendly and helpful. Thanks are given to Dr Jicheng Gong for equipment training and expert guidance on micro-mechanical testing. Thanks are given to Dr Phani Karamched, Dr Hamidreza Abdolvand and Dr Arantxa Vilalta-Clemente for their help and expert guidance on the SEM and EBSD. Thanks go to Dr David Collins for his help with Matlab and general advice. Thanks go to Mr Laurie Walton, Mr Ian Lloyd, Mr Tony Wheeler and Mr Robin Vincent for their help with the material processing and sample preparation. Thanks go to Matthew Jordan and Selim Barhli for their help with the Shimadzu tester and DIC software. I am grateful to the technical support team of electron microscopy: Gabriella Chapman, Gareth Hughes and Graham Wyatt. Most of my time for the last four years was spent in the office with my wonderful colleagues: Dr Chris Jones, Dr Andrew London, Kris Bhojwani, Luke Hewitt, Bo-shiuan Li, Tomohito Tanaka and Daniel Celis Garza.

Finally, my thanks to my family, great parents: Chuntang Jiang and Fuxiu Shi. Thank you for all your support for my studies in the UK. A special thank you to my partner, Yujing Wang, for cheering me up during the thesis write-up.

Nomenclature

2D Two-dimensional

3D Three-dimensional

CAD Computer-Aided Design

DCT Diffraction Contrast Tomography

DIC Digital Image Correlation

EBSD Electron Backscattered Diffraction

EDM Electrical Discharge Machining

ESRF European Synchrotron Radiation Facility

FEA Finite Element Analysis

FIB Focused Ion Beam

GBDs Grain Boundary Dislocations

GBS Grain Boundary Sliding

LabDCT Laboratory DCT

PCT Phase Contrast Tomography

Contents

Chapter 1

Introduction

1.1 Scientific Background

Grain boundary sliding (GBS) denotes the movement taking place at, or in the immediate vicinity of the mutual interface of two grains in response to an external stress [2]. GBS is an important mode of deformation in polycrystalline materials and one of the dominant deformation mechanisms of high temperature creep and superplasticity. High temperature creep is a time-dependent deformation process that could lead to degradation and even failure of materials at high homologous temperatures. An example is shown in figure 1.1a that a tantalum-based alloy failed under fatigue loading due to the massive grain boundary decohesion from sliding of the neighbouring boundaries [3]. Understanding the mechanism and kinetics of GBS is vital to the material integrity in engineering applications. Superplasticity is a phenomenon in which metals can exhibit spectacularly large tensile elongations to failure under certain conditions (the world record approaches an engineering strain of 10 000%). The large strains are achieved by the sliding of grains over one another and necking is resisted by virtue of a high strain rate sensitivity. There are widespread commercial applications of superplasticity, which are used for making parts for luxury automobiles (e.g. Rolls-Royce, Aston Martin, Morgan), aeroplanes (Boeing, Airbus), jet engines – most notably the high performance cellular fan blades

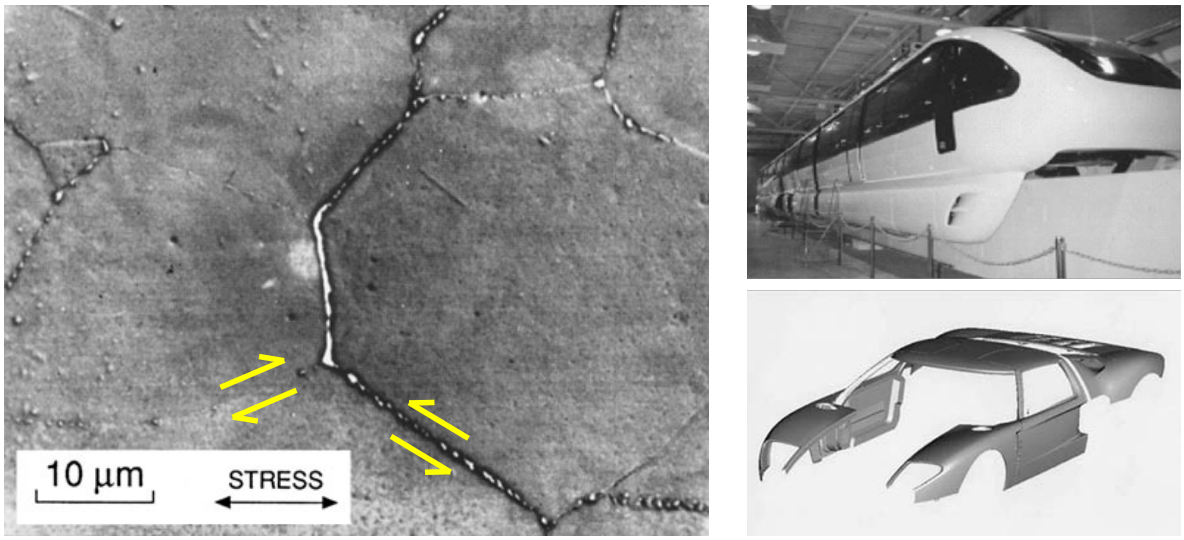

(a) After [3] (b) After [4]

Figure 1.1: (a) Grain boundary decohesion that resulted from sliding of the neighbouring boundaries in a tantalum alloy during high temperature creep (~0.44 homologous temperature) [3]. (b) Examples of engineering applications of superplastic formed products, i.e. train and automobile bodies [4].

on Rolls-Royce Trent engines, bodies for trains, cable cars and a host of smaller high quality items (examples shown in figure 1.1b). Finite Element Modelling (FEM) is used commercially to define the schedule of gas pressure used for forming and is successful at a basic level using macroscopic constitutive equations to represent the material behaviour. However, there is now a need for more physically-based constitutive equations so that the models can incorporate failure mechanisms and surface finish and be used to push the forming rates, which are slow (~20 minutes per part) to faster rates without compromising reliability. The potential improvements are strongly based on a better scientific understanding of superplasticity and GBS.

Over decades of research, there were two geometrically distinct models of GBS — Rachinger sliding [5] and Lifshitz sliding [6]. Rachinger sliding is characterised by a net increase in the number of grains along the loading axis, while grains tend to switch their neighbours and retain their original shape. Lifshitz sliding is usually associated with diffusion creep to accommodate the grain elongation, while making no contribution to the total strain [7]. These models are very much idealised cases, assuming that the grains are in regular shapes and all the grains and

grain boundaries behave in the same way. But recent research has shown that individual grain boundaries differ in their ability to participate in sliding and diffusion [1]. This inhomogeneity suggests an underlying complexity to the GBS process. There were mainly two possible accommodation mechanisms of GBS proposed by various researchers — diffusion creep and dislocation motion at the grain boundary. However, the fundamental mechanism of GBS and its role in plastic deformation still remain controversial and the kinetics of the process have never been satisfactorily explained.

1.2 Outline of the Present Research

Despite the large number of macro-mechanical tests carried out on superplasticity in the literature, limited research has been conducted on the behaviour of individual grain boundaries without interference from other grains. Even though considerable effort was made on studies using bi-crystals, these macroscopic samples were not only expensive to fabricate, but also could hardly represent the true grain boundary behaviour at the microscopic scale. The recently developed micro-mechanical testing techniques have enabled investigation into the response of individual grain boundaries to stress at micrometer scale. Thus, this project is focused on micromechanical tests using microcantilevers with individual grain boundaries. A Sn-1%Bi alloy (single phase) is carefully selected for the study as it should exhibit GBS at room temperature. This is because the melting temperature of Sn-1%Bi is around 504K, while room temperature (298K) is almost 60% of its melting point. Furthermore, it is a single-phase alloy, which simplifies the microstructure. The micro-cantilevers are made by FIB milling and tested using a nanoindenter. The response of individual grain boundaries is correlated with grain boundary characters by using electron backscattered diffraction (EBSD) to measure the misorientation angle, rotation axis and grain boundary plane orientation. This links the grain boundary characters to their tendency to sliding.

In addition to the micro-tests using novel techniques (Chapter 4), conventional mechanical

tests on the macroscopic scale have also been carried out (Chapter 3). Deformation in shear is chosen because the surface area remains constant and there is less incentive for out-of-plane grain boundary sliding than in conventional tensile testing. Various strain rates are used and Digital Image Correlation (DIC) analysis is conducted to measure the strain of the specimen accurately. In order to quantify the amount of GBS, surface grids are produced by Focused Ion Beam (FIB) milling. The surface studies are extended to the use of in-situ synchrotron diffraction contrast tomography (DCT) to follow individual grains during superplastic deformation so that the inhomogeneity and mode of deformation in the bulk material can be revealed for the first time (Chapter 5). Finally, all the experimental results are compared to the literature and correlated with the classical models of superplasticity in Chapter 6.

Chapter 2

Literature Review

2.1 Plastic Deformation at High Temperature

There can be a number of mechanisms operating in the high temperature (above $\sim 0.5T_m$, the absolute melting temperature) deformation process, which do not operate at low temperature, diffusion being a major example. Understanding the mechanisms during high temperature deformation is of great importance to the processing and applications of materials. High temperature deformation at the steady state can be described by equation 2.1 [8]:

$$\dot{\varepsilon} = A\frac{DGb}{kT}\left(\frac{b}{d}\right)^{p}\left(\frac{\sigma}{G}\right)^{n} \tag{2.1}$$

Where $\dot{\varepsilon}$ is the steady state strain rate, A is a mechanism dependent constant, G is the shear modulus, b is the magnitude of the Burgers vector, k is Boltzmann's constant, T is the absolute temperature, d is the grain size, p is termed the inverse grain size exponent, σ is the applied stress, and n is termed the stress exponent. D is the rate-controlling diffusivity term (lattice or grain boundary diffusivity):

$$D = D_0 \exp\left(\frac{-Q_d}{RT}\right) \tag{2.2}$$

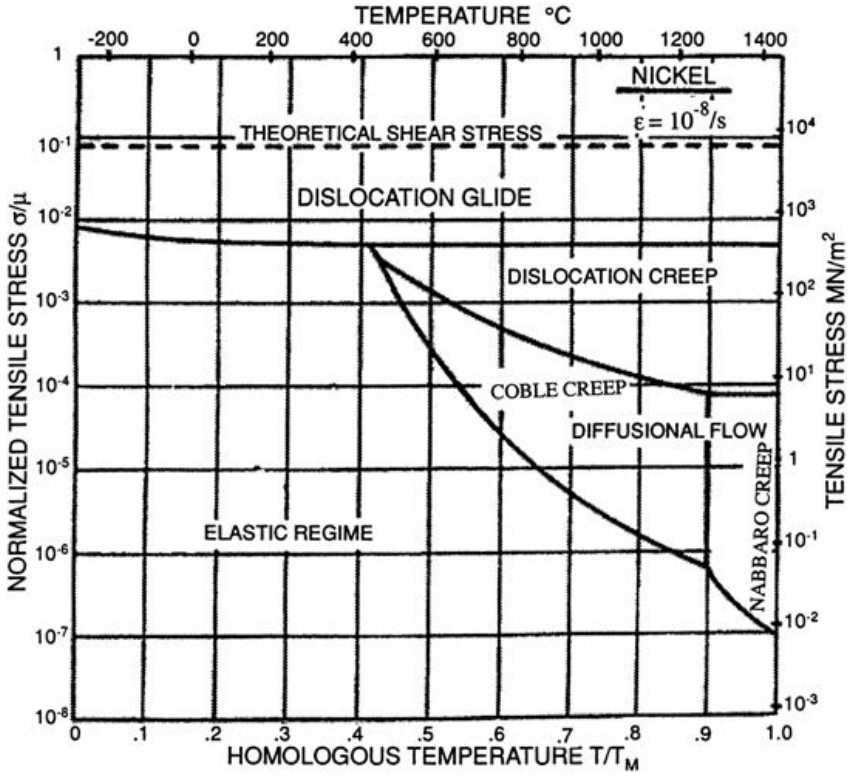

Figure 2.1: A example of the deformation mechanism map illustrating the dominant deformation mechanism at various stresses and temperatures. This map was for nickel with an average grain size of 32 μm at a strain rate of $10^{-8}s^{-1}$ [11].

where D_0 is a pre-exponential and Q_d is the activation energy for diffusion. The rate controlling creep mechanism can be identified by comparing the theoretical and experimental values of n, p and Q_d, together with the microstructural characterisation. Ashby [9] developed a creep diagram (deformation mechanism map) to present the alternative deformation mechanisms competing in high temperature deformation. Figure 2.1 shows an example of the deformation mechanism map for nickel with a strain rate of $10^{-8}s^{-1}$ and an average grain size of 32 μm. The normalised stress was plotted against homologous temperature. The map was divided into a few fields with the dominant mechanism illustrated in each field, which included dislocation glide, dislocation creep and diffusional flow, etc. At high stresses, dislocation motion is the dominant mechanism. While at lower stresses, diffusion-controlled deformation mechanisms become more important. Depending on the active mechanisms, high temperature deformation

mechanisms can be characterised as intragranular and intergranular mechanisms [10].

2.1.1 Intragranular Deformation Mechanisms

This mechanism of deformation occurs in the interior of the grains and therefore the strain rate is independent of grain size. It involves dislocation motion via both glide on slip planes and climb over obstacles. Without the effect of grain size on intragranular deformation, the steady-state creep rate $\dot{\varepsilon}$ can be characterised by a simple power-law relationship with stress σ ($\dot{\varepsilon} = C\sigma^n$), where C has a temperature dependence [12]. Harper and Dorn [13] first reported that the creep at high temperatures and low stresses of high-purity aluminium was controlled by dislocation climb. This type of creep in the low stress-exponent regime was denoted Harper-Dorn (H-D) creep. H-D creep was found to be independent of grain size and the steady-state stress exponent was close to 1 [13]. Later on, more research was carried out on the primary and steady-state creep of various types of materials. Based on the type of the lattice mechanism active, creep behaviour in metallic solid solution alloys can be classified as Class I and Class II type behaviour [14]. Class II solid solution alloys have similar stress and time dependency as that of pure metals, while Class I type creep has distinct characteristics associated only with solid solution alloys [15]. Class II type is generally attributed to some form of dislocation climb process and has a stress exponent n~5. However, this five-power-law creep at higher stresses was distinguished from H-D creep (n~1) even though they were both controlled by dislocation climb [16]. The steady-state creep rate depends on the stacking fault energy of the alloy, which is related to the dissociation of dislocations. A lower stacking fault energy will make dislocation climb more difficult and therefore reduce the steady-state creep rate.

Class I type behaviour is generally associated with a viscous drag (by the solute atoms) process operating on the dislocations during glide and has a stress exponent n~3. Sellars and Quarrell's [17] studies on Au-Ni alloys revealed that the steady-state creep rate of Class I solid solution alloys was independent of the stacking fault energy. Yavari et al. [18] carried out creep tests at various shear stresses on an Al-5% Mg alloy. It was found that at lower stresses, the material

exhibited Class II type creep controlled by dislocation climb. As the stress was increased, the creep behaviour changed to Class I type that is controlled by dislocation glide. Since dislocation glide requires no assistance of point defects whereas climb needs emission or addition of interstitials, climb is favoured at higher temperatures. This is because at higher temperatures, the diffusion of point defects is enhanced.

2.1.2 Intergranular Deformation Mechanisms

Intergranular deformation mechanisms involve deformation processes where the interfaces play a major role and the strain rate is dependent on the grain size. There are two main mechanisms in this type of creep behaviour, which are diffusion creep and grain boundary sliding.

Diffusion creep is the predominant mechanism of deformation at high temperatures and low stresses, when intragranular dislocation activity is very limited. For example, as shown in the deformation mechanism map of Sn-37% Pb (figure 2.2a), when the normalised shear stress is below 10^{-4}, the dominant deformation mechanism above $0.6T_m$ is diffusion creep. Depending on the dominant diffusion path for the matter transport, diffusion creep can be categorised into Herring-Nabarro creep and Coble creep. When a stress is applied to a polycrystalline material, it produces an excess of vacancies along the grain boundaries under a tensile stress and a corresponding depletion of vacancies along those boundaries undergoing a compressive stress. Therefore, a vacancy concentration gradient is generated. As a result, there is a flow of vacancies and a counter flow of atoms in the interior of the grain and along the grain boundaries as shown in figure 2.2b. For coarse grained polycrystalline materials, when deformed at a low stress and a high temperature, lattice diffusion (self-diffusion within the grains) is dominant and this type of diffusion creep is termed Herring-Nabarro creep [19]. In contrast, for fine grained polycrystalline materials with a larger grain boundary area, when deformed at a low stress and an intermediate temperature, diffusion along grain boundaries is dominant and this process is termed Coble creep [20].

Herring-Nabarro creep assumed that the normal flux is fairly uniform over each facet of the

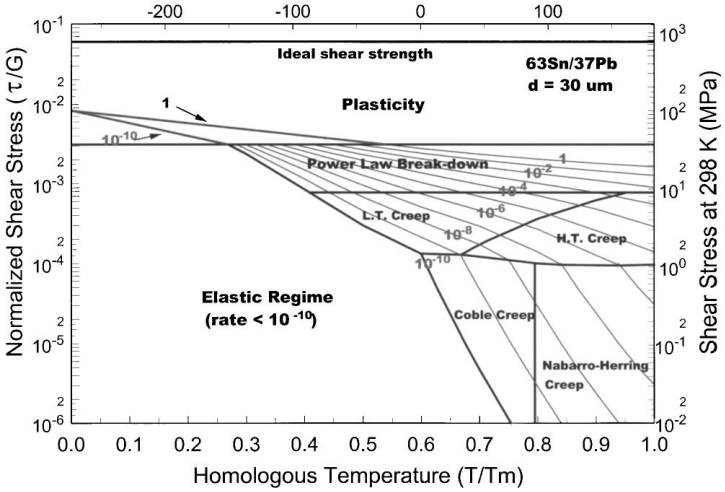

(a)

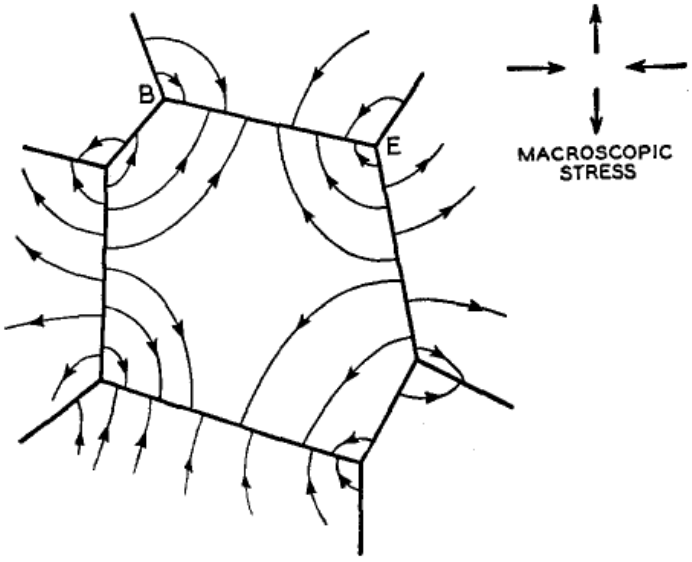

(b)

Figure 2.2: (a) Deformation mechanism map for Sn-37% Pb with an average grain size of 30 μm at a series of strain rates represented by the iso-lines [21]. (b) A schematic diagram showing the diffusion flow of matter in the grain interior and along the grain boundaries in response to an external stress [19].

boundary and a uniform shear deformation occurred in all the spherical grains [19]. The creep rate $\dot{\varepsilon}$ is described by equation 2.3, where D_l is the lattice diffusion coefficient, Ω is the vacancy volume, k is Boltzmann's constant, T is the absolute temperature, d is the grain size and σ is the applied stress. Therefore, the inverse grain size exponent p is 2 and the stress exponent n is 1 in Herring-Nabarro creep. Coble creep was based on the grain boundary diffusion and was found to be insensitive to the uniformity of the vacancy sources and sinks [20]. The shape change by diffusion and the effect of shear stress relaxation at grain boundaries on the creep rate were taken into account. The relationship between creep rate $\dot{\varepsilon}$ and stress σ is illustrated in equation 2.4, where D_b is the grain boundary diffusion coefficient and W is the grain boundary width.

$$\dot{\varepsilon} = \frac{10 D_l \Omega}{kTd^2}\sigma \tag{2.3}$$

$$\dot{\varepsilon} = \frac{150 D_b W \Omega}{kTd^3}\sigma \tag{2.4}$$

Grain boundary sliding is one of the predominant deformation mechanisms at elevated temperatures, typically over $0.5T_m$ [22]. Furthermore, in nanocrystalline materials, grain boundary sliding has been observed at temperatures much lower than $0.5T_m$, even at room temperature [23, 24]. Diffusion creep is always accompanied by grain boundary sliding for geometrical integrity, while grain boundary sliding has to be accommodated by some other mechanisms in polycrystals.

2.2 Superplasticity

Superplasticity is a phenomenon in which metals and ceramics can exhibit spectacularly large tensile elongations to failure under certain conditions. Although there were earlier observations of unusual large elongations, it is generally agreed that Pearson [25] was the first to describe the phenomenon of superplasticity in 1934. Pearson observed neck-free elongations

of almost 2000% in a Sn-Bi eutectic alloy and 1500% in a Sn-Pb eutectic alloy. This was unusual as most metallic materials show necking even after small elongations during tension. Furthermore, Pearson not only identified the crucial role of the strain rate and grain size, but also inferred that grain boundary sliding must have occurred during superplastic deformation. Superplasticity is an inherent characteristic of almost all known types of polycrystals under certain temperature-strain rate conditions, provided that these materials have an average grain size of usually no more than 10 μm for metals (about 1 μm for ceramics) [26]. Therefore, superplasticity provides novel possibilities for materials processing, especially for materials that cannot be readily formed under conventional deformation conditions.

2.2.1 Mechanics of Superplasticity

The applied stress (σ) for superplastic deformation is found to be strongly dependent on the strain rate ($\dot{\varepsilon}$) [27]. Most superplastic materials exhibit a sigmoidal curve of $\log\sigma$ against $\log\dot{\varepsilon}$ as shown in figure 2.3. The slope of the curve is denoted as the strain-rate sensitivity $m = \frac{\partial \log\sigma}{\partial \log\dot{\varepsilon}}$. There are typically three regions in the curve and m peaks at Region II, where superplastic deformation occurs. It is worth noting that the strain-rate sensitivity, m, is the reciprocal of the stress exponent, n. A typical value of m in superplastic materials is ~0.5. Specifically, for Sn-1wt% Bi alloy used in the current study, the highest strain rate sensitivity was found to be $m \approx 0.48$ [28].

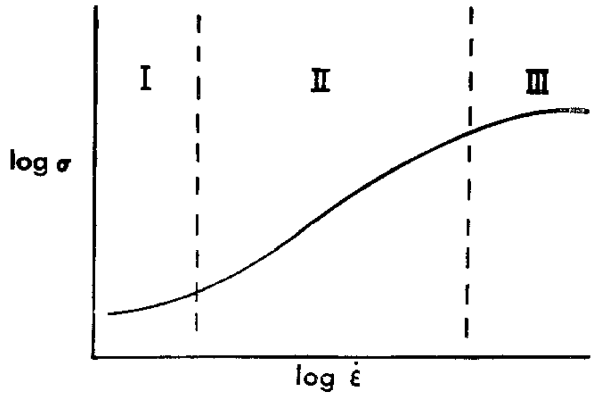

Figure 2.3: A schematic of the relationship between stress and strain rate.

2.2.2 Conditions of Superplasticity

Traditional superplastic alloys with an average grain size below 10 μm show superplasticity at a temperature greater than $0.5T_m$ and strain rates $\dot{\varepsilon}$ between 10^{-4} and 10^{-2} s^{-1} [26]. However, there is a huge demand in industry for higher superplastic forming rates, while lowering the formation temperature. Increased strain rates can enable higher production rates. Low-temperature superplasticity is also desirable as it resists grain growth and allows the use of conventional die and tooling methods [29]. The optimisation of superplastic forming conditions has been promoted by the development of grain refinement methods. The importance of grain structure on superplasticity is described as follows.

2.2.3 Influence of Grain Size on Superplasticity

From equation 2.1, it is evident that at a constant temperature and constant stress, strain rates increase with decreasing grain size. At a constant strain rate, the decrease in grain size from micrometre to nanometre scale can lead to a decreasing superplastic forming temperature [30]. This is explained by the exponential temperature dependence of the Arrhenius expression for diffusivity D as shown previously in equation 2.2. Figure 2.4a qualitatively illustrates the effect of grain size, d, on homologous deformation temperature $T_h = \frac{T_d}{T_m}$ (T_d is the deformation temperature and T_m is the melting temperature) at a constant strain rate and constant stress.

Elongation in superplasticity is primarily governed by the strain-rate sensitivity m. A decrease in grain size usually leads to an increase in the strain-rate sensitivity, therefore resulting in a larger elongation at a constant homologous temperature, strain rate and stress (as shown in figure 2.4b) [26]. This is generally true in the majority of micro- (1-10 μm) or submicrocrystalline (0.1-1 μm) materials. However, a trend has been observed that total elongation decreases with smaller grain size from the microcrystalline to nanocrystalline (0.01-0.1 μm) range [31]. This is attributed to the microstructural instability, i.e. propensity for grain growth at these small grain sizes. Sergueeva et al. [32] claimed that extensive grain growth prevents superplastic flow by prohibiting the formation of sliding surfaces.

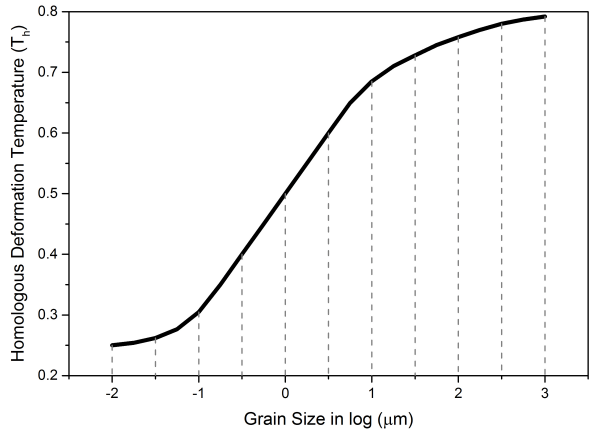

(a)

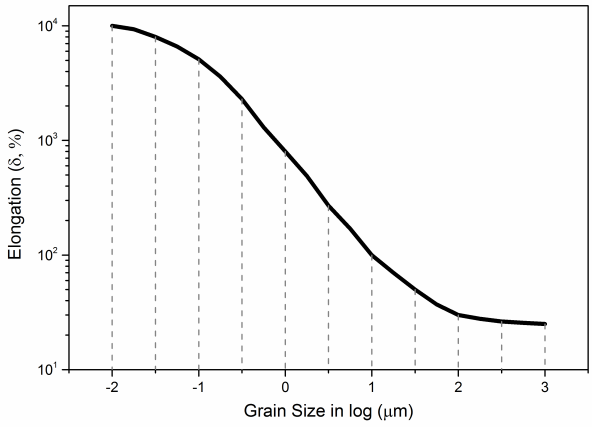

(b)

Figure 2.4: Schematic diagrams showing a qualitative illustration of (a) the effect of grain size on homologous deformation temperature at a constant strain rate and stress. (b) the effect of grain size on the elongation of superplastic deformation at a constant homologous temperature, strain rate and stress (redrawn from [26]).

Typical m values for three low-temperature superplastic alloys at various conditions are shown in table 2.1 [26]. It can be seen that m values vary between 0.3 and 0.6. For an individual type of alloy, the threshold deformation temperature (T_d) decreases with a reduction in the grain size. However, for the titanium VT8 alloys tested at a constant strain rate, the m value increased with temperature even though the grain size was larger as well. This indicates that temperature plays a crucial role in superplasticity.

Alloy	d (μm)	T_d (°C)	$\dot{\varepsilon} \times 10^{-4}$ (s^{-1})	m	σ (MPa)
Al–4%Cu–0.5%Zr	0.3	220	1	0.48	270
	8	500	3	0.5	130
Titanium VT8	0.1	600	7	0.33	230
	0.4	650	7	0.46	155
	5	800	7	0.47	80
Nickel EP962	0.25	800	3.3	0.3	350
	5.5	1075	13.3	0.6	50

Table 2.1: Typical strain rate sensitivity indexes for low-temperature superplastic alloys at different conditions [26].

2.3 Proposed Theories on Superplasticity

Despite the efforts over decades of research, the fundamental mechanisms of superplasticity still remain controversial and the kinetics of the process have never been satisfactorily explained. A number of models supporting different accommodation mechanisms have been proposed. Most of them are based on limited experimental results, but heavily on theoretical calculations or finite element analysis. Correlation was made between grain boundary sliding behaviour and diffusional creep, movement of lattice dislocations along the grain boundary and intragranular dislocation motion.

2.3.1 Classic Models of Grain Boundary Sliding

Based on the distinct characteristics, Cannon [33] classified grain boundary sliding into two types. The first type is designated Rachinger sliding and refers to the process where-by adjacent grains move with respect to each other while retaining essentially their original shapes [5, 34]. However, the retention of the grain aspect ratio alone is not sufficient to identify this type of sliding mechanism. This is because Chokshi [35] found that Lifshitz sliding along with grain

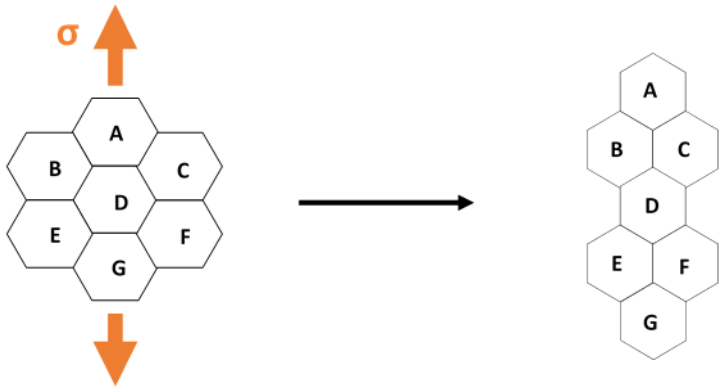

Figure 2.5: A schematic showing the process of Rachinger Sliding, featuring a grain neighbour switching geometry.

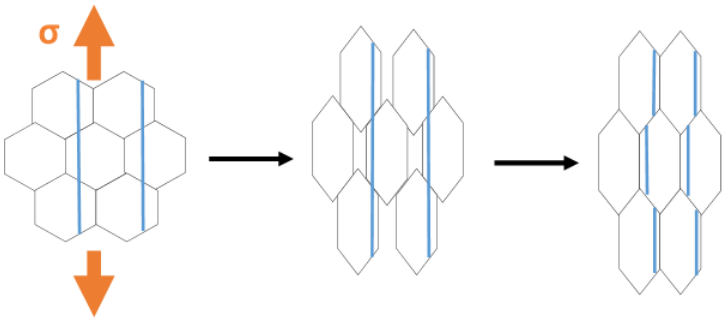

Figure 2.6: The first and last images show the start and finish positions of grains undergoing diffusion creep accommodated by Lifshitz sliding. The image in the middle shows the grain structure of diffusion creep without accommodation by grain boundary sliding.

growth could maintain the equiaxed shape of grains after diffusion creep. A distinguishing characteristic of Rachinger sliding is a net increase in the number of grains lying along the direction of the tensile stress within the gauge length. This is achieved with a grain neighbour switching geometry as shown in figure 2.5. Rachinger sliding must be accommodated by some intragranular dislocation motion or matter transfer by diffusion.

The second type is Lifshitz sliding. It refers to the boundary offsets resulting from the stress-directed diffusion of vacancies. As shown in figure 2.6, the grains become elongated without an increase in number along the tensile axis [6]. Rachinger sliding is widely accepted as the main type of grain boundary sliding. Therefore, all references to grain boundary sliding in the remainder of this review denote Rachinger sliding unless otherwise specified.

2.3.2 Intrinsic and Extrinsic Grain Boundary Sliding

In 1982, Langdon and Vastava [36] categorised the theories of Lifshitz and Rachinger sliding into two distinct types. The first type is intrinsic grain boundary sliding, which refers to sliding without any accommodation mechanism. It is applicable only to smooth and planar boundaries, such as in bicrystal specimens. The second type, extrinsic grain boundary sliding, considers the sliding accommodated by dislocation motion or diffusion flow. Extrinsic grain boundary sliding is observed in polycrystalline materials, where sliding can be hindered by triple junctions and multiple neighbouring grains.

2.3.2.1 Intrinsic Grain Boundary Sliding

Intrinsic grain boundary sliding denotes the type of sliding that does not require accommodation from other grains or grain boundaries. This type of sliding can probably only occur on regular shaped boundaries in microscopic bi-crystals. For example, in a perfectly planar boundary as shown in figure 2.7, a uniaxial load applied on a bicrystal can be resolved at the boundary plane into a normal and shear component. The normal component can either be tension or compression depending on the direction of the externally applied load. Based on the ab initio calculations, Pang et al. [37] suggested that the theoretical shear strength of the grain boundary increased with increasing compressive normal stress and decayed with increasing tensile normal stress. This was explained by the changes in the interplanar potential with the normal stress component. Regardless of the direction of the applied load, the shear component on the boundary plane acts as the driving force for the grain boundary sliding, and the boundary sliding rate is determined by the shear resistance of the boundary plane [38].

The first detailed attempts to analyse intrinsic grain boundary sliding were made by Raj and Ashby [39]. The authors also explored extrinsic grain boundary sliding to be discussed in section 2.3.2.2. Intrinsic grain boundary sliding was assumed to occur in a Newtonian viscous manner for smooth and planar boundaries [39]. Calculations were made to prove that the boundary could slide only an extremely small distance by its intrinsic viscosity. During sliding,

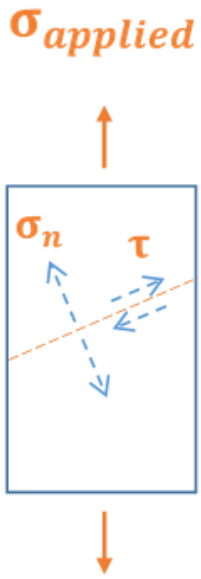

Figure 2.7: Schematic diagram to show the stress distribution at the grain boundary plane of a bicrystal under a tensile stress.

stresses build up at the obstacles such as the boundary ledges, and sliding will stop when the component of these stresses along the boundary balances the applied stress. At low stress and high temperature, obstacles could be overcome by flow of matter by stress-assisted grain boundary diffusion. It was assumed that the diffusional fluxes depend completely on the normal stress and chemical potential gradients at grain boundaries [40]. From studies using bicrystals of pure zinc with very flat grain boundaries, Gifkins [41] suggested that the barriers could be removed by the glide and climb of grain boundary dislocations at higher applied stresses. Gifkins also found out that the stress exponent $n = 1$ for the intrinsic grain boundary sliding in a "good" bicrystal, which was the same as diffusion creep discussed in section 2.1.2 on page 8.

In 1973, Gates [42] argued that the traditional model for grain boundary sliding based on the motion of lattice dislocations along the boundary is unsatisfactory. Using Bollmann's [43] model for high-angle grain boundary structure with the special structural grain boundary dislocations, Gates [42] suggested that it is the structural grain boundary dislocations, rather than the usually observed lattice dislocations in the grain boundary, that move by glide and climb to cause sliding. Later in 1976, Pond et al. [44] proposed another model of grain boundary

sliding associated with grain boundary dislocations. Dislocations pile up at obstacles and generate variable strains, which are subsequently released by diffusion. Contrary to the analysis of Gates, Pond et al. argued that instead of the structural or intrinsic dislocations in the boundary, the extrinsic dislocations are responsible for sliding. The rate controlling process in Pond's model is the diffusion necessary to allow the climb of grain boundary dislocations. Despite the fair number of hypotheses proposed, it is inherently difficult to obtain experimental evidence for these claims. There is still no consensus on which one is the dominant mechanism of intrinsic grain boundary sliding.

2.3.2.2 Extrinsic Grain Boundary Sliding

In reality, grain boundaries are usually non-planar at the microscopic scale as shown in figure 2.8a [39]. What is more, the stress distribution is quite complex on the grain boundaries. Therefore, for a wavy boundary subjected to sliding under a shear stress, some accommodation process is necessary to overcome the interlocking of the asperities and allow further sliding. Raj and Ashby [39] suggested that the accommodation can be purely elastic or diffusion flow or plastic flow by dislocation motion. An example is shown in figure 2.8b, steady-state grain boundary sliding is accommodated by diffusive flow of matter (from regions under compression to regions under tension). The upper half crystal slides in the y direction from the position shown by the full line to that shown by the dashed line.

Diffusion-based Models

In steady-state sliding, the net diffusional flux of matter into or out of each element of the boundary must account for the normal component of the sliding displacement at each point on the boundary. Therefore, the stress distribution for steady-state sliding (figure 2.8b) is quite different from the stress state without diffusion accommodation (figure 2.8a). After comparing the

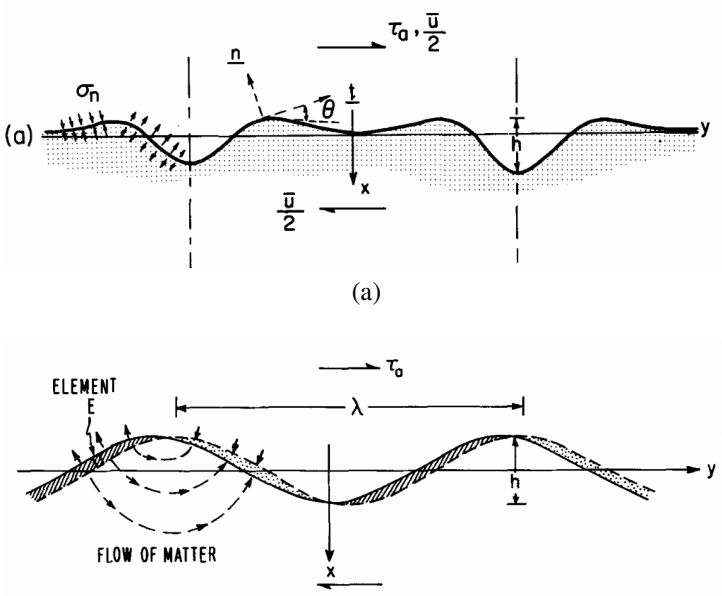

Figure 2.8: (a) An example of a non-planar boundary under a shear stress τ_a, causing a relative displacement of sliding $\bar{u}$. σ_n is the normal stress distributed across the boundary surface, with tension on the top and compression on the bottom of the grain boundary. (b) A schematic shows the steady-state grain boundary sliding accommodated by diffusion. The upper half crystal slides in the y direction from the position shown by the full line to that shown by the dashed line [39].

kinetics of the processes, the authors [39] concluded that grain boundary sliding accommodated by diffusion is identical to diffusional creep ("Herring-Nabarro" or "Coble" creep). Raj and Ashby were pioneers in this research field who realised the importance of accommodation mechanisms of grain boundary sliding. However, their investigation on the diffusion accommodation mechanism was largely based on assumptions and theoretical calculations, which was challenged by the following research.

Another model on grain boundary sliding was proposed by Ashby and Verrall [45]. It was claimed that the diffusion accommodation mechanism is fundamentally distinct from Herring-Nabarro and Coble creep as it involves grain neighbour switching rather than grain elongation. The grain neighbour switching event (figure 2.9) is featured in the process of diffusion-accommodated grain boundary sliding process, but it is absent in the diffusion creep (Herring-Nabarro and Coble creep) model. The accommodation strains in the intermediate state are

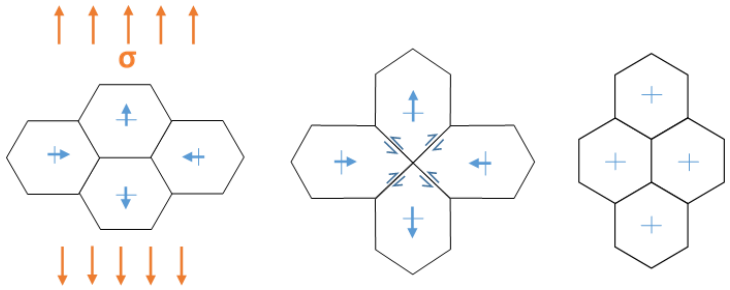

Figure 2.9: A step-by-step schematic diagram of the Ashby-Verrall model on diffusion accommodated grain boundary sliding. The initial and final states of the polycrystal are thermodynamically identical. The grains temporarily change their shapes in the intermediate state [45].

accomplished by diffusion flow within the bulk and along the grain boundaries. In practice, the high-conductivity grain boundary diffusion paths are more important. It was also suggested that as the stress increases, accommodation by dislocation motion is involved as well. Even though the linear stress dependence of strain rate from the Ashby-Verrall model is contrary to most experimental data, their model demonstrated the important role of diffusion in the grain boundary sliding process characterised by neighbour switching.

However, Spingarn and Nix [40] argued that Ashby-Verrall model does not satisfy certain conditions of equilibrium. They suggested that the distributions of normal tractions are symmetric about the mid-points of each grain boundary segment before diffusion flow, which therefore restricts the allowable transient diffusional fluxes. Diffusional flow from one boundary endpoint to the other could not occur, so the Ashby-Verrall model does not satisfy these restrictions. Furthermore, the reaction path proposed by Lee [46] can occur, in which grain neighbour switching occurs by diffusion and grain boundary migration (figure 2.10).

Dislocation-based Models

The accommodation mechanism of dislocation activity was first observed and proposed by Ishida and Brown [47]. Analysis by transmission electron microscopy revealed dislocation climb and glide movements at the grain boundary during creep of pure iron and iron-alloys. It was suggested that dislocations absorbed from the neighbouring grains into a grain boundary

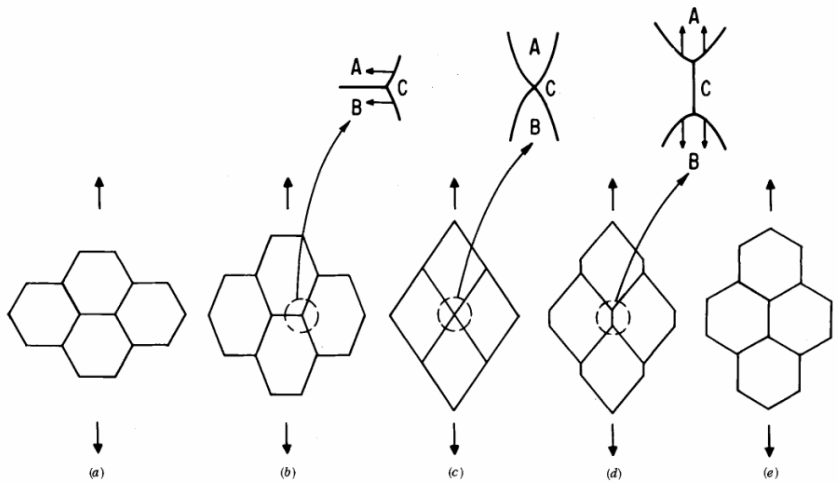

Figure 2.10: Schematic illustration of a grain rearrangement process retaining the equiaxed grain structure after the process of deformation from (a) to (e). The highlighted parts show grain boundary migration to reach equilibrium structure in (c) and (d) [46].

can cause grain boundary sliding to occur, and therefore nucleation of grain boundary dislocations is not essential to this process. In 1968, Lin and McLean [48] further demonstrated that the dislocations primarily originate within the grains and enter the boundary plane by slip. Later, Ball and Hutchison [49] suggested that grain boundary sliding occurs by the movement of grain boundary dislocations along the grain boundary plane. The dislocations are blocked and pile up at grain boundary ledges and triple junctions, which generates stress concentrations. The stress concentrations need to be released by dislocation climbing into and along grain boundaries.

In the 1970s, Langdon [7] further illustrated that if grain boundary sliding occurs by the movement of dislocations along or adjacent to the boundary by dislocation climb and glide, the strain rate is proportional to σ^2/d. However, Mukherjee [50] suggested that grain boundary sliding is controlled by dislocation motion within the grains. Large ledges or obstacles on the grain boundary surface would cause dislocations to generate at these sites. The dislocations generated will travel through the blocked grain and pile-up at the opposite grain boundary. The rate of dislocation generation and movement in the pile-ups is controlled by the rate of continuous removal of the leading dislocation in the pile-up by climb along grain boundaries to

the annihilation sites at a distance of the order of grain diameter. Crossman and Ashby [51] further explored the accommodation of grain boundary sliding by plasticity within the grains. The plastic flow of polycrystals above $0.3T_m$ is usually non-uniform. Superimposed on the uniform deformation within the grains is an additional non-uniform contribution to flow. This is because as a boundary slides freely, both the displacement and the stress field become non-uniform. Finite element analysis was conducted to simulate the creep of the composite – grain and grain boundary. A power-law creep relationship was proposed to describe this accommodation process (equation 2.5):

$$\dot{\gamma} = A\left(\frac{f\tau}{\mu}\right)^n \tag{2.5}$$

where $\dot{\gamma}$ is the shear strain rate, A is a constant dependent on temperature but not on stress, f is the stress enhancement factor, τ is the shear stress, μ is the shear modulus and n is the stress exponent. However, this model could not explain superplasticity as the constitutive equation above does not take into account of grain size and Burgers vector.

In the 1980s, Kaibyshev and Valiev [52] proposed a new model that grain boundary sliding begins with the generation and motion of grain boundary dislocations (GBDs). Since different boundary thresholds and triple junctions inhibit GBDs motion, GBDs pile-ups are formed at triple junctions. In order for the deformation to further develop by GBDs motion, the dislocations in pile-ups need to be dissipated by some accommodation mechanisms. Lattice dislocation generation is the most effective mechanism of this kind. These lattice dislocations pass through the grain body and are absorbed at the opposite boundaries as shown in figure 2.11, which results in the activation of grain boundary sliding and diffusion.

The dislocation pileup models described above consider the climb of the lead dislocation to an annihilation point as the rate controlling process. The climb rate of the lead dislocation is proportional to τ^2, which could potentially explain the stress component of $n \approx 2$ in superplasticity [53]. However, there is a lack of direct experimental observation of dislocation pileup at

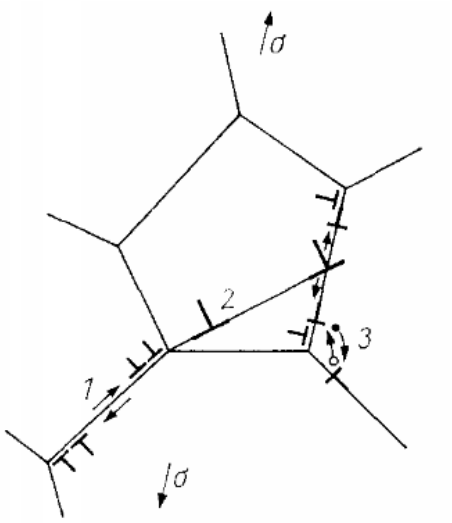

Figure 2.11: Schematic illustration of the development of main processes during grain boundary sliding accommodated by dislocation activity: 1. grain boundary dislocations, 2. lattice dislocations, 3. local diffusion flow [52].

the grain boundary. Efforts were made to examine a superplastic Zn-Al alloy quenched under load [54, 55]. Despite that the dislocation arrays were well preserved, there were no lattice dislocations found to be absorbed into the grain boundaries. Instead, there was experimental evidence of a lack of dislocation activities in the same material [56]. By in-situ TEM mechanical testing, Naziri et al. [57] observed grain neighbour switching events with little dislocation motion..

2.4 Experimental Studies of Grain Boundary Sliding and Diffusion Creep

2.4.1 Grain Boundary Sliding in Bicrystals

Investigation on grain boundary sliding using bicrystals dates back to 1948, when King et al. [58] observed a significant displacement across the grain boundary at high temperatures. A tin bicrystal with a straight boundary was prepared by fusion of two seed single crystals. A constant tensile stress was applied on the bicrystal, which provided a component of shear

stress acting on the boundary. The homologous temperature was 0.98 (i.e. the temperature was a few degrees below the melting point). The relative displacement of the two crystals was observed by means of fine marks on the sample surface. This was the first time that quantitative evidence of grain boundary sliding was obtained. For example, the displacement rate was found to be around 2 nm/s with a shear stress component of 0.05 MPa at 222°C. The rate of displacement was initially high and diminished with time. Even though the grain boundary behaviour was still described as being like "viscous liquids", the experiment revealed the relative displacement at the grain boundary at high homologous temperatures, which was later termed as "grain boundary sliding". King et al.'s work was the first attempt to characterise grain boundary sliding both qualitatively and quantitatively.

After bicrystals of tin could be produced with consistent structure, more research was carried out to investigate the effect on grain boundary sliding of parameters such as velocity, stress and temperature. Puttick and King [59] first explored the dependence of initial sliding velocity on the stress and temperature. Shear tests were conducted at a range of stresses and temperatures. The tests were carried out in-situ under an optical microscope. The displacement at the grain boundary was measured at five-minute intervals by the reference lines drawn normal to the boundary. Displacement-time plots were then analysed to calculate the initial sliding rate. The initial sliding rates were found to increase with higher shear stresses and temperatures.

Tuck [60] followed the experimental setup of Puttick and King. The initial rate was correlated to the stress and temperature in the log scale. The relationship is summarised by equation 2.6, where υ the initial rate of sliding, A is a constant, σ is the applied shear stress, n is the exponential index, Q is the activation energy for boundary sliding, R is the gas constant and T is the absolute temperature. In most specimens, the sliding rate diminished with time after the initial period, which was referred to as "sliding hardening". However, there were also anomalous cases when the sliding rates increased abruptly after some distance of sliding, which was referred to as "secondary sliding". There was also an anomalous group of specimens (16% of the total number of specimens) that showed greater initial sliding rates than the standard

group. Even though the author calculated the activation energy for both "standard" and "anomalous" sliding (very similar in both cases), there was no sensible explanation of the differences observed in the initial and secondary sliding rates between different boundaries. This is due to the lack of characterisation of the grain boundaries (misorientation angle, rotation axis and grain boundary plane orientation).

$$\upsilon = A\sigma^n \exp(-Q/RT) \tag{2.6}$$

Grain boundary sliding has also been studied in other metals with a relatively low melting temperature, such as zinc. Bell et al. [61] investigated the reason of "sliding hardening" that was generally observed in grain boundary sliding. Zinc bicrystals were used to measure sliding rate with time under shear stress at homologous temperature of 0.54. It was found that while sliding velocity decreased with time, there were irregularities at the grain boundary and slip lines in one of the crystals. Crystal slip took place because of the relatively low homologous temperature compared to the experiments on bicrystals of tin [59, 60]. However, their work couldn't determine whether the increased resistance to sliding was due to the irregular shape of the grain boundary or the work-hardened surrounding grains.

2.4.2 Characterisation of Grain Boundary Sliding in Polycrystals

The possibility of GBS in polycrystalline materials was first inferred a century ago, by Rosenhain and Ewen [62], from observation of steps at the grain boundaries during deformation. Based on the qualitative observation of GBS, the authors proposed an "amorphous cement" model of grain boundary structure. Subsequently, Moore et al. [63] used surface marker lines to observe the sharp offsets on the surface of a Pb-2% Sn alloy. Bell and Langdon [64] first proposed a quantitative approach to calculate the contribution of grain boundary sliding to the overall strain by measuring the sliding vector. When an axial stress is applied on a bicrystal as shown in figure 2.12, the two grains move over each other along their mutual boundary. The displacement or sliding vector can be resolved into the three orthogonal components – u, v and w. The grain boundary orientation with respect to the tensile axis can be defined by two angles

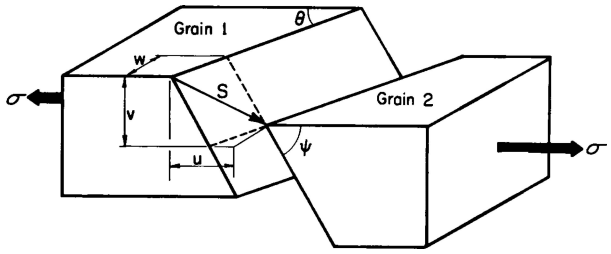

Figure 2.12: Grain boundary sliding occurs between grains 1 and 2 under an applied stress, σ; the sliding vector S, can be resolved into three orthogonal components – u, v and w [34].

θ and ψ, where θ is the angle between the boundary trace on the upper exposed surface and the tensile axis, and ψ is the angle between the tensile axis and the boundary trace on a plane perpendicular to the upper surface.

The elongation due to grain boundary sliding (ε_{gbs}) can be calculated by measuring the sum of the component along the tensile (longitudinal) axis, u_l, divided by the mean grain size, $\bar{L}$ (equation 2.7). An example of measuring u_l is shown in figure 2.13a, where a transverse marker was scribed on the sample surface and the longitudinal offsets (along the horizontal direction) at the intersections with every boundary were measured. However, measuring these longitudinal offsets (u_l) at each grain boundary is not only time-consuming but also inaccurate, because it requires measuring the separations between the end points of a broken marker line [65]. Langdon [66] later developed a method to measure the vertical offset, v, normal to the specimen surface using interferometry as shown in figure 2.13b. This approach using an interference microscope is not only more convenient, but also more accurate than measuring the u or w offsets. Both measurement methods indicated that the strain due to grain boundary sliding accounted for 50-70% of the overall strain during superplastic deformation [65].

$$\varepsilon_{gbs} = \frac{1}{\bar{L}} \sum u_l \tag{2.7}$$

Rust and Todd (2011) have carried out surface studies on superplastic aluminium alloys using focused ion beam (FIB) to mill mesogrids as shown in figure 2.14a. Following a single grid line, it is evident that most of the grain boundaries show offsets under the shear stress resolved

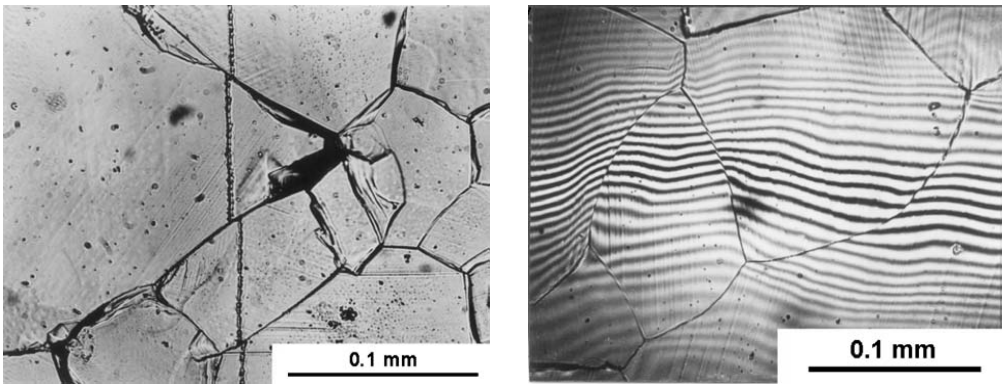

(a) (b)

Figure 2.13: GBS revealed by the boundary offsets for a Mg-0.78% Al alloy tested under creep conditions at 473K using (a) a transverse marker line [64] (b) interferometry [66].

on the grain boundary. However, the essential geometry change associated with grain boundary sliding – grain neighbour switching was not observed directly on the surface due to the surface artefact from oxidation. For example, the surface grids on the microscopic scale, as shown in figure 2.14b, revealed the process of grain neighbour switching during grain boundary sliding. Grains A and B were initially in contact, but became separated by Grain C and D that approached towards each other. Even though Grain C and D were not connected on the surface, FIB milling confirmed that they were in contact beneath the surface. On the one hand, the surface studies not only demonstrated the diffusional transfer of matter accommodating grain boundary sliding, but also indicated the absence of intragranular plasticity based on the non-distorted grid lines inside the grains. On the other hand, the research has illustrated the difficulty of direct observation of grain neighbour switching in 2D, due to the surface artefacts.

2.5 The Dependence of Grain Boundary Sliding on Grain Boundary Structure

The crystallography of a grain boundary can be specified by eight degrees of freedom in total, which can be classified into macroscopic and microscopic degrees of freedom [67]. The five

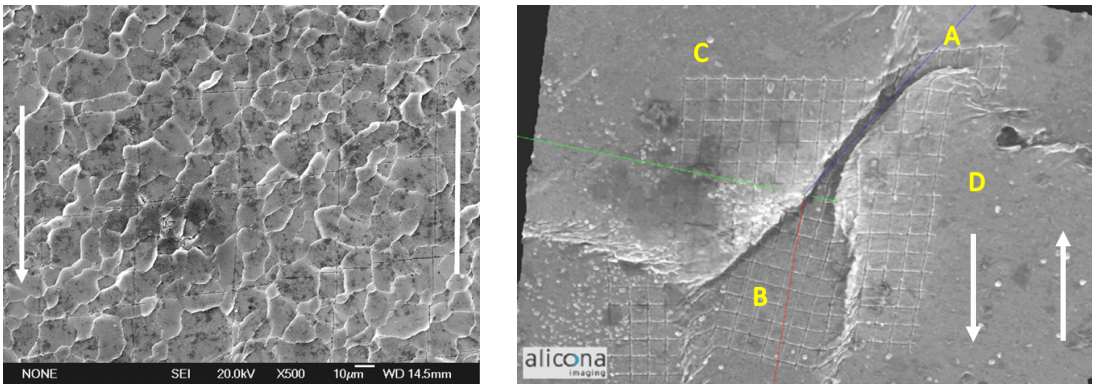

(a) (b)

Figure 2.14: (a) Typical FIB milled mesogrids after a shear strain of 0.20. The arrows show the sense of the shear stress (b) FIB milled microgrids showing grain rearrangement and the approach of C and D grains. The white arrows show the sense of the shear stress [1].

macroscopic geometric degrees of freedom include three variables that represent the misorientation relation between the crystals (two for the unit vector along the rotation axis, $\hat{\rho}$ and one for the rotation angle, θ) and another two variables that specify the the grain boundary plane normal, $\hat{n}$ [68]. The three microscopic degrees of freedom characterise the atomic structure of the grain boundary, which are determined by relaxation processes at the interface. In a periodic atomic structure of the interface, the rigid body displacement, t, of one crystal relative to the other specifies three microscopic degrees of freedom [67]. In summary, the macroscopic degrees of freedom set up the boundary conditions far away from the grain boundary, while the microscopic degrees of freedom adjust in such a way as to reach the equilibrium subject to those boundary conditions with the minimum free energy of the system.

According to the misorientation angles between two crystals, grain boundaries can be classified into low-angle and high-angle grain boundaries. Read and Shockley [69] described the low-angle tilt grain boundary by a configuration of edge dislocation array accommodating the small misorientation between two adjacent grains. As is shown in figure 2.15, the dislocation wall can represent the equilibrium arrangement of primary grain boundary dislocations with Burgers vector having the same sign [70]. However, with increasing misorientation, the dislocation spacing (identified as D in figure 2.15) becomes so small that the individual dislocations lose

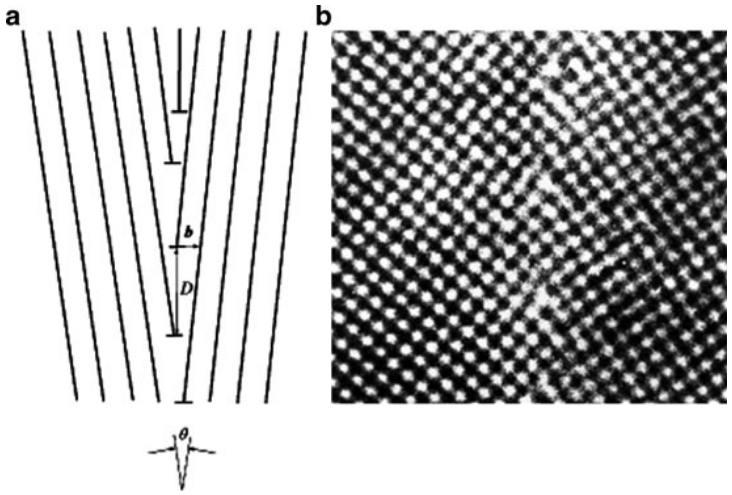

Figure 2.15: (a) Schematic diagram to show the edge dislocation array illustration of a low-angle grain boundary. (b) High-resolution electron microscopy reveals a [100] low-angle grain boundary in molybdenum [70].

their character and overlap one with the other. Overcoming this limit of misorientation angle (usually lying between 13 and 15º) between two adjacent crystals, the dislocation model cannot be further applied to the grain boundary structure, and these boundaries are called high-angle grain boundaries.

The structural unit model was then developed to describe the atomic structure in a high-angle grain boundary, by repeated structural units that represent the particular arrangement of a group of atoms. Due to the limited types of basic structure units, there are only limited number of grain boundaries formed by exclusively single structural units, which are called *singular* grain boundaries [67]. The majority of grain boundaries known as *general* grain boundaries are described by a combination of the basic structural units. The singular grain boundaries usually exhibit sharp minima in the energy-orientation dependence and sharp extremes at any property-orientation dependence [70]. Another widely used model to identify special grain misorientations is the *coincidence-site lattice* (CSL) model. When two crystals are superimposed on each other, if some atomic lattice sites coincide, then these "superlattices" are called *coincidence-site lattice*s. If a grain boundary contains a high density of CSL lattice points, then it is called a CSL misorientation, which has a lower energy than general grain boundaries. This is because

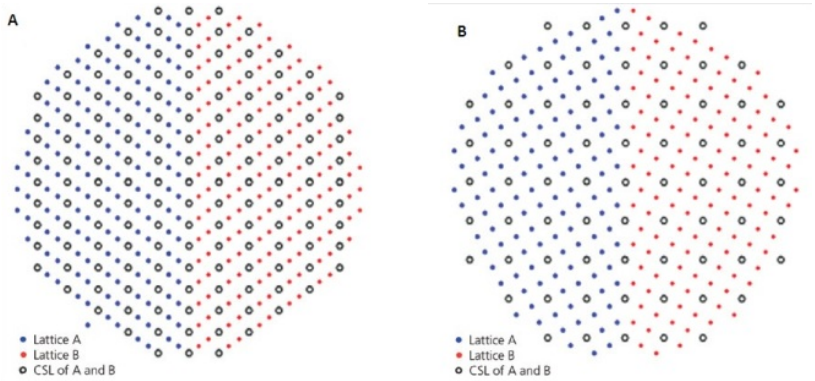

(a) (b)

Figure 2.16: (a) A schematic showing a sigma 3 boundary (twin boundary), which is a 60° rotation about the [111] direction with simple cubic lattice. (b) A sigma 5 boundary is a 36.9° rotation about the [100] direction in a simple cubic material [71].

in a CSL boundary, more atoms coincide with the positions of the perfect crystal as fewer bonds are broken across the grain boundary [70]. A common example of CSL boundaries is a twin boundary as shown in figure 2.16a, in which one out of three lattice sites coincides between the two lattices. A parameter, sigma Σ, is defined as the reciprocal value of the density of coincidence sites to characterise the CSL. Therefore, a twin boundary can be represented by a Σ3 boundary (in a cubic crystal structure) as shown in figure 2.16a. Since sigma value is always an odd number and Σ1 boundary denotes a perfect crystal, a twin boundary has the largest number of coincidence lattice points. It is followed by the Σ5 boundaries, for example, a symmetrical tilt grain boundary with simple cubic lattice as shown in 2.16b.

2.5.1 The Influence of Grain Boundary Structure on Sliding in Cubic and HCP Metals

Grain boundary sliding has been studied in various metals and alloys, such as aluminium [72, 73, 74], copper [75], magnesium [76, 77], zinc [78, 79] and stainless steels [80], etc. Lagarde and Biscondi [72] investigated the initial grain boundary sliding rates in bicrystals of aluminium and copper with a wide range of misorientation angles of grain boundaries. The shapes of the curves (initial sliding rate against misorientation angle) as shown in figure 2.17a and 2.17b are rather similar for aluminium and copper. The low cusps in the curves correspond

to the special grain boundaries related to the FCC crystal structure. Michaut et al. [80] revealed that grain boundaries of exact- or slightly off-coincidence misorientations are relatively resistant to sliding, using stainless steel bicrystals. Watanabe and Davies [75] further studied the difference in grain boundary sliding behaviour and intergranular fracture between low-angle and high-angle grain boundaries. It was found that low-angle grain boundaries had minimal sliding and no intergranular fracture at all.

With the development of transmission electron microscopy, more experimental evidence were obtained to reveal that the grain boundary sliding can take place by crystal lattice dislocations being absorbed into the grain boundary dissociating and moving along the boundary plane by a combination of climb and glide [73, 74]. Researchers have then investigated the relationship of grain boundary structure and crystal lattice dislocations. Pond and Smith [81] and Kokawa [78] have revealed that the crystal lattice dislocations are more difficult to dissociate in the grain boundaries of higher degree of ordering compared with random boundaries. This is due to the lower grain boundary energy associated with the exact- or slightly off-coincidence orientations. Observation of extrinsic grain boundary dislocations by TEM has further demonstrated the difficulty of dissociation and absorption of lattice dislocations at the ordered grain boundary [82]. Moreover, Assassa et al. [83] have found that grain boundary diffusion is more difficult in those highly ordered boundaries, which is possibly due to the low vacancy concentration in these boundaries than in random high-angle boundaries [84]. However, in 1970s and 1980s, there was still no systematic research to directly correlate the tendency to initiate grain boundary sliding with grain boundary structure.

In 1993, Kato and Mori [85] investigated the boundary-dependent capability of grain boundary sliding by measuring the internal friction using bicrystals of copper with various [001] twist boundaries. Cylindrical rod-like bicrystal specimens underwent torsion tests at elevated temperatures, and the specimens were twisted by an angle at the boundary induced by grain boundary sliding. Assuming the grain boundary slides in a viscous manner, the angle measured at the grain boundary could be correlated to the activation energy of the grain boundary

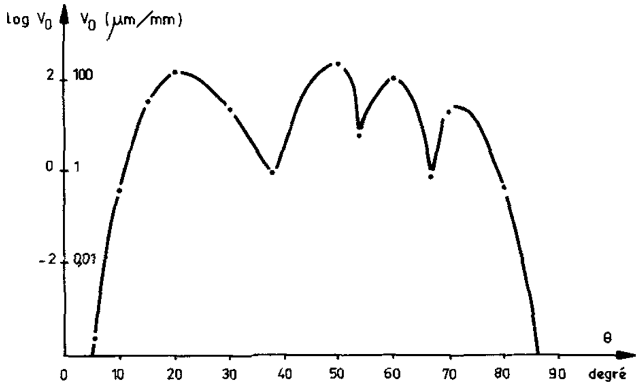

(a) Aluminium

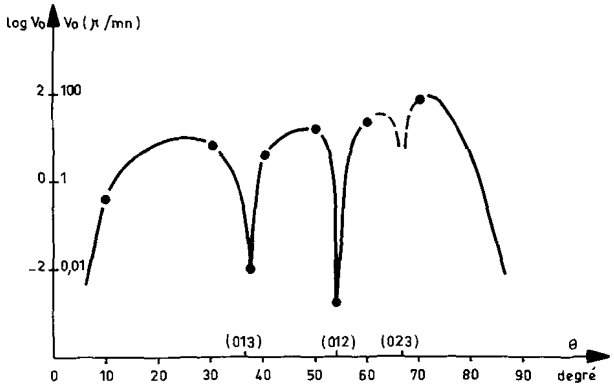

(b) Copper

Figure 2.17: Influence of grain boundary misorientation on the initial sliding rate in bicrystals of (a) aluminium under a shear stress of 0.2 MPa along the <100> axis at 400°C. (b) The same plot on bicrystals of copper, under a shear stress of 1 MPa along the <100> axis at 600°C [72].

sliding. It was found that the activation energy depends heavily on the misorientation angle, θ, as shown in figure 2.18a. The lower the activation energy, the easier the grain boundary sliding becomes. The minimum activation energy corresponds to $\theta = 34^{\circ}$, while the activation energy increases by three times at $\theta = 36.9^{\circ}$. Such a misorientation-dependent sliding capability could be related to the boundary energy as shown in figure 2.18b. Mori et al. [86] measured the energy of the [001] twist boundaries using Cu-SiO2 bicrystals. The copper boundary energy γ_B is normalised by the interfacial energy γ_I between copper and SiO2 particles, which was found to be sensitively dependent on the misorientation angle as well. The low energy cusps in the curve correspond to the low coincidence site lattice (CSL) boundaries, for example $\theta = 36.9^{\circ}$, $\sum 5$ boundary. A comparison between the two figures 2.18 indicates that low-energy CSL boundaries have a larger activation energy for grain boundary sliding than

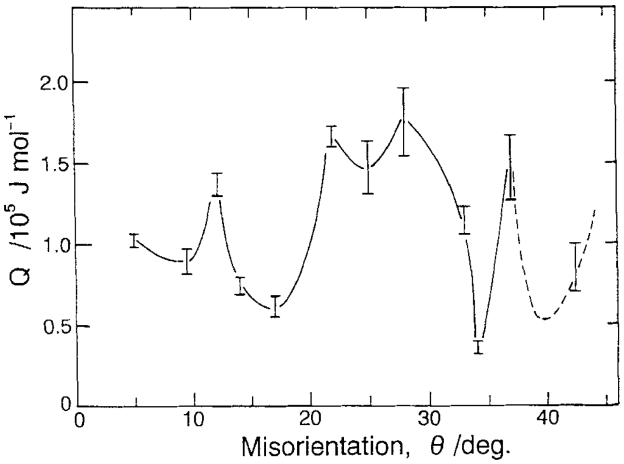

(a) Measured activation energy for grain boundary sliding for boundaries with various misorientation angles [85].

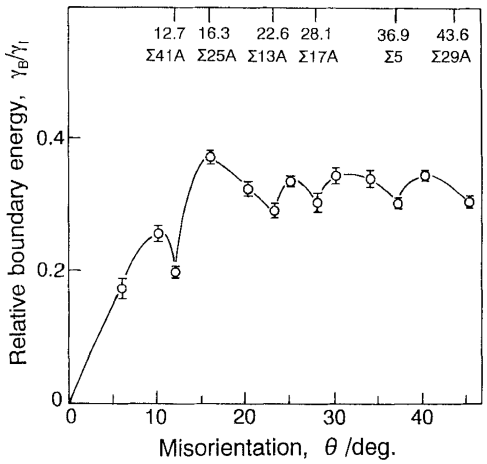

(b) The dependence of normalised grain boundary energy of copper [001] twist boundaries on the misorientation angle [86].

Figure 2.18: The comparison of the misorientation-dependence of activation energy for grain boundary sliding and grain boundary energy of copper [001] twist boundaries.

high-energy boundaries. Therefore, high-energy random boundaries slide more easily due to the less ordered atomic structure. Unlike Kokawa et al.'s [82] approach of correlating crystal lattice dislocation to grain boundary sliding, Kato and Mori [85] attributed sliding to grain boundary diffusion. They believe that the activation energy of both grain boundary sliding and diffusion depends on the inherent structure of a grain boundary. Low-energy CSL boundaries have higher activation energies for diffusion and thus sliding as they are poorer sources or sinks for fluxes of atoms.

2.5.2 The Influence of Grain Boundary Structure on Sliding in Tin

Research on the thermomechanical properties of tin-based solder joints have revealed the dependence of reliability on Sn grain size, orientation and grain boundary characters. Grain boundary sliding has been identified as one of the main causes of damage in lead-free solder joints [87]. It was found that boundary damage by grain boundary sliding tends to occur on random boundaries rather than on low-energy CSL boundaries [88]. Furthermore, intergranular cracks prefer to propagate through random boundaries due to their high energies. In Terashima et al.'s [88] work, the special boundaries were defined as high-angle $\sum$ boundaries, which were

Low-angle Boundaries			High-angle Boundaries					
Angle	7.3º	14.3º	22.3º	28º	43º	58º twin	62º twin	71º
Axis	[110]	[100]	[110]	[001]	[100]	[100]	[100]	[100]
CSL	$\Sigma 30$	$\Sigma 16$	$\Sigma 27$	$\Sigma 17$	$\Sigma 21$	$\Sigma 11$	$\Sigma 31$	$\Sigma 21$

Table 2.2: Commonly observed special boundaries in Sn-based solder joints [87].

found to be resistant to grain boundary sliding. Telang and Bieler [87] found that thermomechanical fatigue causes low-angle tilt boundaries to form, which were found to have sliding and lead to damage. The authors have summarised the most frequently present special boundaries observed in Sn-based solder joints (table 2.2).

Telang et al. [89] further identified that the favoured misorientations are ~7º, ~14º and ~22º with rotations about a [110] axis, which have coincidence site lattices (CSL) as shown in figure 2.19. These misorientations are close to, but not at CSL orientations. Then misfit dislocations are necessary in the boundary plane to keep the boundary energy as close to that of the CSL boundary. The authors believe it is climb of misfit dislocations in the boundary plane that causes grain boundary sliding. However, there was no direct evidence provided of climb of misfit dislocations in the boundary planes of these low-angle boundaries.

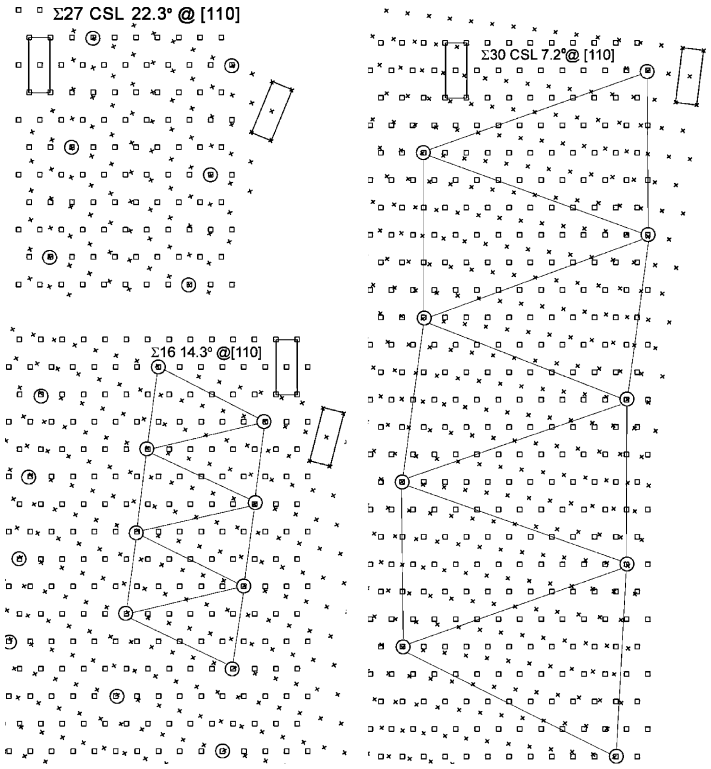

Figure 2.19: Coincident site lattice (CSL) arrangements for favoured misorientations ~7º, ~14º and ~22º with rotations about [110] axes. These misorientations are close to, but not at exact coincidence orientations. Then misfit dislocations are necessary in the boundary plane to keep the boundary energy as close to that of the CSL boundary [89].

2.6 Micro-cantilever Testing

A variety of mechanical techniques at micro- and nano-scale have been developed. Photolithography was initially used to manufacture micro-mechanical testing specimens in silicon-based materials. Mechanical properties of the substrate material or deposited material have been measured using micro-bending, tensile or compression tests. For example, micro-cantilevers produced by conventional lithography and wet etch techniques were used by researchers to measure the mechanical properties of thin films, including residual stress [90], elastic and plastic properties [91] and fracture toughness [92]. However, the cantilevers fabricated by these conventional techniques have a number of serious problems. The repeatability of Young's modulus or yield stress measurements is poor [93]. The initial deflection from residual stresses is inevitably present in these cantilevers [94]. In addition, the range of materials that can be

studied by testing these cantilevers is rather limited as the materials have to be deposited on a silicon substrate. Thus, other micro-mechanical testing methods were developed for accurate measurement of mechanical properties of various materials.

Nanoindentation was adopted to measure the elastic modulus and hardness. In spite of its ease of use, speed and applicability to almost all materials, it has a few limitations as well. Firstly, the stress states of the materials under the indenter tip are relatively complex. There is a plastic and elastic zone of deformed material around an indent, but the size and magnitude of them are not well understood [95]. Secondly, the elastic and plastic properties are greatly dependent on crystallography [96]. The mechanical properties obtained by nanoindentation will be an average over many crystallographic directions. Finally, measuring mechanical properties (such as yield stress or fracture toughness) from the load-displacement data is rather difficult and inaccurate. These limitations of nanoindentation drive the development of other micro-mechanical testing techniques.

In 2000, a focussed ion beam (FIB) was used by McCarthy et al. [97] to mill cantilevers in silicon to study the mechanical properties of thin films. Since then, the development of FIB techniques has enabled the fabrication of micro-test specimens in various geometries in the scale of micro- and even sub-micrometres. These micro-specimens can be deformed using a high-sensitivity instrumented indentation device like a nanoindenter. A Berkovich indentation tip is usually used in micro-cantilever tests and a flat-punch tip is usually adopted in micro-pillar tests. In 2005, Maio and Roberts [98] first applied this technique to studying the fracture properties of cantilevers in a thin hard tungsten carbide coating on steel. Since then, the method of milling micro-cantilevers has been employed to investigate a variety of mechanical properties of bulk materials, such as elasticity [99, 100], plasticity [101, 102, 103, 104], fracture [98, 105], fatigue [106] and stress corrosion cracking [105, 107]. By placing some particular microstructural features (e.g. grain boundaries) in the cantilevers, the mechanical properties of these features can be investigated individually [107, 108]. Such site specific investigations were not possible through traditional macro-mechanical tests.

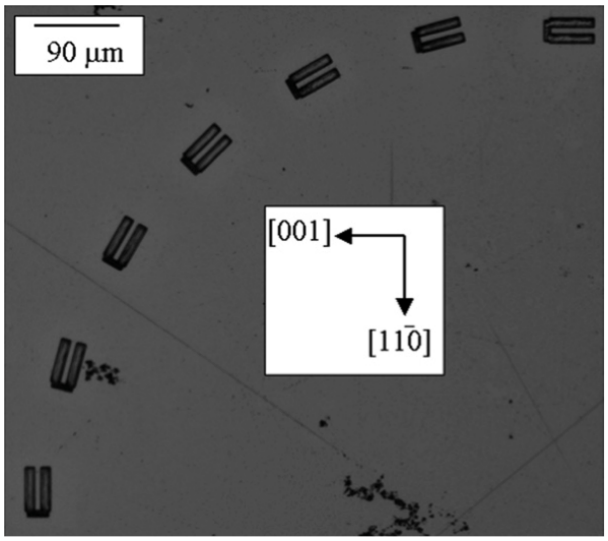

Figure 2.20: Optical micrograph showing a series of micro-cantilevers with various crystallographic directions in (110) face of single crystal copper, including 0°, 15°, 30°, 45°, 54°, 60°, 75°, and 90° with respect to the [001] direction [99].

2.6.1 Single Crystal

Since many engineering materials show considerable anisotropy in their single crystal mechanical properties, there is great importance to understand their anisotropic elastic and plastic behaviour using single crystalline materials. For example, Armstrong [99] investigated the anisotropy in elastic properties of single crystal copper. A series of micro-cantilevers with the same dimension were milled with their long axes at a variety of angles to the [001] direction as shown in figure 2.20. Armstrong et al. [99] have developed a novel approach to study the anisotropy of mechanical properties through micro-cantilever tests, which provided experience and inspiration for later research.

Gong and Wilkinson [100] carried out similar microcantilever tests to measure Young's moduli of hexagonal α-Ti in various crystallographic orientations. A series of cantilevers were made at various orientations in a single grain as shown in figure 2.21a. Multiple loading method was used to separate bending of the cantilever from flexure at the "fixed" end. The elastic modulus was calculated using the the simple beam theory, which was found to decrease as the load point moved closer to the built-in end. Unlike Armstrong et al.'s method of keeping the aspect

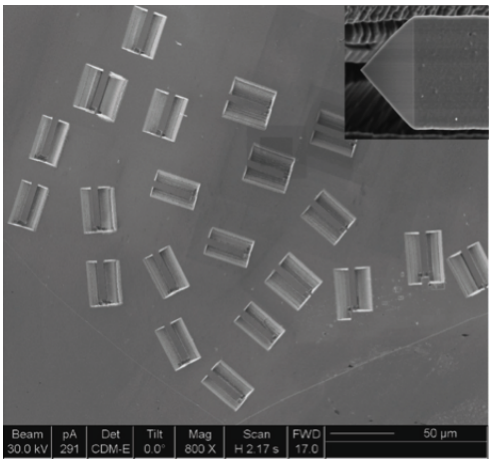

(a)

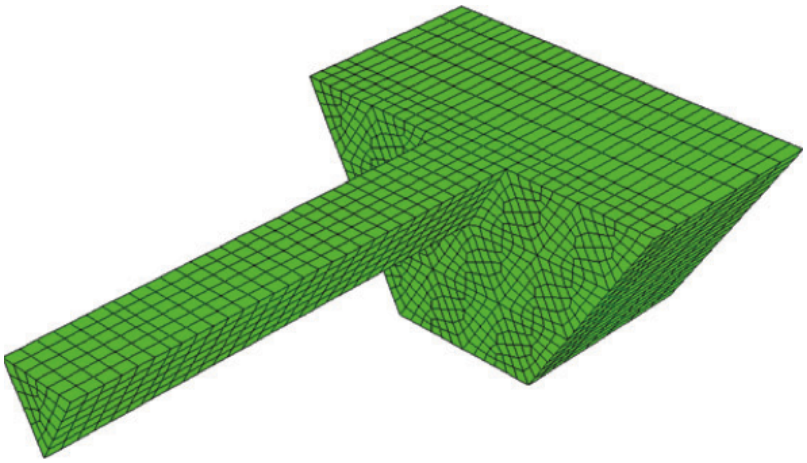

(b)

Figure 2.21: (a) SEM micrograph of the cantilevers milled at various orientations in that grain (b) Finite-element modelling (FEM) of a cantilever to measure the Young's modulus [100].

ratio greater than 6 for the multiple loading tests, Gong and Wilkinson have instead used finite-element modelling (FEM) to account for the effects of flexure at the built-in end (figure 2.21b). The value of Young's modulus is determined by fitting the stiffness of the beam in the model to that of experiments. This study was one of the first to apply FEM to the measurement of mechanical properties using microcantilever tests. Using the same approach of microcantilever testing coupled with FEM, plastic properties were also measured, such as the critical resolved shear stress [109, 110], yield stress [111] and fracture toughness [112].

Other than triangular cross section in micro-cantilevers, there are other geometries investigated. For example, Motz et al. [102] investigated the size effect of the flow stress in micro-

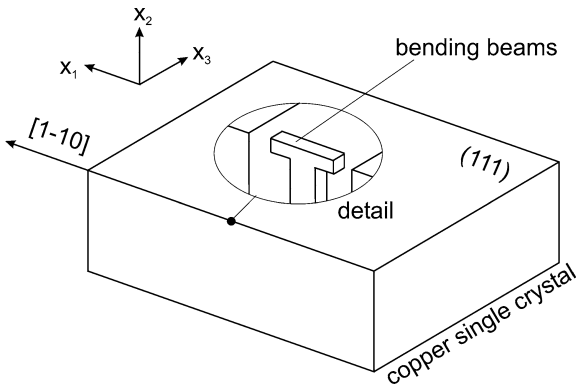

(a)

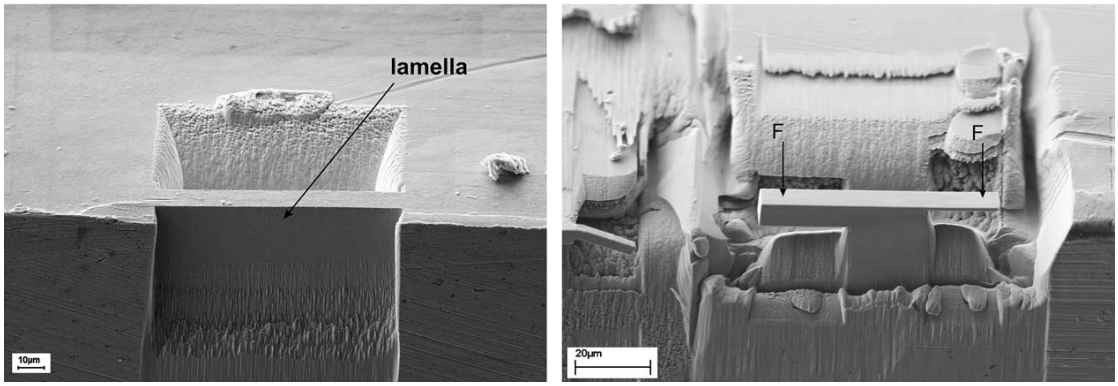

(b)

Figure 2.22: (a) Orientation of the micro-bending beams on the edge of the copper single crystal (b) The fabrication procedure of the micro-bending beams: from milling a lamella in the vicinity of the sample's edge to machining out the beams from the lamella [102].

bending beams with a rectangular cross section fabricated by FIB. The micro-bending beams were milled on the edge of the sample (figure 2.22a). The advantage of using the rectangular cross-sectioned beams is that the strains are equal at the top and bottom surfaces, whereas in triangular cross section design, plasticity is always initiated at the bottom of the cantilever [110]. However, Motz et al.'s method of fabricating the micro-beams is relatively difficult, and also dependent on there being a suitable specimen edge available with a desirable crystallographic orientation. What is more, from figure 2.22b it can be noted that the aspect ratio of beams was not held constant. Compared to this procedure, Armstrong et al.'s [99] approach is

more applicable to manufacturing cantilevers anywhere on the sample in most materials.

2.6.2 On Grain Boundaries

Grain boundaries play an important role in engineering materials. The mechanical properties of grain boundaries have been studied by growing bicrystals at the macro scale [113, 114]. This was not only time consuming and expensive, but also had limitations on the type of material and the number of boundaries to be studied. What is more, the grain boundaries in bicrystal samples are usually special ones. The grain boundary crystallography, structure and chemistry in these bicrystals are not representative of the general grain boundaries in polycrystalline materials. Therefore, new techniques were needed to measure the mechanical properties of individual general grain boundaries.

2.6.2.1 Crack Growth along Grain Boundaries

Armstrong et al. [105] have developed a method for manufacturing micro-cantilevers containing a single grain boundary in a 304 stainless steel. In addition to the general procedure of milling micro-cantilevers, care was taken when milling trenches to make sure that a single grain boundary was located close to the fixed end of the cantilever. A small notch was made at the grain boundary. Then the cantilever was tested by the nanoindenter/atomic force microscope system. The specimen was held at a certain load and submerged in the active solution to induce stress corrosion crack (SCC). The displacement of the indenter as a function of time, which was associated with the crack growth, was compared among micro-cantilevers submerged in and out of the active fluid. It was found in this work that stress corrosion crack growth was the main cause of the rapid increase of displacement with time of the micro-cantilevers tested in the active solution. The method used has inspired more mechanical properties of individual grain boundaries to be measured by machining micro-cantilevers. However, there were no quantitative measurements of the crack length. Furthermore, the resistance to SCC of individual grain boundaries was not correlated to grain boundary character and composition.

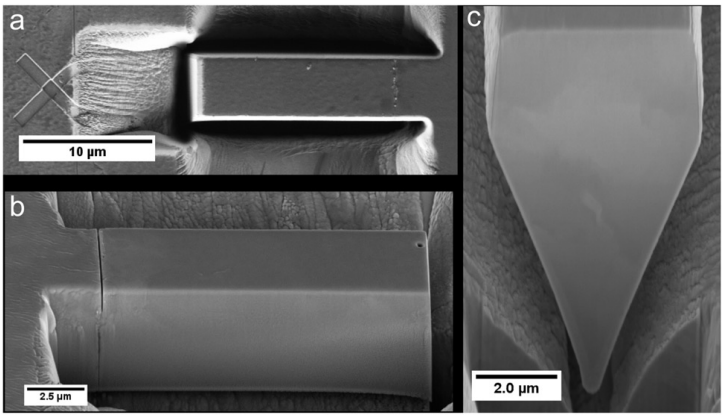

Figure 2.23: (a) Trenches were milled to ensure accurate placement of the grain boundary with the help of an automatic alignment cross. (b) The orientation of the grain boundary plane is examined by the side profile of the cantilever. A sharp notch can be seen at the grain boundary as well. (c) Tilt-corrected end image of micro-cantilever showing the pentagonal cross section [108].

2.6.2.2 Fracture Toughness of Grain Boundaries

Armstrong et al. [108] applied the micro-cantilever testing method to measuring the fracture toughness of selected grain boundaries in bismuth-embrittled copper. Micro-cantilevers were milled by FIB with a single grain boundary near the fixed end. The grain boundary was close to normal to the sample surface (figure 2.23). EBSD analyses were carried out to characterise the grain boundaries, including the boundary misorientation angle, the orientation of the crystallographic axis and the crystallography of the grain boundary plane in the associated pair of grains. After the cantilevers were tested by the nanoindenter/AFM system, the grain boundary misorientation and fracture toughness were tabulated.

SEM images were taken before the test to measure the dimensions of cantilevers. The fracture surface or side view of undeformed cantilevers were also inspected in SEM after testing. It was found that some cantilevers failed suddenly with fracture at the grain boundary, while some cantilevers yielded by plastic deformation but did not fracture. The fracture toughness is plotted against the grain boundary misorientation angle as shown in figure 2.24(a). There is no clear relationship between the fracture toughness of individual grain boundaries and the angle of rotation in each pair of grains associated with the grain boundary. The grain boundary

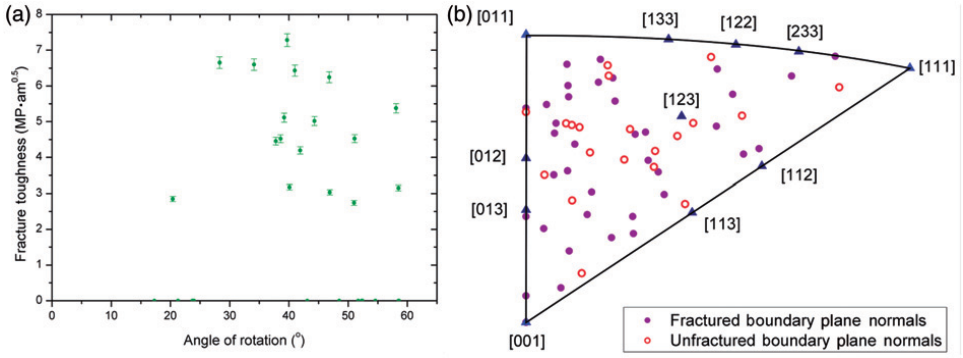

Figure 2.24: (a) Plot of fracture toughness versus angle of rotation about a shared crystallographic axis in each pair of grains. (b) Both fractured and unfractured grain boundary normals are plotted in an inverse pole figure [108].

plane normals are also identified in the inverse pole figure 2.24(b), which again shows little correlation between grain boundary normals and fracture behaviour. TEM-EDX analysis was also carried out to investigate the influence of bismuth segregation to grain boundaries on their fracture behaviour.

2.6.2.3 Elastic-plastic Fracture of Grain Boundaries

Kupka and Lilleodden [115] carried out similar micro-cantilever tests to quantitatively measure the fracture properties (fracture strength) of individual grain boundaries in an aluminium-lithium alloy. They made cantilevers with a rectangular cross-section rather than a pentagonal one in Armstrong et al.'s [108] work. A rectangular cross-section maintained a constant crack width, which made the calculation easier. However, these cantilevers could only be fabricated on the edge of the sample. A U-notch was made by FIB milling from the side of the cantilever at the location of grain boundary (figure 2.25a). Compared to the sharp notch made by FIB line milling [108], the U-notch not only introduces a stress concentration, but also overcomes the problem of determining the notch radius for further analysis. However, the U-notch is blunt and there is no sharp pre-crack. Figure 2.25b shows that crack initiated at the notch and propagated along the grain boundary. A nanoindenter system was used to deflect the cantilevers as well as constantly measure the stiffness during the test, in order to monitor crack initiation and propagation at grain boundaries. In Gong and Wilkinson's [100] work, FEM was applied

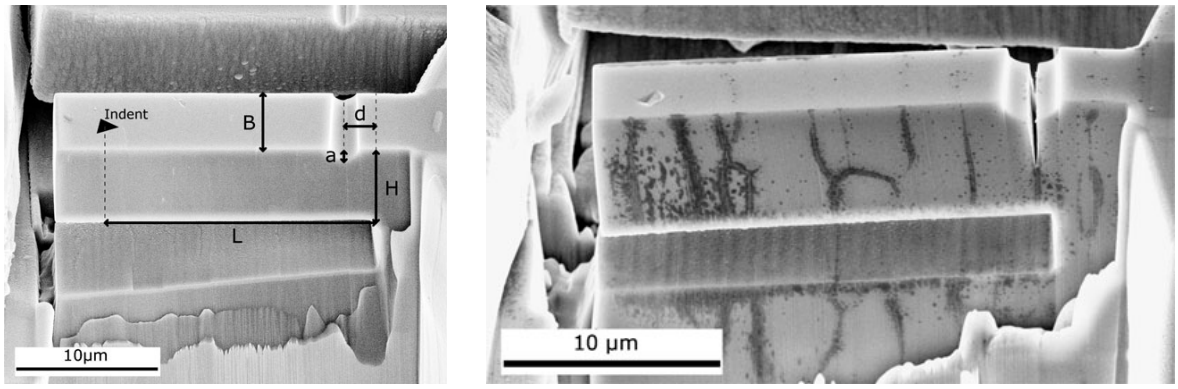

(a) (b)

Figure 2.25: (a) SEM image before testing shows the dimensions, location of grain boundary with a U-notch. (b) SEM image after testing shows that fracture occurred at the selected grain boundary [115].

to account for the flexure at the fixed end of the cantilever. Similarly, Kupka and Lilleodden [115] carried out finite element analysis to normalise the load and stiffness in order to allow quantitative comparison between boundaries. In the authors' following work [116], fracture analysis of individual grain boundaries was performed using a traction-separation law associated with cohesive zone modelling of the grain boundary. Furthermore, the anisotropic plastic deformation of individual grains was described in a crystal plasticity finite element method (CPFEM), which was incorporated into the finite element model of fracture analysis. This enabled simulation of the fracture behaviour of the grain boundary and the anisotropic plastic deformation in the vicinity of a grain boundary. The combination of micro-mechanical testing and finite element modelling allowed a better understanding of the fracture properties of grain boundaries.

2.7 Micro-pillar Testing

The manufacture of micropillars by FIB is another method to investigate the mechanical properties and deformation mechanisms of metallic materials. Annular milling patterns in FIB are used to machine cylindrical compression samples into the surface of a bulk material [117]. A series of decreasing beam currents are used to reduce the tapering effects on the edge of the

pillars. The final micropillar samples are attached to the bulk at the end. Micropillars are then tested by compression using a nanoindenter device with a flat-punch tip. The load and displacement data can be converted to a stress-strain curve in a straightforward process that is similar to that used in macro-compression tests [118]. Due to the ease of manufacture, test and data analysis, micro-compression tests on micropillars have been carried out by many researchers to investigate various mechanical properties. Similar to micro-cantilevers, individual microstructural features like grain boundaries can be isolated and studied in micropillars.

2.7.1 Size Effects in Single Crystals

Uchic et al. [117] carried out compression tests on Ni and Ni alloy micropillars to investigate the size effects on the mechanical properties of single crystals. Micropillars were produced with diameters ranging from 0.5 to 40 μm on a bulk single crystal of pure Ni in a single slip orientation. These were compressed by a nanoindentation device fitted with a flat-punch indentation tip. As shown in figure 2.26(a), the micropillars with diameters from 20 to 40 μm exhibit similar behaviour to that for bulk samples. In samples with a diameter of 10 μm, the yield stresses are much higher than that for bulk samples and there are a few bursts of deformation. For samples 5 μm in diameter, the yield stresses are significantly higher than the micropillars with diameters of 20 μm or larger. What is more, there are large and rapid strain bursts which are absent in bulk samples. SEM images after testing suggest that there are fewer but much more active slip bands (indicated by the large single-slip plane displacements). Uchic et al. proposed that the size effect is related to the change in the mechanisms for plastic flow (e.g. defect multiplication and storage). However, they did not give a persuasive explanation of the large yield stresses and rapid strain bursts observed in small length-scale samples.

Greer et al. [119] explored the size effects on single-crystalline gold by making pillars with diameters from 300 to 7450 nm. It was found that the micro- and nano-pillars have a much higher yield strength than that of bulk gold at 2% strain. What is more, flow stresses at 10% strain increase sharply as the pillars get smaller than a critical diameter. This relationship is

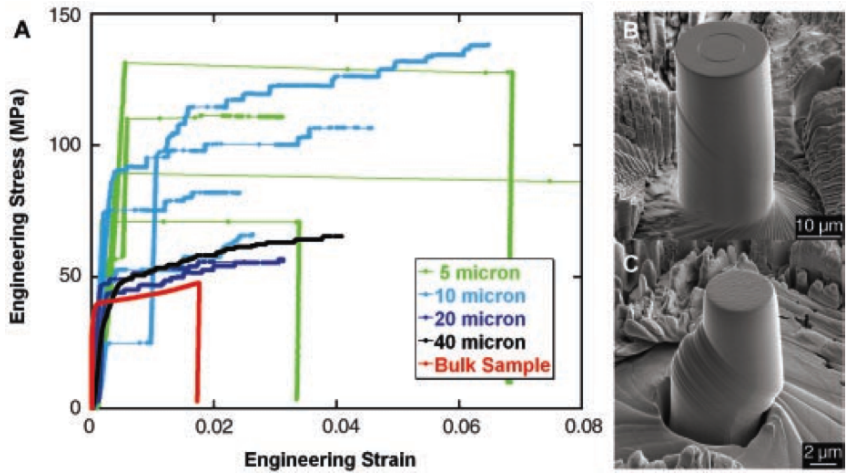

Figure 2.26: (a) Stress-strain curves for micropillars with diameters ranging from 5 to 40 μm, in comparison with a bulk single crystal pure Ni sample. (b) SEM image of a micropillar of 20 μm in diameter tested to 4% strain. (c) SEM image of a 5-μm-diameter micropillar after testing, where a rapid burst of deformation occurred within 0.2 seconds to a strain of 19% [117].

governed by an exponential law as shown in figure 2.27. The authors attributed this significant size effect to "dislocation starvation" in the crystal. The dislocation starvation model claims that dislocations inside small crystals travel much shorter distances before annihilating at the free surface, which inhibits multiplication of dislocations. Therefore, new dislocations have to nucleate either at surfaces or in the bulk of the crystal to accommodate further deformation. This requires much a higher stress than that for the dislocation multiplication mechanism. Even though Greer et al. [119] proposed a model to explain the extraordinarily high stresses for nano-pillars, the hypothesis was not fully developed at that point. No experimental evidence could support the proposed model of dislocation starvation.

Other than Ni and Au, this "smaller is stronger" trend has been found in a wide variety of materials, such as Cu [120], Mo [121, 122], W and Nb [123]. This size effect was attributed by Kim et al. [122] and Lee et al. [124] to the influence of free surfaces on the behaviour of dislocations as the sample size is reduced below some critical value. Furthermore, the stress-strain curves of the compression tests on single-crystalline micro- and nano-pillars show intermittent discrete strain bursts, which suggests a dislocation avalanches mechanism distinctive from the bulk [125]. However, the observations made from the cubic crystal structures could not

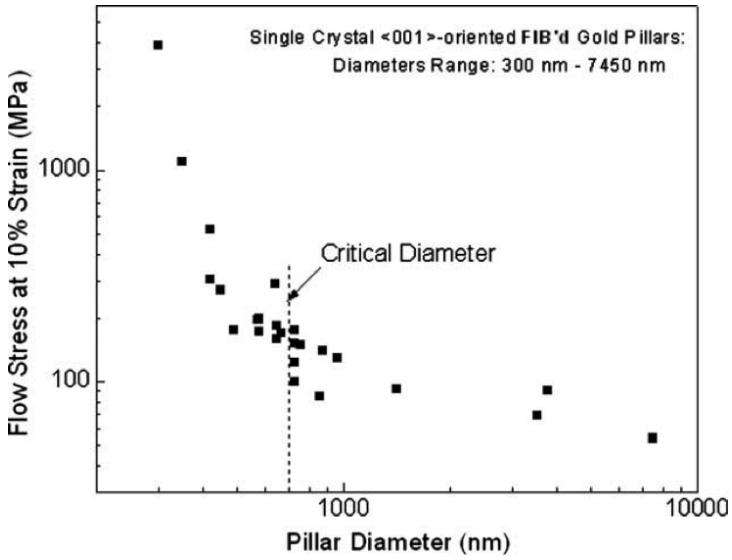

Figure 2.27: The relationship between flow stress at 10% strain and the diameter of pillars in single crystal gold, which shows micropillars smaller than a critical diameter have much higher flow stresses [119].

be extrapolated to other more complex systems, such as Sn with a Body Centred Tetragonal (BCT) structure. Philippi et al. [126] used various sized micropillars of Sn to explore the size effects for single crystalline BCT β-Sn at room temperature (60% of the melting point). In order to investigate the effect of orientation anisotropy on the deformation behaviour, similar compression tests were conducted on micropillars with two different crystal orientations.

The stress-strain curves for cylindrical micropillars orientated in [110] (along the loading direction) with a diameter of 10 μm, 5 μm, 3 μm and 1 μm are shown in figure 2.28a. The larger 10 μm pillars show similar flow stress values as that for bulk samples, while smaller pillars exhibit increasing flow stresses with decreasing sample sizes. The pillars with the same size show similar deformation behaviour, indicating the reproducibility of the compression tests. Another set of pillars of various sizes were made in a different orientated single crystal with [001] direction along the loading axis. For the same sample size, the flow stress values in the [001] direction are evidently higher than those in the [110] direction. This indicates that the crystal is stronger when loaded parallel to the shorter c-axis of the BCT structure than perpendicular to the c-axis. Nonetheless, as shown in the log-log plot of flow stress versus sample

width (figure 2.28b), the size effect is comparable in both orientations. The post-mortem SEM analysis revealed that deformation occurred by multiple slip events, and the two orientations had different operating slip systems.

Philippi et al. [126] also carried out μLaue diffraction analysis on the deformed pillars and found that geometrically necessary dislocations (GND) were almost absent. This ruled out the possibilities of strain hardening and twinning during the deformation. The size dependence of flow stress was attributed to the ability of highly mobile dislocations to overcome obstacles at almost 60% of the melting temperature. The high homologous temperature provides the activation energy for dislocation climb or cross slip. The low scatter of flow stress levels for pillars with the same size and orientation, together with the lack of GND storage, further indicated that the highly mobile dislocations accommodated the imposed large strains at such a high homologous temperature. Philippi et al.'s studies not only investigated the notable anisotropy of mechanical properties of Sn, but also suggested distinguishable deformation mechanisms at high homologous temperatures.

2.7.2 Plastic Deformation Mechanisms of Tin

2.7.2.1 In-situ SEM Testing of Tin Micropillars

The development of compact nanomechanical test instruments has enabled in-situ observation of the deformation process throughout the test. The testing probe is controlled with extreme accuracy while simultaneously imaging in the SEM. Lupinacci et al. [127] have conducted in-situ micropillar compression tests to investigate the deformation mechanisms of pure Sn at room temperature and below the ductile-to-brittle transition temperature (DBTT). A number of micropillars were manufactured in the same grain and compressed in-situ inside a scanning electron microscope (figure 2.29 [127]). Half of the pillars were tested at room temperature, which exhibited slip, i.e. dislocation plasticity. The other half of them were tested under the same strain rate at –142°C, well below the macroscopic DBTT of Sn, which showed a significant increase in strength and and uncontrolled strain bursts after reaching maximum strength.

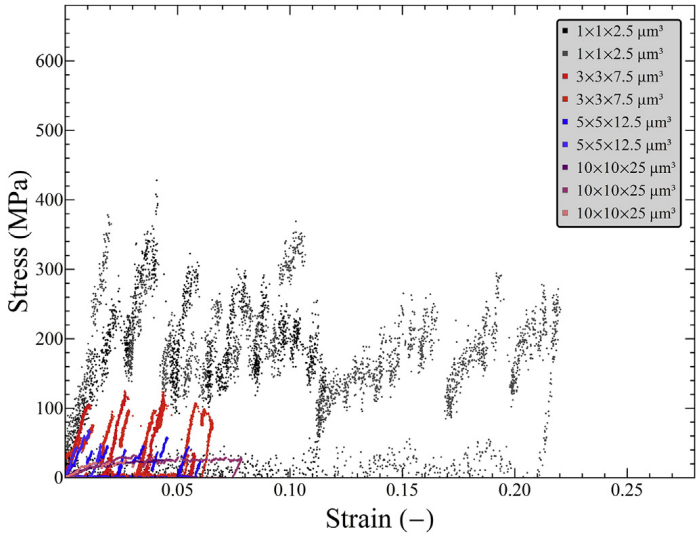

(a)

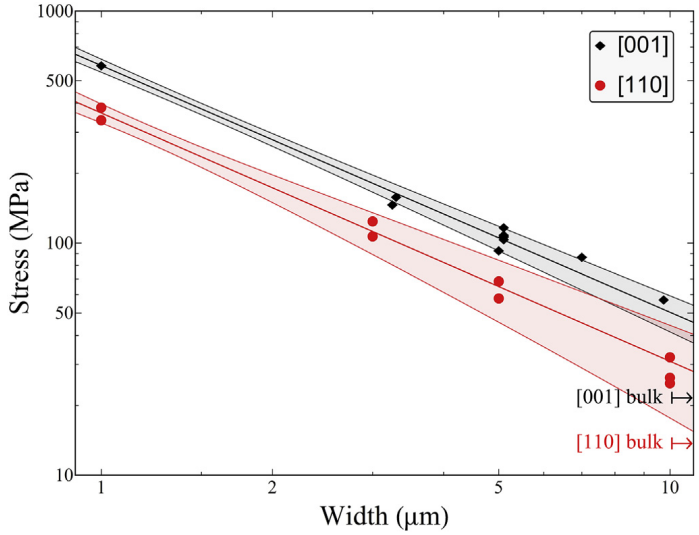

(b)

Figure 2.28: Micropillar compression test results show the size dependence of flow stress. (a) Engineering stress-strain curves for pillars with a diameter of 1, 3, 5 and 10 µm orientated in [110] direction. (b) The flow stress versus pillar width data for [001] and [110] orientations can be represented by a power-law like behaviour (log-log plot). The stress values for [001] and [110] single-crystal compression tests on samples with 6 mm nominal diameter, are shown by black and red arrows respectively. The stress values for larger 10 µm pillars are comparable with those for bulk samples [126].

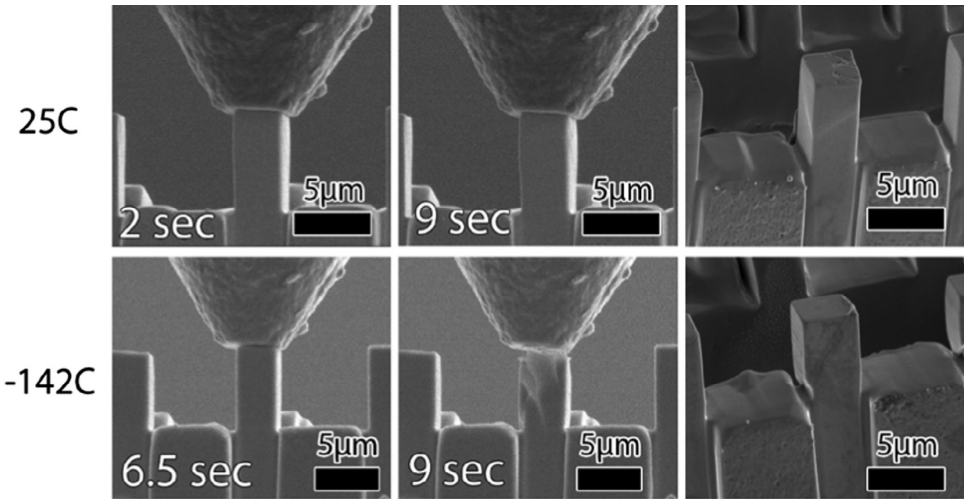

Figure 2.29: SEM micrographs from in-situ compression tests on Sn micropillars at room temperature (top row) and -142°C (bottom row). Top row: images from left, middle to right shows the micropillar near the start of the room temperature test, towards the end of the room temperature test, and after the room temperature test. Bottom row: the same set of images for the cryogenic compression test. Note that in the middle image, the cryocompressed pillar lost contact with the indenter tip towards the end of the test [119, 127].

Through subsequent electron microscopy characterisation using EBSD and transmission EBSD (t-EBSD), it was found that all of the cryocompressed micropillars exhibited twinning. The two twin orientations observed were consistent with previous observations of the {301} and {101} twin planes in Sn [128]. TEM analysis further confirmed that the room temperature compressed micropillar had a high density of dislocations without any evidence of twinning. In the cryo-compressed micropillars, twin boundaries were revealed in TEM micrographs and the interiors of the parent and twinned grains were relatively free of defects. The in-situ SEM cryogenic compression tests have enabled a systematic study of plasticity mechanisms below DBTT for the first time. It also provided a better understanding of the plastic deformation by twinning, when dislocation motion becomes limited at the very low temperature.

2.7.2.2 Interaction between Slip and Twin/Grain Boundaries in Tin

Most of the micromechanical studies have been focused on FCC and BCC materials. The deformation behaviour cannot be extrapolated to Sn as it has a Body Centred Tetragonal (BCT) structure, which induces highly anisotropic elastic and plastic properties [129]. Research has

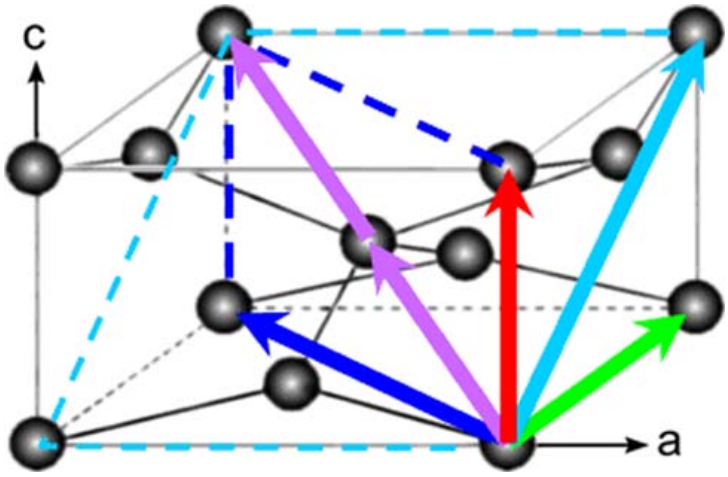

Figure 2.30: A unit cell in Sn with a Body Centred Tetragonal (BCT) crystal structure with $a = 5.832\mathring{A}, c = 3.182\mathring{A}$, $c/a = 0.5456$. The coloured arrows reveal the slip directions in Sn [131].

been carried out to reveal the slip systems in Sn as shown in figure 2.30 [130, 87, 131]. However, there is not enough understanding on the effect of different kinds of boundaries on its deformation behaviour. Kaira et al. [132] used micropillars of pure Sn to study the deformation behaviour at twin and random grain boundaries in comparison to that of single crystals. A special directional solidification technique enabled grain boundaries to be aligned perpendicular to the sample surface. Bicrystalline micropillars were fabricated at both special and random grain boundaries, while single-crystalline ones were milled on either side of these respective boundaries. The micropillars were tested under displacement control at a nominal strain rate of $\sim 10^{-3}s^{-1}$.

Two major types of twin boundaries in Sn, 57.2°[100] along (301) twin plane and 62.8°[100] along (101) twin plane, were selected to mill a few micropillars. It was found from the engineering stress-strain curve that bicrystalline pillars with twin boundaries showed an early yielding behaviour with multiple small strain bursts, in comparison to their single-crystalline counterparts. Post compression SEM micrographs revealed the similar slip behaviour between the bicrystalline and single-crystalline micropillars of one of the component crystals. As shown in figure 2.31, the slip direction in the bicrystalline pillar (b) is similar to that in the single-crystalline counterpart (a). The slip traces and shear bands running through the boundary

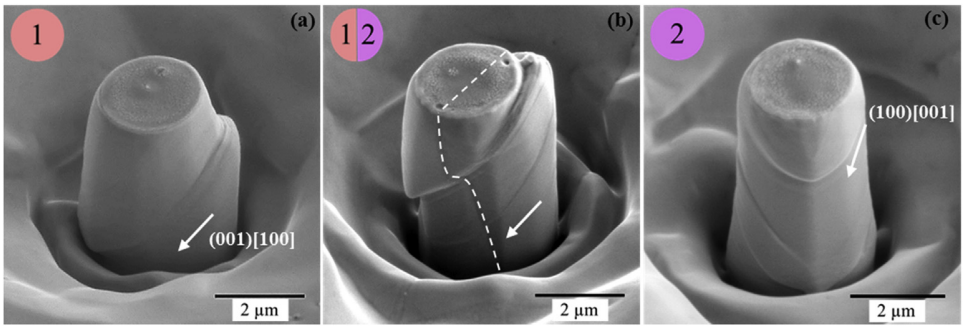

Figure 2.31: Post-compression SEM micrographs showing the deformation behaviour in micropillars around the (301) twin boundary that is highlighted using dashed line in (b). (a) and (c) show the single-crystal pillars on either side of the twin boundary with the slip systems identified. Direction of slip (indicated using white arrows) in the bicrystalline micropillar (b) is similar to that in the single-crystal counterpart (a) [132].

indicated that slip transmission occurred at the twin boundary. This behaviour was similar to that found in copper [133], which was attributed to the symmetry caused by the coherent twin boundary's special orientation. Twin boundaries were also found to migrate as a result of deformation. TEM analysis revealed that twin dislocations formed as a result of the interaction between incoming dislocations and the twin boundary. The glide of twin dislocations along the twin boundary caused twin boundary migration. The single-crystalline pillars showed only one active slip system, which correlated to the absence of strain hardening observed in the stress-strain curves. The bicrystalline pillars with randomly oriented grain boundaries showed a significant increase in yield strength compared with their single-crystalline counterparts. The post compression SEM micrographs revealed that slip traces from a component grain were terminated at the grain boundary, which indicates that grain boundaries impede dislocations and slip.

Kaira et al. compared the different interaction mechanisms between slip and twin or random angle grain boundaries. However, there are a few limitations of their studies. Firstly, even though the unique deformation behaviour of twin boundaries was demonstrated, there was only (301) type twin boundary but no investigation on (101) twin boundary. Secondly, only one low-angle and two high-angle random angle grain boundaries were selected, with only one bicrystalline micropillar on each boundary. This could have experimental uncertainty in the

data. Finally, as Sn has a remarkably low melting temperature, one of the main deformation mechanisms, grain boundary sliding, could not be investigated using this micropillar design. Furthermore, in the cases where the boundary was inclined at an angle to the loading axis, grain boundary sliding would have influence on the deformation behaviour. However, the authors were only focused on the slip transfer across the boundaries.

2.7.3 Grain Boundary Sliding in Micro-bicrystals

In the same design as the micropillar with a specific grain boundary [132], if the grain boundary forms an angle with respect to the loading axis, grain boundary sliding could occur under the shear stress on the grain boundary plane. Aitken et al. [134] used micro- and nano-pillars with inclined grain boundaries to investigate grain boundary sliding in aluminium bicrystals. Each pillar contained a high-angle grain boundary with the plane normal oriented at 24~28° to the loading direction. After uniaxial compression testing, rather than crystallographic slip and extensive dislocation activity as would be expected, the dominant deformation mechanism was grain boundary sliding.

As mentioned above, several studies have investigated the deformation of bi-crystalline pillars with a grain boundary oriented along the compression axis [135, 136]. Aitken et al. produced pillars with the grain boundary plane inclined from the loading direction so that there was a shear stress component applied along the grain boundary. The micropillar before uniaxial compression test is shown in figure 2.32(a), with the grain boundary inclined at an angle of 24° from the compression loading axis. The post mortem SEM image (figure 2.32(c)) reveals that even though there were slip lines shown near the top of the pillar, most of the plastic deformation occurred by a single shear offset along the grain boundary plane. Taking a closer look at the image, it can be noticed that the sheared off regions have wavy features that are periodically spaced ~50 nm apart.

The stress-strain response is shown in figure 2.32(b). The micropillar underwent elastic loading until reaching a maximum axial stress of 156 MPa, followed by an abrupt drop of stress to 100

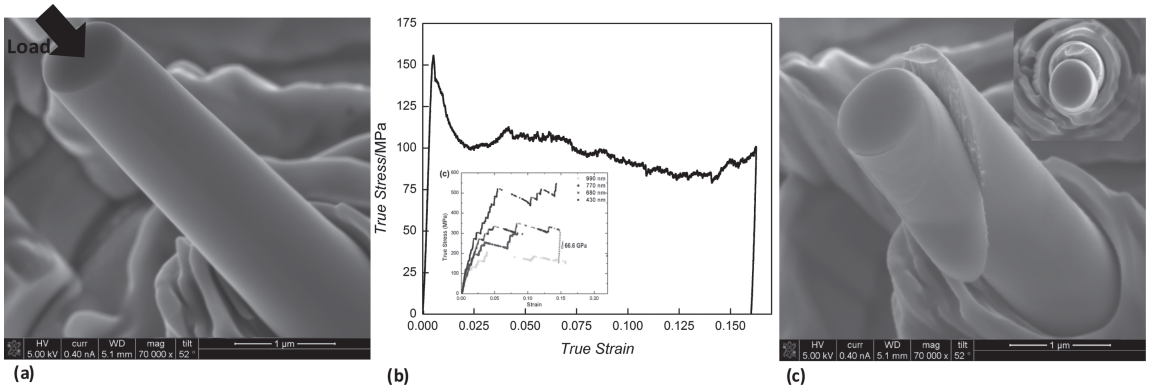

Figure 2.32: (a) An SEM image of an aluminium nano-pillar with a diameter of 900 nm before uniaxial compression. (b) Stress-strain curve of the same pillar, in contrast to that of a bi-crystalline aluminium pillar of equivalent dimensions with a grain boundary vertically oriented (on the bottom left corner) [136]. (c) Post-deformation SEM image showing the top grain sheared off from the bottom grain along the grain boundary plane [134].

MPa at a strain of 2.5%. Then the stress started to increase to 112 MPa at 4.2% strain, before generally decreasing to 79 MPa at 14% strain. Compared to the curves for bicrystalline Al pillars of the same dimension with the grain boundaries parallel to the loading axis (bottom left corner in figure 2.32(b)), there are a few differences between them. The pillars with the grain boundaries along the compression direction exhibited post-elastic hardening, stochastic stress-strain signature (strain bursts that range from 1 nm to 100 nm) and significant crystallographic slip, which were all absent in pillars with grain boundaries inclined from the loading axis. This indicates that the sliding can only occur when there is a shear stress applied along the grain boundary plane.

The most distinct difference of the three discussed above is the continuous stress-strain curve of frictional sliding rather than the stochastic signature of slip. This indicates that the deformation mechanism when there is a shear stress applied to the grain boundary is distinctly different from plasticity driven by dislocation activities. From the perspective of mechanics, the shear stress component along the grain boundary was obtained by resolving the uniaxial compressive stress onto the grain boundary plane, which gave a maximum shear stress of 58 MPa at a strain of 0.5% (the peak compressive stress 156 MPa). In comparison, using uniaxial compression tests on a bi-crystalline Al nanopillar with a vertically oriented grain boundary, Kunz et al.[136]

reported a shear stress of 95 MPa at 7.5% strain resolved onto the principal slip system. This suggests that the critical resolved shear stress for the boundary sliding mechanism is lower than that for crystallographic slip. During grain boundary sliding, softening started to occur after the peak stress with an initial abrupt decrease in stress to 2.5% strain, followed by a gradual softening until 14% strain. The initial abrupt softening was attributed to the inertia at the start of sliding after the initiation of the shear offset on the grain boundary [134]. However, as sliding proceeds, friction force increases until comparable to the shear stress that drives sliding. Then it reaches a steady state of sliding and the stress gradually decreases because the cross-sectional area decreases as the top grain shears off from the bottom one.

Aitken et al.'s [134] work on grain boundary sliding of Al nanopillars at room temperature pioneered the micro-mechanical testing of grain boundary sliding, using micro- and nano-specimens of bicrystals in low-melting-temperature materials. Furthermore, the mechanical tests were carried out on Al bicrystals at room temperature, in contrast to those previous experiments conducted at elevated temperatures [137, 138, 139, 67]. Another contribution of their work is that they developed a physical model to qualitatively capture the features shown in experiments, i.e. an initial peak stress, an abrupt and then gradual softening until reaching a steady state. Together with experiments, the model demonstrated that grain boundary sliding dominates the deformation process of nano bicrystals with a shear stress component applied along the boundary plane. However, only one type of grain boundary was selected and tested at only one strain rate. Therefore, the effects of sample size, grain boundary structure and strain rate on grain boundary sliding remain unclear.

Gong and Wilkinson [140] used the bicrystalline micropillar design to investigate the sample size effect on grain boundary sliding in pure Sn. On a long grain boundary, micropillars with a square cross section in a range of sizes (5 μm, 2 μm, 1 μm and 500 nm) were fabricated. In the bicrystalline micropillar, the grain boundary was orientated at 45° to the compression loading axis. Therefore, a large shear stress was resolved upon the grain boundary plane to promote sliding. The grain boundary chosen had a misorientation of 65° about the shared

[100] axis. Single-crystal micropillars of similar sizes were made in the grains on both sides of the boundary. The micropillars were tested at a constant displacement rate of 20 nm/s at room temperature. The engineering stress against displacement curves for single-crystalline and bicrystalline micropillars in different sizes are shown in figure 2.33(a) and (b). In smaller pillars from 2 μm, 1 μm to 500 nm, there are abrupt load drop segments with displacement bursts. However, this phenomenon is absent in larger pillars. What is more, a hardening effect (the increase in flow stress) is found in the single-crystal pillars after displacement bursts, while the flow stress keeps decreasing with some occasional displacement bursts in the bicrystalline pillars. The compressive flow stresses corresponding to various pillar sizes are compared between single and bicrystalline pillars in figure 2.33(c). Both of them show a significant increase in flow stress as the pillar size reduces. However, the difference in flow stress between single-crystalline and bicrystalline pillars is minimal for the larger pillars (2 μm and 5 μm), but significantly evident for the smaller pillars (1 μm and 500 nm). The shear stress on the grain boundary plane shows a "smaller is stronger" size effect as well as the flow stress.

The SEM micrographs before and after compression tests are shown in figure 2.34. The micrographs of single-crystalline pillars revealed the multiple slip events and the increased cross-sectional area, which could explain the hardening effect during the compression test. The deformation of bicrystalline pillars was localised on the grain boundary plane without sign of multiple slip inside the grains. It could also be found from the micrographs that the contribution of grain boundary sliding to the total displacement increased as the pillar width reduced. It was also evident that the grain boundary area reduced with the ongoing sliding, and therefore the stress required to maintain the deformation kept decreasing. The slip features on the bicrystalline micropillar indicated that dislocation activity occurred within the grains before the onset of grain boundary sliding. The same dislocation theory discussed in Section 2.7.1 could explain the size effects seen in bicrystalline pillars. For the larger sized pillars, the similar flow stresses found in single and bicrystalline pillars suggest that continued slip of lattice dislocations is required to accommodate sliding. However, for the smaller sized pillars, a smaller number of

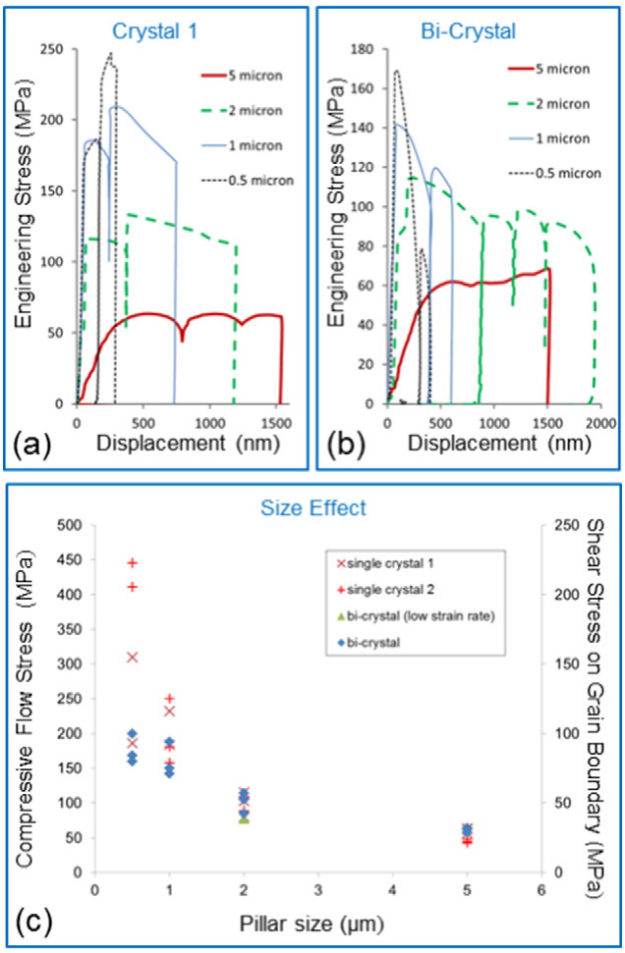

Figure 2.33: (a) Micromechanical testing data showing the size effects for single crystal and bicrystal micropillar compression test. Engineering stress versus displacement curves for different sized micropillars in (a) single crystal, and (b) bicrystals. (c) Compressive flow stress (left axis) at the onset of plastic deformation as a function of pillar size for single and bicrystalline samples. For bicrystals, shear stress on the grain boundary is also shown on the right axis) [140].

dislocations formed during the loading part are sufficient to promote continued sliding. Thus, the size effect on grain boundary sliding in bicrystalline pillars is not as strong as that for lattice dislocation mediated plasticity.

Gong and Wilkinson's research, for the first time, investigated the size effects on grain boundary sliding down to sub-micrometer scale. The comparison between flow stresses of grain boundary sliding and single-crystal multiple slip enables to a better understanding of the accommodation mechanisms of grain boundary sliding. The size effects of grain boundary sliding

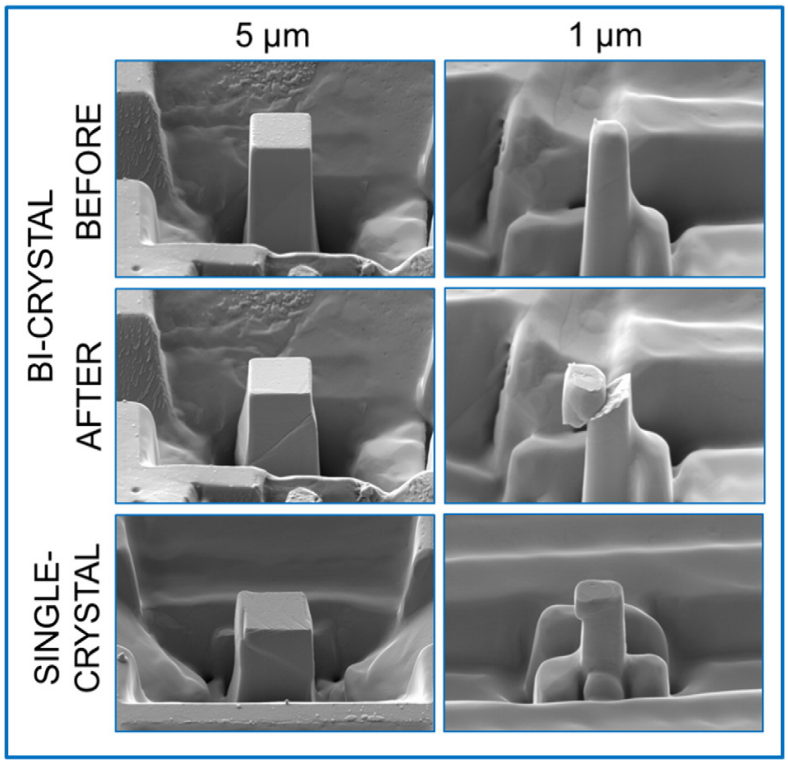

Figure 2.34: SEM micrographs showing the micropillars before and after compression test. Top row: bicrystal pillars of 5 μm and 1 μm width before compression test. The grain boundary is orientated at 45° to the compression loading axis. Middle row: the bicrystal micropillars after compression test, showing grain boundary sliding with different displacements. Bottom row: the single-crystal pillars of 5 μm and 1 μm width after compression test, showing multiple slip [140].

were explained by two factors. One was that the strain caused by the movement of a defect across the sample on the grain boundary is much larger for the smaller samples than for the larger ones. The other was that the smaller pillars have fewer chances to have strong obstacles to the grain boundary dislocation motion. This finding further illustrated that smaller grains are easier to have grain boundary sliding than the larger grains.

2.8 Summary of Literature Review

This review has described the various deformation mechanisms at relatively high temperatures, which include power-law creep, diffusion creep and grain boundary sliding. The conditions and characteristics of each mechanism are discussed in detail. An emphasis is put on superplasticity and intrinsic and extrinsic grain boundary sliding. The accommodation mechanisms of extrinsic grain boundary sliding remain unclear, which can involve both diffusion and dislocation activities. Characterisation of grain boundary sliding has proved to be challenging. However, a recent technique using surface grids milled by FIB has been demonstrated, which could assist quantitative measurements of the amount of grain boundary sliding in macro-mechanical tests. On the microscopic scale, even though nanoindentation is a relatively easy technique to obtain elastic modulus and hardness values, it is difficult to measure some important mechanical properties such as yield stress and fracture toughness. Therefore, micro-mechanical tests using micro-specimens prepared via FIB have been developed. Combined with nanoindentation technique, micro-specimens, such as micropillars and micro-cantilevers, can be used to measure a range of mechanical properties (elastic, plastic and fracture) for a great variety of materials.

Chapter 3

Macro-mechanical Testing to Reveal Grain Boundary Sliding

Overview:

Sn-1%Bi is a single-phase alloy that can be superplastic at room temperature [141]. Despite the large number of macroscopic mechanical tests conducted on this material, the detailed mechanism of its superplastic behaviour, especially the inhomogeneity of deformation remains unclear. This chapter describes the processing of fine-grained superplastic material and ex-situ and in-situ macro-shear tests. Deformation in shear was chosen because the surface area remains constant and there is less incentive for out-of-plane grain boundary sliding than in conventional tensile testing. A series of ex-situ shear tests were conducted on the same specimen at various strain rates to investigate the strain rate sensitivity. Digital Image Correlation (DIC) was used to measure the actual displacement of the specimen. In-situ SEM tests were carried out in the superplastic regime on a polished specimen with surface grids produced by Focused Ion Beam (FIB) milling. Most of the grid lines were offset on many of the grain boundaries. However, some grid lines in the regions with inactive grain boundaries remained unchanged.

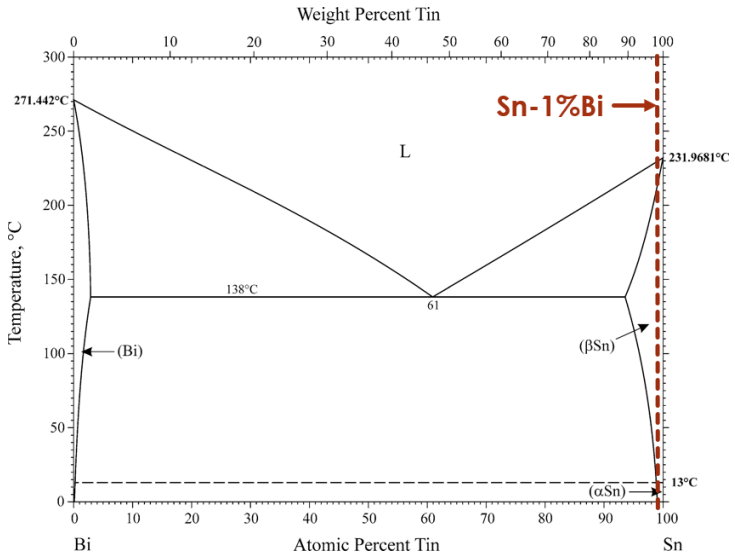

Figure 3.1: Sn-Bi phase diagram showing the Sn-1wt%Bi alloy with a single phase microstructure in theory [142].

3.1 Materials and Experimental Methods

Most research on superplasticity has been conducted on materials showing grain boundary sliding at relatively high temperature, such as aluminium, magnesium and zinc alloys. The macroscopic mechanical testing of these materials requires accurate temperature control. However, it is difficult to conduct microscopic tests or in-situ macro-mechanical tests at high temperature. Therefore, Sn-1%Bi alloy was selected for this project as it exhibits grain boundary sliding at room temperature. This is because the melting temperature of Sn-1%Bi is around 504K, so that room temperature (298K) is almost 60% of its melting point. Furthermore, as shown in the phase diagram (figure 3.1), it is a single-phase alloy, which simplifies the microstructure. The addition of one weight percent of bismuth inhibits grain growth of pure tin at such a high homologous temperature.

It was discussed in the literature review that the threshold on the grain size for superplasticity is generally below ~10 μm. The material was manufactured in house through casting, homogenisation, extrusion and rolling. The samples were polished with alumina suspension for microstructure characterisation via SEM and EBSD. Attempts were made to extrude the cast ingot (28 mm in diameter) to a thin wire (2.2 mm in diameter) at room temperature, but

the microstructure of the extrusion was not fine enough for superplasticity. Further grain size reduction was achieved by inducing cold deformation. Colder ingot, lower extrusion speed and faster cooling were used to reduce the temperature of extrusion. The extruded wires were then rolled down to thin sheets of 0.5 mm, before being cut into specimens for macro-tests.

For the ex-situ shear tests, after grinding and polishing, some parallel straight-line scratches (marker lines) were made on the specimen surface with a diamond paste. The microstructure and surface features were characterised using SEM imaging (Zeiss EVO and Merlin) and EBSD analysis (Bruker e^- Flash detector and Espirit 2.0 software). The specimen was mounted on a shear testing rig and fitted to a Shimadzu tensile tester. The deformed specimen was examined in the SEM again, looking for offsets of the marker lines on the grain boundaries. For the in-situ shear tests, the surface marker lines were made by a FIB. Shear tests were conducted using a compact tensile tester in an SEM, with images taken at various magnifications during the deformation process.

3.1.1 Materials Processing

The material processing route is summarised in figure 3.2. The raw materials of high purity tin (99.96%) and bismuth (99.99%) were obtained from Alfa Aesar. The right amount of tin and bismuth were mixed according to the alloy composition, which were then melted and superheated to 340°C in the furnace in air. After approximately 50 minutes of heating, the melt was taken out of the furnace and the oxide layer on top was scraped off, followed by a thorough stir before being put back into the furnace. After another 10 minutes of soaking, the melt was chill cast into a brass mould immersed in cold water. An ingot of 30mm in diameter and 8 mm long was obtained, which was homogenised in a vacuum furnace for one week at 130°C. The ingot was then machined on a lathe to 28 mm in diameter (removing the oxide layer). The ingot (billet) and extrusion die were both submerged in liquid nitrogen for 2 hours before extrusion to ensure cold deformation. As shown in figure 3.2b, the billet was extruded to a thin wire with a diameter of 2.2 mm. Guided by a copper pipe that was fixed on the extrusion machine,

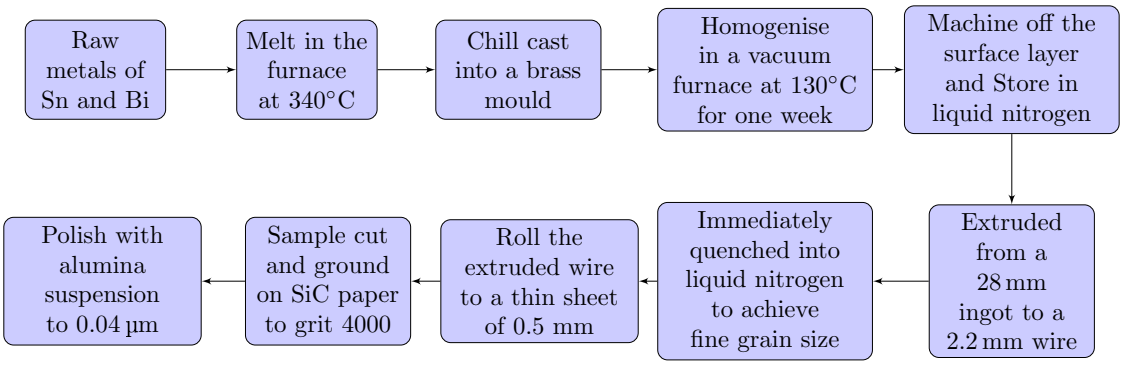

(a)

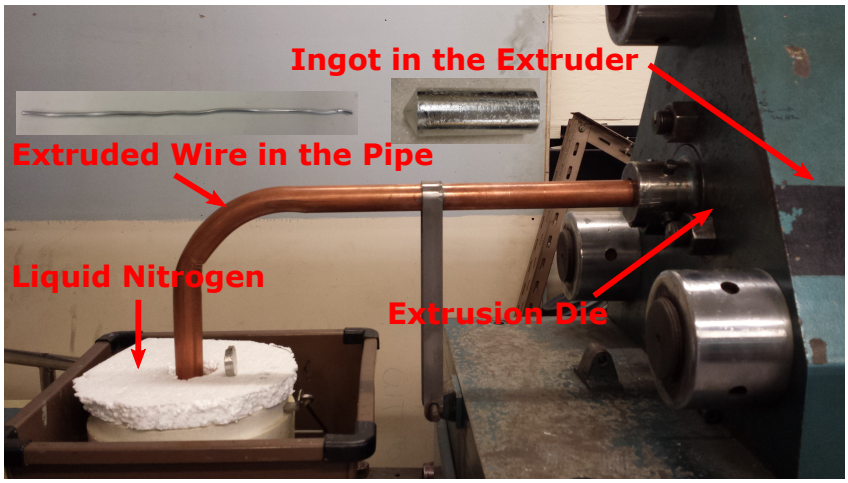

(b)

Figure 3.2: (a) A flow chart of the material processing and sample preparation for macro-shear tests. (b) The experimental setup of the cold extrusion process, which was the key to the fine microstructure of the sample.

the wire was immediately quenched into liquid nitrogen. Heat is inevitably generated during extrusion. An intermediate extrusion speed (8 m/min) was used so that the ingot was quickly squeezed through the die while not generating too much heat. This process ensured that the material stayed at very low temperatures from the billet to the extruded wire, and so produced a fine microstructure.

The extrusion was then rolled down to a thin sheet using a hand roller. The rolling was conducted in about eight passes, with a thickness reduction of ~0.2 mm for each pass. The final rolled plate was about 0.5 mm thick and 8 mm wide. The specimen plate was ground on silicon carbide papers and polished using alumina suspension. For the ex-situ shear tests, fine diamond

paste was used to generate parallel surface marker lines. The shear testing rig was manufactured by Rust [1] based on the design by Bae and Ghosh [143] with some modifications. The rig consists of two halves, one of which could be pulled up while the other stayed fixed (figure 3.3a). The rollers were between the two parts at the corner to avoid rotation of the rig during loading. A 26 mm long specimen plate was cut off to fit into the gauge of the shear testing rig. The specimen was bolted between the two halves of the rig as a sandwich structure, with the two metal plates on top for fixation. The edges of the specimen were also glued to the rig (on the bottom) and the metal plate (on top). Therefore the only place for deformation to occur was at the gauge, which was not covered by the plates. The width of the gauge was 3 mm, which gave a length to width ratio of 8.7 and thickness to width ratio of 0.2. These ratios were chosen to avoid buckling and the effect of the free ends [143].

A similar design was used for the in-situ testing rig as shown in figure 3.3b. The specimen has a much smaller gauge (1.5 mm wide) and the same thickness as above (0.5 mm). Due to the complex geometry of the specimen, it was machined by a waterjet cutter. The edges were ground to remove the residual debris from the cut. The surface of the specimen was ground and polished, before milling surface marker lines (in the centre of the gauge) using a FIB. The rig was designed and manufactured by Dr Enrique Alabort [144] to be mounted on a tensile micro-test module (facility provided by Oxford Solid Mechanics Group) that could fit into the chamber of an SEM (Zeiss EVO). The specimen adhered to the rig by an electrically conductive adhesive. When the two halves of the shear rig were pulled apart, the gauge of the specimen underwent simple shear deformation.

3.1.2 Sample Preparation and Microstructural Characterisation

In order to demonstrate the effect of extrusion on the microstructure, both as-cast and as-extruded materials were characterised in an optical microscope. The as-cast ingot has a large diameter of 30 mm, therefore a slice of the ingot was cut off and mounted in a cylindrical mount using epoxy resin. Then the sample was ground and polished in the resin mount. For

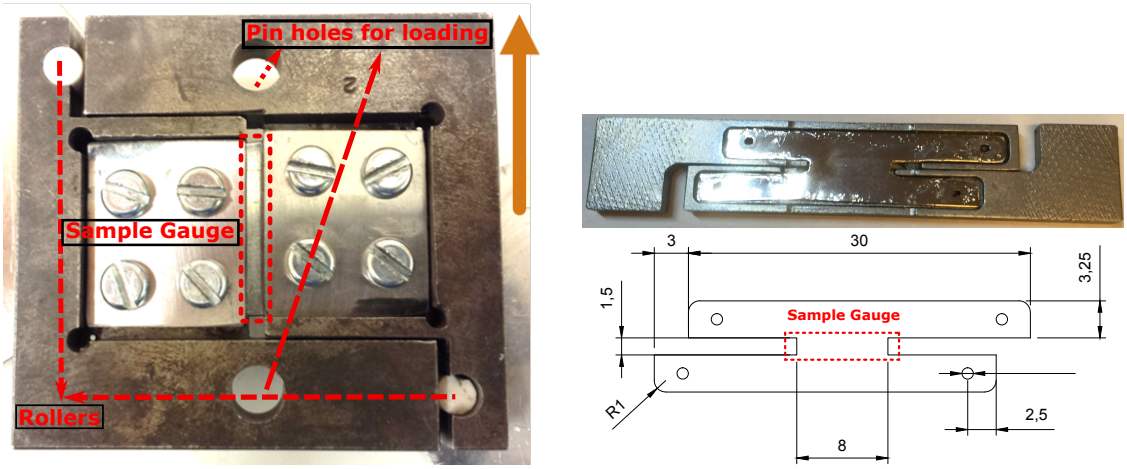

(a) (b)

Figure 3.3: (a) The extrusion was rolled to a thin sheet of specimen that was mounted to a shear testing rig for the ex-situ tests. (b) The specimen for the shear test was machined by a waterjet cutter and fitted into the in-situ testing rig, together with the dimension of the in-situ shear testing specimen.

the extruded wire, a 7 mm long sample was cut off, which was then mounted using epoxy resin into an aluminium stub with a 2.4 mm diameter hole. Then three of these samples were adhered to a polishing plate with cyanoacrylate glue. The samples were then ground with silicon carbide papers to a 4000 grit finish, followed by 6, 3 and 1 μm alumina suspension. Finally, 40 nm γ-alumina suspension was used to achieve a scratch-free sample finish. The as-cast and as-extruded (to 2.2 mm in diameter at room temperature) microstructures are compared in figure 3.4a and 3.4b. The grain size was reduced from several hundreds of microns to tens of microns (20~30 μm). This grain refinement effect could be compared to that for the micro-test samples, which were extruded to 7.5 mm rods from the same sized as-cast ingot. It can be noted that the grain size of the thin wire is much smaller than the rod, due to the larger deformation induced from the further reduction in size. In addition, the effect of cold deformation on the grain size is illustrated by comparing figure 3.4b and figure 3.4c. The diameter of the circle was the same, while there were apparently many more grains in the cold extruded sample. The mean linear intercept grain size was 8.5 μm, calculated by the traditional metallurgical method of drawing straight lines and counting the number of grains across the line. Furthermore, the microstructure of the cross section along the extrusion direction was also

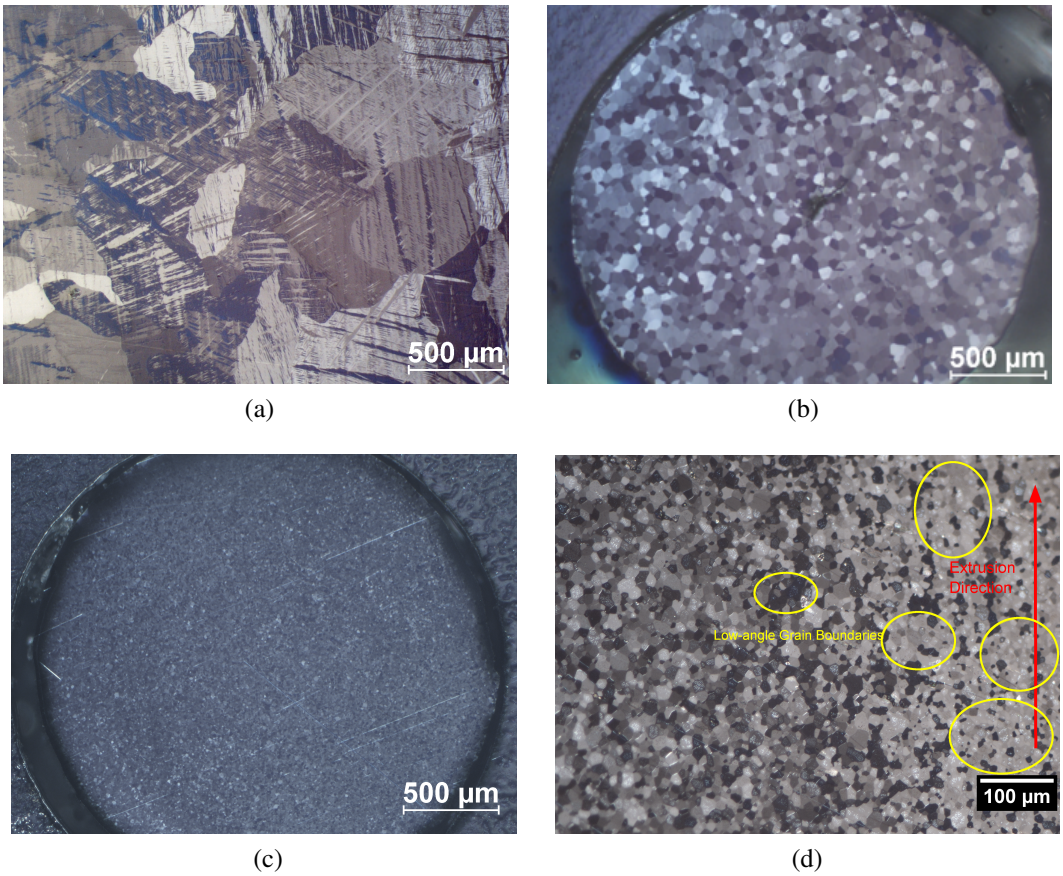

(a) (b)

(c) (d)

Figure 3.4: (a) to (d) showing the optical images with polarised light, comparing the microstructure of the (a) as-cast sample, (b) sample extruded at room temperature, (c) sample extruded with liquid nitrogen (on the cross section normal to the extrusion direction) and (d) cross section parallel to the extrusion direction. The grains became smaller after cold deformation but were still equiaxed on the cross section plane.

characterised in figure 3.4d. The grains were still equiaxed in this direction. The optical image with polarised light could indicate the orientation of the individual grains. There are patches of grains showing similar contrast, which indicates that those grains might have recrystallised from a large columnar one. In these patches of grains, there are large amounts of low-angle grain boundaries, which will be discussed in section 3.3.4.

3.1.3 Ex-situ Shear Test

3.1.3.1 Displacement Controlled Tests

The specimen was prepared and fixed on the shear testing rig as described in section 3.1.1. The rig was mounted onto the Shimadzu tensile tester as shown in figure 3.5a. The pins went through the holes of the shear rig and grips. The bottom grip was fixed on the frame, while the top grip was held by a rod connected to the load cell (figure 3.5b). The machine was controlled by TrapziumX software. The load and displacement signals were recorded by the load cell (5 kN) and movement of the crosshead. One side of the specimen surface was polished, which faced towards the camera. The displacement of the crosshead recorded by the software includes the total movement of the system, i.e. the displacement of the specimen, the shear rig and the connecting rod that transferred load. The actual displacement of the specimen was obtained from the Digital Image Correlation (DIC) analysis on the images taken by the camera throughout the test. In order to introduce features for the DIC software to track, small dark dots were spray-painted on the polished surface as shown in figure 3.5c. The DIC software would track the displacement of the dark dots and calculate the displacement of the specimen. The details of the DIC analysis is described in section 3.1.5.

The top half of the rig was pulled upwards while the other half was fixed at the bottom. Therefore, the right edge of the specimen moved upwards and the left edge stayed still. When the rig with the specimen was initially mounted onto the frame of the machine, the pins were quite loose as the rig was not in close contact with the grips. Therefore, a preload was added to the rig little by little until the contact was firmly tight. The test was carried out under crosshead displacement control, i.e. at a constant displacement rate. In order to measure the strain rate sensitivity index, a strain rate jump test was carried out with a few different displacement (or strain) rates. The strain was continued until a steady state was reached. The mechanics to calculate shear stress and strain are illustrated in figure 3.5d.

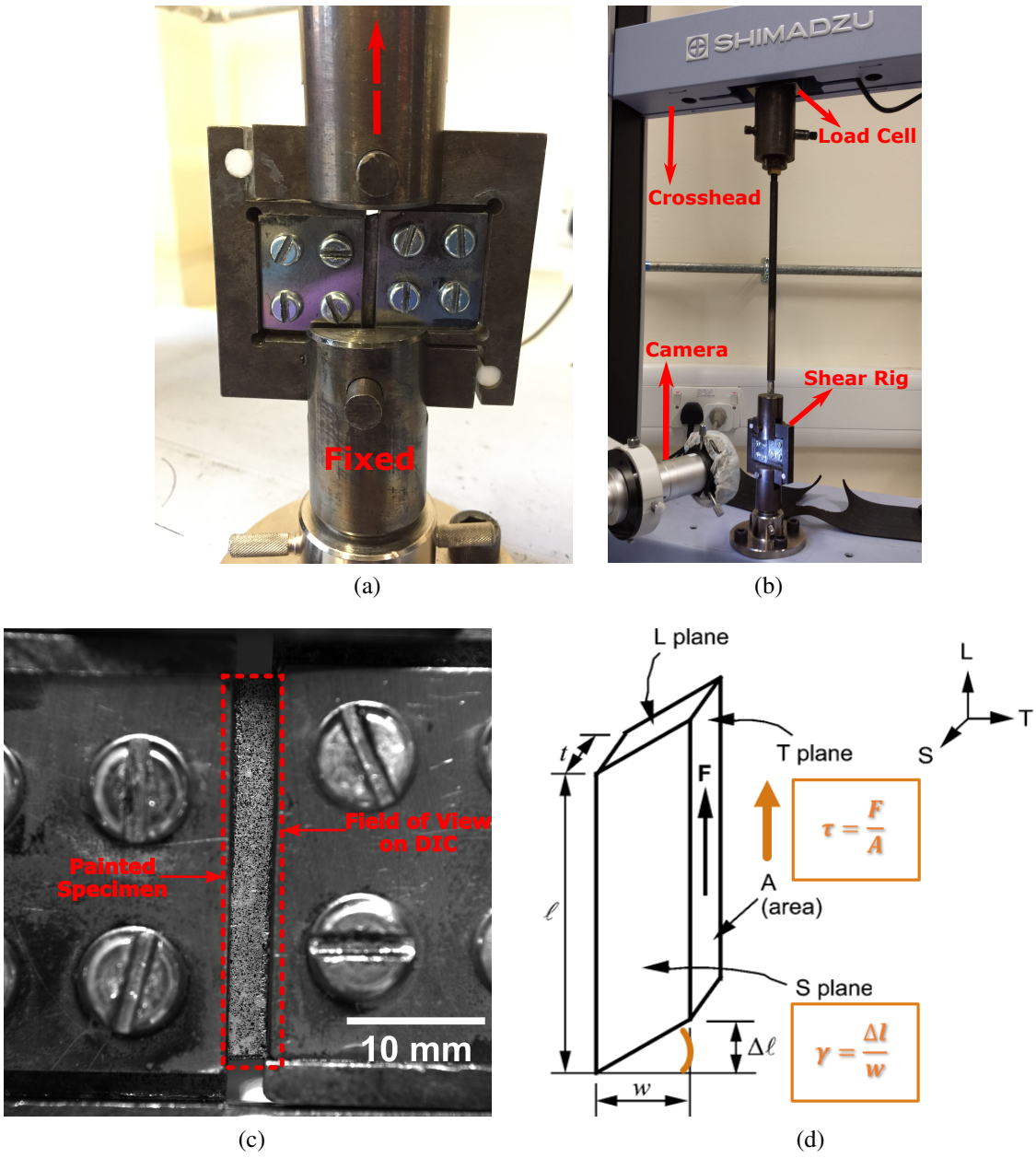

Figure 3.5: (a) The shear testing rig was fixed to the grips by the pins. (b) The rig and grips were mounted on the tensile tester frame by a rod, with the polished specimen surface facing to the camera. (c) The polished surface of the specimen was painted with small dark dots to introduce features for the DIC software to track the displacement of the specimen. (d) The mechanics to calculate the shear stress and strain of the specimen.

Figure 3.6: The experimental setup of the load controlled test by hanging a dead weight on the shear rig.

3.1.3.2 Load Controlled Test

The lowest strain rate available under displacement control was $5 \times 10^{-6}/s$, which lay between the transient regime between Region II and III (section 2.3 on page 11 of Chapter 2). In order to explore further into Region II, shear tests at lower strain rates were required. Attempts were made on load controlled tests using the Shimadzu machine. A load of 40 N would apply a shear stress of 3 MPa, which was estimated to be well into Region II in the stress-strain rate plot. However, due to the large capacity of the load cell, it could not hold a constant load accurately as low as 40 N. An alternative load controlled test was designed by hanging a dead weight below the shear testing rig as shown in figure 3.6. A camera was set up in front of the shear rig in the same way as shown in figure 3.5b. The images were taken every two minutes, which were used in the following DIC analysis. The light conditions were ensured to be relatively consistent across daytime and night. The temperature was logged every two hours. The fluctuation was within 3°C.

3.1.4 In-situ SEM Shear Test

The tensile micro-test module is shown in figure 3.7a, which was designed by Kammrath Weiss GmbH. The shear specimen was prepared and adhered to the shear testing rig as described in section 3.1.1. The testing rig was clamped on the tensile module with the specimen grips. The module could be mounted on the SEM stage, with the electron beam pointing towards the gauge of the specimen as shown in figure 3.7b. The polished surface faced towards the SEM column. The displacement of the specimen was achieved by the precise movement of the gearbox, which was controlled by DDS software. The load was measured by a 5 kN load cell. The shear stress and strain were calculated using the mechanics in figure 3.5d. During the in-situ shear test, the slowest displacement rate of 0.1 μm/s was used, giving a shear strain rate of $6.67 \times 10^{-5}/s$.

Two sizes of surface marker grids were made in the centre of the gauge in a FIB. The wider meso-grids with a spacing of 50 μm (figure 3.7c) were milled using a beam current of 100 pA for 60 seconds. The micro-grids were milled inside a meso-grid with a spacing of 1 μm (figure 3.7d) by a beam current of 50 pA for 60 seconds. The SEM images were taken every 1.33% strain (200 seconds). In order to capture grain boundary sliding in both a local area and deformation within the surface meso-grid, SEM images were taken at four different magnifications. The images were taken in roughly the same sample area at the same magnification for each strain level. At the end of the test at a 60% strain, all the images with the same magnification were sorted together and combined into a video.

3.1.5 Digital Image Correlation (DIC)

DIC analysis could provide more accurate measurement of displacement/strain of the specimen than the stroke measurement of the overall crosshead displacement. The DIC software — LaVision DaVis (acknowledgements to Prof Marrow's research group) tracks the displacement of the features (paint dots in this case) on the specimen surface. The algorithm used in the DIC

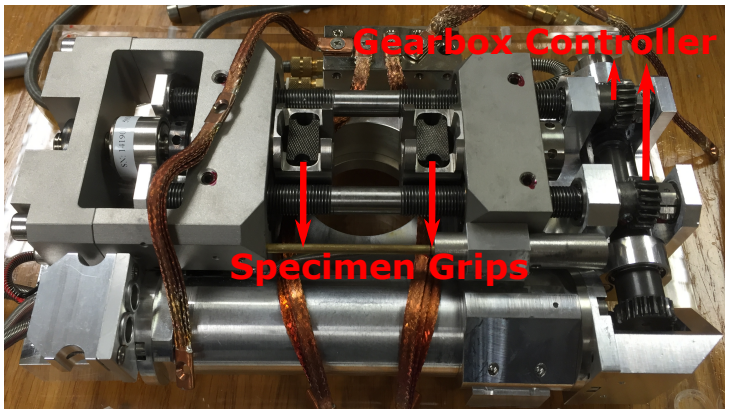

(a)

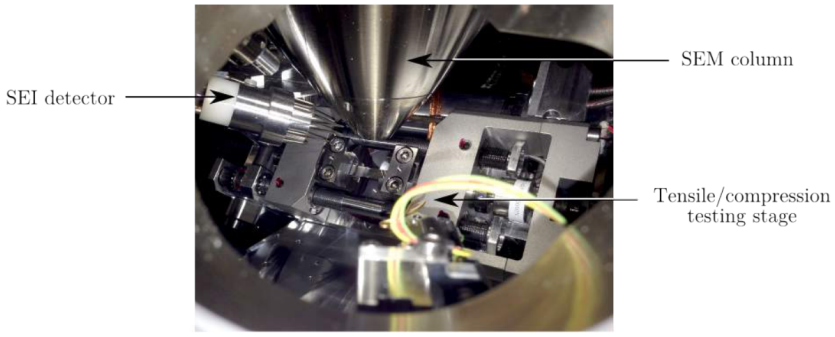

(b) (Image from [145])

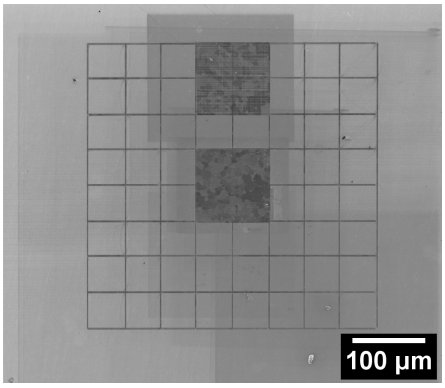

(c)

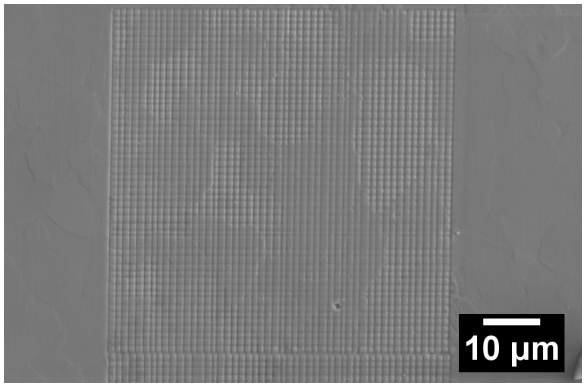

(d)

Figure 3.7: (a) The tensile/compression module was used in the in-situ shear test. (b) The module was mounted onto the SEM stage, with the shear testing specimen under the electron beam column (image after [145]). (c) and (d) show the meso- and micro- surface grids (before testing) milled by a FIB, respectively.

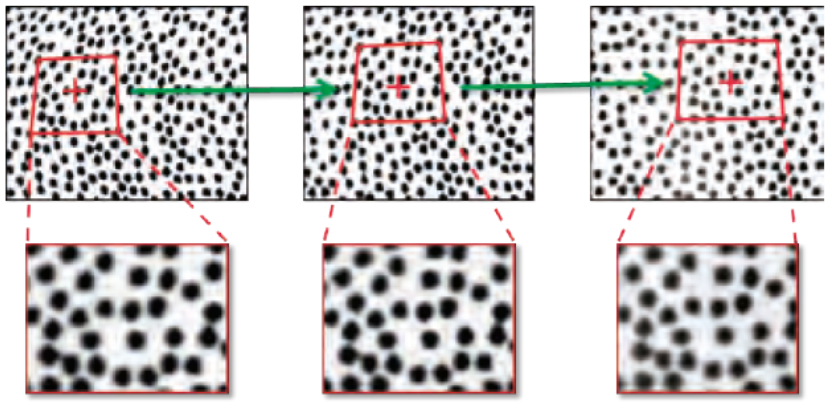

Figure 3.8: An example of the DIC analysis on the displacement of features via comparing the subsets of a series of images [147].

analysis is a Least Squares Matching (LSM) approach with subset deformation. To be more specific, the specimen or region of interest is divided into hundreds of subsets with distinguishable particles as shown in figure 3.8. Each subsequent image is compared to the initial state (first image). The DIC analysis is essentially an iterative least squares (a standard method in regression analysis) procedure to calculate the displacement field of each pair of images after applying a transformation on the interrogation areas [146]. Typical transformation parameters include rotation, shear and strain.

3.2 Results: Ex-situ Shear Test

3.2.1 Microstructure Characterisation using EBSD

The specimen has a very fine microstructure after cold deformation as mentioned above. After being rolled to a thin sheet, EBSD analysis was carried out as shown in figure 3.9a (with the rolling direction along the vertical direction). The threshold misorientation angle to define a grain boundary was 4°, which was chosen based on the in-situ SEM observations to be described in section 3.3. The colours in the grain map were assigned randomly to identify grains. There were many patches of grains showing the same colour in red or blue. The pattern quality image in figure 3.9b also reveals the grain and subgrain boundaries. The subgrain structures were elongated along the rolling direction (vertical axis in the EBSD images). The boundaries within the subgrain structures were mostly low-angle grain boundaries (<4°), as shown in red in figure 3.9b. The regions populated with red boundaries correlated well to the patches of subgrains in figure 3.9a. The distribution of low and high-angle grain boundaries is shown in figure 3.9c. Low-angle boundaries (in red) made up 37% of the grain/subgrain boundaries. Since there were many large grains with subgrain structures, the number fraction was chosen over area fraction. The average grain size was 6.2 μm with a 4° threshold angle to define grains (figure 3.9d).

3.2.2 Constant Displacement Rate Tests

3.2.2.1 Stress and Strain

The slowest displacement rate, 1 μm/minute, was used in the constant displacement rate test. The strain rate was $5 \times 10^{-6}/s$. The shear stress and strain plot is shown in figure 3.10. Since a preload was already conducted, the initial increase in load totally corresponded to the load applied to the specimen. The displacement was obtained from the DIC analysis as discussed in section 3.1.5. It could be seen that the stress reached a plateau after about 5% strain, where it levelled off at around 10 MPa. Then the superplastic deformation started and continued

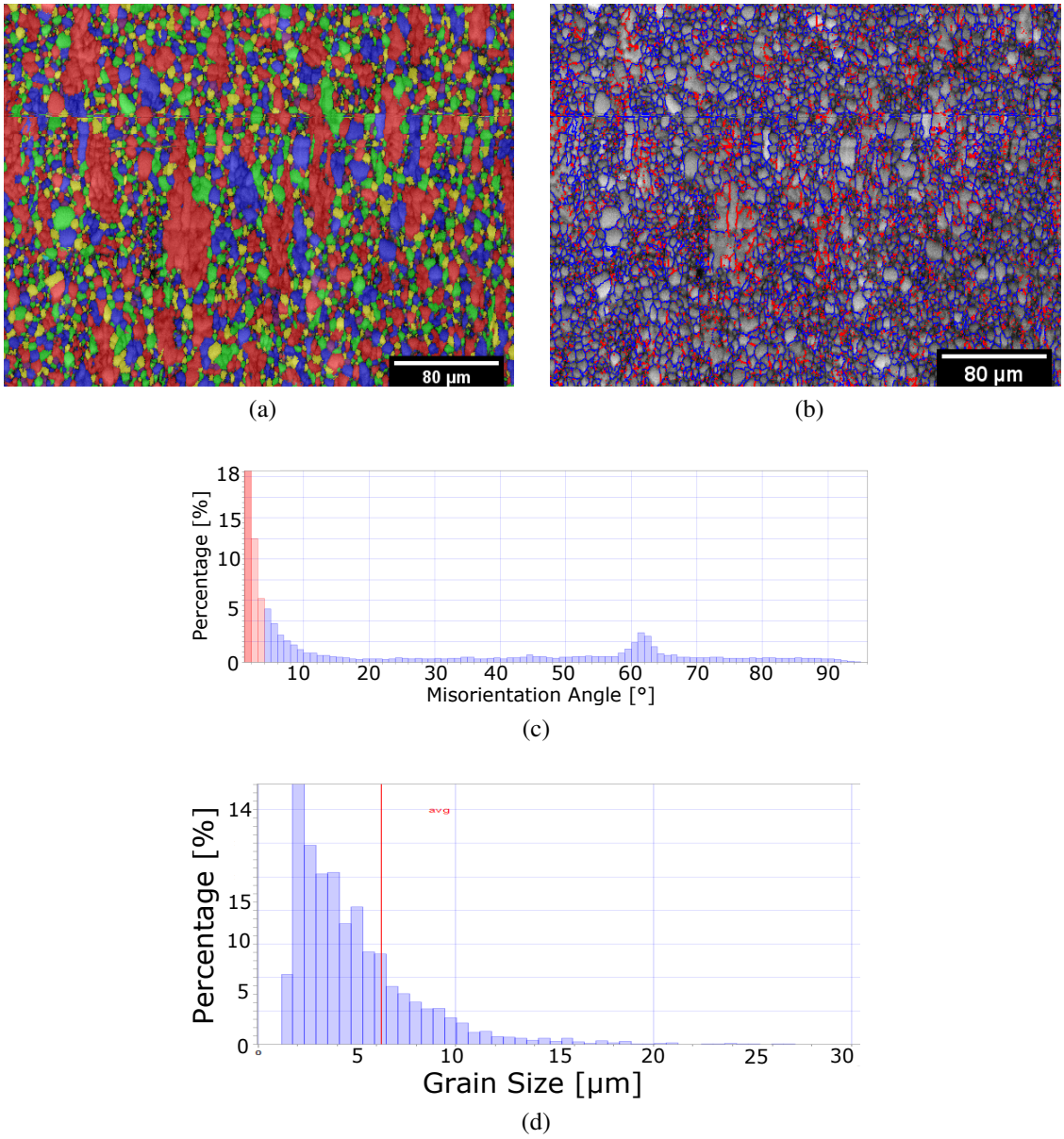

Figure 3.9: (a) EBSD and pattern quality overlay image of a cold extruded and rolled specimen. The threshold misorientation angle to define a grain was 4°. The colours were assigned randomly independent of the grain orientation. There were subgrain structures in the long and large grains showing the same colour (in red and blue). (b) The image of pattern quality revealed the subgrain structures with low-angle grain/subgrain boundaries ($< 4°$). (c) Distribution of grain boundary misorientation angles, showing 37% of the grain/subgrain boundaries were low-angle boundaries. (d) Grain Size distribution histogram of the rolled specimen, showing an average grain size of 6.2 µm.

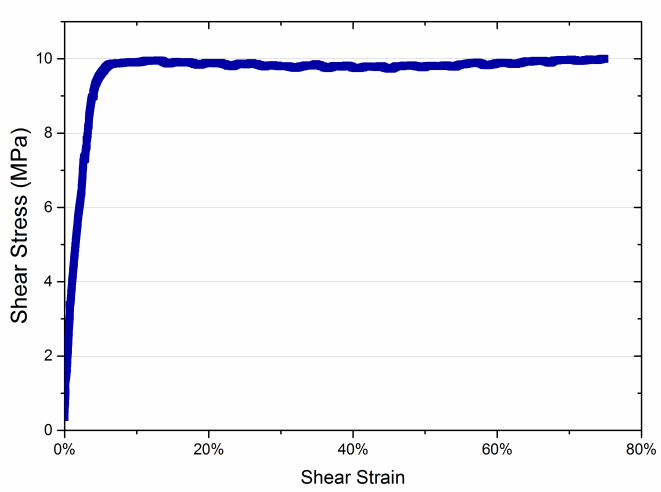

Figure 3.10: Shear stress-strain curve of the ex-situ shear test at a constant displacement rate.

to ~75% strain at the constant stress. The test was stopped at this point due to the limited strain capacity of the test rig rather than a limitation of the superplastic material response. The constant-stress plastic deformation is one of the characteristics of superplasticity, which was different from the increasing stress during work hardening for non-superplastic materials.

3.2.2.2 Observation of the Surface Profile after Deformation

The polished specimen was mounted on the shear rig as shown in figure 3.11a. The shear direction was along the vertical axis. This was an image taken by the camera set up for the DIC analysis. It could be seen that some horizontal deep scratches were marked on the surface to assist DIC in tracking features. What couldn't be seen from the image were the fine scratches made by diamond paste that were only visible in the SEM. At the end of the test, an image of the specimen sheared to 75% strain is shown in figure 3.11b. Some of the deep scratches were still visible though. The specimen was sheared to 75% strain without any sign of buckling. The gauge was kept to be ~3 mm wide, which indicated that no rotation of the rig occurred during deformation. The surface was no longer flat and was filled with many particle-like features.

The sheared specimen was unmounted from the testing rig by removing the adhesives with acetone in the ultrasonic bath. It was then examined in the SEM. Images were taken at a few

locations in the gauge region before and after the test (figure 3.11c and 3.11e). It could be seen that the surface was quite flat before test. Furthermore, the grain boundaries were not clearly shown before test. However, after a large strain of 75% (figure 3.11e), the surface became very rough and the individual grains could be clearly identified with the boundaries shown on the contoured surface. There was also a large amount of out-of-plane deformation at the grain boundaries, which made some individual grains even "standing out" as highlighted in the image. There were also areas where no grain boundary contours were shown. The surface of those areas was also relatively flat. This indicated that the grain boundaries in those areas did not slide as much or not at all. It was very likely that those areas corresponded to the patches of grains with similar orientations (figure 3.9a), and that the non-sliding grain boundaries in the patches were low-angle boundaries. The correlation between misorientation angle and tendency to sliding will be further demonstrated in section 3.3.4 on page 91.

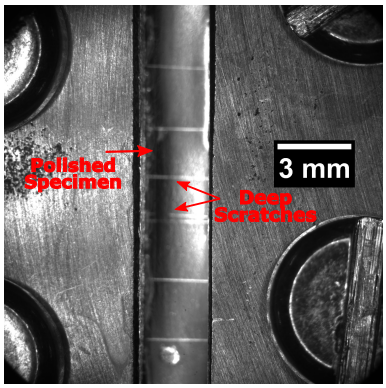

(a)

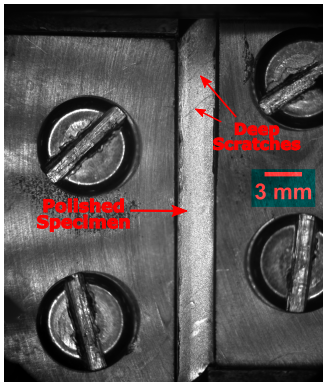

(b)

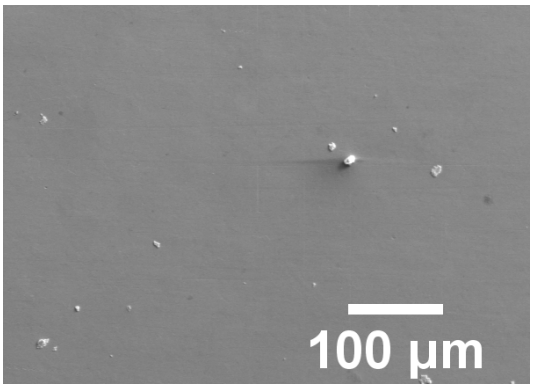

(c)

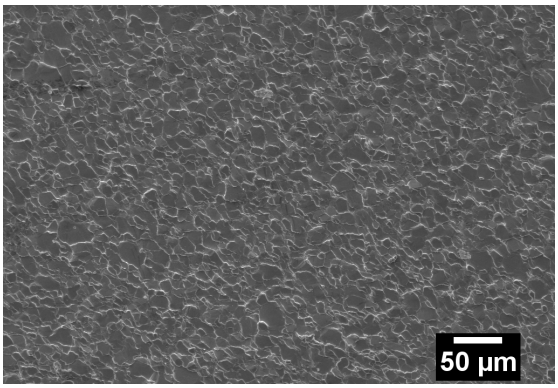

(d)

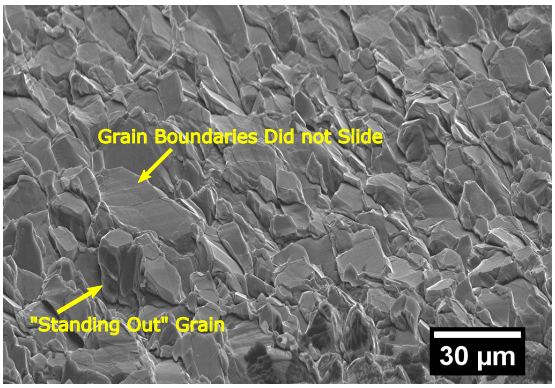

(e)

Figure 3.11: (a) The polished surface faced towards the camera, which was marked with horizontal deep scratches before the test. The shear deformation was along the vertical direction. (b) The specimen was sheared to a strain of around 75%. The surface showed no buckling. (c) The SEM image of the ex-situ shear specimen before testing. (d) After a large amount of deformation, the surface became quite rough. The in-plane and out-of-plane deformation (mainly by grain boundary sliding) made the grain boundary contours clearly revealed. (e) A tilted view of the specimen surface after 75% strain.

3.2.3 SEM Investigation of the Surface Markers

The specimen used in section 3.2.2 was deformed superplastically to 75% strain at a constant strain rate, which was then investigated in the SEM. The shear direction was along the vertical axis in all the following images. At a high magnification, figure 3.12a shows that inside the grains, the originally straight scratch lines remained straight. But the three parallel scratch lines all had offsets at the grain boundaries. This indicates that deformation occurred mostly on the grain boundary via sliding, while there was not much intragranular plasticity. Due to the similar grain boundary plane alignments, the three highlighted boundaries had similar shear stresses (on the boundary planes) that drove grain boundary sliding. However, they exhibited different amounts of sliding, which were quantified by the sliding displacement over the total grain boundary length. These three grain boundaries were displaced along the shear direction in the plane of page. There were also boundaries displaced along the direction perpendicular to the plane of page as shown in figure 3.12b.

At a lower magnification in figure 3.12c, the grain boundary planes had different alignments with respect to the shear direction (vertical axis). Different boundaries had slid to different extents. Figure 3.12d further illustrated that different grain boundaries had different abilities to participate in sliding. Most grains were revealed by deformation, where the grain boundaries dislocated the scratch lines. However, some regions were not deformed that much and the grain boundaries were not revealed. In those areas, the scratch lines were still straight. This indicated that not much grain boundary sliding occurred in those regions, which might be consisted of low-angle grain boundaries. This inhomogeneity is further demonstrated by the in-situ tests in section 3.3.4 on page 91.

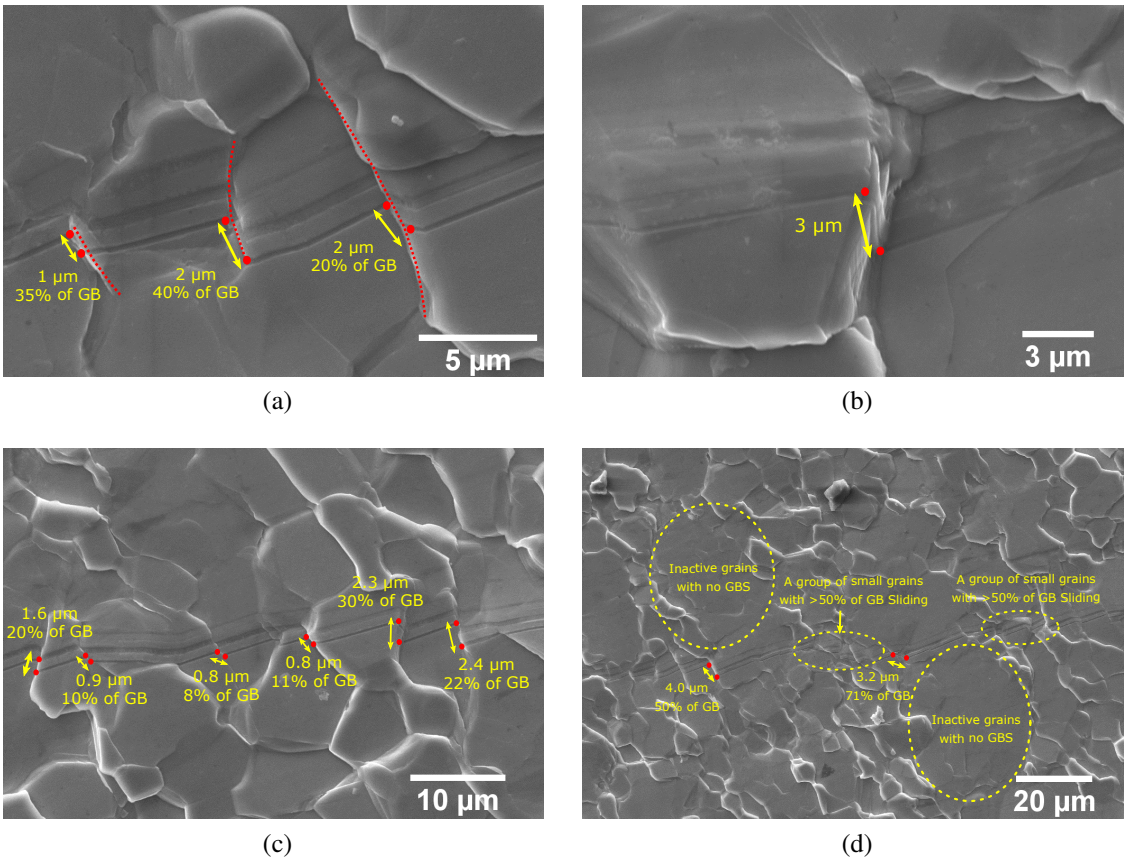

Figure 3.12: The shear direction was along the vertical axis in the plane of page. (a) The scratch lines were dislocated on the grain boundaries, but still straight in the bulk grain. The displacements of the scratch lines were different on different grain boundaries, even though the alignment of the three boundaries was similar. (b) A scratch line with an offset along the direction out of the plane. (c) The scratch lines had offsets of different length on differently aligned grain boundaries. (d) An overview of a large area of the specimen with scratch lines going across many grain boundaries, some of which had offsets while some remained straight. There were also areas without any grain boundaries being revealed.

3.2.4 Displacement Controlled Strain Rate Jump Tests

3.2.4.1 Stress-Strain and Displacement-Time

The strain rate jump test was carried out to investigate the strain rate sensitivity of this fine-grained material. There were five different strain rates used in the shear test on the same specimen. The shear strain obtained from DIC is plotted against time in figure 3.13a. The test started with the slowest displacement rate that was available on the tensile machine — 1 µm/minute. The shear strain reached ~15% after 500 minutes of testing. The displacement/strain rate was

increased by 5 times at each "jump" (i.e. from 1 μm/minute to 5, 25, 125, 625 μm/minute) whenever a stable stress was achieved as shown in figure 3.13b. The displacement rate was changed back to 1 μm/minute towards the end of test. This last segment was carried out to check how the stable stress would change from that at the beginning of test. It could be seen the stress relaxed a little bit each time when the test was speeded up by 5 times. However, after high strain-rate deformation for ~55% strain, there was no stress relaxation when the strain rate decreased to the slowest value (same as the initial segment). The stable stresses were similar (14% difference) between the first (6.9 MPa) and last segments (5.9 MPa) of the test at the same strain rate.

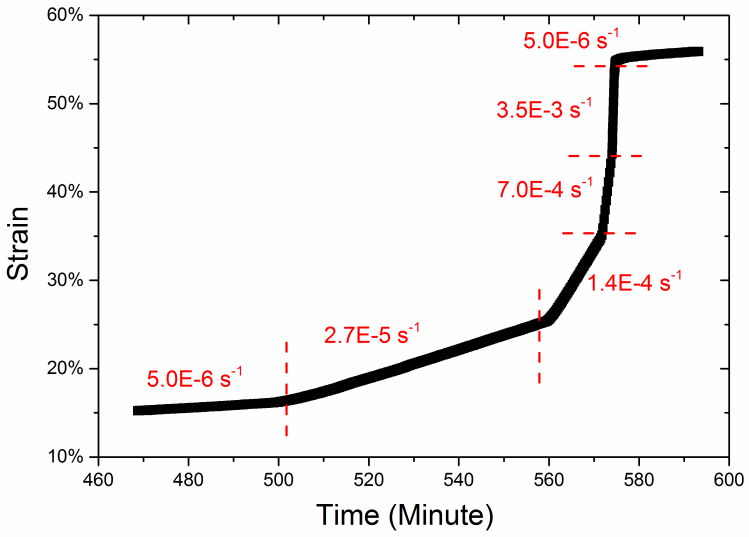

(a)

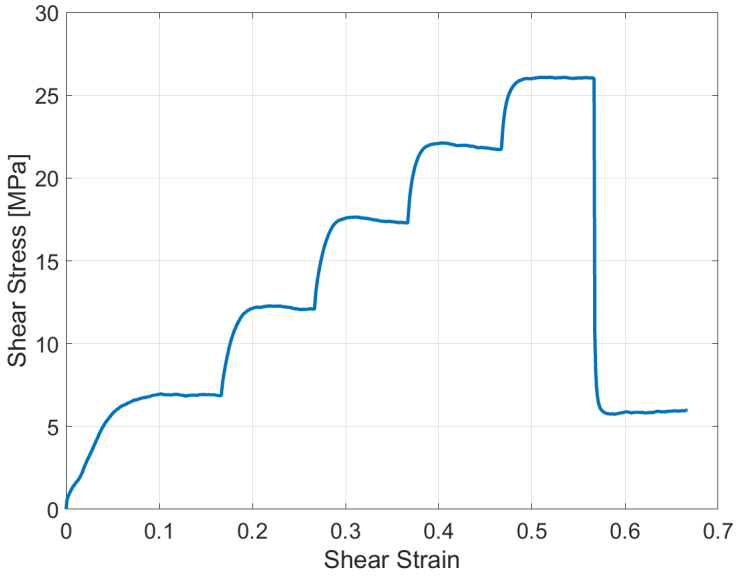

(b)

Figure 3.13: (a) The displacement/strain rate was increased by 5 times during the strain rate jump test on the same specimen. (b) The shear stress-strain curve of the whole test. The strain rate was only changed when the stress reached a plateau.

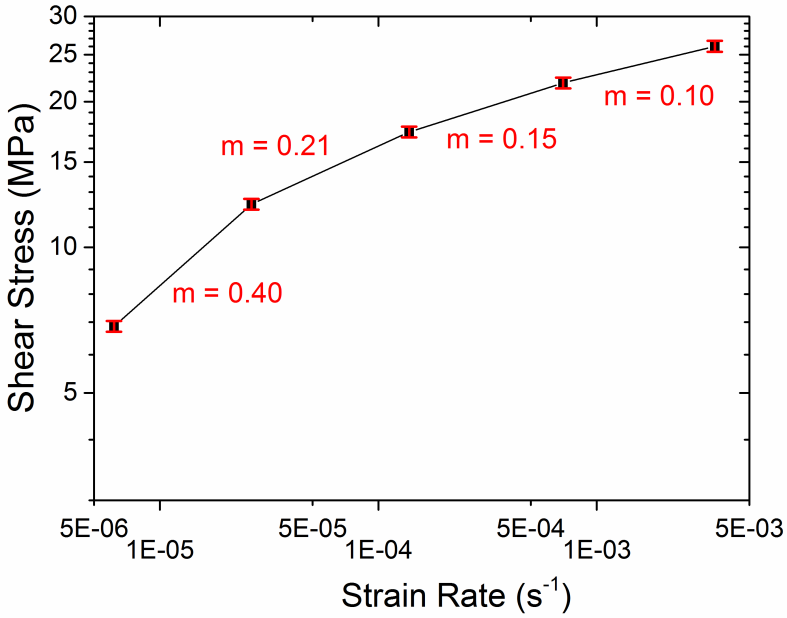

Figure 3.14: The stable stress at each strain rate was used in this stress-strain rate plot of the strain rate jump test on the same specimen.

3.2.4.2 Stress and Strain Rate

The stress-strain rate plot is usually used to characterise the strain rate sensitivity of a material. The strain rate sensitivity, m, is the gradient of the line joining two data points in the stress-strain rate plot in log scale. As shown in figure 3.14, m decreased from 0.40 to 0.10 as the strain rate increased. The shape of the curve indicates the first two data points are in the transient regime between Region II and III (see figure 2.3 on page 11). The largest m value was 0.40, which is a typical strain rate sensitivity for a superplastic material (0.40~0.50). The data points for the three highest strain rates are in Region III.

3.2.5 DIC Analysis of Strain in the Load Controlled Tests

Some images taken during the load controlled test that were used in the DIC analysis are shown in figure 3.15a to 3.15d at different strains. A mask was applied to the specimen. It could be seen that the left hand side of the specimen was gradually pulled downwards. There are clear vertical stripes in different colours across the specimen representing different displacement

levels. The time interval of the series of images was an input to the software so that the displacement was plotted as a function of time in figure 3.15e. The cyclic fluctuation in the strain rate was possibly due to the temperature change from day to night, which is also shown in the top left corner of the image. This indicates the sensitivity of the deformation to temperature. The overall strain rate was found to be $1.0 \times 10^{-6}/s$. Therefore, an additional data point was added to the stress-strain rate curve in figure 3.15f (based on figure 3.14 on the previous page). The strain rate sensitivity was calculated to be ~0.45 from the two points at the lowest strain rates.

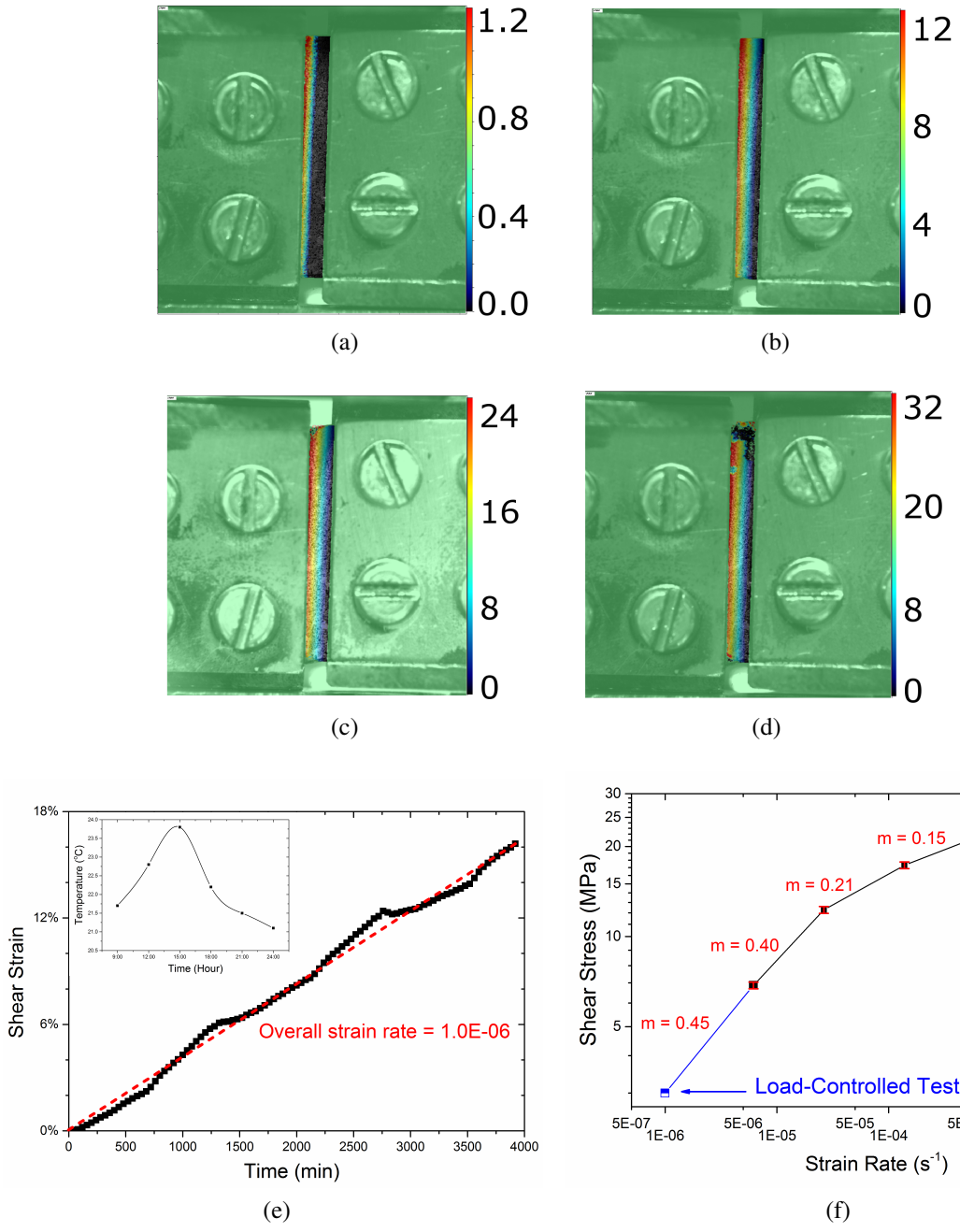

Figure 3.15: DIC analysis of the actual displacement of the specimen. Images taken (a) before loading; (b) 5% strain; (c) 10% strain; (d) last image taken at 15% strain. The scale is in pixels and changes for each image. (e) The displacement/strain rate was found to be relatively stable, though with cyclic fluctuations in response to the slight variations in the room temperature. (f) The data point from the load-controlled mechanical tests is plotted in the stress-strain rate curve.

3.3 Results: 2D In-situ Shear Test in SEM

3.3.1 Microstructure Characterisation using EBSD

EBSD analysis was carried out for two reasons: grain size and grain boundary characterisation. For grain size analysis, a large area was selected as shown in figure 3.16a. The threshold misorientation angle to define a grain was 4°. The threshold was chosen based on the critical misorientation angle below which the grain boundaries had a very low tendency to slide. This was observed from the in-situ SEM test in section 3.3.4. The rolling direction was along the vertical axis. As mentioned in section 3.2.1, there were subgrain structures aligned along the rolling direction. Within the patches of elongated large grains showing the same colour, there were mostly low-angle subgrain boundaries (<4°). The distribution of all the grain/subgrain boundaries is shown in figure 3.16b. In total, the fraction of low-angle grain/subgrain boundaries (in red) was 36%. The grain size was characterised based on this particular property — grain boundary sliding. The distribution of grain size in number fraction is shown in figure 3.16d. The grain size was 8 μm on average with a threshold misorientation angle of 4°. The grain boundary characteristics from the EBSD map will be linked to their tendency to sliding in section 3.3.4.

3.3.2 Low Displacement Rate Controlled Shear Tests

The results from the strain rate jump tests (section 3.2.4) provided guidance on the optimum conditions for in-situ tests. Limited by the lowest displacement rate of the testing device, two in-situ shear tests were conducted at strain rates of $6.7 \times 10^{-5}/s$ and $1.3 \times 10^{-4}/s$. The SEM images of the specimen tested at $6.7 \times 10^{-5}/s$ are analysed in section 3.3.3. The specimen tested at $1.3 \times 10^{-4}/s$ was characterised using EBSD before the test, which is correlated to the SEM observations in section 3.3.4.

The shear stress and strain plots are shown in figure 3.17a and 3.17b, respectively. At the lower strain rate, the stress had more fluctuations than for the higher strain rate test. This

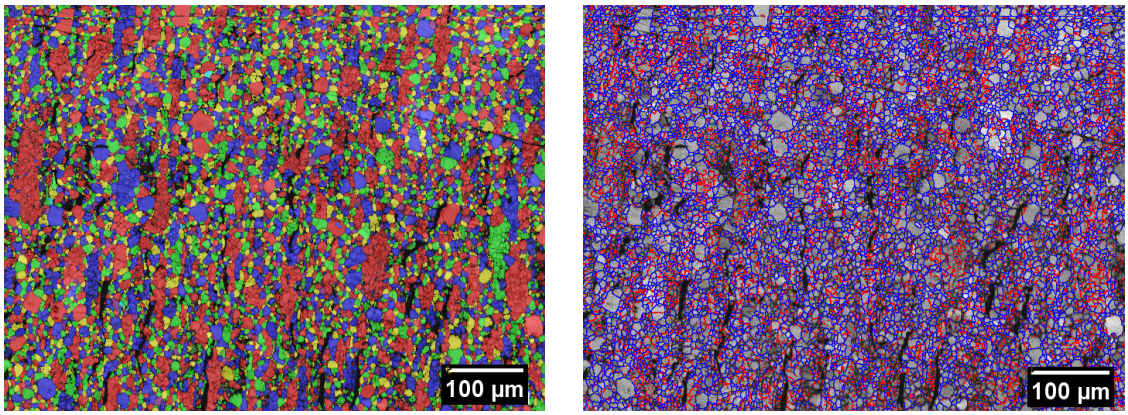

(a) (b)

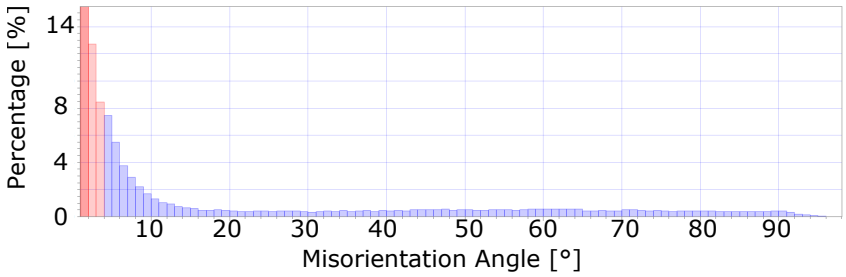

(c)

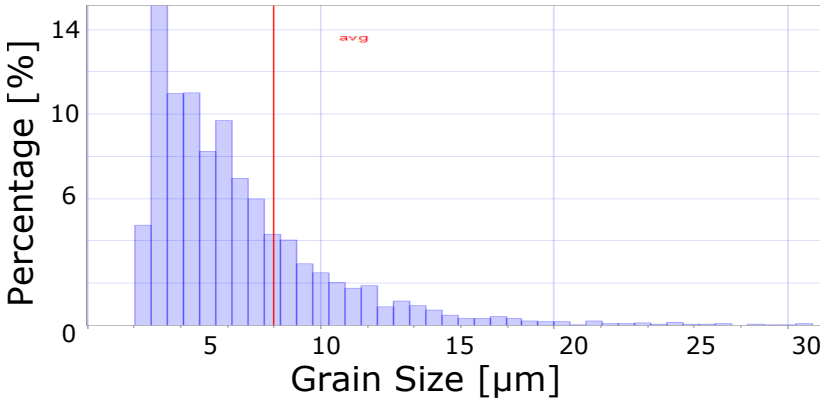

(d)

Figure 3.16: (a) Grain and pattern quality map of a rolled specimen with a threshold misorientation angle of 4°. The microstructure contains subgrain structures in the long and large grains. (b) The grain boundaries are revealed in the pattern quality image, showing a dense distribution of low-angle boundaries (<4°) in the large grains from (a). (c) The distribution of misorientation angles of the grain boundaries shows that 36% are low-angle grain boundaries. (d) Grain Size distribution histogram (number fraction) of the rolled specimen after cold extrusion, showing an average grain size of 8 µm.

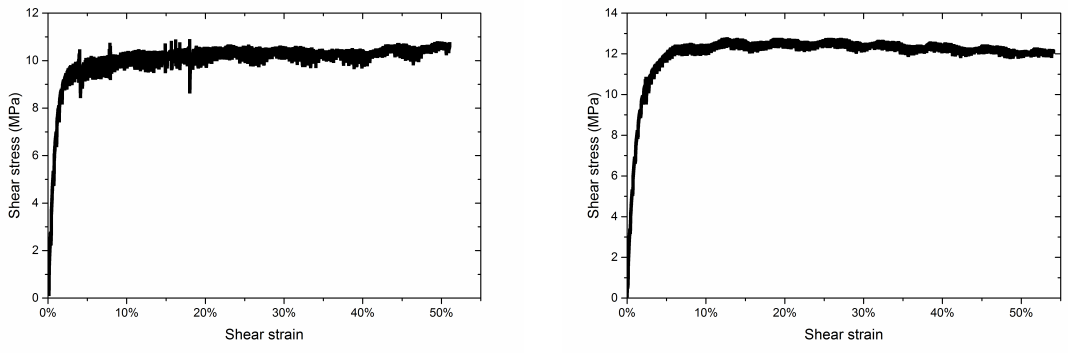

(a) (b)

Figure 3.17: Shear stress-strain curve of the in-situ shear test at a constant strain rate at (a) $6.7 \times 10^{-5}/s$ and (b) $1.3 \times 10^{-4}/s$.

might be attributed to the thermal and mechanical drifts. The stable shear stresses were around 10.3 and 12.5 MPa, respectively. The strain used in these two plots were obtained from the displacement measured by the test device, which would not represent the actual strain of the specimen, especially the local region with the surface grids. Therefore, the actual strain of the grid was measured as follows.

The SEM images with and without strain are overlapped with each other in figure 3.18a, which indicates that the displacement of the macro-grids was 5 μm. The strain of the 100 μm long grid was therefore ~5%, which was smaller than the overall strain of the specimen — 6%. The displacement of the macro-grid after 15% strain of the whole specimen was measured in figure 3.18b. It was found that the actual strain of the grid was 12%, which was again smaller than the overall strain of the specimen. Therefore, the actual local strain or strain rate is around 20% lower than that measured by the test device.

The stress and local strain rate (of the grids) data are plotted together with the ex-situ shear tests as shown in figure 3.19a. The strain rate sensitivity was calculated to be ~0.28. This indicates that these two in-situ tests were not in the superplastic regime. The stable stresses during creep deformation were much lower than those for the ex-situ shear tests at the similar strain rates. The strain rate sensitivity was higher than that for the ex-situ tests at the similar strain rates. This is probably due to the difference in the microstructure (grain size and grain

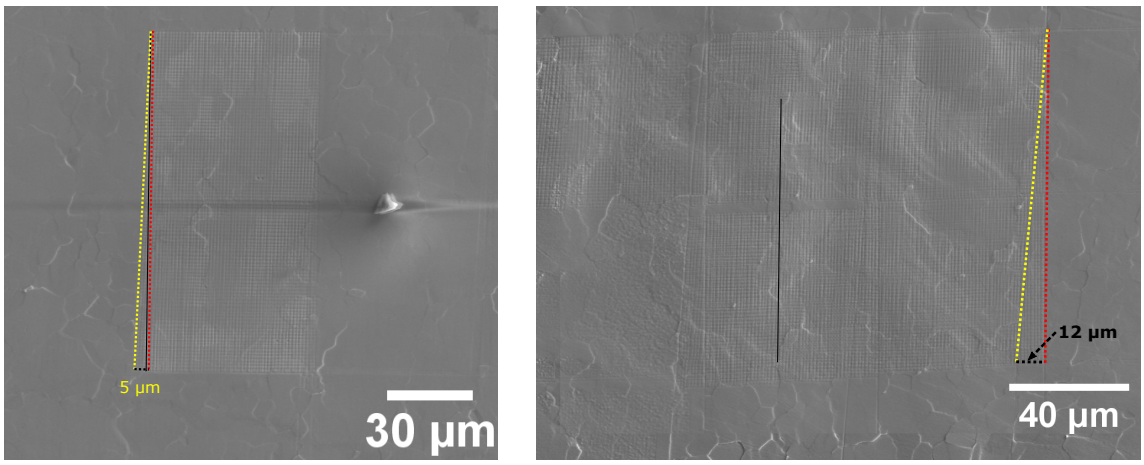

(a) (b)

Figure 3.18: (a) The two images before loading and at 6% strain (for the whole specimen tested at $6.7 \times 10^{-5}/s$) were overlapped with each other so that the displacement/strain of the macro-grids was measured. (b) On another sample, the actual displacement/strain of the macro-grid is compared with the 15% overall strain of the specimen tested at $1.3 \times 10^{-4}/s$.

boundary misorientation angles) between the in-situ and ex-situ shear tests. They were from the different batches of material with nominally the same processing method.

3.3.3 Analysis of the SEM Images

The SEM images were taken at four different magnifications every 2% strain. The shear deformation occurred along the horizontal axis in all the images. Figure 3.20a and figure 3.20b show two images of the same area at the same magnification at no strain and 6% strain, respectively. It revealed no microstructure or clear grain boundaries with no strain, but many of the grain boundaries became visible after 6% strain. This result correlated well to the stress-strain curve where the stress reached the plateau at ~6% strain. The visibility of grain boundaries was attributed to the deformation localised on the boundaries that generated abrupt surface steps. Furthermore, the coarse surface grids (50 by 50 µm squares) were sheared horizontally as indicated by the arrows.

Taking a closer look at the fine surface grids, figure 3.21a was taken when the grain boundaries started to be visible (i.e. at a strain of 6%). The surface grids were almost all straight without

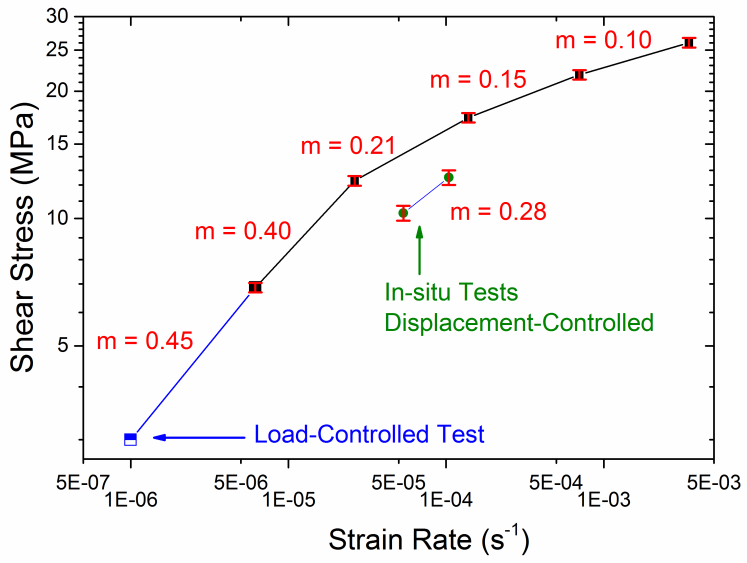

(a)

Figure 3.19: The shear stress and strain rate data from all the in-/ex-situ tests are plotted together, showing a discrepancy between the two types of shear tests. This is probably attributed to the slight difference in the grain size.

much interference from the grain boundaries. Only at the highlighted grain boundaries were the grids slightly distorted. This example of grain boundary sliding at the very initial stage of deformation was accommodated by grain rotation. It could be noticed that some areas showed no presence of grain boundaries at all, which could be attributed to the inactivity of low-angle grain boundaries. In figure 3.21b at 50% strain, there were four types of features worth noting. Firstly, some grains had obviously rotated, thereby distorting the grid lines on the grain boundaries all around them. Interestingly, the grid lines inside the bulk grains were almost perfectly straight. Comparing the fine grids inside the grain circled in yellow, there was almost no distortion. Secondly, some grains showed distorted grid lines on the boundaries, especially the boundaries aligned parallel to the shear direction. Thirdly, microcracks were formed on some grain boundaries in the "inactive region" from figure 3.21a. Those failed grain boundaries tend to be at 45° to the shear (horizontal) direction, i.e. with the maximum tensile stress applied across the grain boundaries. Lastly, there were grain boundaries that still remained inactive after 50% strain. Those boundaries, together with the ones generating

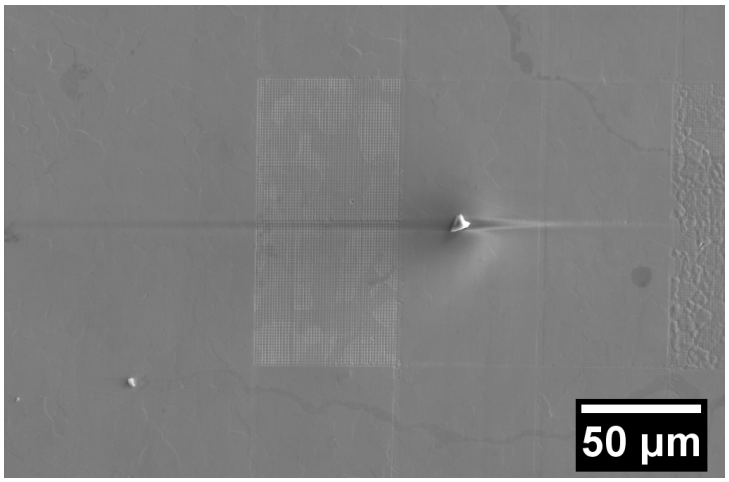

(a)

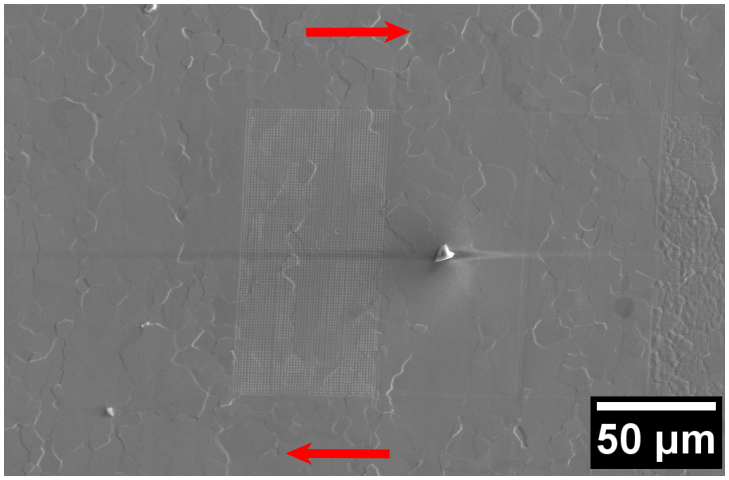

(b)

Figure 3.20: The specimen was sheared along the horizontal axis at a strain rate of $6.7 \times 10^{-5}/s$. SEM images of the surface grid area, which were taken at low magnifications (a) before loading and (b) 6% macroscopic strain of the specimen.

microcracks, had much less tendency to grain boundary sliding compared to those that rotated or distorted the grid lines.

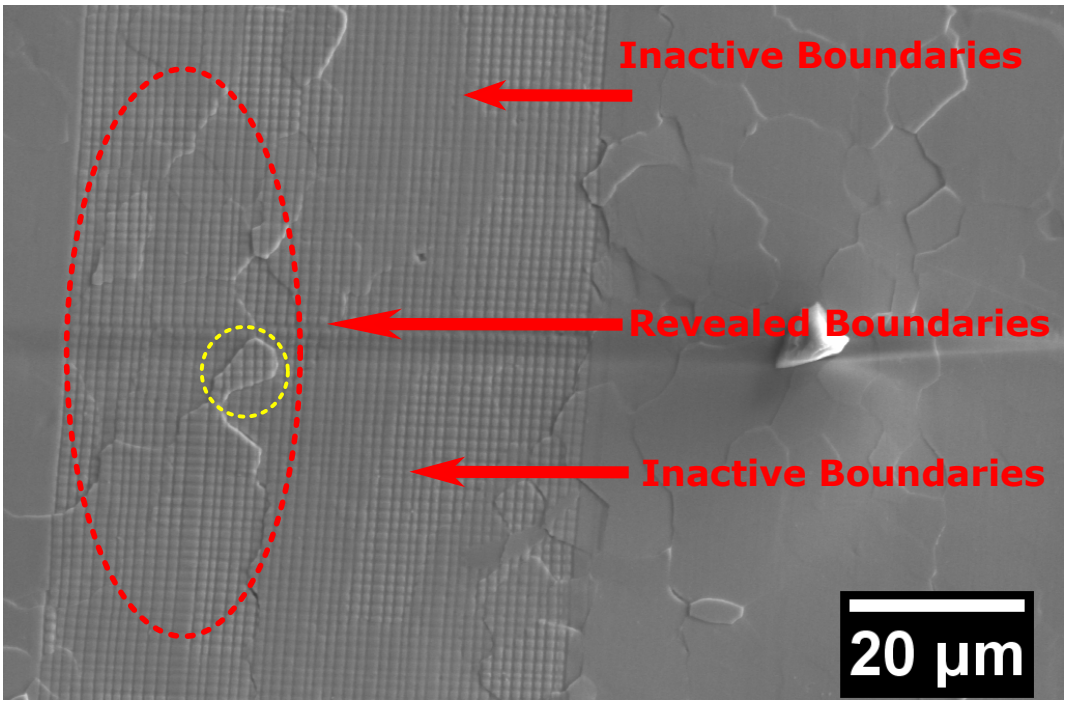

(a)

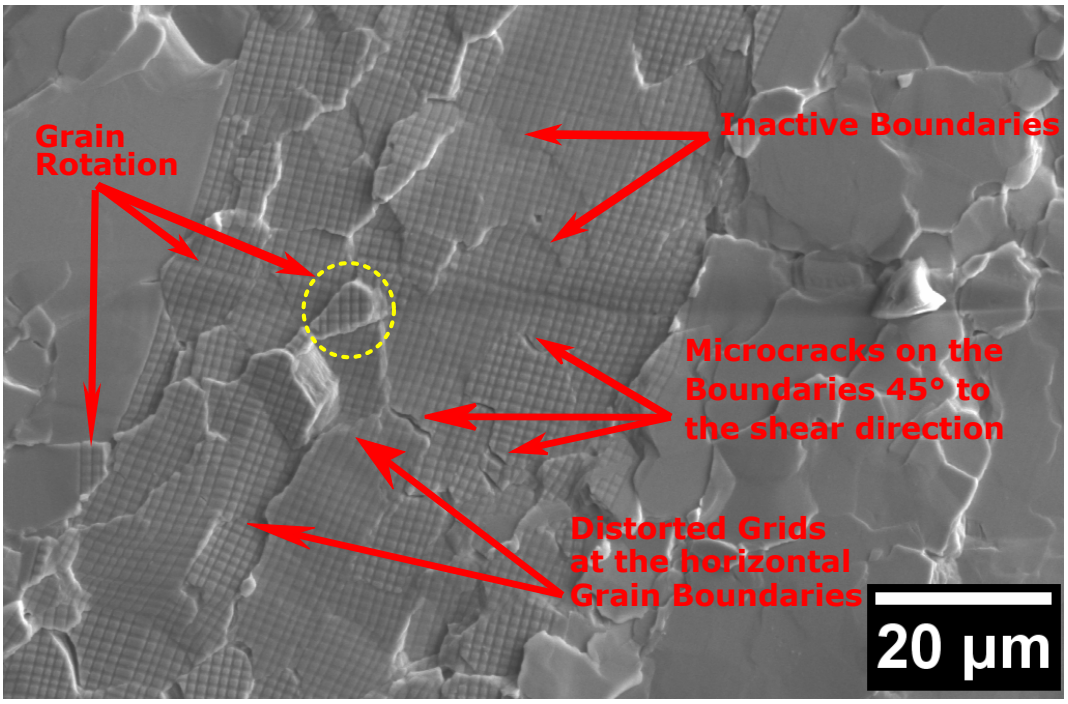

(b)

Figure 3.21: SEM images of the region with micro-grids at high magnifications at (a) 8% strain and (b) 50% strain. Some grain boundaries were revealed in (a) but some boundaries were still not visible. After 50% strain in (b), there were grain rotations, grain boundary sliding induced distortion of surface grids and inactive boundaries.

3.3.4 Correlation between Grain Boundary Characters and Sliding

The EBSD map of the area with surface grids is highlighted in figure 3.22a. The threshold misorientation angle to define a grain was 4°. It is part of the whole map in figure 3.16a. The grain boundaries are revealed in figure 3.22b, where low and high-angle boundaries (4° as the threshold angle) are displayed in red and blue, respectively. The distribution of misorientation angles of the grain boundaries in the area with surface grids are illustrated in figure 3.22c. It could be seen that more than a third (35%) of the grain or subgrain boundaries were low-angle boundaries. The EBSD map was overlaid with the SEM image in the region of fine surface grids (figure 3.22d).

From figure 3.23a (15%to 3.23c and 3.23e where the SEM images and EBSD map overlay, most grain boundaries were revealed by deformation on the boundaries. The SEM images are placed on the side for reference. It could be seen that there were also some inactive areas remaining flat without boundaries being revealed. Some of the boundaries aligned at 45° to the shear direction had microcracks generated by the tensile stresses across the grain boundaries. Those inactive regions during deformation corresponded well to the areas formed of low-angle boundaries shown in red.

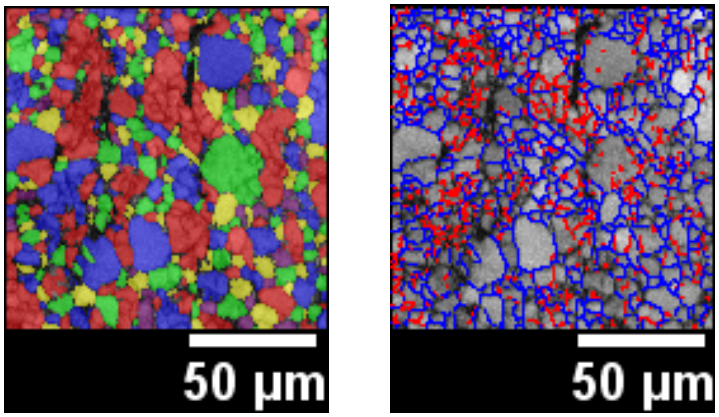

(a) (b)

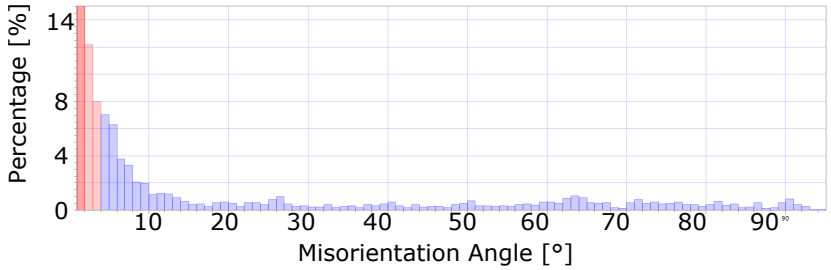

(c)

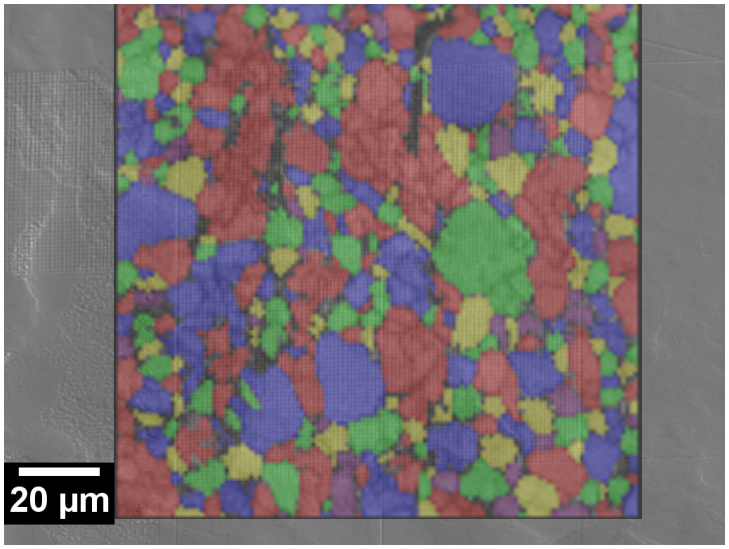

(d)

Figure 3.22: (a) EBSD map of the area with fine surface grids. (b) High and low grain boundaries (including subgrain boundaries) are revealed in blue and red, respectively. (c) Misorientation angle distribution of all the boundaries in the subset area, indicating a 64% proportion of low-angle ones. (d) SEM overlapped with EBSD map of the surface grids taken before loading.

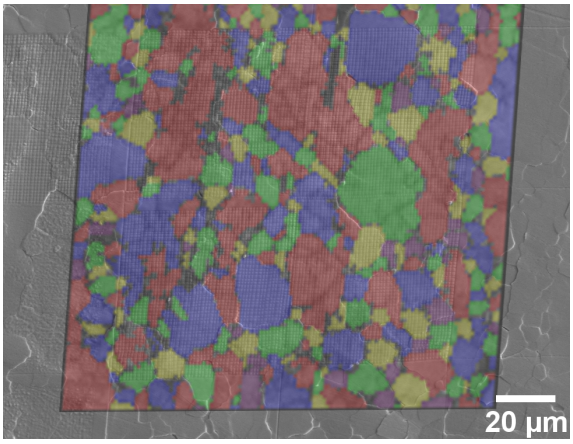

(a) 15% strain

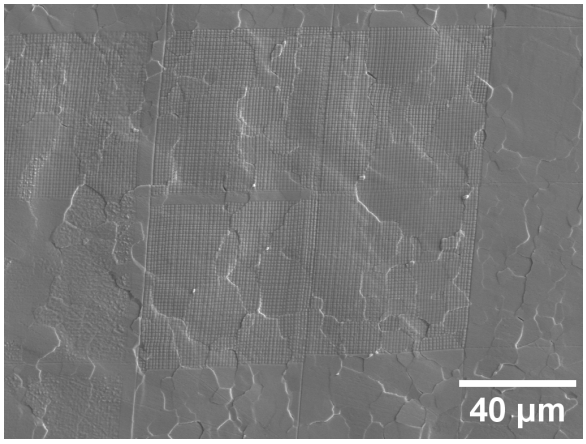

(b) 15% strain

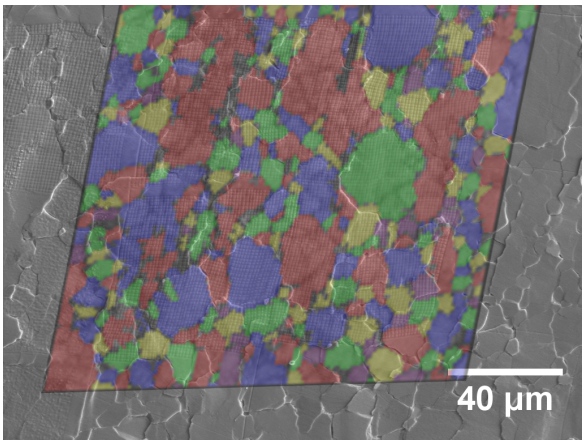

(c) 36% strain

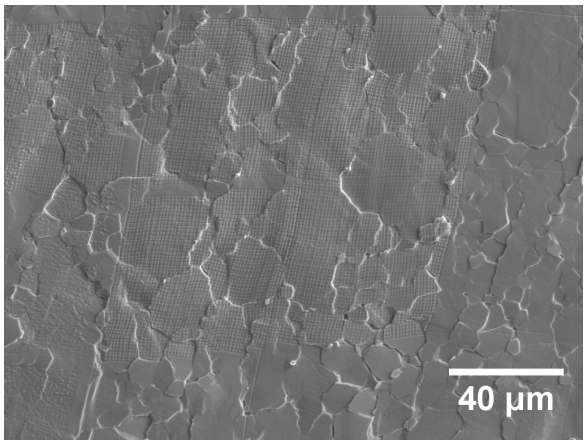

(d) 36% strain

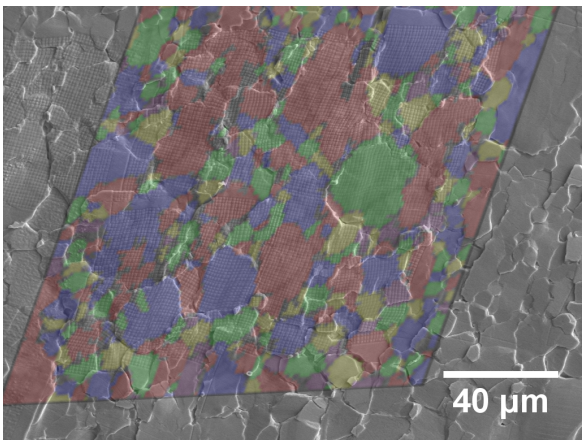

(e) 60% strain

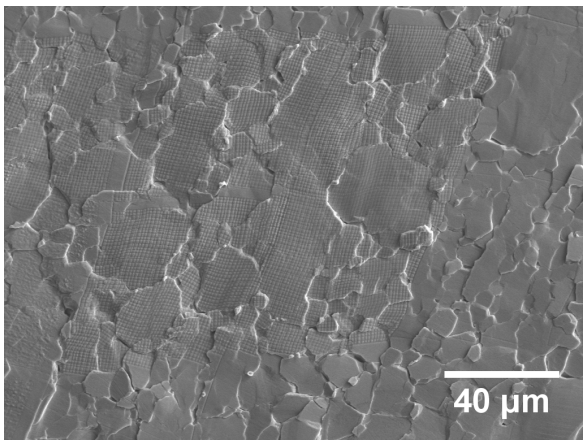

(f) 60% strain

Figure 3.23: The SEM images overlay with the EBSD grain map. (a) and (b): at 15% strain, some grain boundaries were revealed. (c) and (d): after 36%, some grain boundaries remain inactive. (e) and (f): even after 60% strains, those grain boundaries still remain inactive, even though the surrounding boundaries have had in-plane and out-of-plane deformation. The inactive grain boundaries corresponded to the low-angle grain boundaries (<4°) in the EBSD map, indicating that they have less tendency to sliding.

3.4 Discussion

3.4.1 Grain Boundary Misorientation Angles and Sliding

The threshold misorientation angle was 4° to define low and high-angle boundaries in this work. The general definition of low-angle boundaries was that the boundary structure can be represented by an array of edge dislocations [69]. Beyond about 15°, the boundary structure could no longer be described by the dislocation model. It is widely accepted that high-angle random boundaries have larger tendency to slide, which is attributed to the ease of absorbing lattice dislocations [148, 149]. Using zinc bicrystalline specimens, Watanabe et al. [79] found that low-angle boundaries (6° and 13°) had extremely low contribution of grain boundary sliding to the total creep strain, while high-angle random grain boundaries could slide easily. The authors also found a temperature dependence of the grain boundary sliding rate in boundaries above 20° but not in a low-angle boundary (16.5°). Therefore, Watanabe [148] concluded that low-angle boundaries are very resistant to sliding, which were defined as below 20°. Similarly, in many works [150, 151, 152], including in tin alloys [87, 153], 15° has usually been chosen as the threshold angle to differentiate low and high-angle grain boundaries.

However, it was found that some low-angle grain boundaries could also slide from the in-situ SEM shear tests. As shown in figure 3.24a, the target low-angle boundary was a subgrain boundary at a threshold angle of 5° for the EBSD grain map. However, when the threshold angle was 4°, the target boundary was defined as a grain boundary. Comparing the SEM images at 15% strain (figure 3.24c) and 36% (figure 3.24d), the low-angle grain boundary was initially visible after 15% strain, and gradually sliding to almost the same extent as the high-angle grain boundaries (with the same boundary orientation to the shear direction). This indicates that this low-angle boundary could also slide when there was a large enough driving force. As discussed in section 3.3.4, almost all the subgrain boundaries below 4° did not slide, most of which were not revealed by deformation at as large strain as 60% in figure 3.23e. Therefore, 4° was chosen as the threshold misorientation angle below which there was no sliding. This

definition of low- and high-angle boundaries was specifically made for this particular material's property — grain boundary sliding, which is more appropriate than the general definition of low-angle grain boundaries as below 15°. The findings in the current study are consistent with the testing results on bicrystals of aluminium that the initial grain boundary sliding rate dropped to zero with misorientation angles below 6° (refer to figure 2.17 in the literature review) [72]. It was also found in Telang et al.'s [89] studies on the tin-based solder joints that low-angle grain boundaries (~6° and ~13°) slid at room temperature. When the resolved shear stress is sufficiently high, sliding could occur by climb of the misfit grain boundary dislocations [89].

The fraction of low-angle grain boundaries (<4°) in this cold extruded material (at liquid nitrogen temperature) was quite high (36% in figure 3.22c). In order to maintain the fine microstructure, the material had not been annealed. The fraction of boundaries below 15° was as high as 64%. A similar grain boundary character distribution was found in an aluminium alloy (5056 series) after "cold" extrusion at 200°C [154]. In that alloy, the fraction of boundaries below 15° was 83%, which abruptly decreased to 10% when annealed at 400°C. This indicates that low-angle grain boundaries were induced by the large amount of cold deformation without recrystallisation. The high-angle random boundaries have a larger grain boundary energy, which had more tendency to sliding. As shown in figure 3.25a, there were many fine grid lines dislocated on the high-angle random grain boundaries. When orientated at 45° to the shear direction, the high-angle random boundaries tended to fail and generate microcracks as shown in figure 3.25b. This finding highly agreed with that in an Fe-0.8at%Sn alloy, where high-angle random grain boundaries were preferential sites for creep intergranular fracture [148].

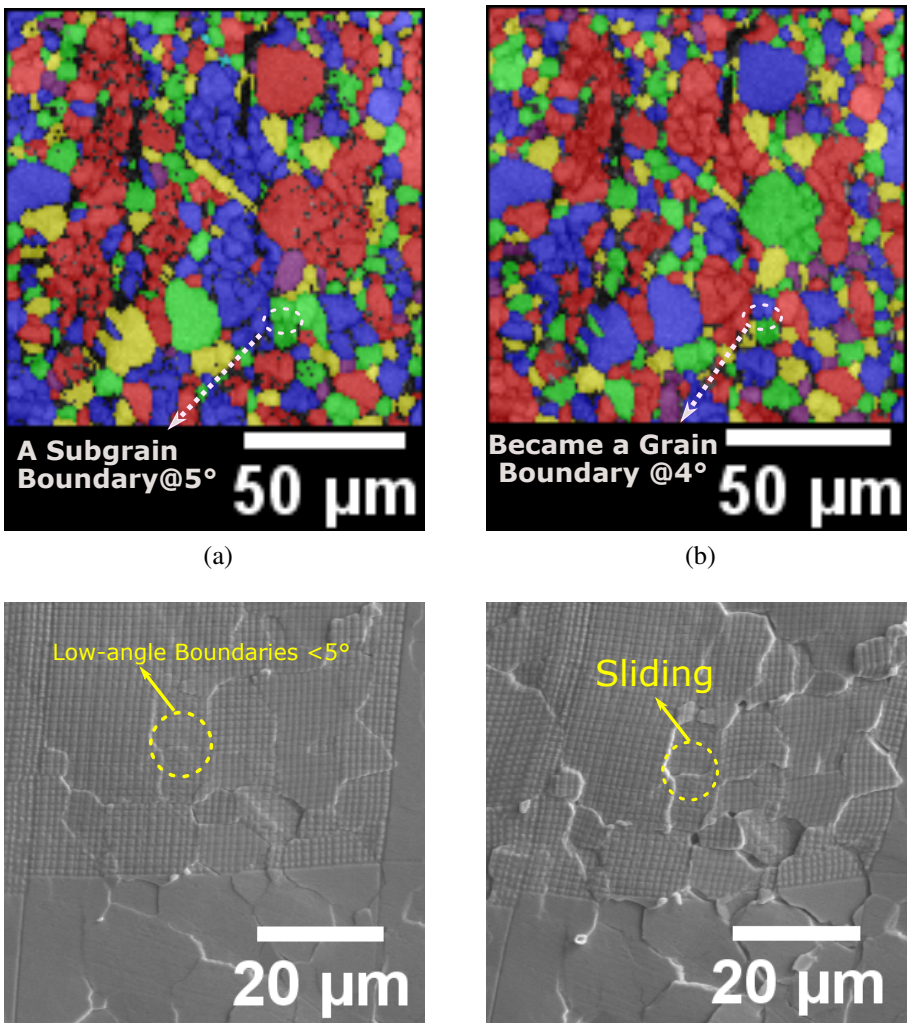

Figure 3.24: (a) EBSD grain map showing a subgrain boundary in a large grain at a threshold angle of 5°. The colours are randomly assigned to the grains. (b) EBSD map showing that the same boundary became a grain boundary at a threshold angle of 4°. (c) The low-angle grain boundary was revealed by deformation at 15% strain. (d) The low-angle grain boundary has obviously slid for some displacement.

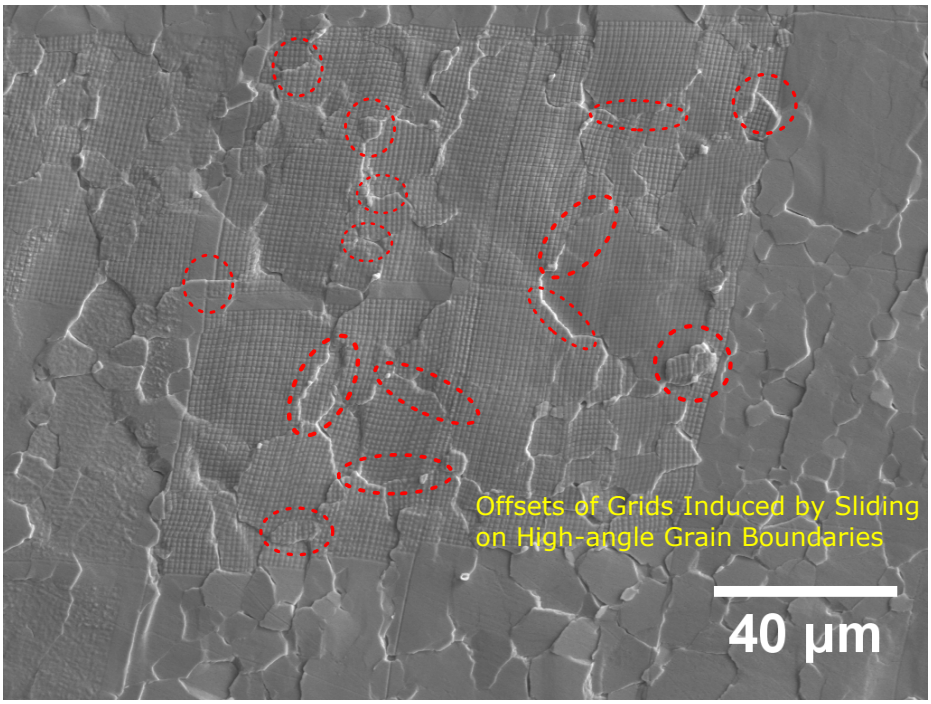

(a)

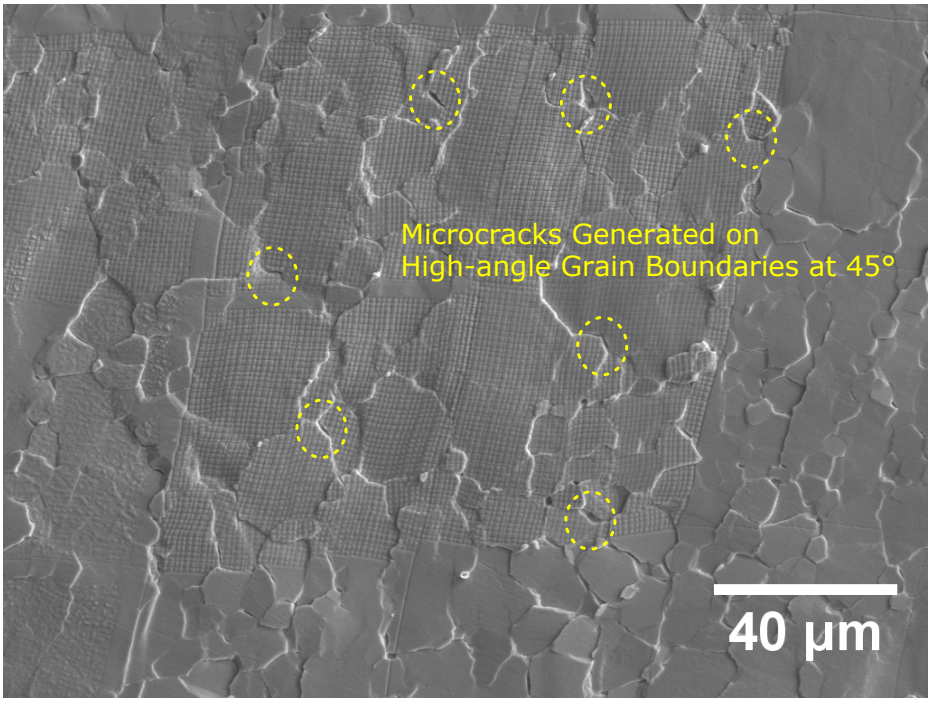

(b)

Figure 3.25: (a) Many high-angle grain boundaries had grid line offsets on the boundaries due to sliding. (b) Some high-angle grain boundaries at 45° to the shear direction failed and generated microcracks at 36% strain.

3.4.2 Grain Neighbour Switching

It is widely accepted that a characteristic geometry of grain neighbour switching (figure 2.5 on page 15 and 2.9 on page 20) is usually coupled with the grain boundary sliding process. Grain neighbour switching was also observed experimentally from surface studies on a titanium alloy [145] and an aluminium alloy [1]. For these materials, heating is necessary to reach the required homologous temperature for superplasticity. However, this has largely promoted oxidation during deformation, thereby introducing oxide artefacts on the sample surface. These artefacts have significantly obscured the identification of the grain neighbour switching events. For example, the oxide formed on the prior grain positions will lead to ambiguous observation of grain's actual position after deformation [145]. Furthermore, the oxide could even prevent direction observation of grains in connection or separation on the surface, requiring FIB milling to reveal grain neighbour switching events beneath the surface [1]. With the low melting point of Sn-Bi as an advantage to exhibit superplasticity at room temperature, there were no apparent oxidation issues in the present surface study. Some grain neighbour switching events are shown in figure 3.26a to 3.27b. In all the three examples, Grain A and B were connected to each other at a low strain, while Grain C and D were well separated. Upon superplastic deformation partially via grain boundary sliding, those regions have shown the grain neighbour switching phenomenon that Grain C and D became neighbours after a shear strain of 50%. It could also be noticed that the surface grid lines were interrupted by the new material plated out at some grain boundaries, which indicated the possibility of diffusion creep occurring at those boundaries.

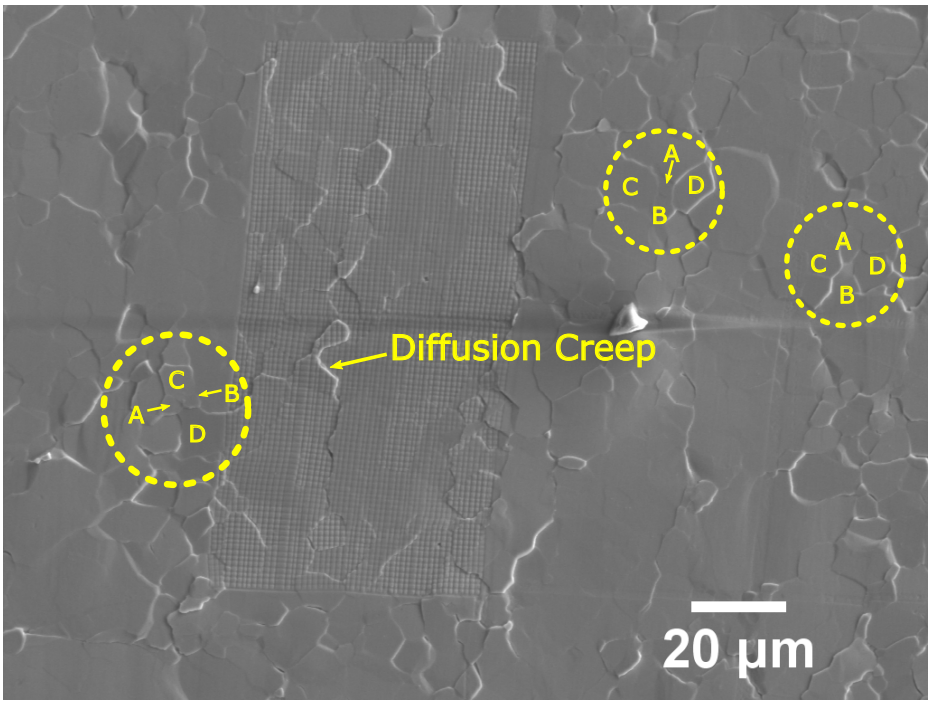

(a)

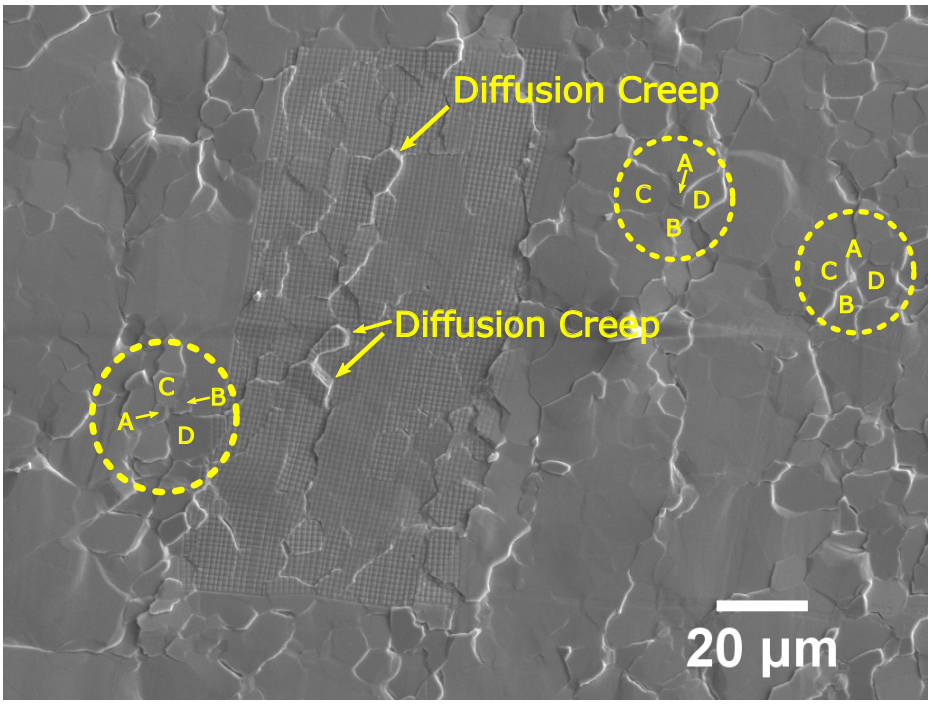

(b)

Figure 3.26: The SEM images taken during the in-situ shear test ($6 \times 10^{-5} s^{-1}$) at different (engineering) strains (a) 13% strain (b) 26% strain. At some grain boundaries, the grid lines were disturbed possibly due to diffusion creep at the grain boundaries.

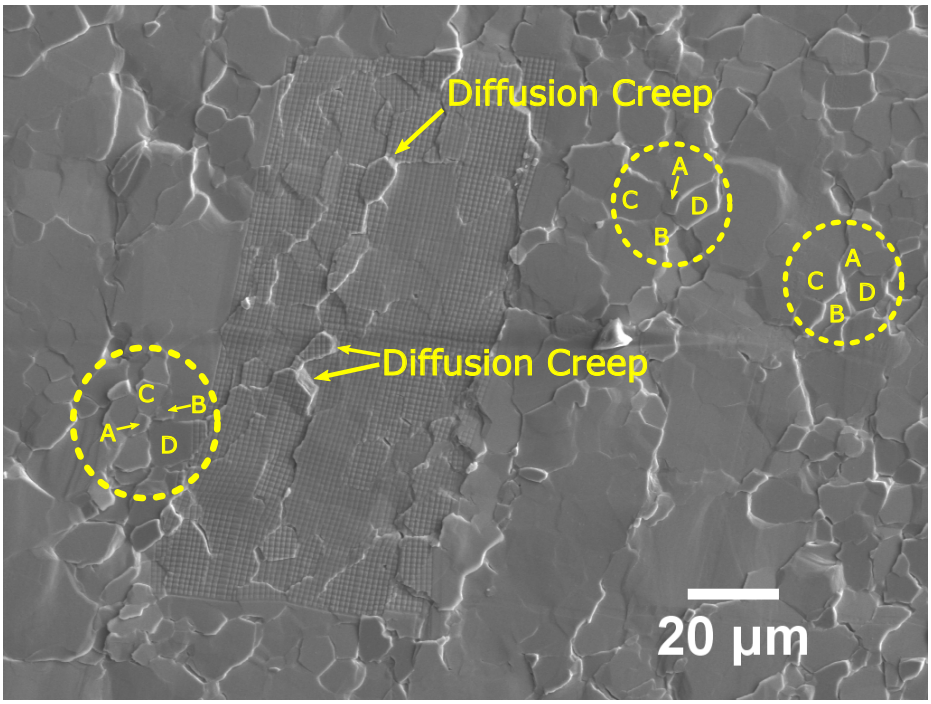

(a)

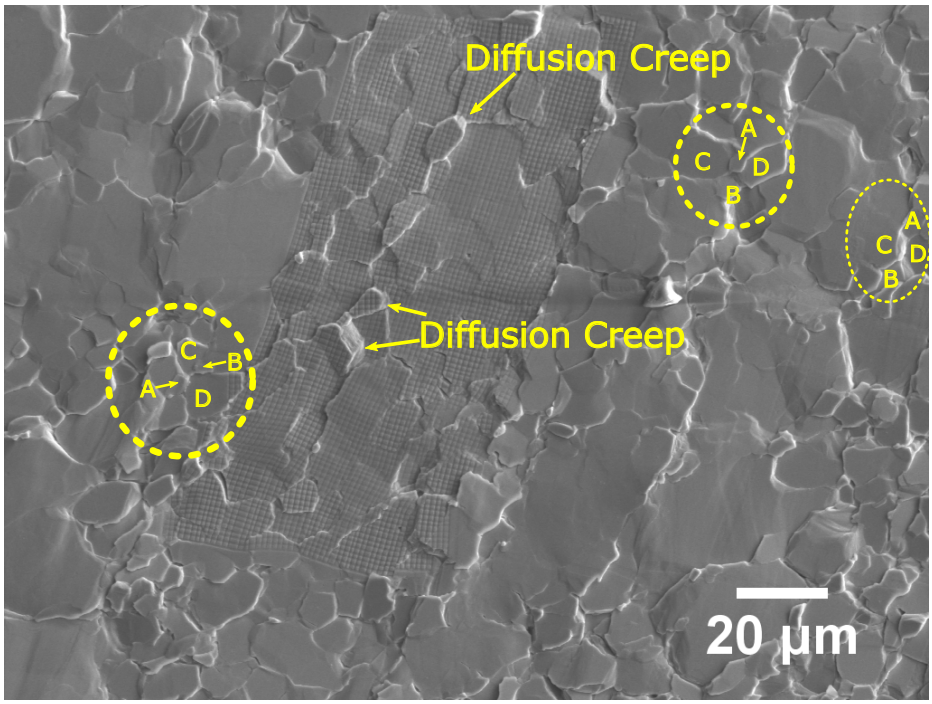

(b)

Figure 3.27: Continued from the figures above to (a) 33% and (b) 50% strains. There are a few grain neighbour switching events identified.

3.4.3 Grain Boundary Sliding Coupled with Migration and Grain Rotation

It has been found in many superplastic materials that some grain boundary sliding events are coupled with boundary migration [155, 156, 157, 158, 137, 159]. An example is shown in figure 3.28a that the grain boundary has slid and migrated [155]. There were also intergranular cracks repeatedly generated on the grain boundary during the long-time creep deformation. The phenomenon of migration coupled with sliding was explained by the motion of DSC dislocations on the grain boundary plane (sliding) and normal to the grain boundary (migration) [139]. Sheikh-Ali [159] argued that the grain boundary migration was caused by the motion of extrinsic secondary grain boundary dislocations as shown in figure 3.28b. The glissile motion of the extrinsic secondary grain boundary dislocations along the grain boundary lead to sliding. However, the motion of intrinsic secondary grain boundary dislocations could not provide a driving force for shear behind a migrating grain boundary, and therefore could not cause sliding coupled with migration [159].

Similar features were found in the current study from the ex-situ shear tests. As shown in figure 3.28c, the two grain boundaries had clearly migrated together with sliding that displaced the straight scratch lines. Furthermore, figure 3.28d shows that the grain boundary had a microcrack formed under the maximum tensile stress applied on the boundary. There were also a few examples showing grain rotation accommodating grain boundary sliding (section 3.3.3). The grains did not change their shapes when the boundaries slid. These findings are consistent with the shear tests on a Sn-Pb eutectic alloy carried out by Zelin [160].

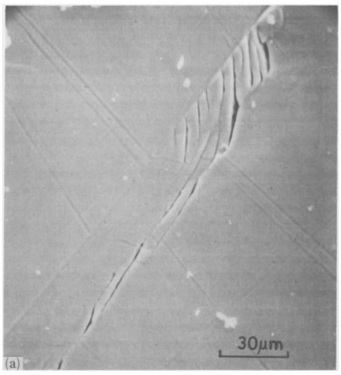

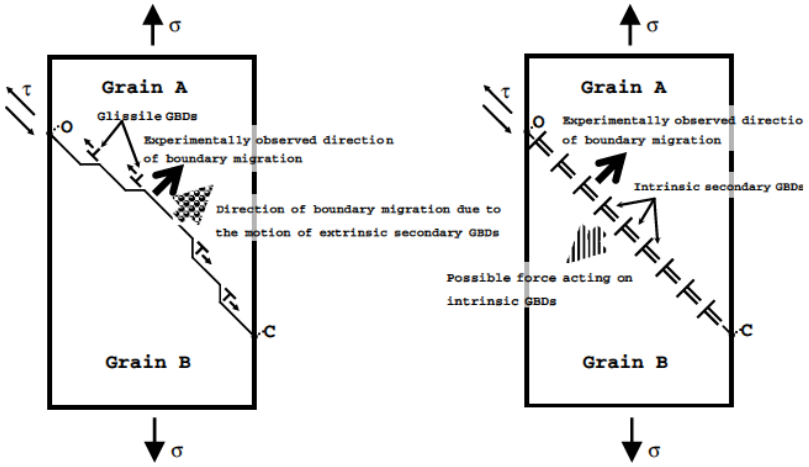

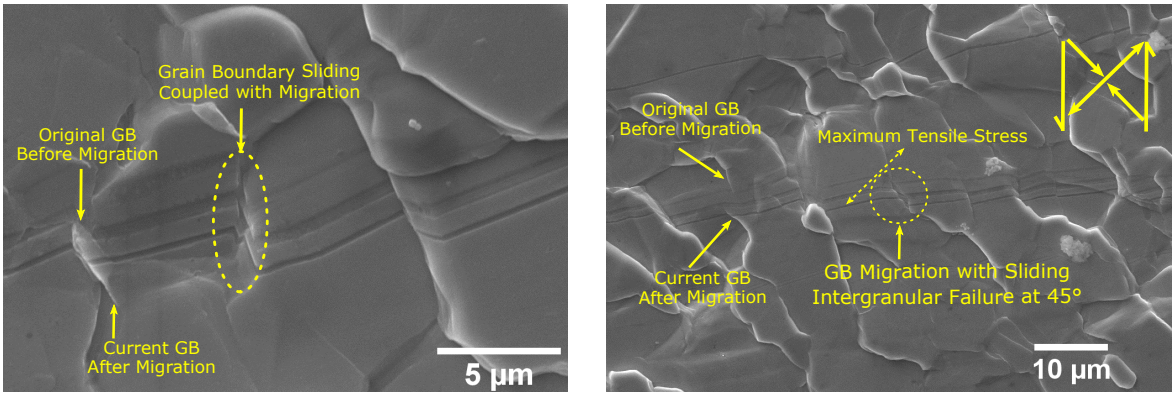

Figure 3.28: (a) An example of grain boundary sliding coupled with migration found in an Fe-0.8at%Sn alloy [155]. (b) The motion of extrinsic secondary grain boundary dislocations normal to the grain boundary caused grain boundary migration [159]. (c) and (d) show examples of the sliding and migration of the grain boundaries after 75% strain tested at a constant strain rate of $5 \times 10^{-6}/s$. In (d), there is a microcrack failure on the grain boundary at 45° to the shear direction that has slid and migrated.

3.5 Conclusions

Classical models for diffusion creep and superplasticity assume that all grains undergo the same process, but recent research results have shown that this is not true [1]. Surface studies using both meso- and micro-grids were conducted to characterise this inhomogeneity. The following findings were made:

- The material processed via casting, cold extrusion and rolling proved to be superplastic via strain rate jump tests. The strain rate sensitivity of this Sn-1wt% Bi alloy (8.5 μm grain size) was found to be $m \sim 0.45$, which was slightly lower than that ($m \sim 0.48$) for a 5 μm grain-sized Sn-1wt% Bi alloy [28].

- Quantified analysis was made on the ex-situ shear test with straight marker lines perpendicular to the shear direction. Different grain boundaries exhibited sliding to different extents. But this single-direction grid lines may introduce biased observation on the extent of sliding, because the boundaries perpendicularly intersecting the lines would have more obvious offsets. Therefore, meso and micro grid lines were used for the in-situ tests.

- The SEM images taken from the in-situ shear tests indicated that some grain boundaries were more active in sliding than the others. The active boundaries distorted the surface grid lines on the boundaries, while the grid hardly changed in the bulk of the grain.

- The inactive grain boundaries were not visibly revealed after 5% strain, when a plateau stress was reached. They either remained inactive or generated microcracks until 50% strain.

- Correlation between EBSD and activity of grain boundaries confirmed that low-angle grain/subgrain boundaries (below 4°) did not participate in sliding.

- However, there are limitations of the surface studies that the 2D observation might not represent the bulk material behaviour. This chapter has provided the foundation for the 3D diffraction contrast tomography (DCT) experiments in Chapter 5.

Chapter 4

Micro-mechanical Testing: Cantilevers with Individual Grain Boundaries

Overview: Micromechanical testing of grain boundary sliding is the core part of the project. A microcantilever design containing a single grain boundary has allowed the grain boundary sliding behaviour of individual boundaries to be investigated. A nanoindenter was used to apply a load to the grain boundary and measure the sliding displacement. The iterative development of the microtest piece geometry and test procedures to its final state is briefly described. In order to examine the reproducibility of the results, the tests were repeated under nominally identical conditions on the same cantilever. Pairs of cantilevers were made on the same grain boundary so that their behaviour could be compared with each other. A number of grain boundaries were selected with a range of various misorientation angles. The steady-state shear stress for grain boundary sliding was compared among those grain boundaries. Special grain boundaries such as a twin boundary were also investigated. Since strain rate sensitivity is expected to be significant for grain boundary sliding, some cantilevers were tested at several different displacement rates. The design of microcantilever tests can potentially separate grain boundary sliding from diffusion creep by varying the stress conditions on the grain boundary plane.

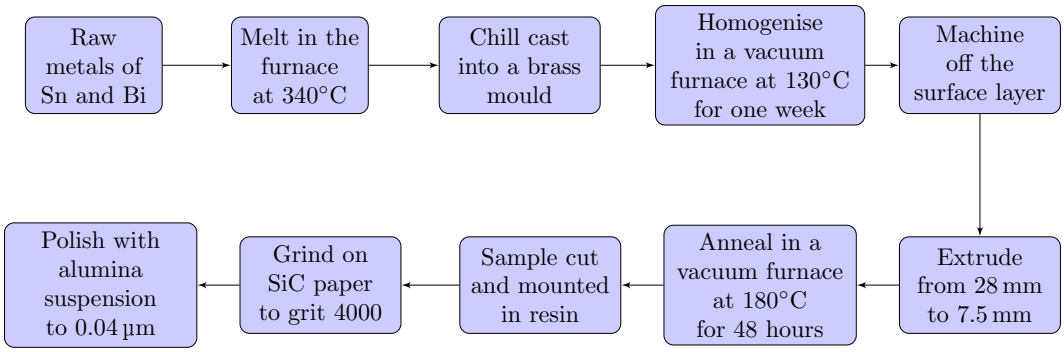

Figure 4.1: Material processing and sample preparation for micro-tests.

4.1 Materials and Experimental Methods

The material manufacturing process for micro-tests was similar to that for the macro-tests (as described in Chapter 3), except for the extrusion process. For micro-test material, extrusion was carried out at room temperature with a smaller extrusion ratio. The average grain size of the extrusion was over ~200 µm, which allowed multiple cantilevers to be made on the same grain boundary. Microcantilevers were manufactured by using a focused ion beam (FIB) microscope and subsequently tested using a nanoindenter. The data were analysed in MATLAB and OriginLab. The details of the materials processing and experimental methods are described as follows.

4.1.1 Materials Processing and Sample Preparation

As described in the flow chart in figure 4.1, after chill casting and homogenisation, the ingot was machined to 28 mm in diameter. The ingot was then extruded at room temperature to a rod 7.5 mm in diameter (in comparison to 2.2 mm for the macro-test samples). In order to remove the texture and intragranular plasticity developed from extrusion deformation, an annealing heat treatment was carried out at 180°C for 48 hours. A 7 mm long cylinder was cut from the rod, which was then mounted into a stub using epoxy resin. The sample was ground and polished to a scratch-free surface finish using the standard recipe as shown in the flow chart (figure 4.1).

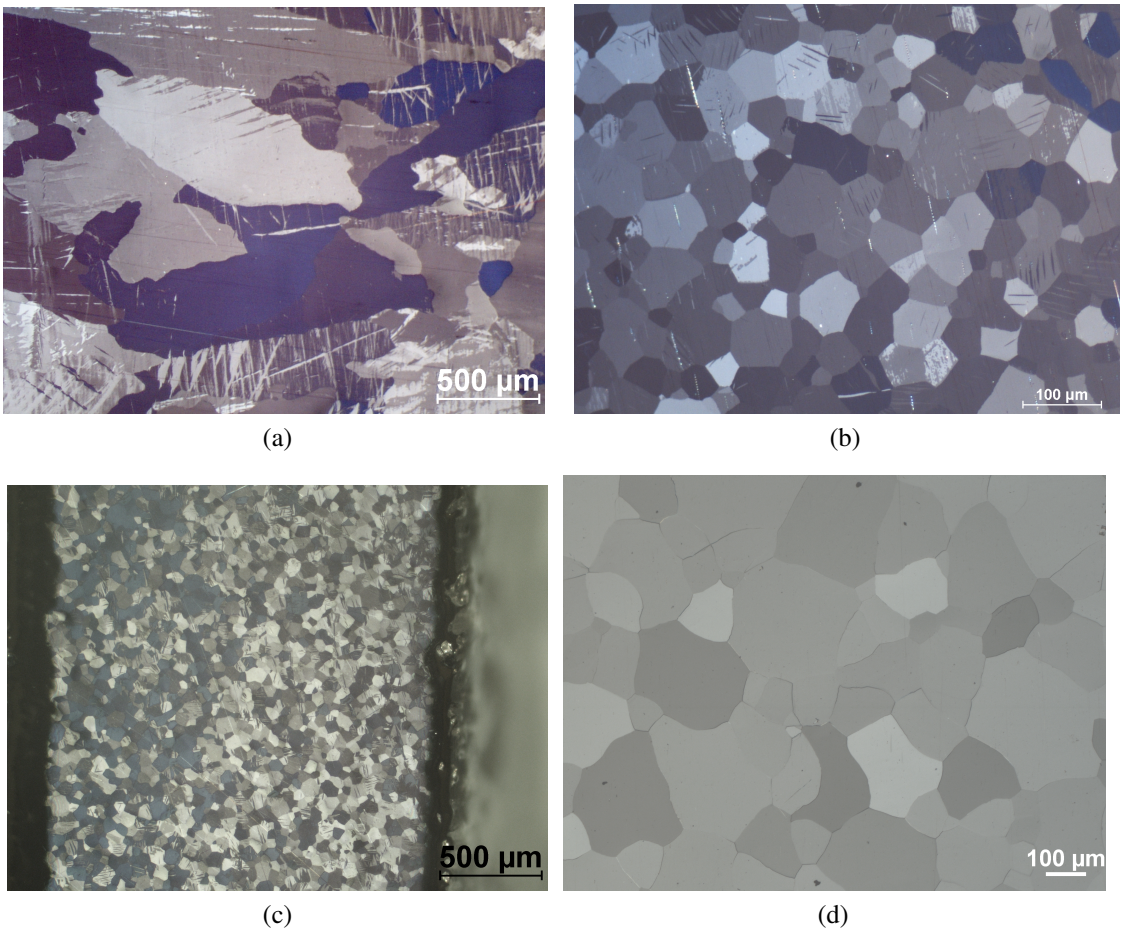

(a) (b)

(c) (d)

Figure 4.2: Comparison between the microstructure of the (a) as-cast and (b) as-extruded samples (viewing along the extrusion direction). (c) Cross section along the extrusion direction showing the equiaxed grains. (d) As-annealed microstructure showing that the grains have grown.

4.1.2 Microstructure (Including Grain Boundary) Characterisation

The microstructure of the sample was characterised in a Carl Zeiss optical microscope after polishing. Polarised light was used to reveal the grains. The as-cast (figure 4.2a) and as-extruded (figure 4.2b) microstructure were characterised and compared as shown below. The grains became smaller in size and more equiaxed in shape viewing along the the extrusion direction. The microstructure of the cross section along the extrusion axis was also characterised in figure 4.2c. The grains were also equiaxed in this direction. The microstructure after annealing is shown in figure 4.2d, in which the grains had grown.

The grain structure of the material was further characterised by EBSD in SEM (figure 4.3a). The threshold misorientation angle to define a grain was 4°. The grain boundary characteristics were obtained, including the misorientation angle, rotation axis and the grain boundary plane normal (with an assumption that the grain boundary plane is normal to the sample surface). The grain boundary misorientation angle and rotation axis were obtained from the TSL OIM software. Since the grain boundary plane is almost normal to the sample surface, the grain boundary plane orientation can be described by the orientation of the plane normal relative to the two grains on either side of the boundary. This information could be obtained by drawing a straight line along the cantilever axis as shown in figure 4.3b. The grain boundaries identified in figure 4.3a are categorised to low-angle (light blue lines) and high-angle (purple lines) boundaries with the threshold misorientation angle of 15°. The distribution of grain boundary disorientation angles is shown in figure 4.3c and 95% are high-angle boundaries. Both low and high-angle grain boundaries are present, providing a wide range of grain boundary misorientations.

4.1.3 Microcantilever Manufacturing by Focused Ion Beam

The idea of focusing an ion beam to small dimensions was first described in the 1970s. In 1979, Seliger et al. [161] managed to form focused ion beams with a liquid-metal gallium source (Ga^+). The probe size and current of Ga^+ beam were comparable to a scanning microscope using the electron counterpart. Since then, the focused ion beam (FIB) technique was increasingly applied to ion microscopy and microcircuit fabrication. The Ga^+ ions are field-extracted from a reservoir to a sharp needle by an extractor electrode. Then the ions are accelerated down a column by a voltage between 5 and 30 keV. The typical emission current from the tip is around 2 μA and the beam current is controlled by electrostatic lenses and beam apertures.

The ion beam interacts with the surface of the specimen and both secondary ions and electrons are generated and collected for imaging. The collisions between the Ga^+ ions and atoms in

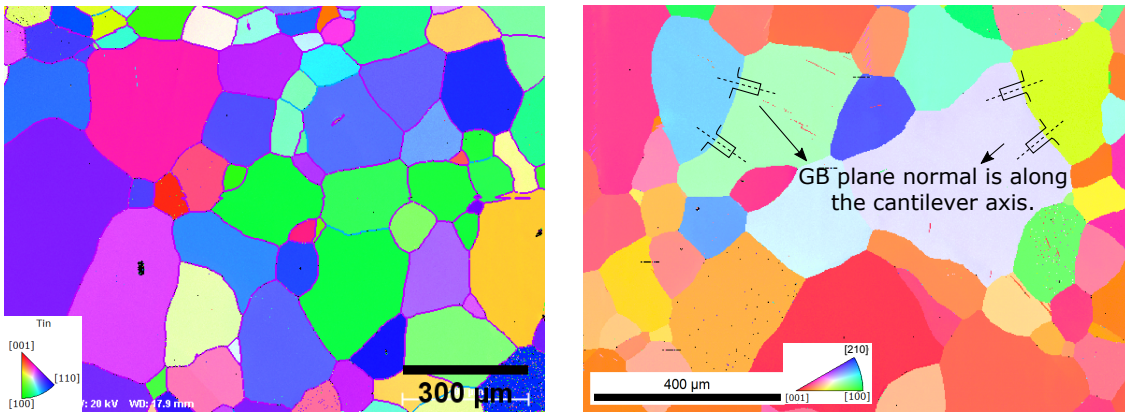

(a) (b)

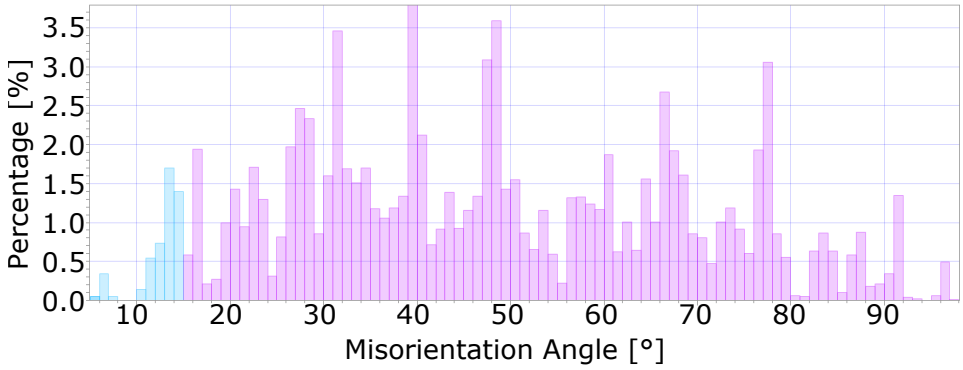

(c)

Figure 4.3: (a) EBSD map of the region to manufacture microcantilevers on the as-annealed sample. The threshold misorientation angle to define a grain boundary is 4°. In this inverse pole figure (along x-axis) plot, the similar coloured grains have similar crystallographic orientation. (b) Characterisation of the grain boundary plane orientation on the TSL OIM software. (c) Grain boundary distribution of the boundaries in (a).

the sample result in sputtering of atoms and ions. Therefore, the surface layer of the sample is removed when the ion beam is scanned over the sample. Even low dosage ion imaging will cause surface damage due to the sputtering of the atoms. The dose and position of the ion beam are accurately controlled by the software, which enables well-defined micro-machining and micro-fabrication.

It has been established in the literature review that micro-pillars milled by FIB can be used to investigate grain boundary sliding behaviour. However, the control over the boundary orientation with respect to the loading direction proved to be difficult. Therefore, a microcantilever design (figure 4.4a) was developed in the current study to explore the grain boundary sliding

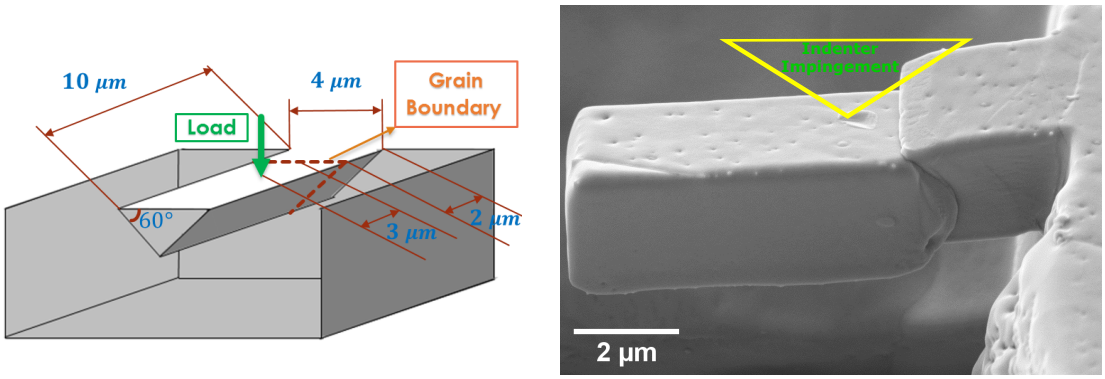

(a) (b)

Figure 4.4: (a) A microcantilever design with dimensions of 10 μm by 4 μm was used in the current study. The grain boundary was 2 μm from the fixed end and the load point was 3 μm further out from the grain boundary. (b) An example showing the issue of indenter impingement on the cantilever when the load point is 1 μm from the grain boundary.

phenomenon. In order to distinguish grain boundary sliding from beam yielding, the boundary has to be a short distance away from the fixed end. The grain boundary was chosen to be 2 μm from the fixed end. The load was applied in the middle of the cantilever along the width direction to avoid torsion. In principle, the load point should be located as close to the grain boundary as possible so as to maximise the shear stress on the boundary plane relative to the bending moment. In the preliminary tests, load was applied at 1 μm from the grain boundary. A clear step was produced on the grain boundary plane as sliding occurred. However, further sliding was prohibited due to the impingement of the indenter tip on the top surface as shown in figure 4.4b. Therefore, the load point was chosen to be at 3 μm from the grain boundary in the final design.

The microcantilevers were manufactured on two FIB microscopes, a FEI FIB200 and a Zeiss NVision 40. The dual-beam microscope – Zeiss NVision 40 allows constant SEM imaging while FIB milling. The grain boundaries were identified using SEM imaging, which was correlated to the EBSD map as shown in figure 4.5. Therefore, the misorientation angle, rotation axis and grain boundary plane of the grain boundaries are known. The alignment of the grain boundary plane was ensured to be perpendicular to the sample surface, and thus would be parallel to the loading axis. Annealing at room temperature for long enough time facilitated

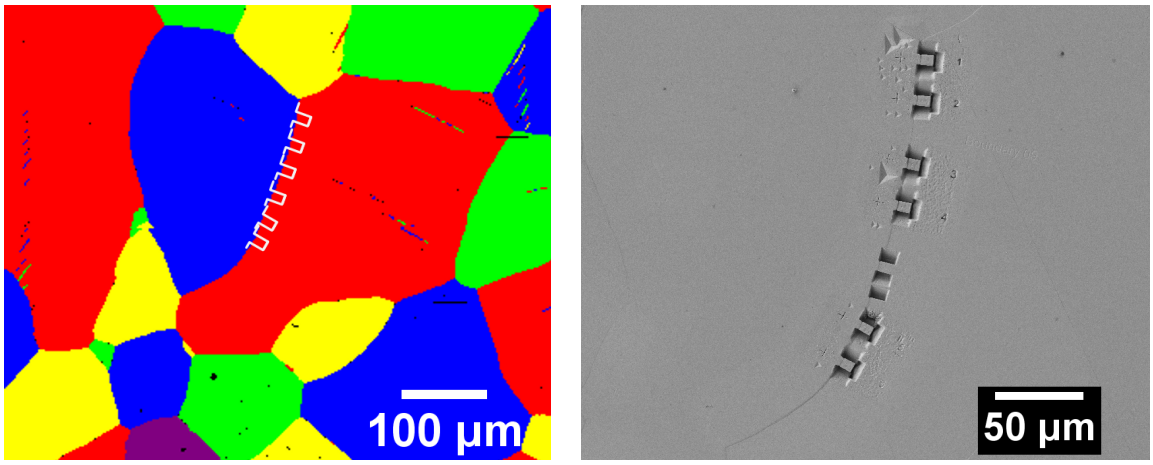

(a) (b)

Figure 4.5: (a) EBSD map scanned before any FIB milling. The colours were assigned randomly to grains independent of their orientation. (b) Microcantilevers containing an individual grain boundary are made by focused ion beam (FIB) on the same location of the sample.

the alignment of grain boundary planes close to being perpendicular to the sample surface. The grain boundary plane alignment was inspected in SEM at a tilted angle after milling the trenches (figure 4.7a on page 113). If the boundary plane was not perpendicular to the surface, the cantilever would be discarded.

As Sn-Bi alloy has a low melting temperature, exposure to high energy ion beams for a long time would destabilise the microstructure. The EBSD map taken after manufacturing the cantilevers illustrates the issue of grain migration due to FIB exposure as shown in figure 4.6. The cantilevers without grain boundary migration have the boundaries close to the fixed end. But some cantilevers have no boundaries any more after FIB milling. This is because the high energy ion beams have made the grain boundary migrate from its original location. Therefore, lower FIB currents were used to mill the cantilevers with grain boundaries.

The general procedure for manufacturing a microcantilever is illustrated as follows and in figure 4.7.

1. A rectangular trench (12 µm long × 8 µm wide × 5 µm deep) was milled on each side of a grain boundary segment using a beam current of 300 pA. The grain boundary segment was 6 µm long in between the two trenches.

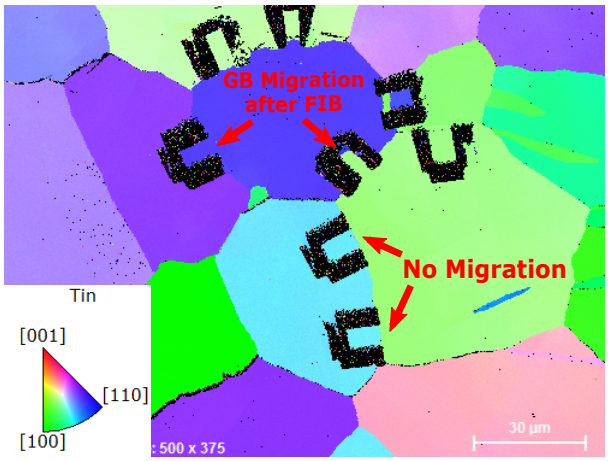

Figure 4.6: EBSD map showing grain boundary (GB) migration taken after manufacturing the cantilevers due to high energy FIB exposure. In this inverse pole figure (along x-axis), the colours of the grains represent the crystallographic orientation.

2. On both edges of the grain boundary, grooves were made to reduce the grain boundary area (figure 4.7b). This is to suppress grain boundary migration on both sides before the subsequent milling procedure.

3. The sample was then tilted by 31° for undercutting at 150 pA (figure 4.7c), producing a triangular cross section. The aimed tilt undercutting angle was 30°, while taking 1° more to account for the tapering effect of the ion beam.

4. A trench on the far end of the beam away from the grain boundary was milled at 150 pA.

5. Beam currents of 80 and 40 pA were then used to remove the redeposited material on the two sides and the free end of the beam. The surface finish is shown in figure 4.7d.

6. In order to ensure accurate positioning of loading, alignment marker lines were milled beside the cantilevers (figure 4.7f).

7. A set of images of the cantilevers after fabrication were taken before testing, so that the morphology of the grain boundary could be compared before and after testing. An image of the front view (figure 4.7e) was taken as well to measure the angle of the triangular cross section and the height of the cantilever.

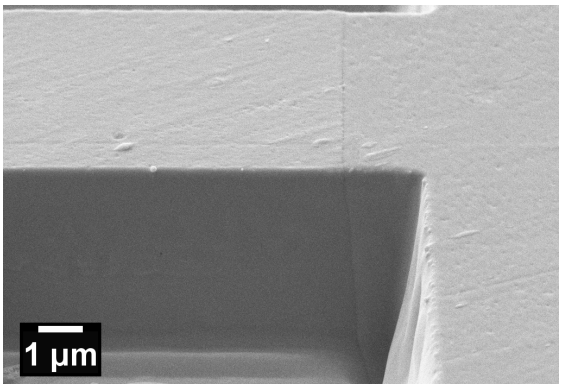

(a) The grain boundary plane orientation is inspected at a tilted angle after milling the trenches.

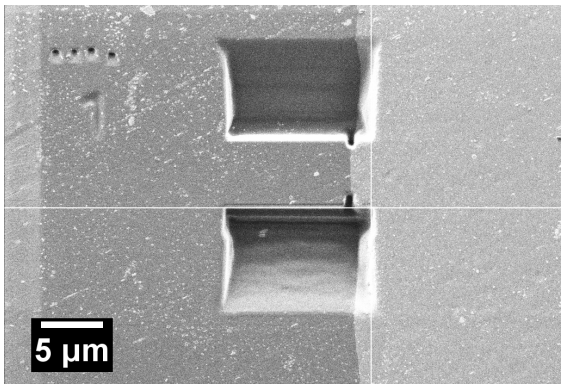

(b) Grooves are made on both sides of the grain boundary to suppress grain boundary migration.

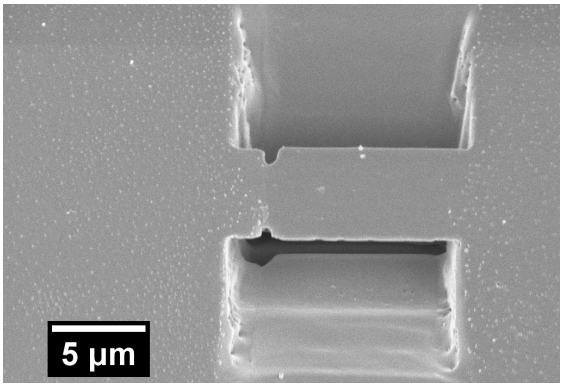

(c) The sample is then tilted by 31° for undercutting on both sides.

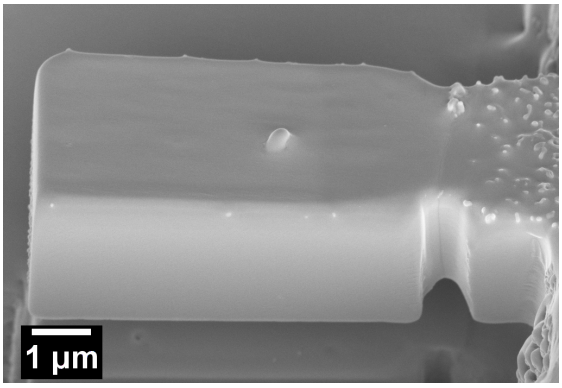

(d) A trench on the far end is milled and the redeposited material is removed by fine milling.

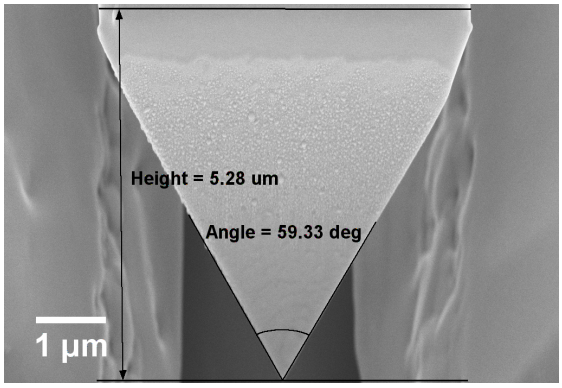

(e) The cantilever has a triangular cross section with the three sides of approximately equal length.

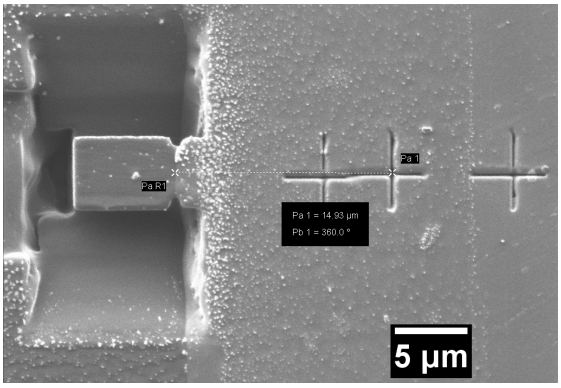

(f) Alignment marker lines are milled beside the cantilevers to ensure accurate loading position.

Figure 4.7: (a) – (f) SEM images showing the procedure to manufacture a microcantilever.

4.1.4 Nanoindentation

A nanoindenter (Agilent G200) was used to perform micro-mechanical tests on the cantilevers. The nanoindenter system (figure 4.8a) is equipped with the ultra-low load and ultra-high resolution Dynamic Contact Module (DCM) [162]. The DCM is a Nano Mechanical Actuating Transducer (NMAT) which achieves highly accurate control of force and displacement. The electromagnetic actuation-based force transducers apply loads through the coil/magnet assembly, and displacements are measured using a capacitance gauge during indentation tests. The load and displacement resolutions of the DCM Indentation Head option are 3 nN and 0.2 pm, respectively. The two leaf springs (figure 4.8a) keep the indentation column stable and prevent lateral deflection during indentation tests. The nanoindenter system is controlled through the Agilent NanoSuite Professional software. NanoSuite provides a variety of pre-written test methods, including methods for nanoindentation, scratch tests, constant load, constant displacement rate, and strain rate sensitivity measurements. The software also has a tool to determine the indenter area function and load-frame stiffness, which simplifies the data analysis process. The advantage of using the test-method based controlling software is that no further configuration or calibration of the hardware is required on a day to day basis by the user [163].

The nanoindenter has a continuous stiffness measurement (CSM) option that allows measurements of contact stiffness as a function of depth or frequency throughout the indentation test. Essentially, the CSM mode applies a small oscillation amplitude on the load signal and measures the displacement response [164]. This enables modulus and hardness of the material to be determined against indentation depth. The CSM technique is effectively performing multiple load-unload tests to measure the surface contact without the need for full unloading cycles. At the end of the test, the load, displacement into surface and time are obtained from the nanoindenter. The modulus of material is derived from the unloading slope of the load (P) - displacement (h) curve (figure 4.8b) using the Oliver-Pharr method. At the peak, the load and displacement are P_{max} and h_{max}, respectively. The final depth of the residual hardness impression after unloading is h_f, with the elastic displacement recovered. The unloading data can be

described as an empirical equation 4.1 with a power law relationship [165], where α and m are empirical constants. For conical indenter tips, the power law exponent m is around 2.

$$P = \alpha \left(h - h_f\right)^m \tag{4.1}$$

The initial unloading contact stiffness is the slope of the initial unloading curve, marked as S in figure 4.8b. It can be written as equation 4.2:

$$S = \frac{dP}{dh} = \frac{2}{\sqrt{\pi}} E_r \sqrt{A} \tag{4.2}$$

where A is the projected area of contact at peak load and E_r is the reduced modulus defined as:

$$\frac{1}{E_r} = \frac{\left(1 - \nu^2\right)}{E} + \frac{\left(1 - \nu_i^2\right)}{E_i} \tag{4.3}$$

where E and ν are Young's modulus and Poisson's ratio of the test material, respectively, and E_i and ν_i are those of the indenter. Therefore, the modulus of the specimen can be determined if the contact area at the peak load can be measured independently. Oliver and Pharr [165] assumed that the cross-sectional area of the indenter, *F(h)*, could be related to the distance from its tip, h. This relationship must be established experimentally for the indenter tip prior to analysis of the nanoindentation data. The hardness (H) of the test material can be determined via $H = \frac{P_{max}}{A}$. The contact area determined by the Oliver-Pharr approach may be different from that directly measured from the size of the residual hardness impression, because the Oliver-Pharr method takes into account the plastically deformed portion of the contact area. Thus, the hardness measurement may be different from that obtained using the conventional methods.

Before the indentation tests, the Berkovich tip is calibrated by performing a number of indents on the reference material (fused silica in the current study). The load-displacement data are imported into NanoSuite Analyst software to calibrate the calculated modulus and hardness values using the known mechanical parameters of the reference material. Then it is ready to

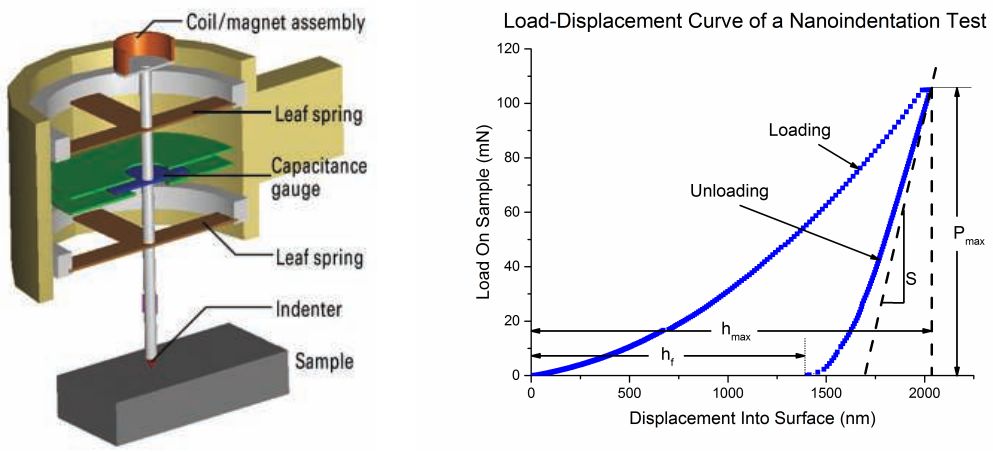

(a) (b)

Figure 4.8: (a) Schematic illustration of the nanoindenter system with the Dynamic Contact Module (DCM) – Nano Mechanical Actuating Transducer (NMAT) (image courtesy to Agilent Technologies [162]) (b) Typical load-displacement curve obtained from a nanoindentation test on fused silica. The parameters are identified to calculate the modulus and hardness of the material.

perform indentation tests on the test material. A typical indentation test procedure is described as follows:

1. Perform microscope to indenter calibration. This ensures accurate control over the location of the indents.

2. Set up the location on the sample to make indents, which requires the X and Y coordinates of the desired location. Then put in the typical settings for nanoindentation tests as shown in table 4.1.

3. The test begins with the surface approach from around 1 μm above the sample surface. As soon as the indenter reaches the surface, load is applied at a predetermined rate based on the strain rate target and current load on the sample [162]. The loading rate is continuously recalculated and varied as a function of the indentation depth. When the depth limit is reached, the load is held at the peak value for 10 seconds before the indenter is retracted from the sample surface (unloading). The unloading rate depends on the predetermined strain rate and current load on the sample as well.

Panel Inputs	Value	Units
Depth Limit	2000	nm
CSM Frequency Target	42.0	Hz
Harmonic Displacement Target	2.0	nm
Poisson's Ratio	0.30	–
Strain Rate Target	0.05	1/s
Surface Approach Detection Stiffness	100	N/m
Surface Approach Distance	1000	nm
Surface Approach Velocity	10	nm/s

Table 4.1: Typical setting for the nanoindentation tests on the bulk of the grain.

4. Thermal drift can have a significant impact on the measured displacements. It is essentially the displacement rate due to thermal expansion/contraction of the system. The thermal drift rate is measured at the end of the test by holding at 10% of the maximum load for 60 seconds. This removes the thermal drift effect on the displacement into the sample.

5. The modulus and hardness of the test material are calculated from the load-displacement data using the Oliver-Pharr method.

4.1.5 Microcantilever Testing Methods

The microcantilevers were tested using the DCM head of the G200 Nanoindenter, which enables higher accuracy and resolution in load and displacement than the XP head. Since the load point has to be controlled at nanometre precision, the Agilent NanoVision Nanomechanical Microscopy method was used to generate a 3D map of the sample surface. In this method, a nanopositioning stage was used in conjunction with DCM head to produce a contact mode topographical map of the surface (similar to an AFM (atomic force microscope) map). The typical contact load for scanning is 1 μN. Since the Sn-Bi alloy is relatively soft, scanning the cantilever with the indenter tip would cause damage on the surface. Therefore, an offset test

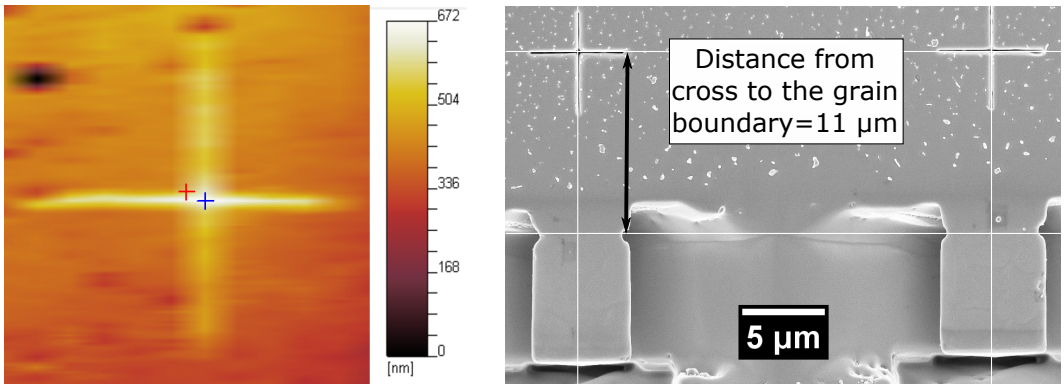

(a) (b)

Figure 4.9: (a) A typical topographical map of the alignment marker milled on the sample surface using the NanoVision nanomechanical microscopy (b) SEM image showing the alignment marker milled at a certain distance from the grain boundary on the cantilever.

method was used to apply a load on the cantilever. Figure 4.9a shows a topological map of the alignment marker milled at a known distance away from the grain boundary. The colour gradient indicates the difference in the depth of the surface. As the distance from the alignment marker to the grain boundary is measured in the SEM (e.g., in figure 4.9b, the distance is around 11 µm), the method allows the user to choose a point (the blue cross in figure 4.9a) and define an offset distance during the test setup. The load point is expected to be 3 µm from the grain boundary, so the offset distance is 14 µm in the case of figure 4.9b. The microcantilever tests were carried out in two different modes – load controlled and displacement controlled.

4.1.5.1 Load Control

In order to investigate the effect of diffusion creep on the deformation behaviour of the grain boundary, creep tests were carried out at a constant force under load control. The initial procedure of the cantilever test method is the same as the nanoindentation test, such as the surface approach. After getting in contact with the cantilever surface, the indenter moves at a certain displacement rate until reaching the target raw load, which is then held constant for a predefined period of time. The indenter is retracted in the same way as that in the nanoindentation test. Thermal drift is also measured at the end of test, however, after the indenter has fully left the sample surface. This is different from the nanoindentation test, because the contact between

the indenter and sample even at 10% of the peak load for 60 seconds (as in the nanoindentation case) will induce further deformation on the cantilever. The typical test parameters are summarised in table 4.2.

Panel Inputs	Value	Units
Depth Limit	500	nm
Displacement Rate	0.1	nm/s
CSM Frequency Target	42.0	Hz
Peak Load	0.10	mN
Dwell Time at the Peak Load	3600	s
Strain Rate Target	0.05	1/s

Table 4.2: Typical setting for the microcantilever test on the grain boundary.

Figure 4.10a illustrates the variation of raw load and displacement into surface (both "zeroed" from surface contact) with time. In this load controlled test, the raw load (produced by the transducer) is constant while the displacement into surface varies during the dwell time. The load on sample is plotted against displacement into surface for this load controlled test in figure 4.10b. The displacement into surface and load on sample are measured by equation 4.4 and 4.5, respectively. Even though the raw load is kept constant, it differs from the load on the sample as some of the force is transferred to the leaf springs in the transducer. That is why the load on the sample drops during the load holding period. This happens especially when the test material creeps during the long dwell time [162].

$$Displacement\,into\,Surface = Raw\,Displacement - Displacement[SurfaceMarker] \quad (4.4)$$

$$\begin{aligned} Load\,on\,Sample = Raw\,Load - Load[SurfaceMarker] \\ -Displacement\,into\,Surface \times Spring\,Stiffness \end{aligned} \quad (4.5)$$

In order to keep the load on sample constant during the dwell time, the raw load can be corrected to allow for any changes in the load on the sample. This was achieved by continuously

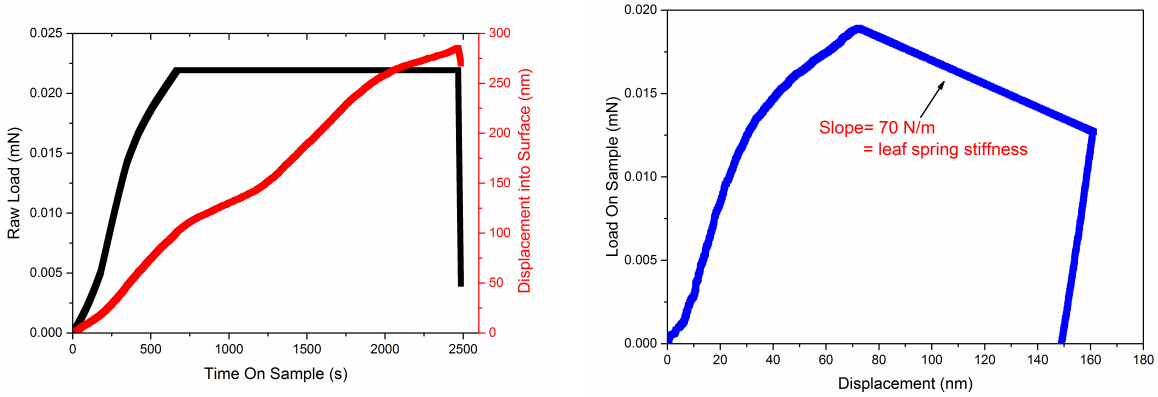

(a) (b)

Figure 4.10: (a) load on the sample against displacement curve of the cantilever test under load control. The raw load was kept constant, but the load on the sample drops due to the creep effect of the sample. (b) Load on the sample and displacement of nanoindenter against time.

updating the commanded force signal to be produced by the transducer (defined as the set point) as follows:

$$Set\ Point = Raw\ Load - (Load\ on\ Sample - Target\ Load) \tag{4.6}$$

where raw load is the current force signal out of the transducer, load on sample is the true force applied on to the sample through the indenter tip after correcting for the amount of force supported by the leaf spring deflection (calculated by the displacement into surface times the support spring stiffness). The target load is the desired constant load to be applied to the sample. In this case, the load on the sample should be kept constant as seen in the following results (see section 4.2.7.1).

4.1.5.2 Displacement Control

Inherently, the nanoindenter is load-controlled, i.e. there is a simple linear relationship between the current passed through the coil and the force applied. In order to conduct displacement controlled tests, the electromagnetic force is adjusted so that the indenter moves at a constant displacement rate both before and after being in contact with the sample. This is accomplished via a rapid feedback loop using proportional-integral-derivative (PID) controls. Rather than

continuously updating the force signal based on a formula as in the load controlled method, the NanoSuite software adopts tunable PID settings to control the nanoindenter using data signals other than raw load (i.e. displacement) [162].

The majority of the microcantilever tests were carried out under displacement control in this study. This is because the threshold stress for grain boundary sliding is unknown beforehand. So it is impossible to set a load level required for grain boundary sliding. Therefore, the test was performed at a constant displacement rate until a predetermined displacement limit, after which the indenter was retracted from the sample surface at the same rate as that for loading. In order to minimise the thermal drift effect on the total displacement of the cantilever, the nanoindenter system was stabilised by engaging the indenter with the sample for at least 24 hours before the test. Two typical load-displacement curves for tests on the same cantilever at two different target displacement rates are shown in figure 4.11a. The black curve shows the first test carried out at 0.1 nm/s. The red curve indicates the fourth test carried out on the same cantilever at a much higher target displacement rate – 10 nm/s. In both curves, the load increases until a maximum value is reached, after which the load drops slowly as a result of the reduced grain boundary area.

There are three differences worth noting. Firstly, the slope of the initial segment that corresponds to the elastic deformation of the cantilever differs in the two tests. This is because in the first test the indenter tip embedded into the cantilever surface. This caused a reduction in the slope of the loading segment and made the initial curve obviously non-linear (P is a function of h^2 for a constant hardness). By the fourth test (red curve), the indent crater was already mostly made so that the response was stiffer and closer to linear. Secondly, the maximum load is different in the two tests at different rates. The higher displacement rate corresponds to a higher maximum load, and therefore stress, for grain boundary sliding. Thirdly, given that the data points are recorded at a constant frequency in time, the increased spacing between discrete data points in the red curve (10 nm/s) near the maximum load indicates that the initial grain boundary sliding rate is faster than the input target displacement rate. The displacement rate

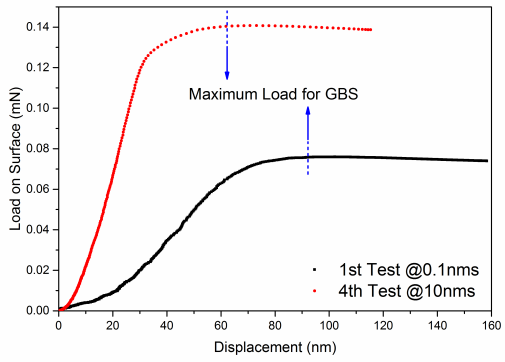

(a)

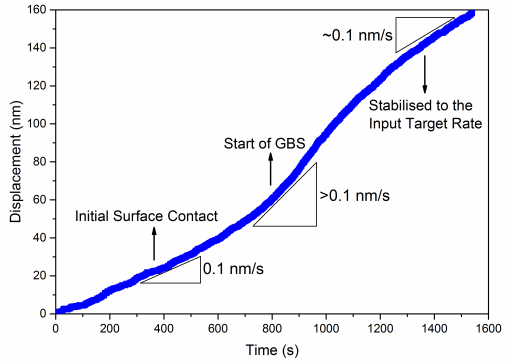

(b)

Figure 4.11: (a) Typical load-displacement curves for two tests conducted on the same cantilever at different displacement rates. The maximum load is defined as the point before the load starts to drop. (b) A graph showing the variation of displacement with time for the test with a nominal displacement rate of 0.1 nm/s in (a), from initial surface contact to grain boundary sliding (denoted as GBS in the graph).

stabilises to the target value towards the end of the test. The displacement is plotted against time in figure 4.11b, which corresponds to the test with a nominal displacement rate of 0.1 nm/s. The increase in displacement rate occurred at the displacement of around 60 nm, which is where the load-displacement curve (the black curve in figure 4.11a) deviates from the linear regime. Therefore, the start of grain boundary sliding is defined as the start of the non-linear regime of the load-displacement curve after the initial contact of the indenter and sample. The variation of displacement rate with time is as follows: target rate – faster rate at the start of grain boundary sliding – stabilising to the target rate.

4.1.5.3 Calculation of Shear Stress on the Grain Boundary Plane

The load data obtained from the nanoindenter were translated to the shear stress on the grain boundary plane. It was assumed that the load on the indenter was equal to the load applied on the grain boundary plane. The dimensions of the grain boundary plane were measured from the SEM images such as figure 4.7e on page 113. The shear stress on the boundary plane was therefore calculated as:

$$\tau_{gb} = \frac{P}{A_{gb}} = \frac{P}{w_{gb}h_{gb}/2} = \frac{2P}{wh_{gb}} \tag{4.7}$$

where P is the load on the sample, A_{gb}, w and h_g are the area, width and height of the triangular sectioning grain boundary plane, respectively. It should be noted that the dimensions of the boundary plane have a similar triangular relationship with the dimensions measured from the front view of the cantilever (figure 4.12a). Therefore, the width and height of the grain boundary plane (w_{gb} *and* h_{gb}) have the following relationship with the front plane (w_f *and* h_f) that could be directly measured from the SEM images: $\frac{w_{gb}}{w_f} = \frac{h_{gb}}{h_f}$. Therefore, equation 4.7 becomes equation 4.8. As the free end grain slides against the neighbouring grain along the boundary plane, the height and hence area of the boundary plane decrease, which influences the calculation of shear stress. Thus, the area and shear stress of the boundary plane need to be continuously updated during the sliding process.

$$\tau_{gb} = \frac{P}{A_{gb}} = \frac{P}{w_{gb}h_{gb}/2} = \frac{2P}{w_{gb}h_{gb}} = \frac{2P \cdot w_f}{w_{gb}^2 \cdot h_f} \tag{4.8}$$

4.1.5.4 Error Propagation Analysis

The measurement of shear stress has uncertainties derived from the four parameters. Firstly, the load measurement has uncertainties from its own resolution (3 nN), the displacement resolution (0.2 pm) and the leaf spring stiffness (70 ± 0.89 N/m [163]) according to equation 4.5 on page 119. Since the measured load and displacement values in the tests were in much higher

orders than the resolutions, the uncertainties of load on the sample mainly came from the spring stiffness, i.e. ~1.2%. The measurement of dimensions of the cantilever is the largest source of uncertainties of the shear stress. An example is shown in figure 4.12b, the height of the front plane was measured for five times and an average value was taken. Similarly, for the measurement of the width of the grain boundary plane and the front plane, an average value was chosen from five measurements (only three of which are shown in figure 4.12c). The standard deviation was calculated and taken as the uncertainties of the measurements of δw_f, δw_{gb} *and* δh_f. The uncertainty of the shear stress on the grain boundary plane was a result of error propagation as shown in equation 4.9. In this example, the uncertainty is around 1.9%.

$$\frac{\delta \tau_{gb}}{\tau_{gb}} = \sqrt{\left(\frac{\delta P}{P}\right)^2 + \left(\frac{\delta w_f}{w_f}\right)^2 + \left(\frac{2\delta w_{gb}}{w_{gb}}\right)^2 + \left(\frac{\delta h_f}{h_f}\right)^2} \tag{4.9}$$

4.1.5.5 Characterisation of Grain Boundary Sliding

In order to understand the grain boundary behaviour during the test, a series of constant displacement rate tests were carried out on the same cantilever. The load point was kept constant across the series of tests. The shear stress on the grain boundary plane is plotted against displacement for each test in figure 4.13. The first test was interrupted just before reaching the maximum load. It corresponds to the interaction between the indenter and sample surface as well as the very initial stage of grain boundary sliding. The second test was carried out using the same displacement rate as the first one but to a higher displacement so that stable grain boundary sliding was achieved. The steady-state shear stress was higher than that for the first test, which was within the discrepancy range for repeated tests discussed in the following section 4.2.1.1. The third test was performed at a much higher displacement rate, which reached a higher steady-state stress for sliding. The slope of the initial linear segment is comparable to the first test, because it produced a much larger indent impression (figure 4.14g).

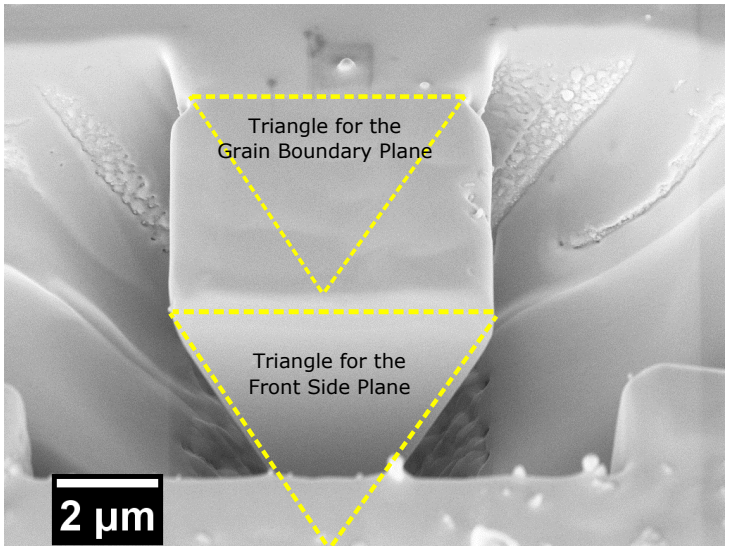

(a)

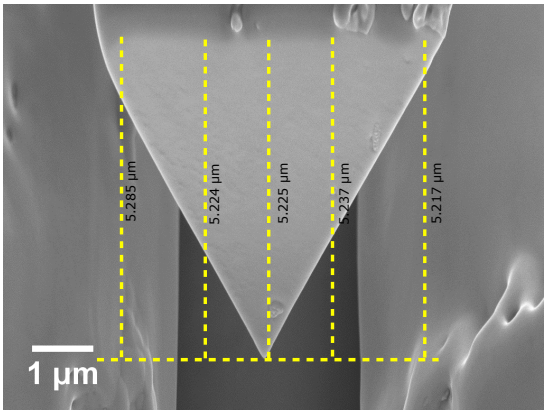

(b)

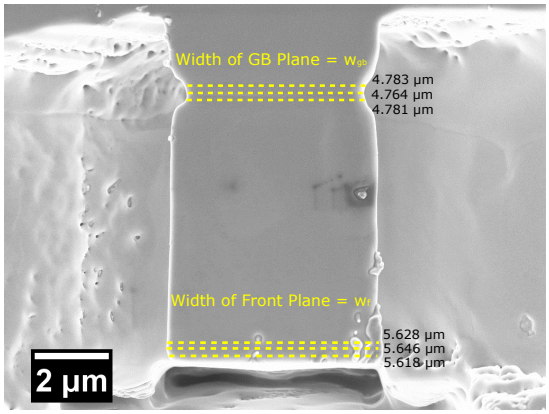

(c)

Figure 4.12: Measurement of the height and width of the microcantilever for the calculation of the shear stress on the grain boundary plane. (a) A micrograph showing the similar triangle relationship between the grain boundary plane and the front plane. (b) and (c) show measurements of the height of the front plane (with tilt correction), width of the grain boundary plane and the front plane.

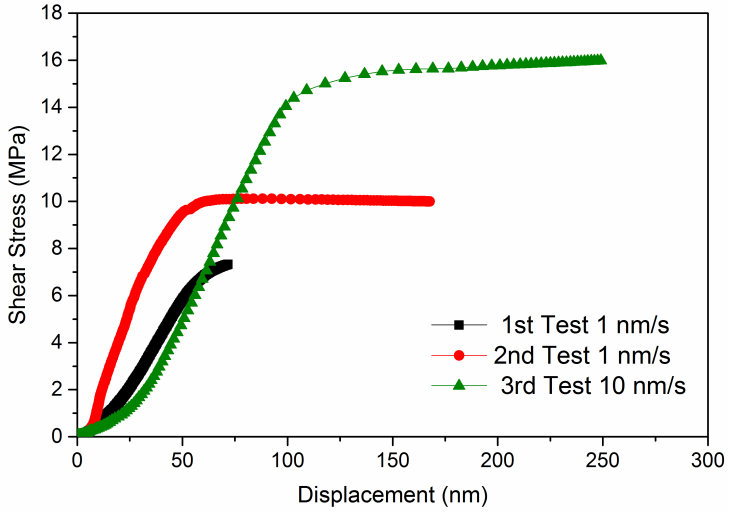

Figure 4.13: A series of progressive interrupted tests were carried out on the same cantilever. The first test was interrupted just before reaching the maximum load. The second test was carried out to a higher displacement to achieve stable grain boundary sliding. A much higher displacement rate was used in the third test, which led to a higher steady-state stress for sliding.

Each cantilever was examined in the NVision SEM after each test to inspect the change in morphology of the grain boundary. Figure 4.14 shows the SEM images at each stage of the progressive interrupted tests. It is the same series of tests as described above in figure 4.13. Before testing, the grain boundary was perpendicular to the sample surface and therefore parallel to the loading direction (figure 4.14a). After the first test (figure 4.14c and 4.14d), the contour of the grain boundary became much more visible than before testing. The indent impression was made on the cantilever surface. After the second test that reached steady-state sliding, there was a clear step on the grain boundary plane as shown in figure 4.14e and 4.14f. The height of the step was measured to be around 165 nm (after tilt correction), which correlates reasonably well to the displacement at the stress plateau shown in the red curve in figure 4.13. The last test was carried out at a higher rate to a larger displacement, which induced a larger step on the grain boundary. It can also be noticed that the boundary became curved after the last test (figure 4.14g). This indicates the phenomenon that grain boundary sliding is coupled with migration (see section 4.3.2). In figure 4.14h, it is apparent that the contrast is different

for the displacement “step” corresponding to each test, suggesting that the morphology of the slid grain boundary plane is different for the different displacement rates.

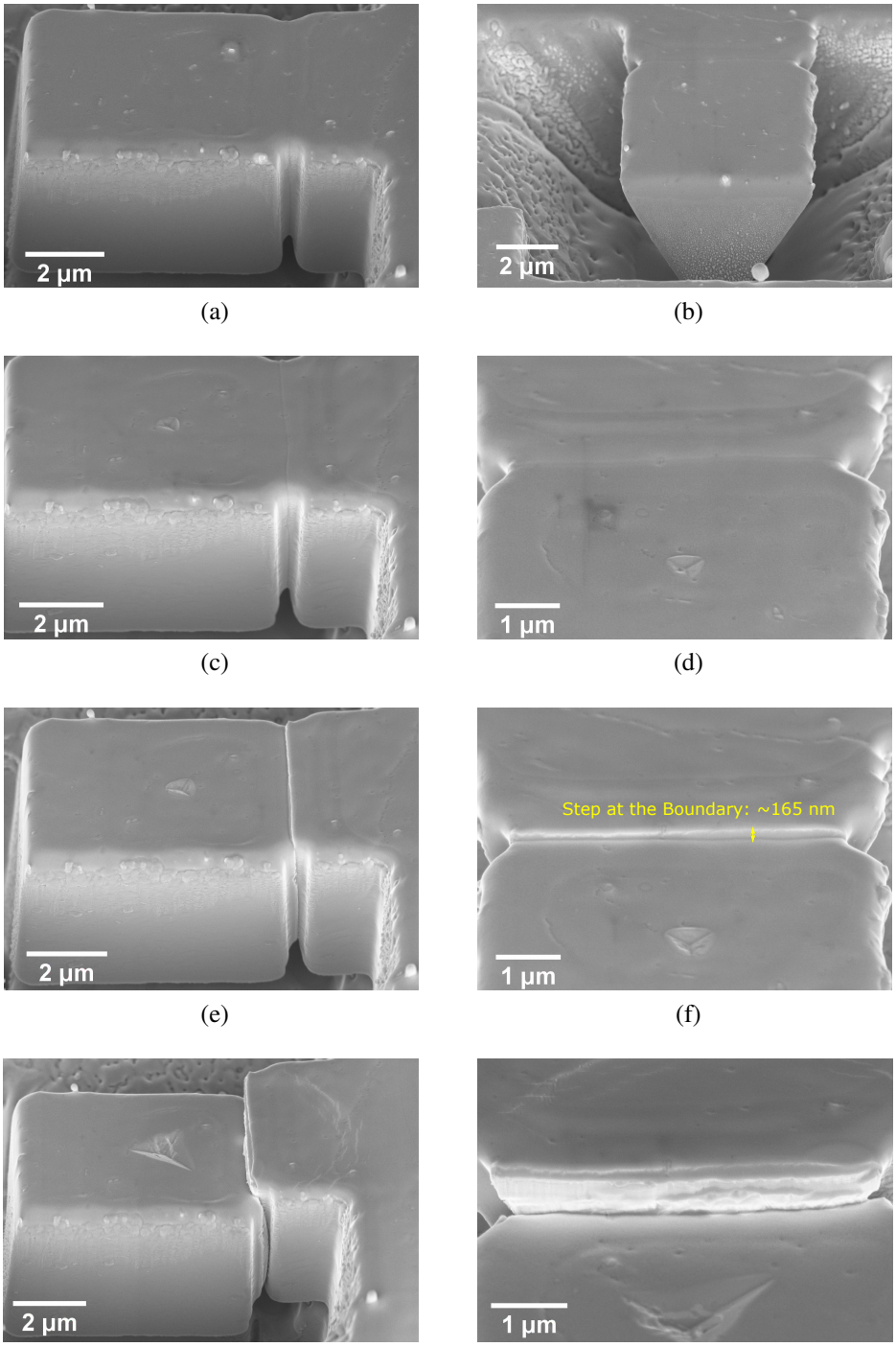

Figure 4.14: (a) and (b) show the side and front views of the cantilever with a grain boundary before testing. (c) and (d) show the side and front views after the first was interrupted test when sliding just started. (e) and (f) show the views of the grain boundary after a small amount of sliding at 1 nm/s. (g) and (h) show the morphology of the grain boundary after sliding for a long distance at 10 nm/s.

4.1.5.6 Accounting for the Effect of Indent Impression on the Displacement of the Cantilever

As mentioned in section 4.1.5.5, the indent impression contributes to the total displacement of the indenter, especially in the initial part of the load-displacement curve. The sliding behaviour can be separated if the effect of indent impression is subtracted from the total displacement. Hence, a few indents were made away from the cantilevers in the bulk of the same grain as the free end grain of the cantilever (figure 4.15a). Comparison can then be made between the load-displacement curves of the cantilever test and bulk grain indentation (figure 4.15b). This cantilever test was the first test discussed above in figure 4.13, which was interrupted when grain boundary sliding just started to occur. It can be seen that the initial section of the cantilever test curve overlaps with the indentation curve until around 45 nm, after which the responses deviated from each other. The short non-linear segment corresponds to the very initial stage of grain boundary sliding. The residual impression of the indent on the free end grain was examined in SEM as shown in figure 4.15c. The area of the impression was correlated to the depth of the indent by equation 4.10 for an ideal Berkovich indenter tip, where A and h_c are the projected area and depth of the indent impression, respectively [165]. From measurement of the projected area, the depth was calculated to be around 69 nm. However, the indenter tip used for cantilever tests was not designed for nanoindentation and it was blunt due to frequent use in scanning the sample surface (see section 4.1.5). Therefore, the actual depth of the indent impression was somewhat lower than 69 nm (calculated for an ideal Berkovich tip), which would be comparable with the "overlapped displacement" of the nanoindentation and cantilever tests in figure 4.15b (~45 nm).

$$A(h_c) = 24.5h_c^2 \tag{4.10}$$

In order to obtain the real displacement of the cantilever, the displacement of the indentation was removed from the total displacement in the cantilever test. This was achieved by fitting

the load-displacement data of the bulk grain indentation to a function $h = \beta\sqrt{P}$, where β is a constant. Then the load data from the tests on cantilevers were used in this function to predict the correction needed for the displacement. The load-displacement curves with and without correction for the effect of indent impression are compared in figure 4.15d. The two tests were carried out under nominally identical conditions on the same cantilever. The slope of the original curve for the first test deviates significantly from that for the second test as the second test has no displacement in generating an indent impression. After subtracting the displacement of the indent impression, the real load-displacement response of the cantilever in the first test is very similar to that for the second test before sliding occurs. It should be noted that the maximum loads were different for the two tests on the same cantilever. The issue of reproducibility will be discussed in section 4.2.1.

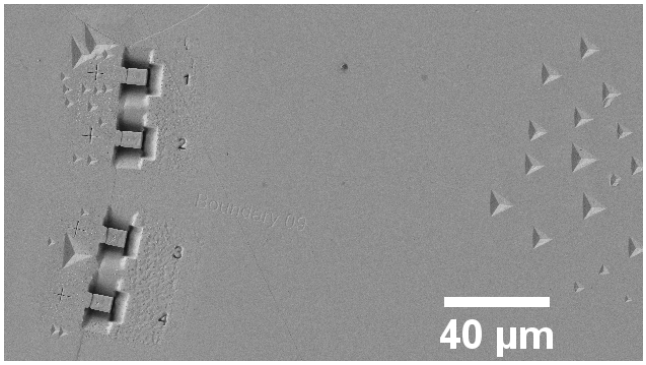

(a)

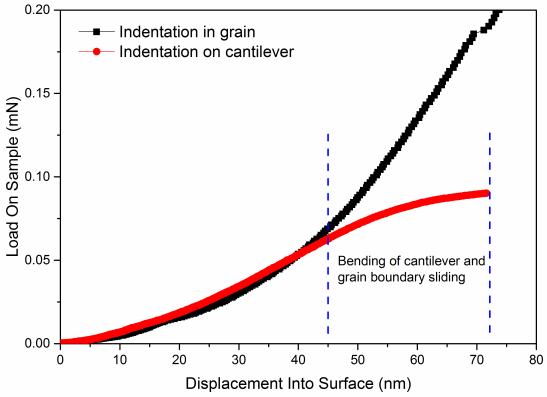

(b)

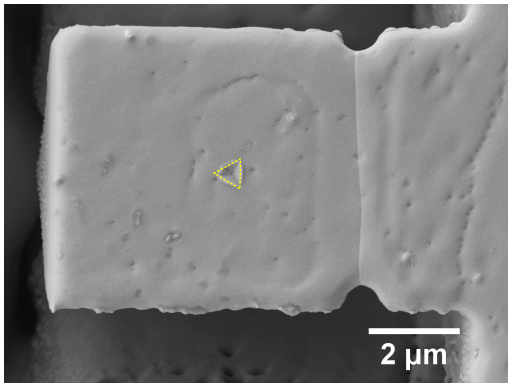

(c)

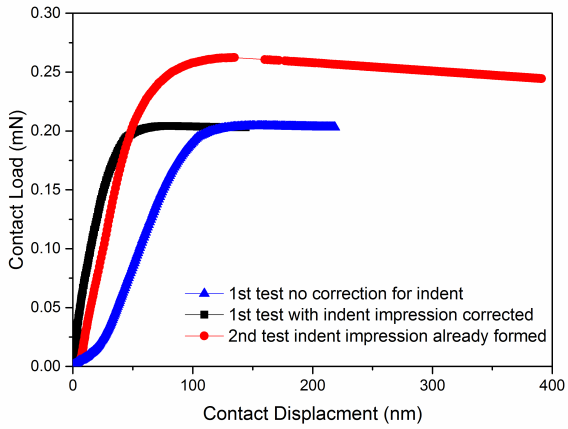

(d)

Figure 4.15: (a) SEM image showing the indents made beside the cantilevers in the bulk grain. (b) Comparison of the load-displacement data for nanoindentation and cantilever tests. (c) SEM image showing the indent impression after the cantilever test. The area of the impression was measured to estimate its depth. (d) Comparison of the load-displacement data with and without correction for the effect of indent impression. The second test with the indent impression already formed is also compared to the first test.

4.1.6 Finite Element Analysis

Finite element analysis (FEA) was conducted (using Abaqus software) on the microcantilever to estimate the shear stress on the grain boundary plane and the tensile, compressive stresses normal to the grain boundary. Two FEA models were built: one for the short cantilever with a dimension of 5×10 μm and the other for the long cantilever of 5×20 μm. The material response was assumed to be elastic and isotropic. The Young's modulus was set to be 60 GPa. The cantilever was considered as a whole part with uniform material properties for both grains (i.e. free-end grain and built-in-end grain) and the grain boundary. The part was meshed so that there were more elements in the cantilever than the bulk material. The grain boundary was 2 μm from the built-in end and no special interface property was assigned to it. The long cantilever model is shown in figure 4.16a. A constant load of 200 μN (obtained from grain boundary sliding experiments) was applied at the free end — 18 μm from the grain boundary. The load was distributed on a line along the whole width of the cantilever (denoted as a distributed load), which could avoid distortion of the elements. The other way to apply a load was to select a node on the cantilever and concentrate the load on that single point, which was analogous to a nanoindenter (denoted as a point load). However, local elements at the load point suffer from distortion. For the short cantilever, a similar model was made with both methods to apply a load as shown in figure 4.16b. The influence of the distance between the load point and grain boundary on the stress conditions of the cantilever was investigated, including the shear stress, tensile and compressive on the grain boundary plane. The models with a load applied on a point at 3 μm and 1 μm from the grain boundary are shown in figure 4.16c and 4.16d, respectively.

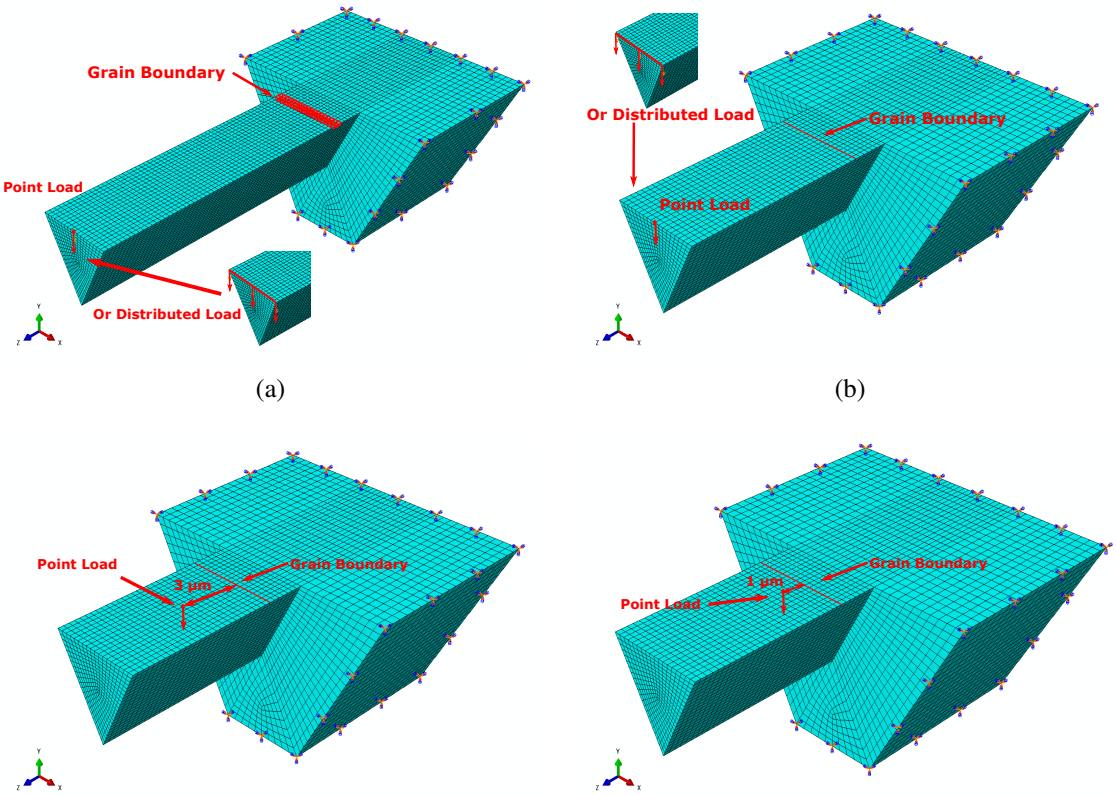

Figure 4.16: (a) FEM analysis of a long cantilever (5×20 μm) with a grain boundary. Two ways of applying load are shown: on a line along the whole width or a point at the free end of the cantilever. The load is applied to the line or point at 18 μm away from the grain boundary. (b) A similar model was made on the short cantilever (5×10 μm). The load is applied 8 μm away from the grain boundary. (c) and (d) FEM of the load applied on a point 3 μm and 1 μm from the grain boundary, respectively.

4.2 Results

4.2.1 Reproducibility of Repeated Tests on the Same Grain Boundary

Since a new testing method has been developed, it is essential to demonstrate that the test results are reproducible on the individual grain boundaries and to evaluate the measurement errors and inherent scatter in material response. Therefore, repeated tests were carried out on the same cantilever under nominally identical conditions (section 4.2.1.1), i.e. indenting on the same point of the cantilever using the same displacement rate. To check the consistency with which test pieces could be fabricated, a few pairs of cantilevers were manufactured on the same grain boundary, and tested under nominally identical conditions (section 4.2.1.2) to establish the consistency of grain boundary sliding behaviour between different cantilevers on the same boundary. Error propagation analysis suggests that the shear stress uncertainty is dominated by measurement of the cross-sectional area and amounts to $\pm 1.9\%$ (see section 4.1.5.4).

4.2.1.1 Same Cantilever Tested under Nominally Identical Conditions

In order to investigate the reproducibility of the data, some cantilevers have been tested repeatedly at a target displacement rate of 1 nm/s. The subsequent test was immediately conducted just after the previous test was complete. So the load point, testing method and conditions were ensured to be nominally identical in both tests. An example of the repeated tests is shown in figure 4.17a. Neither of the tests was the first test so there was no effect of the indent impression. The slopes of the linear region were similar, 0.27 and 0.30 MPa/nm, respectively. The fact that the curves are similar to each other in shape indicates the reliability of the test results.

As mentioned in section 4.1.5.2, the embedment of the indenter tip into the cantilever surface makes a difference in the initial segment of the load or stress with displacement curves. A few more examples of the repeated tests are shown in figure 4.17b, 4.17c and 4.17e. They all involve the effect of indenter impression during the first test. Applying the methods described in section 4.1.5.6 to correct for the indent impression, it can be seen that the initial section of

the curve for the the subsequent repeated test has almost the same shape as the first test with indenter impression corrected. An exception is the curve shown in figure 4.17c, where the second test deviates from the corrected curve for the first test. This is due to the slight change in the indenter impression in the repeated tests (as shown in figure 4.17d). Even though great care was taken to ensure that the load points were consistent across all the tests on the same cantilever, the location of the indenter impression could vary due to the sample orientation and scanning resolution between different tests. The initial linear segment of the curves correlates to the stiffness of the cantilever. It can be seen that the gradients of the linear segments are similar for the cantilevers in the same grain and vary between different grains (figure 4.17a and 4.17b are from the same grain; figure 4.17c and 4.17e are from another grain). After the linear regime, the curves may deviate from each other in the following segments, which corresponds to the process of grain boundary sliding.

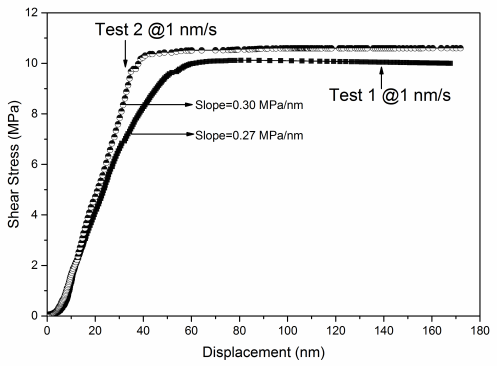

(a)

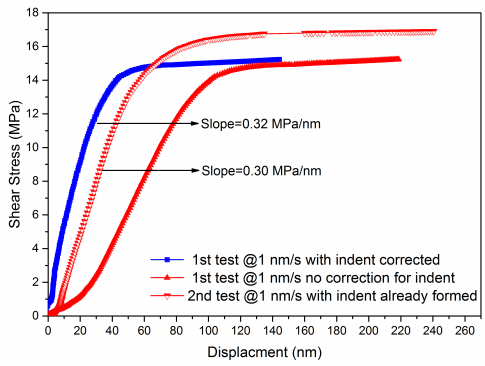

(b)

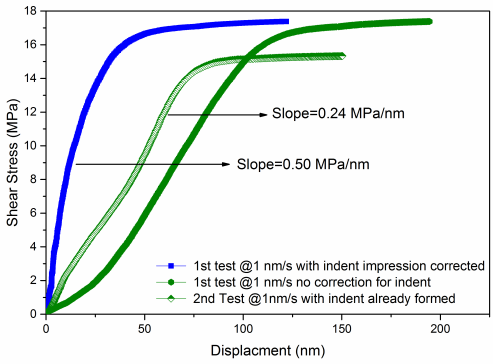

(c)

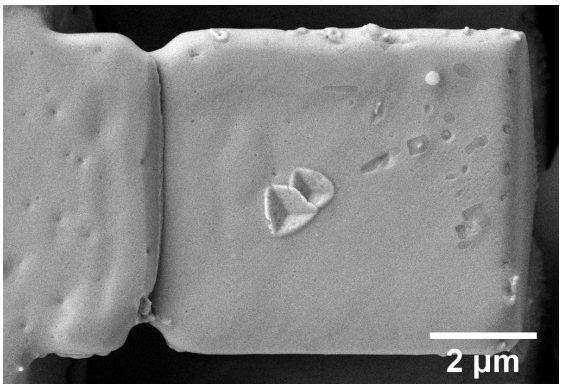

(d)

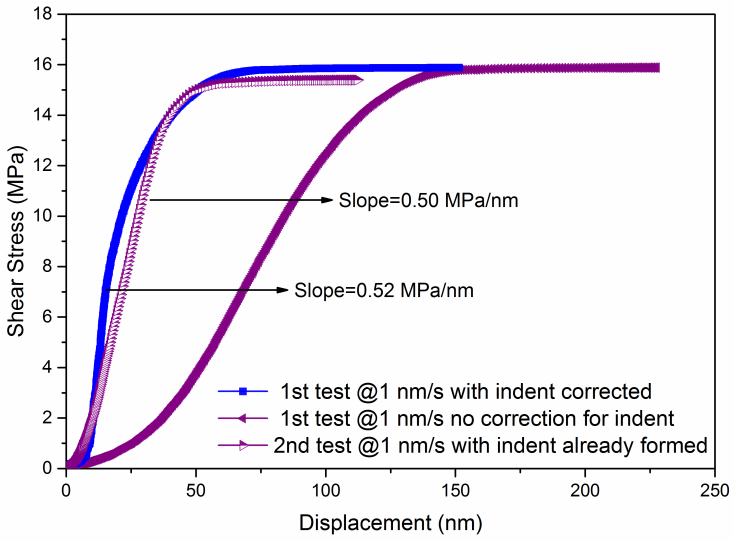

(e)

Figure 4.17: (a) – (d) Shear stress-displacement data for four microcantilevers tested repeatedly under the nominally identical conditions. In the cases where the formation of indent impression was involved, correction was made to the displacement of the cantilever as illustrated in (b), (c) and (d). (a) and (b), (c) and (d) are from the same grain boundary, respectively.

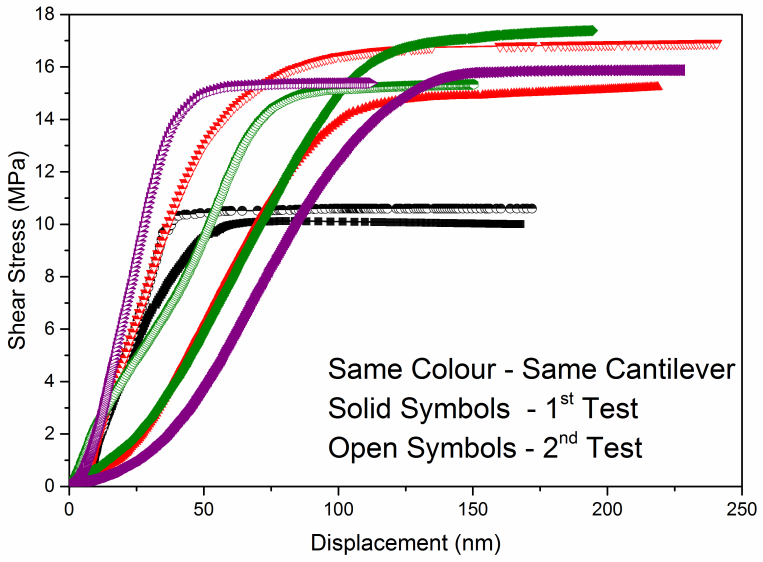

Figure 4.18: Summary of the shear stress against displacement curves for the repeated tests on the same cantilever (shown in the same colour) under nominally identical conditions. Each colour represents one cantilever. The solid symbols correspond to the first tests of the repeated tests.

The shear stress against displacement plots are summarised in figure 4.18. The shear stress tends to level off during grain boundary sliding, because both the grain boundary area and load decrease as sliding occurs. The steady-state shear stress is defined as the stress value at the plateau when grain boundary sliding has reached a steady state. The difference in the steady-state shear stress between the two repeated tests is shown in table 4.3. The maximum discrepancy in the steady-state shear stress for tests on the same cantilever is below 12%. This scatter is much larger than that expected from load measurement errors (~1.2%), which suggests some of the scatter is inherent in the material behaviour. It is worth noting that the errors from dimension measurements are not contributing to the scatter as the tests were conducted on the same cantilever. There is no clear trend of whether the steady-state shear stress increases or decreases in the repeated tests (of the four tests in figure 4.18, two increase and two decrease).

Cantilever Number	GBS Shear Stress (MPa)	Change in GBS Shear Stress (MPa)	Percentage Change
Boundary 08 Cant 04 1st Test	10.1	+0.4	+4%
Boundary 08 Cant 04 2nd Test	10.5		
Boundary 08 Cant 06 1st Test	14.9	+1.8	+12%
Boundary 08 Cant 06 2nd Test	16.7		
Boundary 09 Cant 05 1st Test	17.1	-1.9	-11%
Boundary 09 Cant 05 2nd Test	15.2		
Boundary 09 Cant 06 1st Test	15.8	-0.5	-3%
Boundary 09 Cant 06 2nd Test	15.3		

Table 4.3: Comparison of the repeated tests on the same cantilever at a constant displacement rate of 1 nm/s.

4.2.1.2 Nominally Identical Cantilevers on the Same Grain Boundary

A few pairs of microcantilevers were made on the same grain boundary. An example of a pair of parallel cantilevers is shown in figure 4.19a. The cantilever ID was illustrated by the number FIB milled beside the cantilever, i.e. cantilever 1 and 2, 3 and 4, 5 and 6 are in pairs. Within each pair, the cantilevers should be exactly parallel to each other as they were milled simultaneously using identical FIB patterns without any stage rotation. Therefore, they have the same grain boundary plane, misorientation angle and rotation axis. As shown in figure 4.19b and 4.19c, the stress-displacement behaviour within each pair are quite similar to each other. The scatters in the steady-state stresses for grain boundary sliding are shown in table 4.4 and 4.5, which are again larger than the error propagation from the load and dimension measurements (~1.9%). But they are comparable to or even smaller than that seen from the multiple repeated tests on the same cantilever (table 4.3). This demonstrates the reproducibility of the tests carried out on the cantilevers with the same grain boundary plane, misorientation angle and rotation axis. The scatter between different pairs was due to the differences in the grain boundary plane orientation (to be addressed in section 4.2.2).

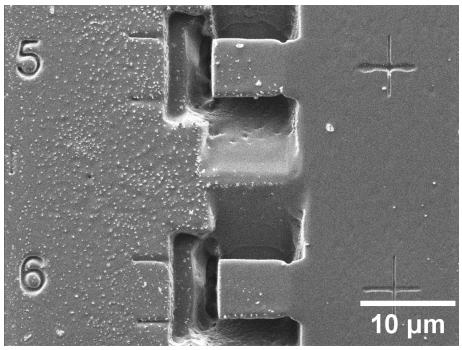

(a)

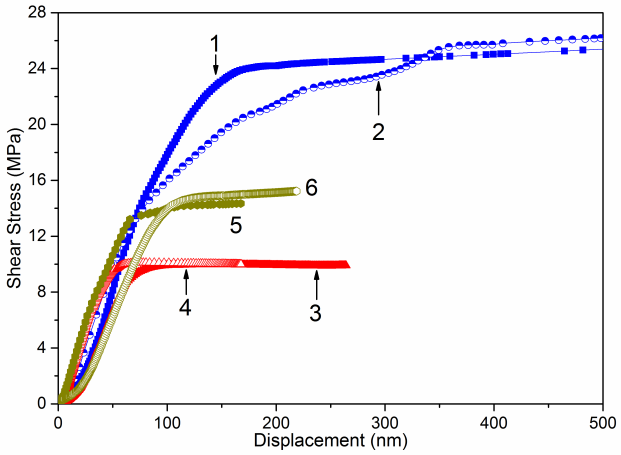

(b)

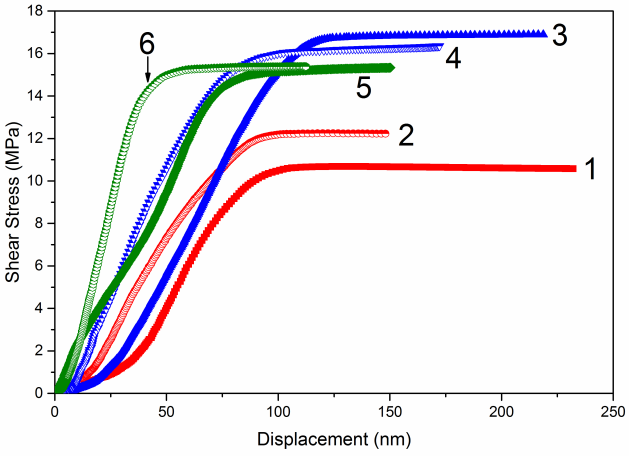

(c)

Figure 4.19: (a) SEM image showing a pair of parallel cantilevers milled on the same grain boundary. (b) and (c) Comparison of the shear stress - displacement curves of the tests conducted on those pairs of parallel cantilevers on the same grain boundary. The tests were all carried out under nominally identical conditions (i.e. at the same target displacement rate). (b) and (c) correspond to two different grain boundaries.

Cantilever Number	GBS Shear Stress (MPa)	Difference in GBS Shear Stress (MPa)	Percentage Change Between the Cantilevers in Each Pair
Boundary 08 Cant 01	24.2	1.5	6%
Boundary 08 Cant 02	25.7		
Boundary 08 Cant 03	9.9	0.2	2%
Boundary 08 Cant 04	10.1		
Boundary 08 Cant 05	14.2	0.7	5%
Boundary 08 Cant 06	14.9		

Table 4.4: Comparison of the tests on the pairs of parallel cantilevers milled on the same grain boundary (Boundary 08) at a constant displacement rate of 1 nm/s.

Cantilever Number	GBS Shear Stress (MPa)	Difference in GBS Shear Stress (MPa)	Percentage Change Between the Cantilevers in Each Pair
Boundary 09 Cant 01	11.0	1.2	11%
Boundary 09 Cant 02	12.2		
Boundary 09 Cant 03	16.8	0.7	4%
Boundary 09 Cant 04	16.1		
Boundary 09 Cant 05	15.2	0.1	1%
Boundary 09 Cant 06	15.3		

Table 4.5: Comparison of the tests on the pairs of parallel cantilevers milled on the same grain boundary (Boundary 09) at a constant displacement rate of 1 nm/s.

Cantilever Number	Angle	Axis			GB Plane1			GB Plane2			Average GBS Shear Stress
	°	u	v	w	h_1	k_1	l_1	h_2	k_2	l_2	MPa
B08 Cant01&02	30.9	-1	-1	-4	0	-1	0	1	2	0	25.0
B08 Cant03&04	30.9	-1	-1	-4	4	-20	-3	-16	23	9	10.2
B08 Cant05&06	30.9	-1	-1	-4	4	-11	-3	-3	3	2	15.0
B09 Cant01&02	12.2	1	0	1	4	10	-25	1	-17	23	11.6
B09 Cant03&04	12.2	1	0	1	0	0	-1	-1	-6	7	16.5
B09 Cant05&06	12.2	1	0	1	2	3	-6	-1	-3	4	15.8

Table 4.6: Grain boundary characters and average steady-state stresses for grain boundary sliding of the pairs of cantilevers on two grain boundaries.

4.2.2 The Influence of Grain Boundary Plane on Grain Boundary Sliding

Three pairs of parallel cantilevers were manufactured on the same grain boundary with an evident curvature. The pairs of parallel cantilevers were milled at different segments of the grain boundary. As shown in figure 4.20a, the angles between the cantilever long axes for Cantilever 1 & 2 and 5 & 6, 3 & 4 and 5 & 6 were 9.46º and 10.03º, respectively. The angles between the cantilever long axes for the pairs on another boundary were 5.2º and 14.9º, respectively, as shown in figure 4.20b. The shear stress against displacement curves for different pairs of cantilevers are compared in figure 4.20c. An average of the two cantilevers in each pair is shown. It can be seen that the grain boundary sliding behaviour varies between the different pairs of cantilevers. This may be attributed to the differences in the atomic structure of the grain boundary in the different grain boundary planes. The grain boundary characters are summarised in table 4.6, including the angle and axis, grain boundary plane orientations with respect to grain 1 (fixed end grain) and grain 2 (free end grain). The steady-state shear stresses were averaged for the repeated tests within each pair of the parallel cantilevers.

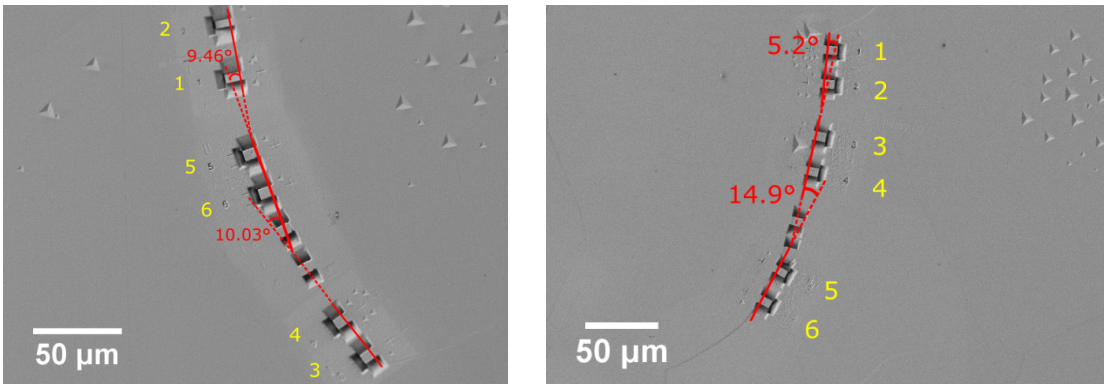

(a) (b)

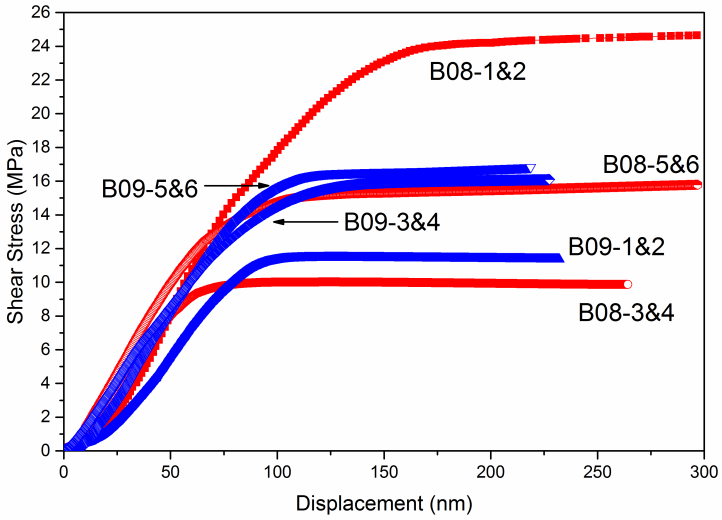

(c)

Figure 4.20: (a) and (b) show the SEM images of the pairs of cantilevers on the curved grain boundaries ("B08" and "B09" denote the two different grain boundaries). The cantilevers are parallel to each other in each pair, but there are angular changes in the grain boundary plane between different pairs. (c) Comparison of stress-displacement curves for the the pairs of cantilevers with different boundary planes. An average of the two cantilevers in each pair is shown (for example, "B08-1&2" corresponds to the averaged curve for the two cantilevers 1 and 2). All the tests were carried out under nominally identical conditions (i.e. at 1 nm/s).

4.2.3 Sliding Behaviour of Grain Boundaries with Different Misorientations

Figure 4.21 shows the variation of average steady-state shear stresses with the misorientation angle of the grain boundary. The grain boundaries chosen have a wide range of misorientation angles, from low to high-angle grain boundaries. The error bars represent the range of the steady-state shear stresses for each grain boundary. It can be seen that the boundaries with very large misorientation angles (above ~70º) are relatively easier to slide (low steady-state shear stresses). This could be explained by the grain boundary energy theory described in the literature review. The very high-angle boundaries have more random grain boundary structure and therefore tend to slide more easily. The boundaries with misorientation angles of around 50 to 60º have notably higher steady-state shear stresses. These boundaries correspond to Boundary 02, 03, 05 and 11 in table 4.7. The higher resistance to sliding of these boundaries could be attributed to their slightly off-coincidence boundary structure. The misorientation angles of these boundaries are close to the typical twin boundaries in tin, which are 57.2°[100] along {301) twin plane and 62.8°[100] along {101) twin plane. Especially Boundary 02 and Boundary 11 have misorientation angles almost the same as those for twin boundaries, while their rotation axes are slightly different to that for twin boundaries. It is widely accepted that sigma boundaries (including twin boundary) are resistant to grain boundary sliding [72, 80, 85, 88]. Even though Boundary 02 and 11 have quite similar misorientation angles as the twin boundaries, the fact that they could still slide indicates that misorientation angle on its own could not determine the grain boundary sliding behaviour. The rotation axis also has a large impact on the grain boundary structure and therefore sliding behaviour. The boundaries with misorientation angles below 40º have the average level of shear stresses for grain boundary sliding. The grain boundary with a misorientation angle of 31º has the largest error bar, which corresponds to the different grain boundary planes on the same boundary. This indicates the significant effect of the grain boundary plane on sliding behaviour. The only low-angle boundary (Boundary 09) shows relatively high shear stresses. This might be due to the relatively ordered structure of the

low-angle boundary, resulting in a low tendency to slide.

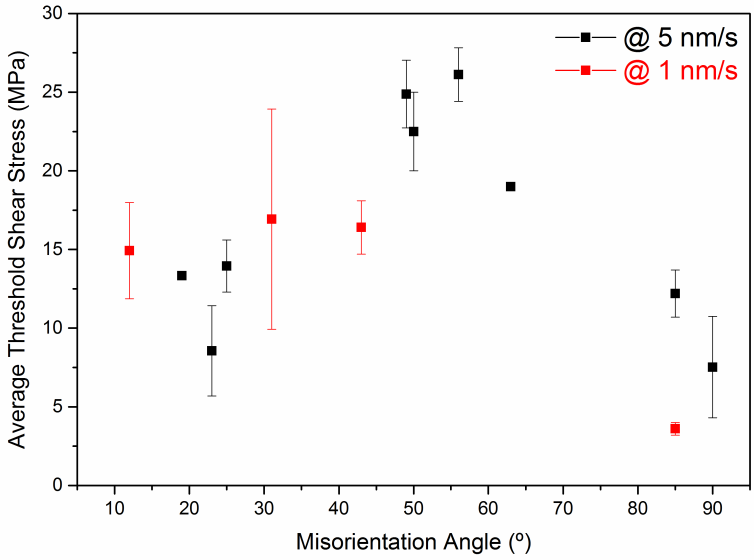

Figure 4.21: Plot of the average steady-state shear stress for grain boundary sliding against the misorientation angle of boundaries tested at 1 and 5 nm/s.

Cantilever Number	Misorientation	Axis			GB Plane 1			GB Plane 2			Displacement Rate	GBS Shear Stress
	°	u	v	w	h_1	k_1	l_1	h_2	k_2	l_2	nm/s	MPa
Boundary 01	24.9	14	9	-19	6	6	1	1	1	0	5	13.9±1.7
Boundary 02	57.5	-2	-3	7	-2	-6	1	-19	7	1	5	26.1±1.7
Boundary 03	48.5	-7	-11	22	0	1	0	4	6	1	5	24.9±2.1
Boundary 04	23.0	0	1	1	9	5	-2	2	1	0	5	8.6±2.9
Boundary 05	49.8	7	-7	2	5	4	-1	1	1	0	5	22.5±2.5
Boundary 06	91.7	-7	1	3	0	1	0	2	1	0	5	7.5±3.2
Boundary 07	86.9	19	5	-5	2	1	0	-6	-1	1	5	12.2±1.5
Boundary 07											1	3.6±0.4
Boundary 08	30.6	1	1	4	Different GB planes - see table 4.6						1	16.9±7.0
Boundary 09	12.4	1	0	1	Different GB planes - see table 4.6						1	14.9±3.1
Boundary 10	43.5	7	5	10	1	3	0	-1	3	1	1	16.4±1.7
Boundary 11	62.9	4	-3	-1	1	1	0	5	4	1	5	19.0
Boundary 12 (Twin Boundary)	61.8	1	0	0	1	1	0	-5	-4	1	1	23.5±1.0 (No GBS)

Table 4.7: Comparison of the steady-state shear stresses for grain boundary sliding at the same displacement rate (either 1 or 5 nm/s), between cantilevers on different grain boundaries with a range of misorientation angle, rotation axis and grain boundary plane orientation.

4.2.4 Shear Testing of a Twin Boundary

Other than the random grain boundaries (Boundary 01 to 11 in table 4.7), a twin boundary (Boundary 12) with the misorientation angle and axis as the typical 62º[100] type twin in tin was investigated. The EBSD analysis of the boundary before milling the cantilever is shown in figure 4.22a. Two bicrystalline cantilevers were manufactured at the twin boundary to reduce experimental uncertainty. The tests were carried out at a target displacement rate of 1 nm/s. The load and stress against displacement curves of the two cantilever tests are shown in figure 4.22b. The black and red curves correspond to the shear stress and load, respectively. The differences in shear stress and load at the steady state are below 10% between the two cantilevers, which indicates that the tests are reproducible. The load drops by less than 1% from the peak value to the end of the test, which is smaller than that observed for the grain boundaries reported earlier that are shown to have slid (load drops by at least 2%). Since the boundary plane showed no evidence of sliding in the SEM images in figure 4.23, the shear stresses were calculated simply by load over the grain boundary area. The steady-state shear stresses (at the plateau) for both cantilevers (around 24.5 and 22.5 MPa) are notably higher than the typical shear stress for grain boundary sliding (usually below 18 MPa for tests at 1 nm/s).

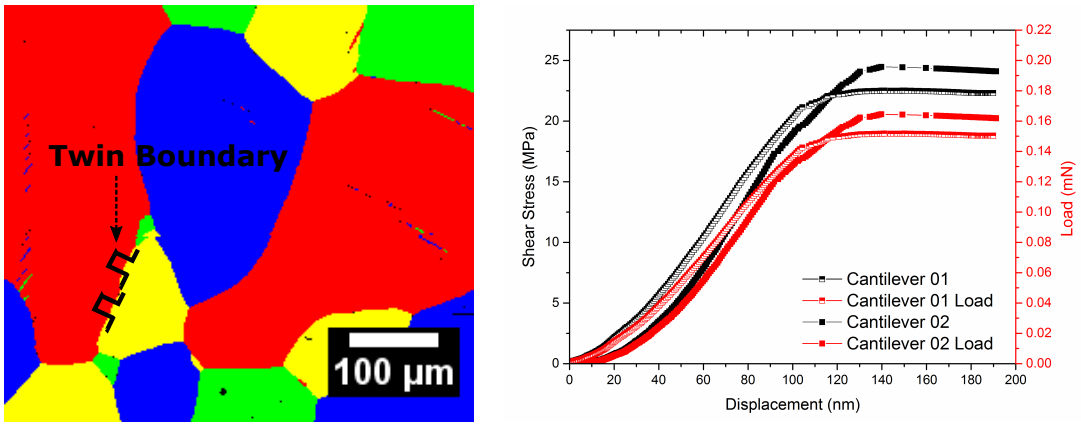

(a) (b)

Figure 4.22: (a) is the EBSD analysis of the twin boundary that is close to a CSL ∑31 boundary before the cantilevers were made. (b) Load and stress against displacement curves of the two cantilevers on the twin boundary.

Figure 4.23a and 4.23b show that the twin boundary was located within the grooves on both sides before the test. Figure 4.23c to 4.23d reveal a clear trace of line around 1 μm away (towards the fixed end) from the grooves. The twin boundary seemed to have migrated towards the grain on the fixed end, in contrast to a step at the grain boundary plane (for grain boundary sliding) reported earlier. Looking close at the side of the grooves, there is some matter transfer occurring at the grain boundary area as highlighted in figure 4.23e and 4.23f. This is probably attributed to the varying gap in the groove.

Hough-based EBSD analysis was conducted on the twin boundary after the test on the microcantilever, which was overlaid with the SEM image before testing as shown in figure 4.24. The grain orientations and grain boundary characters before and after the test have not changed. It could be seen from figure 4.23b that the grain boundary was straight on the top surface of the cantilever before testing. However, the slightly inclined grain boundary after testing shows that the boundary had a tendency to migrate towards the built-in end of the microcantilever. But the groove has apparently restricted the migration of the boundary. Therefore, the line traces shown in figure 4.23c and 4.23d are not migrated boundaries.

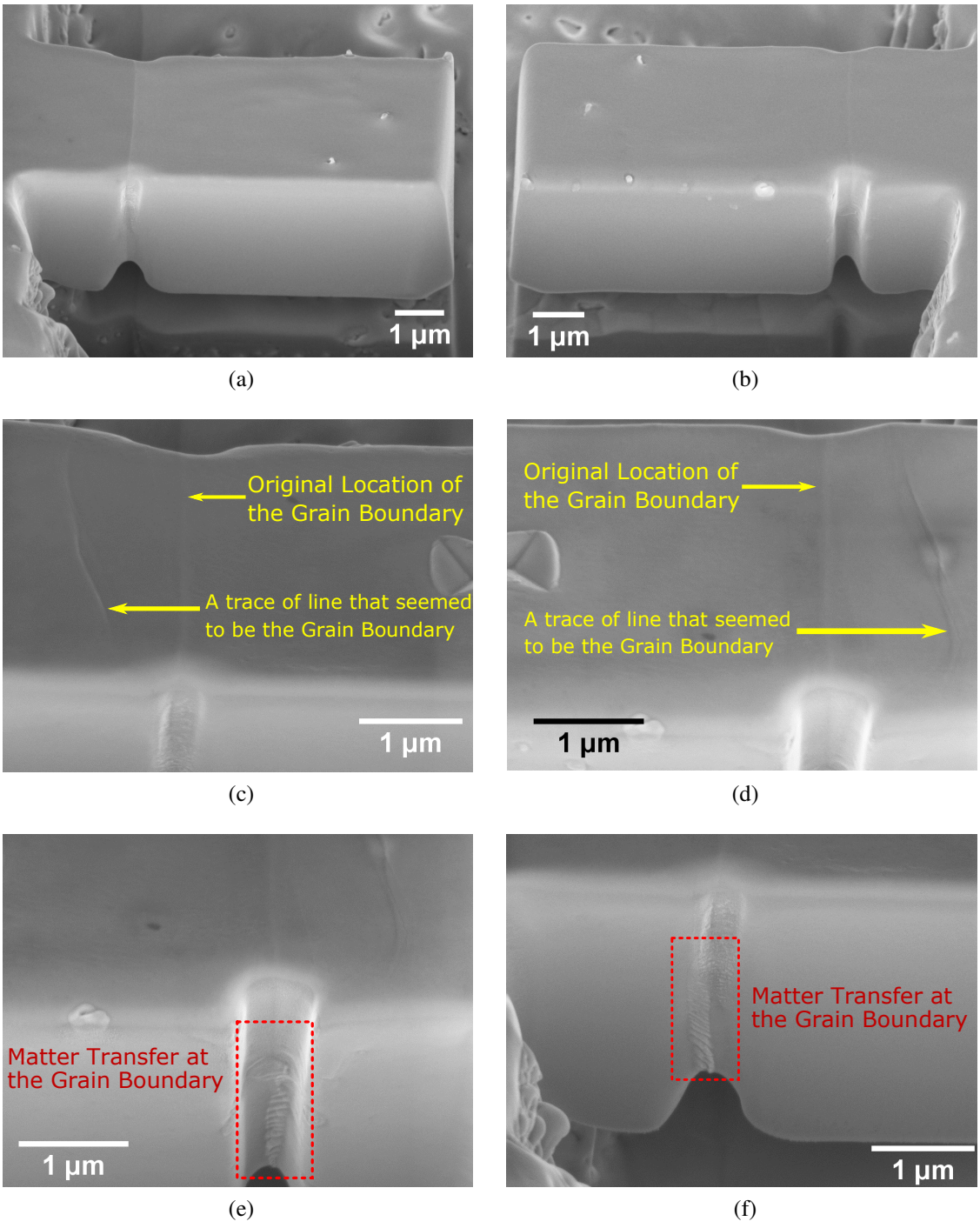

Figure 4.23: (a) and (b) show the side views of a cantilever on the twin boundary before testing, which is located inside the grooves on both sides. (c) and (d) show the side views after testing; a clear trace of line could be seen outside the groove, which seemed to be the migrated boundary. (e) and (f) are the zoomed-in views of the grain boundary in the grooves, showing evidence of matter transfer.

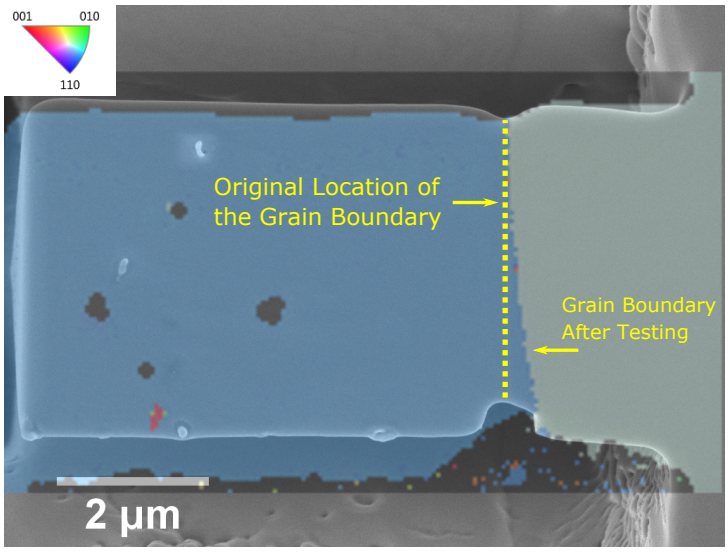

Figure 4.24: Inverse pole figure (along x-axis) after testing overlay with the SEM image of the cantilever before testing.

4.2.5 Displacement Rate Jump Tests on the Same Cantilever

As discussed in Chapter 3 on the macromechanical shear tests, a few strain rates were used in the displacement controlled tests to find the strain rate sensitivity index of fine-grained material. Similarly, in the micro-cantilever tests, a few displacement rates were applied to the same cantilever to investigate the effect of strain rates on intrinsic grain boundary sliding. Figure 4.25 shows a series of tests on the same cantilever with various displacement rates. The tests were carried out under identical conditions except the displacement rates. For example, the load point was the same for all the tests. Similar to the example shown in figure 4.14 in section 4.1.5.5, there was a clear step at the grain boundary after each individual test. The depth of the step was measured in the SEM as shown in figure 4.25d, 4.25f and 4.25h. The side views of the cantilever (figure 4.25c, 4.25e and 4.25g) suggested that sliding occurred along the entire grain boundary plane from the top to bottom and there was minimal bending of the cantilever. It can be found that the morphology of the step at the boundary is smoother when the displacement rate is low (i.e. 0.1 and 1 nm/s). However, for a higher displacement rate (10 nm/s), the "sliding region" is characterised by a columnar void-like structure. This is attributed to the little time for diffusion to occur during fast grain boundary sliding.

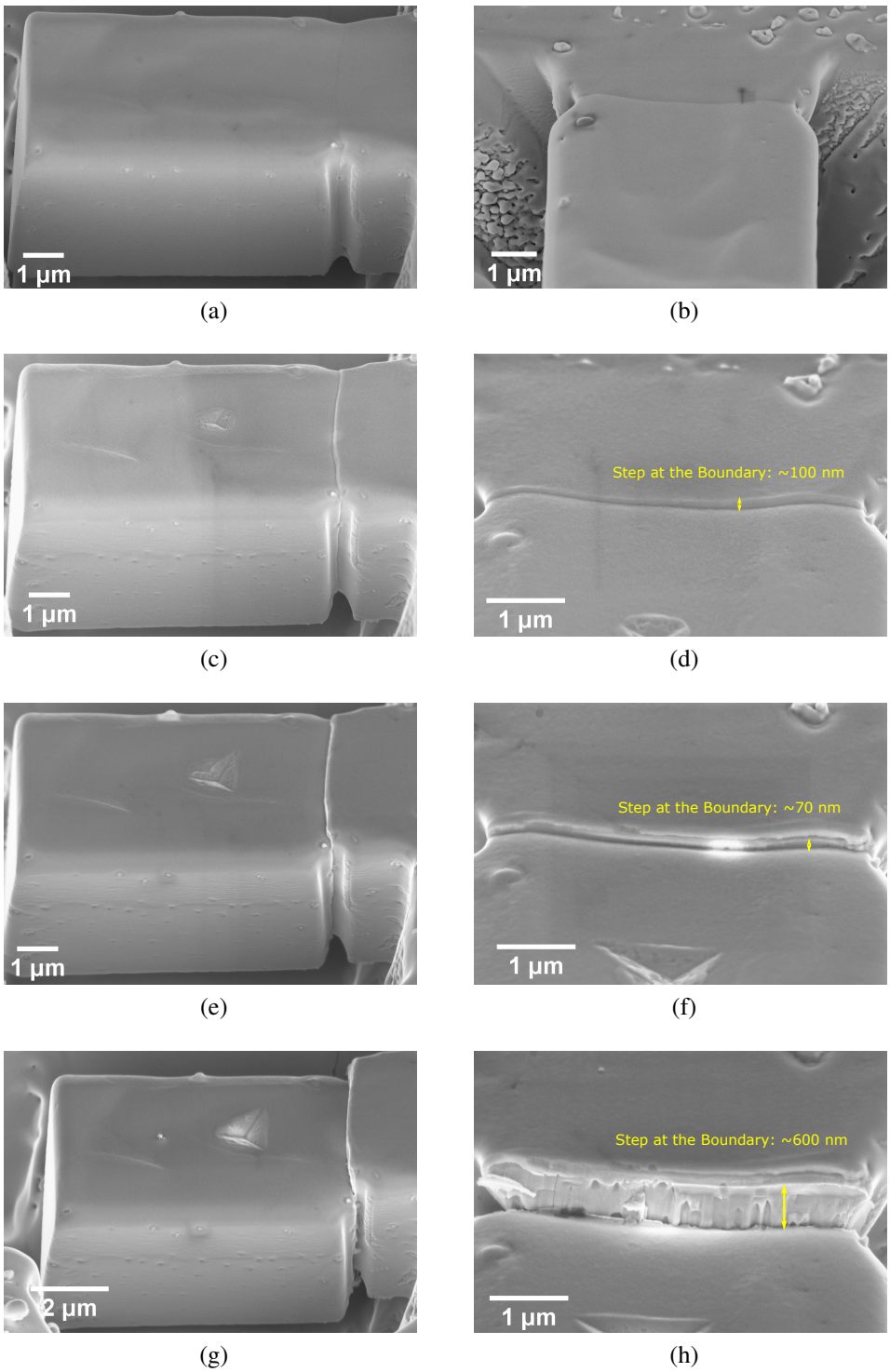

Figure 4.25: (a) and (b) show the side and front views of the cantilever before testing. (c) and (d) show the side and front views after the first test with the lowest displacement rate, 0.1 nm/s. (e) and (f) show the views of the grain boundary after loading at the same point at 1 nm/s. (g) and (h) show the morphology of the grain boundary after sliding for a long distance at a much higher displacement rate of 10 nm/s.

The stress against displacement curves for each individual test is summarised in figure 4.26a. The effect of indenter impression on the total displacement has been corrected for. Therefore, the displacement of the steady state grain boundary sliding should correspond to the depth of the steps at the grain boundary plane (as measured in figure 4.25d, 4.25f and 4.25g). The discrete data points on the stress-displacement curve for the test at 10 nm/s suggest that the initial sliding rate is higher than the target displacement rate. This is due to the high inertia of the grain boundary when sliding is initiated. Later on, the grain boundary sliding rate gradually stabilises to the target displacement rate, which gives an overall average grain boundary sliding rate of 16 nm/s. The displacement rate jump tests were carried out on a few microcantilevers.

Another example is shown in figure 4.26b, where the displacement rates were changed during the test without unloading. The two displacement rate jump tests were conducted on the same cantilever, i.e. the first test at 0.1 and 0.3 nm/s, and the second test at 1 and 5 nm/s. The change in displacement rates at around 180~200 nm in both tests caused the immediate response of shear stresses. As mentioned in the previous sections, the initial grain boundary sliding rate was higher than the target displacement rate and gradually stabilised to it. The displacement rate curve for the 0.1-to-0.3 nm/s test has a smaller fluctuation than the 1-to-5 nm/s test. It can be seen that the shape of the shear-displacement curves is quite similar to that for the macro-shear strain rate jump tests (figure 3.13b in Chapter 3). This novel testing method could potentially allow investigation on the transient deformation events close to the change of displacement rates. However, the limitation is that the control system is unable to keep up with the sudden strain bursts due to the delay in the feedback loops of the displacement-control testing method.

The total displacement of the nanoindenter after the two tests in figure 4.26b was 755 nm, part of which was attributed to the depth of the indent. As shown in figure 4.26c, the depth of indent was around 230 nm. Therefore, the displacement at the grain boundary was 525 nm. Taking into account of the blunt nanoindenter tip, the indenter depth should be lower than 230 nm, then displacement of sliding is higher than 525 nm. The surface profile of the cantilever was further confirmed using an optical profilometer - MicroXam. This technique uses white

light and phase-shifting interferometry to measure the topography of surface profiles [166]. The topography of the cantilever after the displacement rate jump tests is shown in figure 4.26d. It can be noticed that the cantilever area (dark region) was significantly lower than the surrounding sample surface. This is due to the surface material removal during FIB milling and imaging. The depth of the step at the grain boundary was measured to be ~565 nm in figure 4.26e. The measured amount of sliding was in good agreement using both methods.

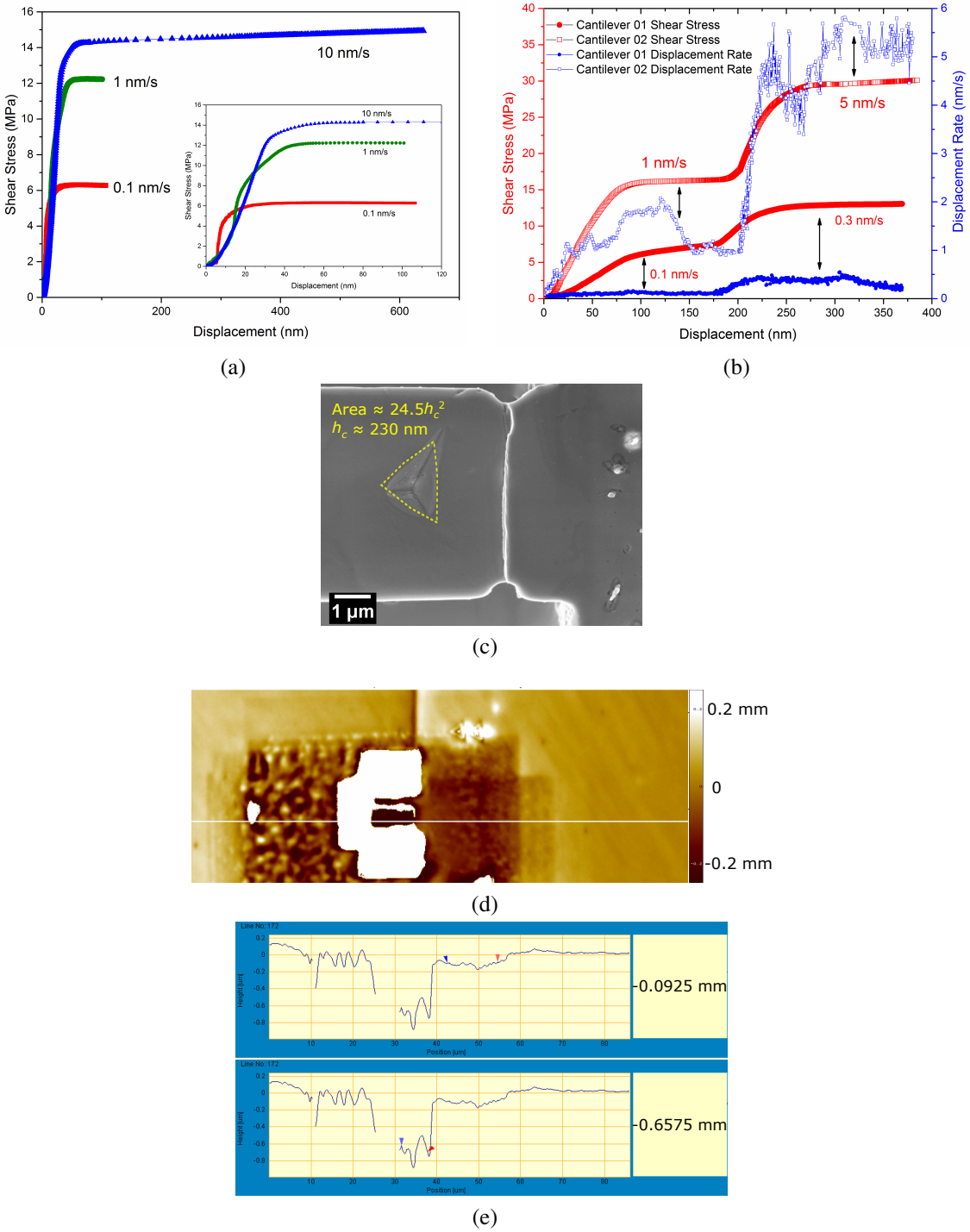

Figure 4.26: (a) Shear stress - displacement curves of the same cantilever tested at various displacement rates. (b) The displacement rates are changed during a continuous test without unloading. The shear stress on the grain boundary and displacement rate are plotted against displacement. (c) An SEM image of the indent impression after testing. The depth of the indent impression can be estimated from the area. (d) The surface profile image of the microcantilever after the displacement rate jump tests (the colour represents different heights). (e) The profile graph showing the difference in height of the regions on either side of the slid grain boundary.

4.2.6 Finite Element Analysis

The effect of the way to apply a load in the model (concentrated on a point or distributed along a line) was investigated as follows. The "10 μm" and "20 μm" in figure 4.27a denote the length of the cantilever for simplicity. The "3 μm" and "1 μm" in figure 4.27b denote the distance between the load point/line to the grain boundary. Since a constant load was applied, the displacement of the load point/line decreased as the load was applied closer to the grain boundary. For example, the displacements of the elements on the load point/line are ~0.65 μm and ~0.17 μm, respectively, for the 20 μm and 10 μm cantilevers. On a 20 μm cantilever (load applied 18 μm from the grain boundary), the difference was minimal between a distributed load and a point load in the tensile or compressive stress on the grain boundary. For a 10 μm cantilever, the difference was still quite small when the load was applied 8 μm from the grain boundary. However, as the load point came closer to the grain boundary at 3 μm and 1 μm (figure 4.27b), the difference in the stresses at the same displacement became more significant. At 1 μm distance, there was a 26% difference in the compressive stresses at a displacement of 0.01 μm. Since a point load was more representative of the actual testing condition using a nanoindenter, a concentrated load on a point was applied to the cantilever in all the models shown below.

The stresses at the grain boundary plane are important to the grain boundary behaviour. The tensile or compressive stresses (normal to the grain boundary plane) and shear stresses (along the grain boundary plane) at a constant load of 200 μN were investigated in more details. An example is shown as follows. For a 10 μm long cantilever, a constant load of 200 μN is applied 3 μm from the grain boundary. The distribution of normal and shear stresses on the grain boundary plane are shown in figure 4.28a and 4.28b, respectively. A path of nodes are highlighted in the centre of the plane. In figure 4.28c, the normal stresses are plotted against the distance of the elements from the top surface. The maximum tensile stress lies on the top surface and maximum compressive stress is on the bottom. The neutral axis lies in the top half of the cross section.

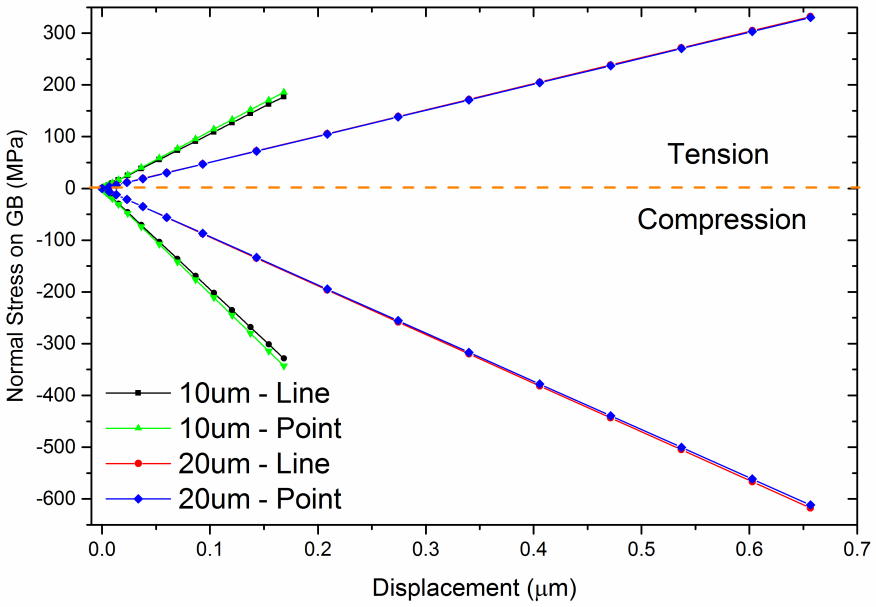

(a)

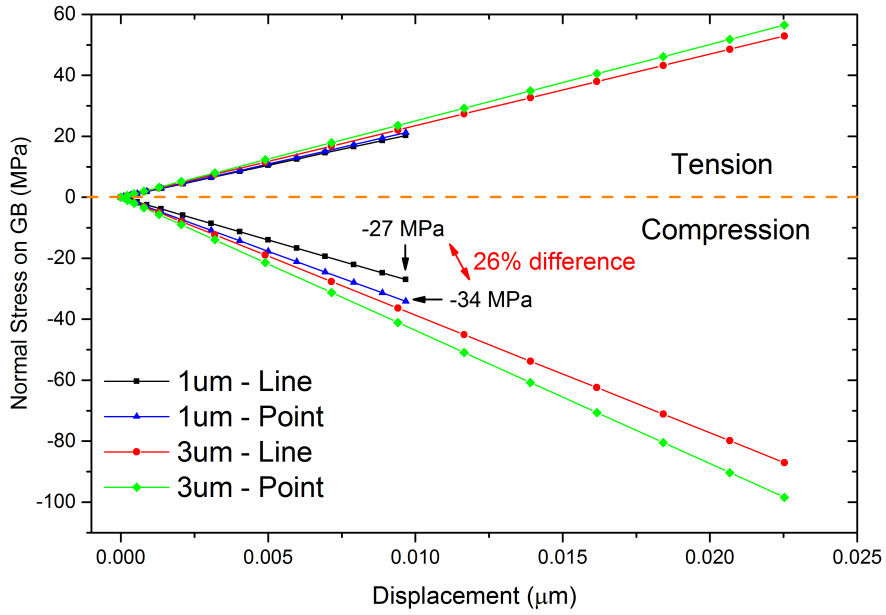

(b)

Figure 4.27: Comparison of the tensile and compressive stresses on the grain boundary after applying the load concentrated on a point or distributed along a line for (a) 20 μm and 10 μm cantilevers; (b) 3 μm and 1 μm from the grain boundary (on a 10 μm long cantilever).

In figure 4.28d, the shear stress along the grain boundary plane is plotted against the distance of the elements from the top surface. The difference in shear stress was not that significant with the change of load point. The shear stresses reach the maximum in the centre of the cross-section of the grain boundary plane (~3 μm from the top surface), except for the case of 1 μm load point when the elements on the grain boundary became distorted under the load. The maximum shear stresses for various load points were around 25~30 MPa, which was comparable to the simple calculation: $Load\ on\ GB \div Area\ of\ GB \approx {}^{200\mu N}/_{10.8\mu m^2} \approx 18.5\ MPa$. This calculation is based on the assumption that the load along the grain boundary plane is the same as the load applied to the cantilever surface. In summary, the maximum shear stress can be assumed to be only linearly dependent on the load, and independent of the location of load point.

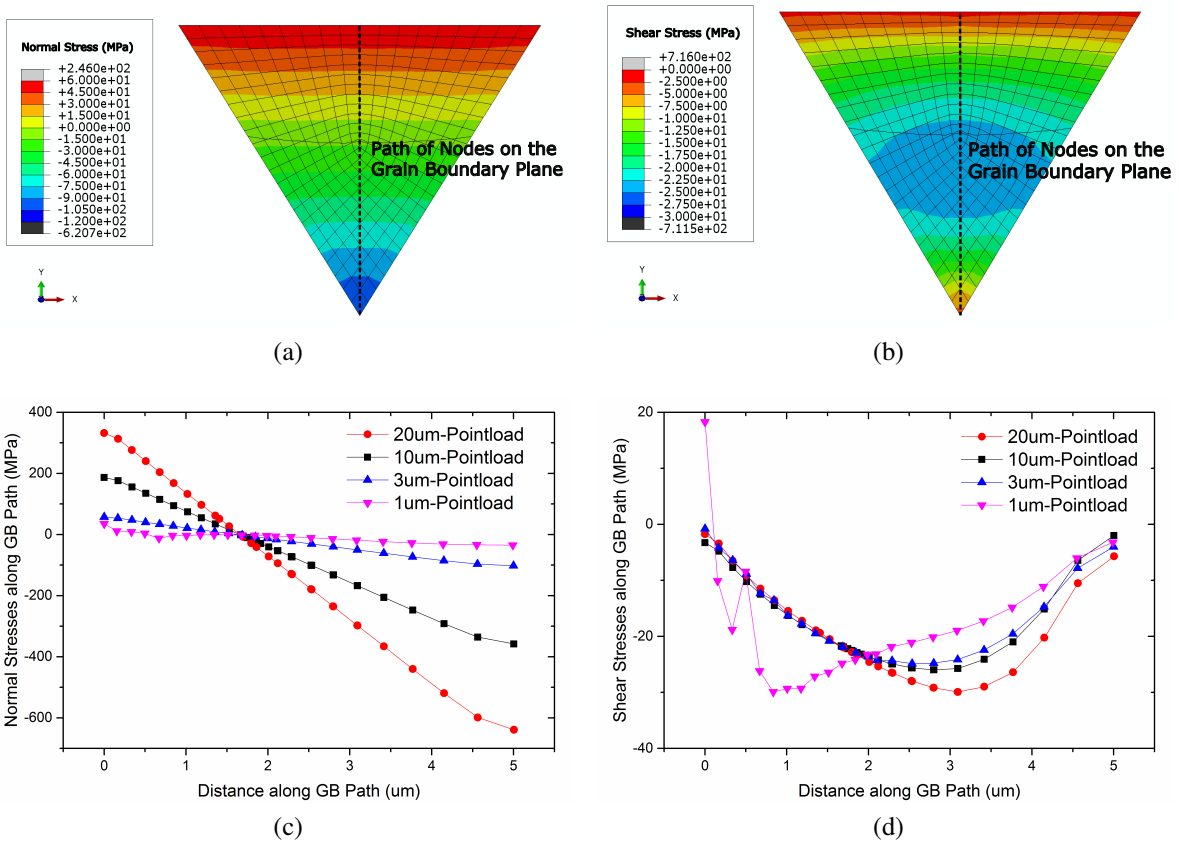

Figure 4.28: For a 10 μm cantilever, when a constant load of 200 μN load was applied 3 μm from the grain boundary, (a) tensile and compressive stresses normal to the grain boundary plane; (b) shear stresses along the grain boundary plane. (c) and (d) compare the normal and shear stresses (described above) on the grain boundary plane along the path of nodes (distance from the grain boundary measured from the top surface) for different load points.

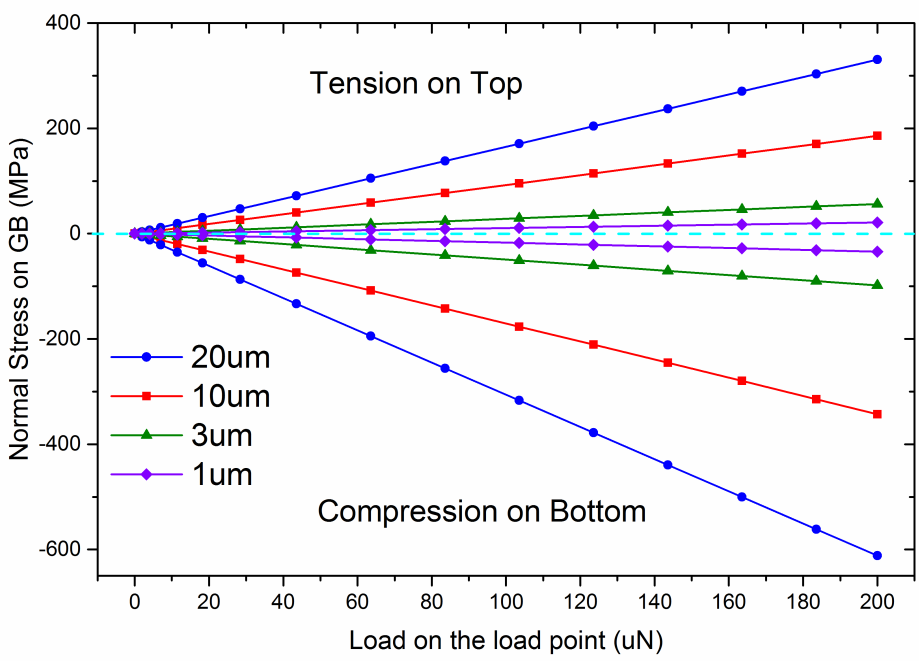

Figure 4.29: The normal stresses on the grain boundary (tension on top and compression on bottom) are plotted against load for different load points.

It is also interesting to investigate how the normal stresses on the grain boundary change with the applied load for different locations of load point. A constant load of various magnitudes is applied at different locations. The maximum normal stresses on the grain boundary plane (tension on top and compression on bottom) for different load points are plotted against the magnitude of load in figure 4.29. The normal stresses increase significantly as the load point gets further away from the grain boundary. Therefore, for the 20 μm long cantilevers loaded at the free end, the normal stresses are much higher than the shear stress. So diffusion creep is more favourable than grain boundary sliding, which is discussed in the next section (4.2.7).

4.2.7 Diffusion Creep Tests on Long Cantilevers

In order to analyse the effect of diffusion creep on the total displacement of the cantilever, tests were carried out on the long cantilevers (5×20 μm, twice as long as the standard ones) with both load and displacement-controlled methods. The long cantilevers were manufactured across a grain boundary (Boundary 04 23.0° [0 1 1] in table 4.7) as shown in figure 4.30a. The cantilever design is the same as the standard ones except for the doubled length. In the bulk grain, long and standard single-crystal cantilevers were also made for comparison (figure 4.30b).

4.2.7.1 Load Controlled Tests

The methodology of load controlled tests was described in section 4.1.5.1. The testing method was set up so that the load on the sample was kept constant instead of the raw load. In order to verify the reliability of this modified testing method, a short cantilever without a grain boundary was tested under load control (figure 4.30b). The maximum load for grain boundary sliding was found to be around 100 μN from the tests on the cantilevers with a standard length. Therefore, a load of 100 μN was applied at the free end of the cantilever. It was held for 1 hour, which was longer than the period of time for grain boundary sliding tests (half an hour for tests to ~180 nm displacement at 0.1 nm/s). The load on the sample against the total displacement of nanoindenter curve is shown in figure 4.31a. A thermal drift correction was made to the displacement data ($thermal\ drift\ displacement = drift\ rate \times time$). It was seen that the load on the sample was kept constant. The SEM image in figure 4.31b shows that the cantilever was heavily bent and the displacement of deflection was comparable to that in the load-displacement curve above (taking into account of the depth of indent marker). However, the thermal drift effect on the total displacement was notable for such a long time hold at a tiny load. The measured displacement of the indenter without thermal drift correction was minimal. Therefore, even though the actual load on the sample was managed to be kept constant, the load-control method was not appropriate for long-term creep tests.

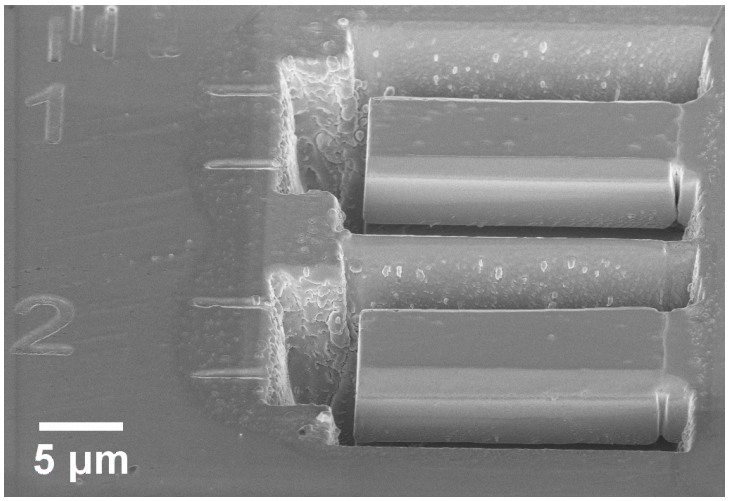

(a)

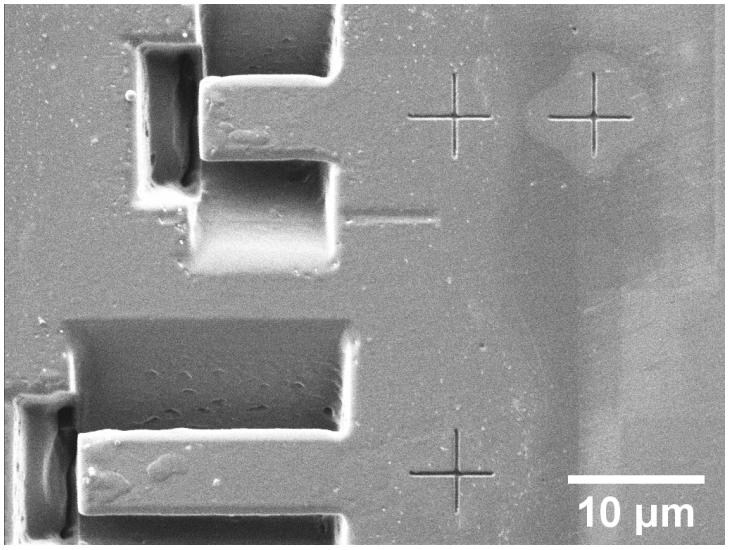

(b)

Figure 4.30: (a) SEM image of a pair of long cantilevers made on a grain boundary. (b) Long and standard single-crystal cantilevers without a grain boundary for comparison.

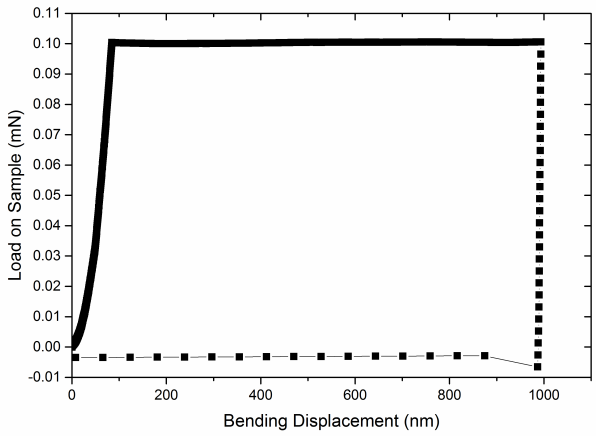

(a)

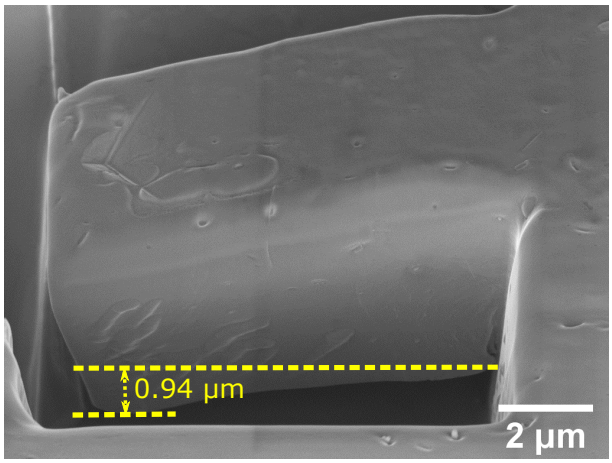

(b)

Figure 4.31: (a) Load on the sample against displacement curve for a load-controlled test on a short cantilever. (b) SEM image showing the bent cantilever after the load-controlled test.

4.2.7.2 Displacement Controlled Tests

Due to the unsuitability of the load-control method, tests were carried out at a constant displacement rate. A low displacement rate of 0.1 nm/s (strain rate $\sim 10^{-5}/s$) was firstly used to test a pair of long cantilevers (5×20 µm). The experimental results are shown in figure 4.32a. The shear stress (on the grain boundary plane) was calculated by the load divided by the area of the grain boundary. For both bicrystalline cantilevers, the shear stress slowly and steadily increased until levelling off at a plateau. In contrast, a test at the same displacement rate was carried out on the single-crystal long cantilever to reach a similar displacement. The shear

stress on a cross-sectional plane 2 μm from the built-in end kept increasing with displacement. The evident difference in the shear stresses of cantilevers with and without a grain boundary indicates the important role of grain boundary. There must be a different deformation mechanism at the grain boundary from that in the bulk material. The SEM image before the test (at 0.1 nm/s) is shown in figure 4.32b. With the two images overlapped with each other in figure 4.32c, there was a slight deflection of approximately 190 nm of the cantilever, which was larger than the residual displacement (~162 nm) measured after unloading. The mismatch of the measured deflection of the cantilever indicates the notable effect of thermal drift on the total displacement of the cantilever, i.e. the residual displacement of the nanoindenter underestimates the actual displacement of the cantilever. The grain boundary was further inspected in figure 4.32d (before test) and 4.32e (after test). There was no strong evidence of material plated out on top of the grain boundary. Neither was there any sign of grain boundary sliding. Therefore, a larger displacement of the cantilever was required.

Further deformation was conducted on these two long bi-crystal cantilevers. In order to shorten the period of test and reduce the thermal drift effect, a relatively higher displacement rate of 0.3 nm/s was used to deform the cantilevers. The load on the sample is plotted against displacement in figure 4.33a. Both cantilevers show a notable drop in load, especially in Cantilever 01. The test for Cantilever 02 (the red curve) was manually stopped as the load started to increase towards the end of test. The SEM images taken after the test illustrate that the cantilevers are further bent but no sliding has occurred on the grain boundary (figure 4.33b and 4.33c for Long Cantilever 01 and 02, respectively). It can be seen that the cantilevers were tilted abruptly at the grain boundary. The built-in end was hardly deformed but the free end grain was still straight on the surface (not bent with curvature as in figure 4.31b). The grain boundaries were closely inspected and both cantilevers seemed to have new material plated out on the top surface of the grain boundaries after testing (figure 4.33e), in comparison to the clean surface on the grain boundaries before testing (figure 4.33d). Especially on Cantilever 01, the dark line is approximately 200 nm (on average) away from the original position of the grain boundary.

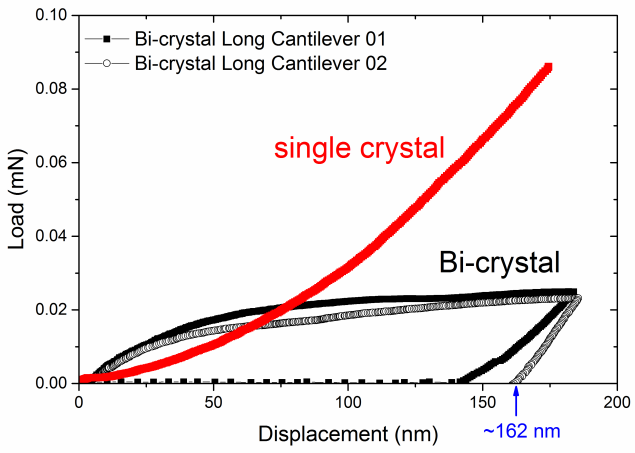

(a)

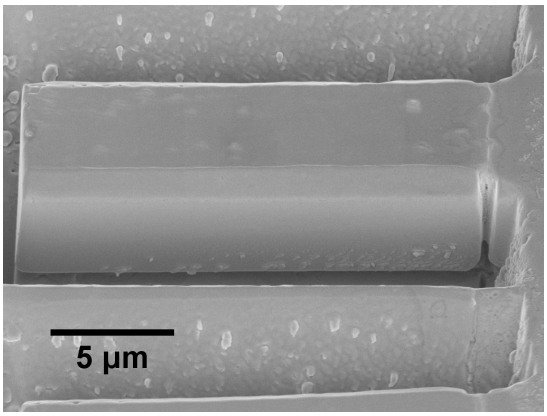

(b) Before Test

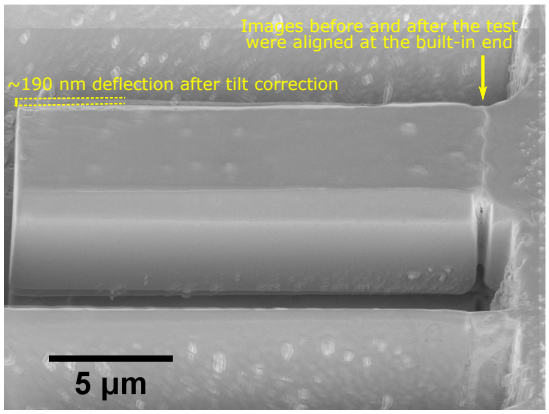

(c) Before and After Test

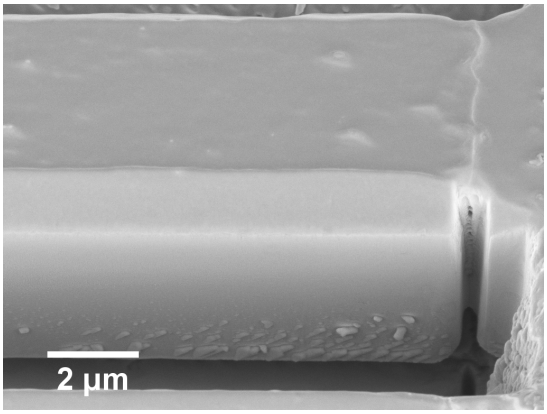

(d) Before Test

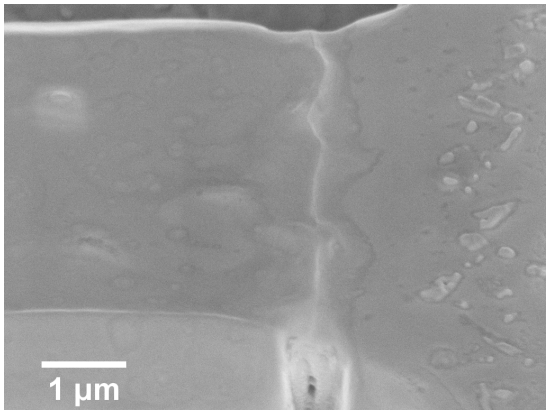

(e) After Test

Figure 4.32: (a) The shear stress on the grain boundary plane (or a cross-sectional plane 2 µm from the built-in end for the single-crystal) against displacement for tests on a single-crystal and two bi-crystal cantilevers at 0.1 nm/s. (b) SEM image of Long Cantilever 02 with a grain boundary before testing. (c) shows the deflection of the cantilever by overlapping the SEM images before and after testing. (d) and (e) are zoomed-in images of the grain boundary of the same cantilever before and after testing, respectively.

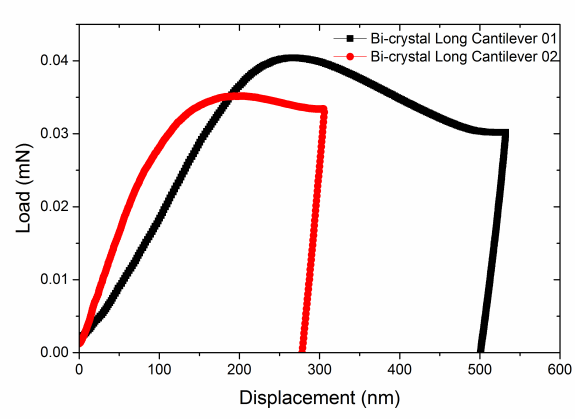

(a)

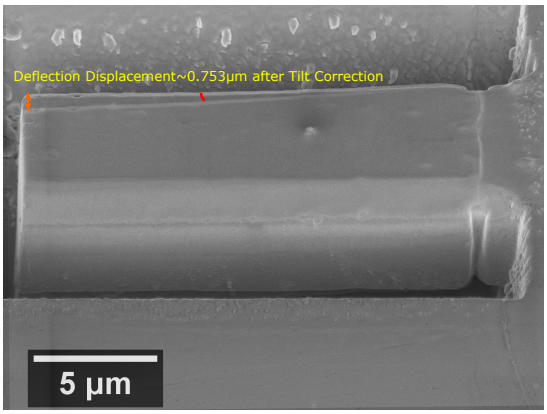

(b)

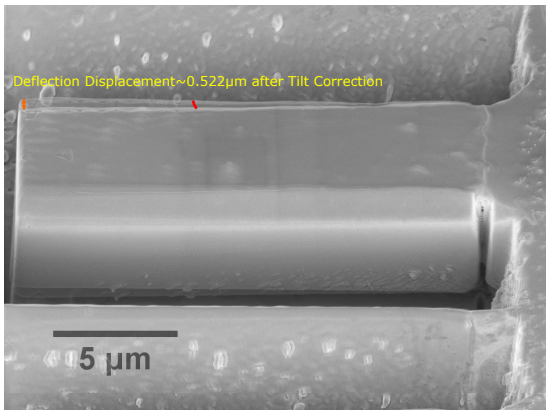

(c)

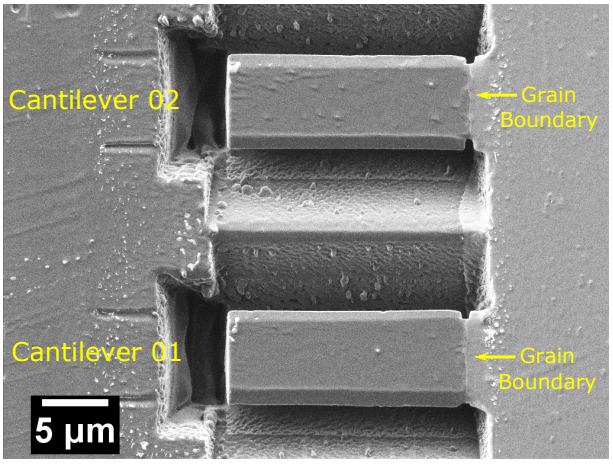

(d)

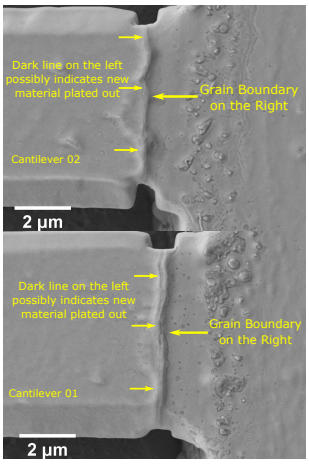

(e)

Figure 4.33: (a) Load-displacement curves of the long cantilevers tested at 0.3 nm/s. Overlapped SEM images before and after testing of (b) Long Cantilever 01 (c) Cantilever 02. (d) An image of the two cantilevers before testing. (e) Images after testing show that material may have plated out on the top surface of the grain boundary.

4.3 Discussion

4.3.1 Grain Boundary Sliding vs. Plastic Yielding

The SEM images before and after testing (examples shown in section 4.1.5.5 and 4.2.5) were compared with each other to confirm that no significant bending was observed in the cantilevers that showed grain boundary sliding. The load-displacement curves for grain boundary sliding are distinguishable from those for plastic yielding of the cantilever. As shown in figure 4.34, the characteristic continuous drop in load only happens for sliding but not plastic yielding. Constant and gradual increase of load and stress during yielding was widely seen in the cantilever tests [104, 109, 110]. Upon loading, as the load and shear stress (on the grain boundary) reach the threshold for grain boundary sliding after the elastic deformation regime, sliding is initiated. Using this micro-mechanical testing design, grain boundary sliding is separated from the various accommodation mechanisms such as diffusion and/or dislocation motion. After only a small amount of plastic deformation, the maximum load/stress is reached. Then the load starts to drop, showing a softening process, which is in agreement with the creep tests on bicrystalline tin [140] and aluminium [134] as well as polycrystalline Sn-Bi alloy [167]. This is because grain boundary sliding requires a lower load to maintain than initiate the deformation. As sliding continues, the grain boundary area reduces. If the sliding rate is low and stable, the shear stress on the grain boundary stays stable as steady-state sliding continues. If the load drops significantly and rapidly, the shear stress drops abruptly as well. This was found in the polycrystalline Sn-5wt%Bi alloy as well, when grain boundary sliding was the dominant deformation mechanism, i.e. a rapid drop in flow stress [167].

4.3.2 Grain Boundary Sliding in Bi-crystal Samples

Compared to Macroscopic Bi-crystals

Grain boundary sliding in tin was investigated using macro bi-crystals by Puttick et al. [168] and Tuck [60] in 1965. They applied a constant shear stress of 0.1~0.15 MPa on a tin bi-crystal

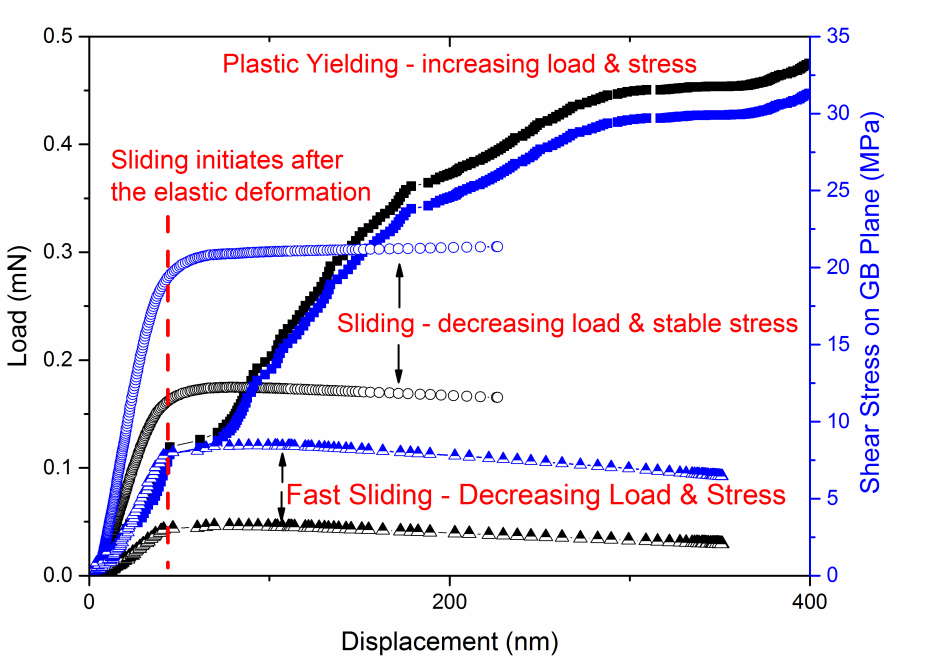

Figure 4.34: Comparison of load and shear stress against displacement curves for the short bi-crystal cantilevers showing grain boundary sliding and a single-crystal cantilever showing plastic yielding.

at 210~230°C (0.96~0.99 homologous temperature). Due to the considerable differences in the sample dimensions and testing conditions, the kinetics of sliding in their studies was significantly different from the microcantilever tests (to be discussed in section 4.3.5). In this section, the grain boundary morphology is compared between the macro bi-crystals and the present microcantilever studies. On almost every tested cantilever that showed grain boundary sliding, there was a step on the top surface normal to the sliding direction. This kind of step was also found in tin bi-crystals [168] but not as sharp as in the microcantilevers. On some cantilevers, grain boundary migration was found to be coupled with sliding. The evidence is shown in the SEM images below. When the movement of the grain boundary was restricted by the groove as shown in figure 4.35a (shown in section 4.1.5.5 before), the boundary could not migrate outside the groove. However, the grain boundary became obviously curved after sliding (figure 4.35b). For the cantilevers that were not restrained by the groove, more obvious grain boundary migration has been observed. Two examples are shown in figure 4.35c and 4.35d. This is in agreement with the experiments carried out on tin bi-crystals by Puttick et al. [168].

In the current study, grain boundary migration was observed on the surfaces parallel to the sliding direction, and the grain boundary tended to migrate in a certain direction — from the grain at the free end to the grain at the built-in end. This direction of migration supports Sheikh-Ali's [159] explanation of grain boundary migration (in zinc bi-crystals) as a result of extrinsic secondary grain boundary dislocations (GBDs) motion, which was discussed in section 3.4.3 of Chapter 3. As shown in figure 4.35e, the extrinsic secondary GBDs are generated at the boundary plane and move along the boundary to allow Grain B to grow into Grain A [159]. This model could explain the grain boundary migration observed in the cantilever tests (schematically shown in figure 4.35f). However, the other (second) type of grain boundary migration (coupled with sliding) claimed by Puttick et al. [168] occurring on the surface normal to the sliding direction was not observed in the cantilever tests. No grain boundary migration was found on the top surface of the cantilever after a step was formed due to sliding. Puttick et al. [168] attributed this second type of migration to the reduction in free surface energy after the step was formed. Therefore, the steps along the grain boundary in their studies were usually rounded, in comparison to the sharp steps found in the cantilever tests. This could be explained by the extremely high homologous temperature used in their bi-crystal experiments. The boundary migrated on the top surface due to its high mobility, which might not be related to sliding.

Compared to Micro-bicrystals

In comparison to the micro-pillar design used in Gong et al. [140] in tin and Aitken in aluminium [134] (detailed in the literature review, section 2.7.3), the micro-cantilever design (tested as close to the grain boundary as possible) enables the largest possible resolved shear stress on the grain boundary plane for a certain load. Further comment from the mechanical point of view is that the strain measurements in the micro-pillar design could be misleading [134], because the deformation at the bottom of the pillar is not considered but could be significant. In the cantilever design, the shear stress is significant compared to the normal stresses

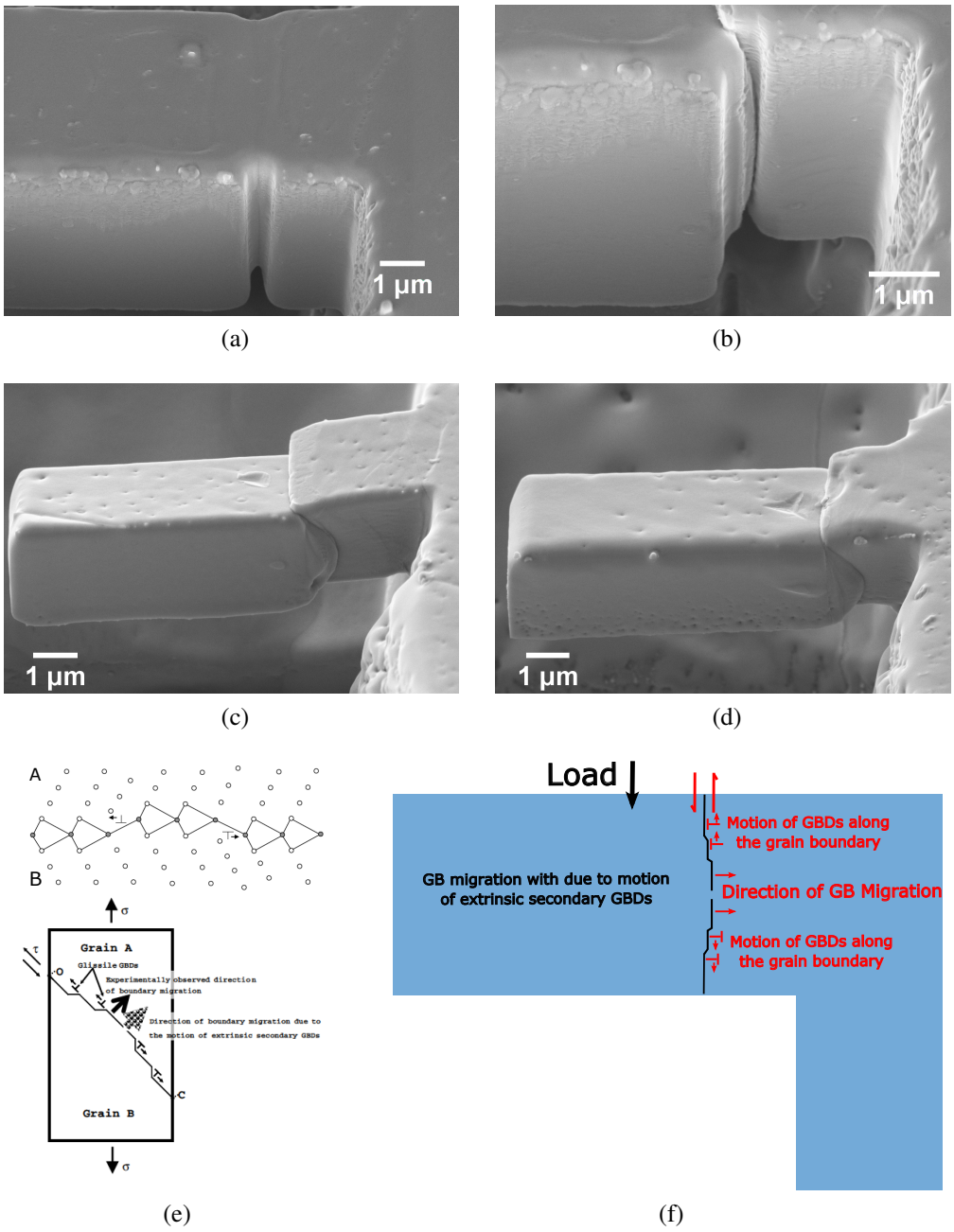

Figure 4.35: (a) A side view of the straight grain boundary restrained in the groove before testing. (b) After testing, the boundary has migrated normal to the boundary plane towards the unloaded grain. (c) and (d) show two examples of sliding coupled with significant migration that occurred to grain boundaries not restrained in grooves. (e) A model of grain boundary migration due to extrinsic secondary GBDs proposed by Sheikh-Ali [159]. (f) Application of the model to the experimental results of the cantilever tests.

on the grain boundary plane. Therefore, the effect of plastic yielding of the cantilever on the sliding behaviour is minimal. However, in both micro-pillar tests mentioned above, the compressive stress is much higher than the resolved shear stress on the grain boundary plane. Therefore, evidence of crystallographic slip was observed in both single- and bi-crystals of tin micro-pillars [140]. For the large pillars (~5 μm), the critical compressive stresses at the onset of plastic deformation were comparable between the single- and bi-crystals, which suggests that crystallographic slip was the dominant deformation mechanism for this sized sample. This was confirmed by the SEM characterisation that the contribution of grain boundary sliding to the total deformation was only ~10% for the large pillars, but not so for the smaller pillars [140]. A remarkable size effect was seen by Gong et al. [140], but this was not examined in the present cantilever study. In contrast, in the present study using cantilevers, the lengths of the steps on the grain boundary after sliding are comparable to the total displacements of the nanoindenter. This indicates quite high contributions of sliding to the total deformation. Furthermore, the threshold or steady-state shear stresses for grain boundary sliding measured in the Sn-Bi cantilever tests are comparable to those measured in the pillars for similar sized bi-crystals of tin. This is illustrated in figure 4.38 of sliding rate against stress to be shown later (cantilever: 15~30 MPa for 10~20 nm/s sliding rate; pillar: around 30 MPa for 20 nm/s sliding rate).

4.3.3 Diffusion Creep at the Grain Boundary

Diffusion creep is driven by stresses normal to the grain boundary plane and matter transfers from the region in compression (bottom) to that in tension (top). In contrast, grain boundary sliding is driven by the shear stress along the grain boundary plane. For long cantilevers (5 × 20 μm), the FEA results (listed in table 4.8) indicate that normal stresses are significantly larger than the shear stress on the grain boundary plane. Therefore, diffusion creep might be more favourable than grain boundary sliding. The load-displacement curve in figure 4.33a shows an abrupt drop in load, which is distinguishable from the strain-hardening phenomenon

	Tensile Stress on Top of Grain Boundary	Compressive Stress on Bottom of Grain Boundary	Shear Stress on the Grain Boundary
Long Cantilever 01 (at 40 μN)	72 MPa	133 MPa	2.3 MPa
Long Cantilever 02 (at 35 μN)	60 MPa	110 MPa	2.1 MPa

Table 4.8: Normal and shear stresses of the grain boundary at the maximum load for the two long cantilevers.

widely seen in the dislocation-mediated plastic deformation of the cantilever [104, 110, 109]. However, dislocation motion might still be involved in the deformation of the cantilever, and the drop in load could be explained by grain boundary acting as a good source and sink for dislocations. The fact that the load tended to level off towards the end of the test indicates that a stable diffusion creep process might have taken place (diffusion creep at a constant load/stress seen in Sn-Pb [169, 170]). Furthermore, new material seemed to plate out at the grain boundary on the top surface (figure 4.33e), which suggested that diffusion creep could have occurred at the grain boundary.

Due to the high concentration of defects of the grain boundary structure, it is the preferential pathways for diffusion [171]. Upon loading at the free end, matter transferred along the grain boundary from the bottom of the grain boundary to the top as shown in the schematic diagram in figure 4.36a. This would cause the beam to tilt abruptly at the grain boundary. The angle formed by the grain boundary and new plated material, θ, and the cantilever deflection angle, δ, could be calculated using equation 4.11 and 4.12, respectively. The width of new material plated on the grain boundary (Δl) was measured by comparing the SEM images before (figure 4.36c) and after testing (figure 4.36d). The distance from top surface to the "middle plane" (dividing the triangular cross section into two halves with an equal area) could be calculated as shown in figure 4.36b. The parameters (Δl, h d and L) were measured for several times to average as shown in table 4.9.

$$\tan\theta = \frac{width\ of\ new\ material\ plated\ on\ GB}{distance\ from\ top\ surface\ to\ half-area\ plane} = \frac{\Delta l}{h} \tag{4.11}$$

$$\tan\delta = \frac{deflection\ of\ cantilever}{distance\ from\ loadpoint\ to\ GB} = \frac{d}{L} \tag{4.12}$$

The angle formed by the grain boundary and new plated material was calculated to be much larger than the deflection angle, i.e. $\theta > \delta$. However, the deflection displacements were measured from the total displacement of the nanoindenter (subtracting the depths of the indenter markers), which did not take into account of the thermal drift. For tests at such a low displacement rate and long time, the thermal drift effect on the actual displacement could be notable. Therefore, the measurements of d and δ have underestimated the actual deflection displacements of the cantilevers. Furthermore, since the amount of material plated out on the grain boundary was not clear on the SEM images, the measurements of Δl and θ probably overestimated the actual volume of matter transfer. Even though the measured δ and θ didn't match perfectly, there was a clear trend that the amount of material plated out on top of the grain boundary increased with the deflection displacement of the cantilevers (i.e. larger d and Δl for Cantilever 01 compared to 02). This indicates the model based on diffusion creep shown in figure 4.36a could partially describe the deformation process.

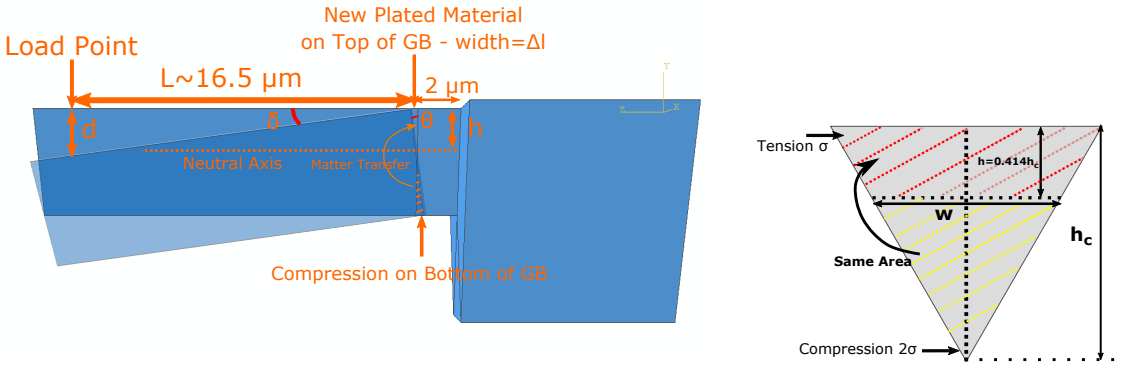

(a) (b)

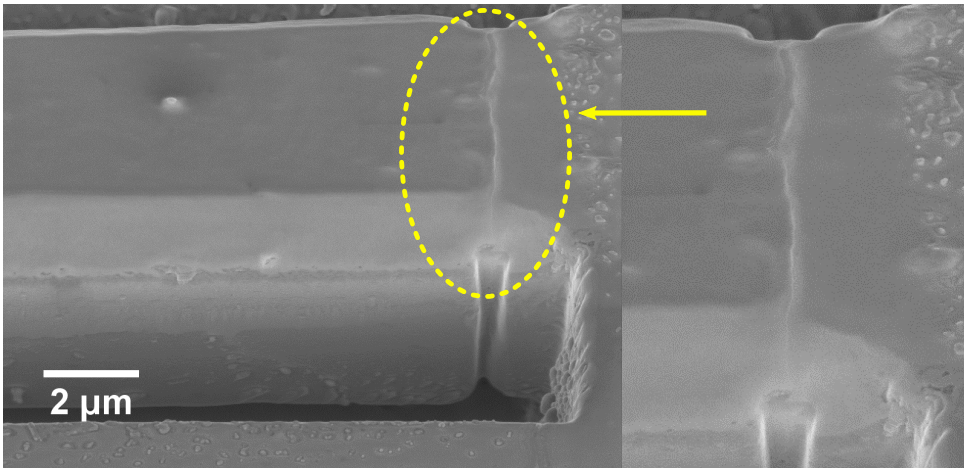

(c) Before Test

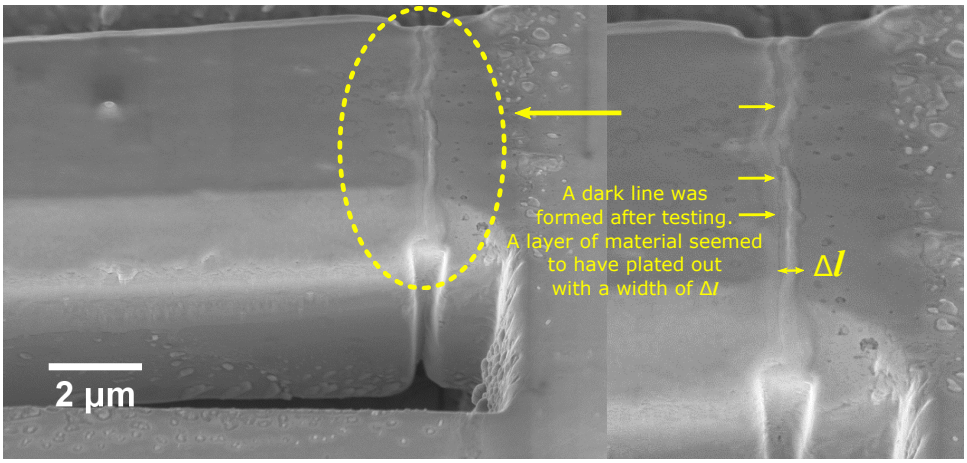

(d) After Test

Figure 4.36: (a) A schematic diagram of the long cantilever before and after the diffusion creep test. (b) Cross-sectional view of the grain boundary plane. (c) and (d) are side-view images before and after testing, respectively, to show the possibility of new material plated out on the top surface at the grain boundary.

	Δl (μm)	h (μm)	d (μm)*	L (μm)	δ (°)	θ (°)
Cantilever 01	0.21	2.38	0.60	16.51	2.1	5.0
Cantilever 02	0.10	2.42	0.40	17.32	1.3	2.4

Table 4.9: Measurement and calculation of the cantilever deflection angle and the tilt angle of the grain boundary plane before and after tests. *The deflection displacement was measured by subtracting the depth of the indenter marker from the total displacement of the nanoindenter.

4.3.4 Diffusion Creep vs. Grain Boundary Sliding

The shear stress against displacement responses of long and short bi-crystal cantilevers on the same grain boundary (23.0° [0 -1 1]) are compared in figure 4.37a. Two long and two short cantilevers were included in the graph to show the reproducibility. The shape of the stress-displacement curves are quite similar to each other. On the one hand, the short cantilevers have a higher shear stress on the grain boundary plane than the long cantilevers. On the other hand, as predicted by the FEM results (listed in table 4.10), the short cantilevers (loaded at 1 μm from the grain boundary) do not have a normal stress gradient at the grain boundary needed for diffusion creep. In contrast, the long cantilevers (tested at the free end) have much larger normal stress gradients that could drive the diffusion creep to occur at a relatively high rate.

Upon loading, the short cantilever reached the threshold shear stress for grain boundary sliding before diffusion creep, and therefore had steady-state grain boundary sliding (figure 4.37b). The long cantilever reached the threshold normal stresses for diffusion creep before grain boundary sliding, thereby having diffusion creep at the grain boundary (figure 4.37c). In the conversional macro-mechanical tests on polycrystals, diffusion creep and grain boundary sliding are almost always coupled with each other [57]. Using the micro-mechanical testing method, the two processes could have been investigated individually and separately. The similar shapes of the load-displacement curves suggested that both grain boundary sliding and diffusion creep occurred at a high load/stress at the beginning and then stabilised to a steady-state

	Tensile Stress on Top of Grain Boundary	Compressive Stress on Bottom of Grain Boundary
Short Cantilever 01 (at 30 μN)	3 MPa	5 MPa
Short Cantilever 02 (at 45 μN)	4 MPa	7 MPa
Long Cantilever 01 (at 40 μN)	72 MPa	133 MPa
Long Cantilever 02 (at 35 μN)	60 MPa	110 MPa

Table 4.10: Normal stresses on the grain boundary plane at the maximum load for the short and long cantilevers (predicted by FEM).

load/stress. However, the grain boundary sliding rate was an order of magnitude faster than diffusion creep. This is in agreement with the studies on bi-crystals of tin that grain boundary sliding could occur at very fast rates as long as the the grain boundaries were free from intersections by irregularities and slip bands [60]. As for diffusion creep, it usually occurs at very low stress ($0.1 \sim 10\,MPa$) and strain rates ($10^{-4} \sim 10^{-9} s^{-1}$) [169]. The distinguishable stress conditions for the short and long cantilevers (exhibiting grain boundary sliding and diffusion creep, respectively) suggest that in order for diffusion creep to occur at a similar rate as grain boundary sliding, the stresses had to be at least an order of magnitude higher. In conclusion, the apparent grain boundary sliding displacements seen in the short cantilever tests were not due to diffusion creep.

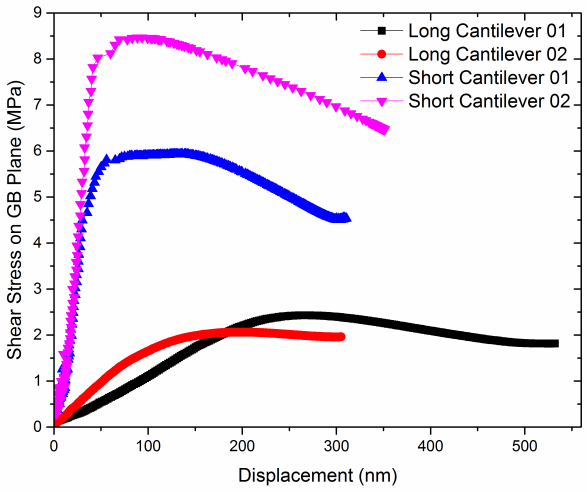

(a)

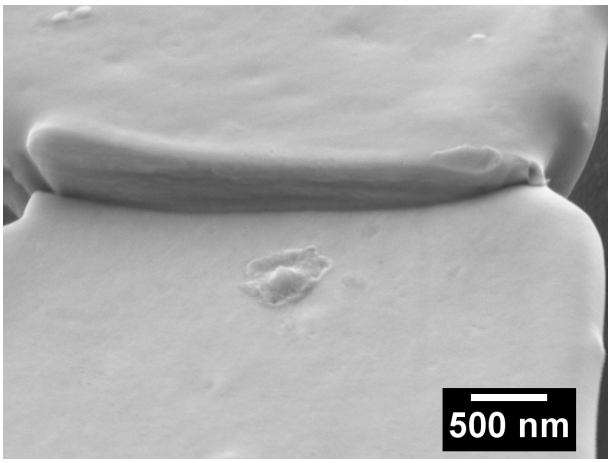

(b)

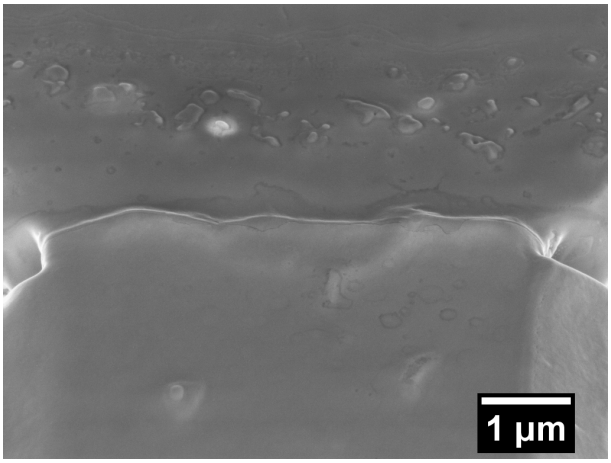

(c)

Figure 4.37: (a) Comparison of the shear stress against displacement curves for the short and long cantilevers. (b) SEM image of the short cantilever that had grain boundary sliding driven by the high shear stress. (c) SEM image of the long cantilever that had diffusion creep but no sliding at the grain boundary.

4.3.5 Grain Boundary Sliding and Diffusion Creep Rate

Grain Boundary Sliding Rate

For those short cantilevers that exhibited grain boundary sliding, the rate of stable sliding is plotted against the stress (at steady state) in figure 4.38 with logarithmic scale. A dashed line with a gradient of $n = 1$ is also illustrated in the graph. It can be seen that the gradient of any segment of the curves for the micro-cantilevers is larger than 1. This indicates that grain boundary sliding occurs at a higher rate than that expected for diffusion creep. Furthermore, the sliding rate could be compared with the empirical equations proposed by Puttick et al. [59] and Tuck [60]. Their equations are in the same form as shown in equation 4.13, where v is the initial sliding rate, σ is the applied shear stress, n is the stress exponent, A is a constant of the order of 10^{-5} $(cm/s)(dyn/cm^2)^{-n}$, Q is the activation energy for grain boundary sliding, R is the gas constant and T is the absolute temperature [60]. The microcantilever testing conditions and data are compared with those of Tuck's study in table 4.11. Despite the large differences in the testing condition, the stress exponent (n) and initial sliding rate (v) are reasonably comparable and in the same order of magnitude. It should be noted that even though there was a slight decrease from the initial to the steady-state sliding rate, there was no significant slowdown in grain boundary sliding in the microcantilever studies. However, the so-called "slide hardening" effect was widely found in large bi-crystals [60, 79, 168, 172]. This was probably due to the large size of the grain boundary in those bi-crystal samples, which contained more irregularities on the grain boundary and required more accommodation to overcome the barriers to sliding.

$$\upsilon = A\sigma^n \exp(-Q/RT) \tag{4.13}$$

Bi-crystal Sn	n	$v\,(nm/s)$	$\sigma\,(MPa)$	T (°C)
Tuck [60]	2.5~3.1	0.5~55	0.10~0.18	200~230°C
Cantilevers in the current study	1.9~3.5	0.1~40	4~30	23°C

Table 4.11: Comparison of grain boundary sliding rates of the (short) cantilevers with Tuck's studies on bi-crystals of tin.

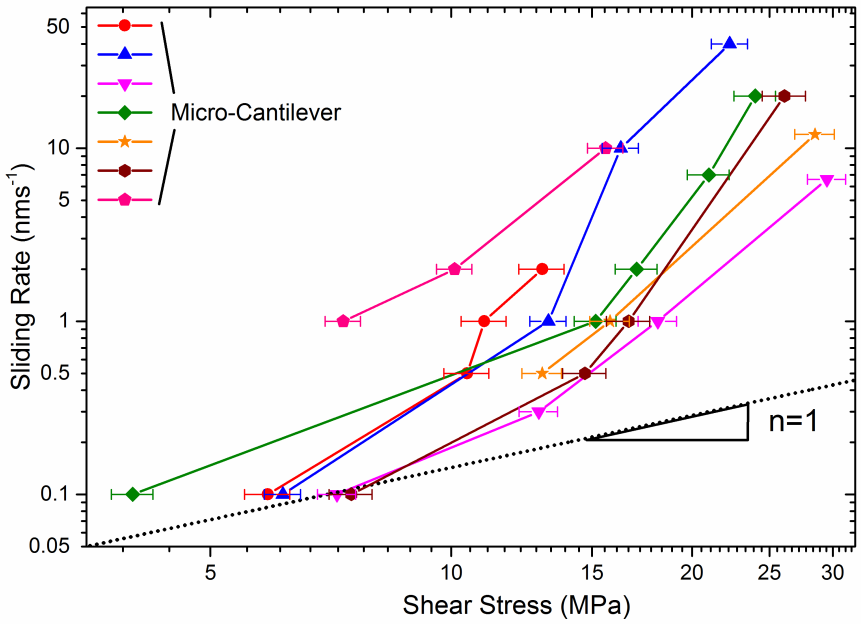

Figure 4.38: Grain boundary sliding rate - shear stress curves of a few short cantilevers tested at various displacement rates. The slope of any segment of a curve is over 1, which is the theoretical stress exponent for diffusion creep.

Diffusion-Controlled Deformation

Table 4.12 shows the grain boundary self-diffusion coefficients either experimentally measured [173, 174] or calculated from the stress and strain-rate data on tin-based materials using the Coble creep equation [167, 169]. Coble creep occurs by grain boundary diffusion. It can be seen that the measured or calculated diffusion coefficients of Sn-Bi and Sn-Pb are one to two orders of magnitude larger than the diffusivities in pure Sn ~ $6.2 \times 10^{-13} m^2 sec^{-1}$ [173]. This indicates that the addition of Bi in Sn could have significantly increased the grain boundary

diffusivity. Using the diffusion coefficients listed in table 4.12, the diffusion creep rate of the long cantilevers can be evaluated as follows.

As shown in figure 4.39, when a stress is applied to the cantilever, the top of the grain boundary is in tension (σ) and the bottom in compression ($\sim 2\sigma$). The concentration of vacancies increases in the top and decreases in the bottom of the grain boundary by the factors C_v^+ and C_v^-, respectively [175]. This is because when a stress is applied, the energy to form vacancies changes by $-\sigma\Omega$, where Ω is the atom or vacancy volume. There is a vacancy flux J from the top to bottom of the grain boundary and an atom flux in the opposite direction. According to Fick's first law of diffusion (equation 4.14), the diffusion flux is driven by the vacancy concentration gradient, $\frac{dC}{dx}$. The diffusion path, Δx, is approximately the distance from the top (maximum tension) to the bottom (maximum compression) of the cantilever, i.e. the height of the cantilever h_c.

$$J = -D_v \frac{dC}{dx} \approx D_v \frac{C_v^+ - C_v^-}{h_c} \approx D_v \frac{C_0 \exp(\frac{\sigma\Omega}{kT}) - C_0 \exp(\frac{-2\sigma\Omega}{kT})}{h_c} \tag{4.14}$$

where k is the Boltzmann constant, D_v is the vacancy diffusion coefficient in the grain boundary, C_0 is the equilibrium vacancy concentration and Q is the activation energy [40]. Since for small stresses, $\sigma\Omega \ll kT$, therefore $\exp\left(\frac{\sigma\Omega}{kT}\right) = 1 + \frac{\sigma\Omega}{kT}$. Then equation 4.14 is simplified to equation 4.15 ($D_b = \Omega C_0 D_v$ [40]).

$$J \approx D_v \frac{C_0(1 + \frac{\sigma\Omega}{kT} - 1 - \frac{-2\sigma\Omega}{kT})}{h_c} \approx D_v \frac{3C_0\sigma\Omega}{h_c kT} = \frac{3D_b\sigma}{h_c kT} \tag{4.15}$$

The volume of diffused material per unit time ($\frac{dV}{dt}$) through an area, A , could be calculated using the diffusion flux ($A = \delta w$, where δ is the grain boundary width, w is the width of the "middle plane" that divides the triangular cross section into two halves with an equal area as shown in figure 4.36b). Using $\sigma = 60\,MPa$, $\delta = 0.7\,nm$, $\Omega = 2.7 \times 10^{-29}\,m^3$ [169]:

$$\frac{dV}{dt} = J \cdot A_c \cdot \Omega = J \cdot \delta w \cdot \Omega \approx \frac{3D_b\sigma\delta w\Omega}{h_c kT} \approx 1.3 \times 10^{-20} \sim 4.2 \times 10^{-22}\,m^3 s^{-1}$$

The volume of diffused material could be related to the width of new material plated on top of the grain boundary – Δl in equation 4.16, where h is distance from top surface to the "middle plane" as shown in figure 4.36b, and w_{gb} is the total width of the grain boundary on the top surface.

$$\begin{aligned} \frac{dV}{dt} &= \frac{1}{2} \cdot \frac{dl}{dt} \cdot h \cdot w_{gb} \\ \frac{dl}{dt} &= \frac{dV}{dt} \cdot \frac{2}{h w_{gb}} \end{aligned} \tag{4.16}$$

This calculation is based on the approximation of the geometry of new diffused material as a regular triangular prism. The calculated values of $\frac{dl}{dt}$ using different D_b values in the literature are attached to table 4.12. Given the time of the test as ~ 3000 seconds, the predicted width of plated material is calculated in the table as well, which could be compared to the experimentally observed width – $0.1 \sim 0.2$ μm. The pure tin grain boundary diffusion coefficient experimentally measured by [173] seemed to give a predicted value comparable to the observed width. The predicted widths of plated material using the Sn-Bi or Sn-Pb grain boundary diffusion coefficients were much too large compared to that observed.

In summary, the observed amount of new material plated out on top of the grain boundary was lower than that predicted by the diffusion creep model. The classic diffusion creep model assumes that grain boundaries are perfect sources and sinks for vacancies and therefore the diffusion rate of vacancies/atoms is rate controlling. The fact that the predicted diffusion rate is much faster than that observed indicates that there are other processes essential to diffusion creep becoming rate controlling [53]. This might include the creation or annihilation of vacancies at the grain boundary, which was quoted as the "interface reaction" by Schneibel and Hazzledine [169].

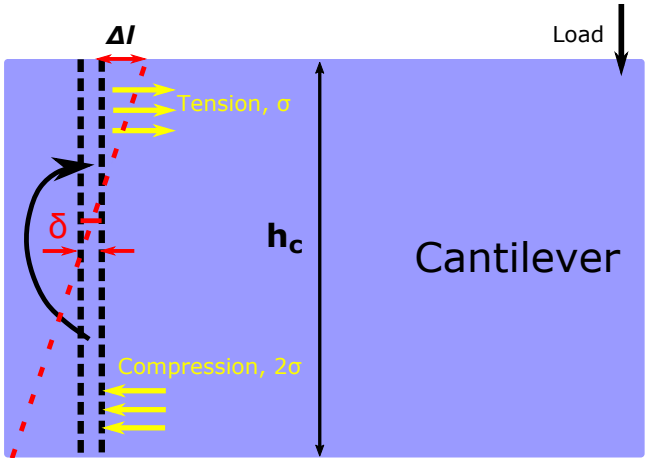

Figure 4.39: A side view of the grain boundary region of the long cantilever. A schematic diagram of the diffusion path from the bottom to top along the grain boundary.

GB Diffusion Creep in tin	GB self-Diffusion Coefficient $D_b\ \left(m^2 sec^{-1}\right)$	$Q(kJ/mol)$	Material Plating Rate $\frac{dl}{dt}\ \left(nmsec^{-1}\right)$	Width of Plated Material $dl\ (\mu m)$
Pure Sn ([173])	6.22×10^{-13}	40	0.1	0.28
Sn-5wt% Bi [167]	3.82×10^{-12}	42	0.6	1.73
Sn-2%wt Pb [169]	1.04×10^{-11}	42	1.6	4.71
Sn-Bi ([174])	1.93×10^{-11}	76	2.9	8.73

Table 4.12: List of grain boundary diffusion coefficients of tin found in the literature (at $T = 298K$). Using these coefficients, corresponding calculations were made on the width of plated material on the grain boundary on the top surface of the cantilever.

4.4 Conclusions

Based on the results and discussion, the following conclusions can be drawn:

- During the microcantilever tests, the initial contact between the indenter and sample surface is to make an indent impression. The shear stress on the grain boundary gradually increases to a critical shear stress to initiate grain boundary sliding. During grain boundary sliding, the load always drops gradually and the shear stress tends to be relatively stable due to the reduction in the grain boundary area.

- The initial grain boundary sliding rate is usually higher than the target displacement rate. The sliding rate stabilises towards the end of the test. No evident bending is found in the cantilevers with slid grain boundaries.

- Repeated tests on the same cantilever under nominally identical conditions have illustrated reasonable reproducibility. In some cases, the scatter in the steady-state shear stresses is larger than the errors propagated from load measurements.

- A few pairs of cantilevers on the same grain boundary were manufactured and tested under nominally identical conditions. With the same grain boundary plane, each pair of cantilevers show similar steady-state shear stresses (with similar scatters as the aforementioned repeated tests). However, a significant difference has been found between pairs of cantilevers with different grain boundary plane orientations.

- Micro-mechanical tests were carried out on individual grain boundaries with various characters (misorientation angle, rotation axis and grain boundary plane orientation). The different steady-state shear stresses show that these grain boundaries differ in their participation in sliding.

- A special boundary — twin boundary proved to be resistant to sliding.

- For longer cantilevers (the aspect ratio is large), loaded at 18 μm from the grain boundary, FEM analysis has revealed that normal stresses are much larger than the shear stress on the grain boundary. Therefore, diffusion creep should be more favourable than grain boundary sliding.

- For short cantilevers, as the load point moves towards the grain boundary, FEM shows that the tensile and compressive stresses on the grain boundary decrease dramatically. However, the shear stress on the grain boundary does not change much with the load point.

- The diffusion creep tests on the long cantilevers were carried out under displacement control. The load drops initially and tends to level off towards the end of the test. The SEM images indicate a vague contour of new material plated out on top of the grain boundary. However, the experimentally observed diffused material is much less than that predicted by the classical diffusion creep models based on grain boundary diffusion.

Chapter 5

3D X-ray Diffraction Contrast Tomography (DCT) Analyses of a Sn-Bi Alloy During In-situ Tensile Tests

Overview:

The main microstructural attributes of superplasticity that have been observed are: grain rearrangement and neighbour switching, grain boundary sliding and relatively small, transient changes in grain shape as grains slide over one another [5]. There are a number of more subtle attributes that suggest an underlying complexity to the process, which include strain induced grain growth [176] and grain rotation [177]. Careful examination of the grain boundary sliding has shown that it is spatially inhomogeneous, with some grain boundaries sliding more than others, often with a number of interconnected boundaries sliding extensively in a cooperative manner [178]. These are all observations made from two-dimensional (2D) sections at the surface. However, grain boundary sliding occurs in three dimensions (3D), and the surface studies may not represent the behaviour of the bulk. In addition, most mechanical tests were carried out in tension, the surface area is not constant and many grains emerge from beneath the surface, which makes it difficult to follow grains to large strains. What is more, the surface material is

usually affected to some extent by the sample preparation processes, such as cutting, polishing, etching, etc. The real grain boundary sliding behaviour can only be represented by the bulk material. Furthermore, the change in constraint on-going from surface to interior is so large that measurements in the interior are required. Therefore, it is important to confirm that the mechanisms of grain boundary sliding seen at the surface (e.g. grain neighbour switching) still happen in the bulk, and thereby explain its role in superplastic deformation and the kinetics of the process.

A number of techniques have been developed to look into the characteristics of bulk microstructures, such as three-dimensional X-ray diffraction (3DXRD) and 3D X-ray tomography. Combining the concepts of image reconstruction from projections (tomography), X-ray diffraction imaging (topography) and 3DXRD techniques, X-ray diffraction contrast tomography (DCT) was developed as a 3D non-destructive tomographic imaging approach [179]. The X-ray beam interacts with the sample material and produces both transmitted and diffracted beams, which are recorded on a high resolution X-ray imaging detector. DCT enables simultaneous access to 3D grain shape, grain orientation and local X-ray attenuation of individual grains in polycrystalline materials [180]. Integrated with other characterisation techniques and in-situ mechanical testing, DCT has been applied to follow the evolution of microstructure occurring in the bulk material, such as grain size and shape [181], grain boundary network [182], intergranular stress corrosion cracking [183, 184], short fatigue crack propagation [185], secondary phase precipitation on grain boundaries [186] and twinning deformation [187]. One of the most used techniques to be coupled with DCT is propagation-based phase contrast tomography (PCT). In contrast to the conventional absorption radiography, propagation-based PCT provides higher contrast images (for the same X-ray dose) based on the variations in the X-ray phase [188]. PCT is usually applied to microstructural characterisation (e.g. revealing grain boundaries), which requires second phase decoration of the grain boundaries [180].

The aim of the DCT experiment described here is to fully describe, at the level of the crystalline grain microstructure, and in three dimensions, the mechanisms that occur during superplastic

deformation. A Sn-1%Bi alloy (single phase) was selected for the study as it exhibits superplasticity at room temperature. Grain boundary sliding is one of the dominant deformation mechanisms of superplasticity and high temperature creep. The occurrence of grain boundary sliding can be observed and measured from 2D sections by carrying out surface studies as discussed in the literature review, but this does not necessarily reflect the bulk material. The experiment was carried out on the beamline - ID11, European Synchrotron Radiation Facility (ESRF), in collaboration with Dr Samuel McDonald from the University of Manchester. Diffraction contrast tomography (DCT) was used to map the shapes and centroid positions of the individual grains contained within a Sn-1%Bi alloy during in-situ tensile loading, thereby measuring the evolution of grain volume and grain boundary sliding as well as searching for grain neighbour switching in three dimensions and in the bulk of samples for the first time.

5.1 Materials and Experimental Methods

There are a few requirements on the material and experimental conditions used in these DCT experiments on superplasticity as follows:

1. On the one hand, the grain size must be fine enough to enable superplasticity to occur at room temperature. The typical critical grain size for superplasticity is 10 μm. However, at sufficiently low strain rates, materials with slightly larger grain sizes (10~20 μm) could still exhibit superplasticity.

2. On the other hand, grains must be large enough to be reconstructed in DCT. The current reconstruction technique requires the grain size to be larger than 10 μm in the undeformed state. Furthermore, annealed specimens are usually required in order to obtain clear diffraction patterns. However, annealing usually leads to coarser grains.

3. The strain rate must be low enough to exhibit superplasticity, especially for the slightly coarser-grained material.

4. However, the strain must also be large enough to induce grain neighbour switching. A

true strain of 0.55 is required to show grain neighbour switching based on Lee's model [46]. Therefore, due to the limited synchrotron beam time, the strain rate must be high enough to achieve relatively high strains.

5. The volume of the sample gauge (width and thickness) must be small enough to have a limited number (typically a few hundreds) of grains in each slice illuminated by the X-ray beam. The whole dimension of the tensile test piece is also limited by the in-situ micro-mechanical testing device.

In summary, the strict requirements on this experiment make it difficult, because some factors push towards fine grain sizes and low strain rates, while others pull towards the complete opposite, i.e. larger grains and higher strain rates. Thus, there is a very small window for success of the experiment. However, the microstructure of the specimen could be carefully designed to fit in the narrow window between superplasticity and DCT. With six days of beam time, there was still the possibility of reaching a high strain with relatively low strain rates. Furthermore, no such 3D studies have been made previously on superplastic deformation in the bulk material. Therefore, the following attempts were made to perform a DCT investigation on a superplastic material during an in-situ tensile test.

5.1.1 Materials and Sample Preparation

The material was manufactured using the same procedure as that used in the macro-shear test described in Chapter 3, i.e. through casting, homogenisation, cold extrusion (using ice instead of liquid nitrogen) and rolling (to a thin sheet of 0.4~0.5 mm thickness). The test pieces were in the form of 'dog-bone' shaped tensile specimens as shown in figure 5.1a. The gauge length was 1.5 mm, measured from the length of the central section with parallel sides (excluding the curved edges). The tensile specimens were machined from as-rolled thin sheet on a waterjet cutter (acknowledgements to Mr Robin Vincent) as shown in figure 5.1b. The sheet was adhered to a plywood substrate using a strong double-sided tape. A computer-aided design

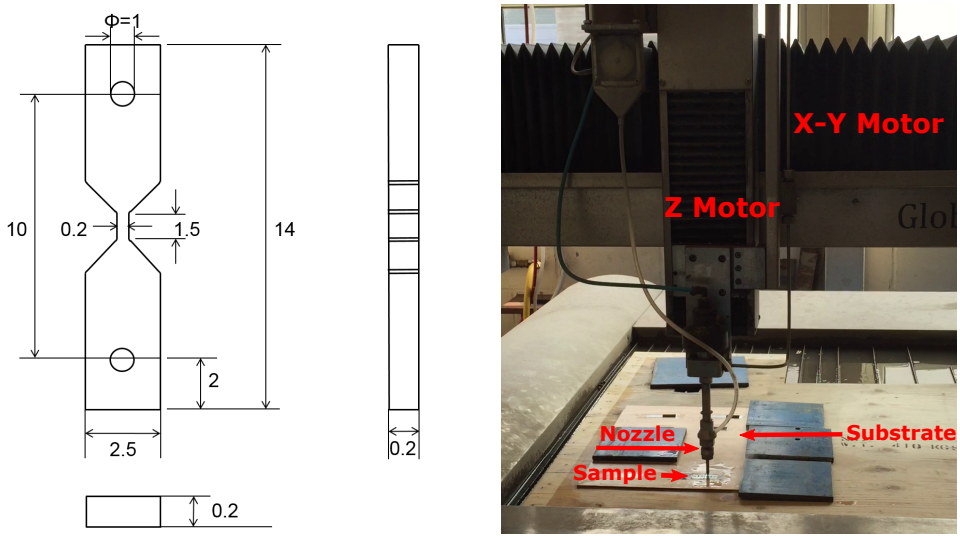

(a) (b)

Figure 5.1: (a) Dimensions of the specimen for in-situ micro-mechanical testing with X-ray diffraction contrast tomography. (b) A waterjet cutter was used to machine the specimens.

(CAD) drawing was created and used to control the waterjet cutting. Conventional Electrical Discharge Machining (EDM) is not suitable for tin due to the low melting point of the material. The heat generated during EDM would affect the microstructure of the specimens. Since tin is a relatively soft metal, a waterjet cutter is a good solution to the manufacture of "dog-bone" test pieces. High pressure water comes out of the nozzle and cuts through the sample. The constantly flowing water effectively cools down the specimen while cutting. Therefore, the fine microstructure was retained after cutting.

The as-cut specimens are shown in figure 5.2a. The thin sheet could accommodate three "dog-bone" specimens to be cut in a row. The specimens were attached to each other on both ends so as not to drop off during cutting. The specimens were released from the substrate by an adhesive-removing solvent. A scalpel was then used to cut the specimens into individual test pieces, which were then adhered to a polishing plate as shown in figure 5.2b. The specimens were ground and polished carefully to achieve the desired thickness (0.2 or 0.3 mm) for DCT scans. The cutting debris on the edges was also ground off to a gauge width of 0.2 or 0.3 mm. Using the procedure described in section 3.1.2 (Chapter 3), the specimens were ground with silicon carbide papers to a 4000 grit finish and then polished using 6, 3 and 1 μm alumina

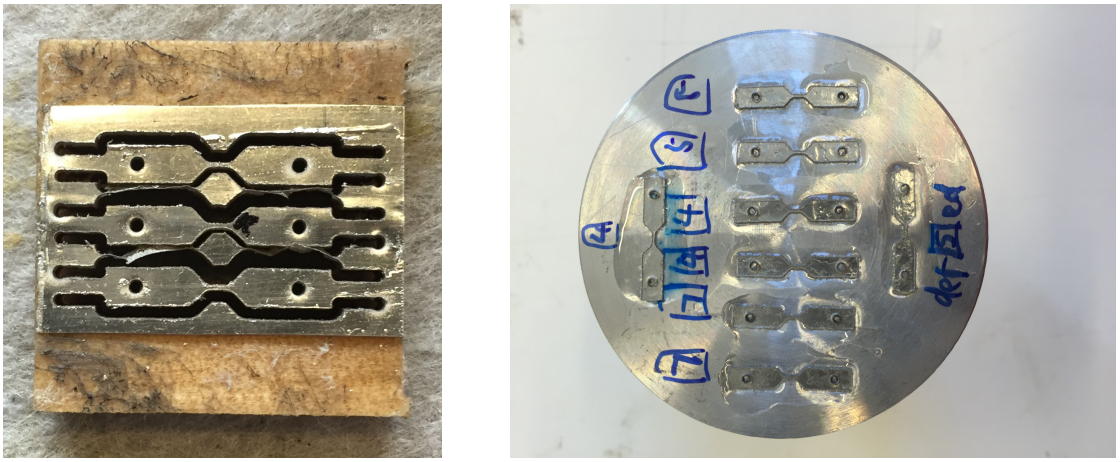

(a) (b)

Figure 5.2: (a) Image of three as-cut samples attached to the plywood substrate. (b) The samples were adhered to a polishing plate (made of aluminium) for grinding and polishing. The final cross-section of the gauge was a square of 0.2×0.2 or 0.3×0.3 mm^2.

suspensions. Finally, 40 nm γ-alumina suspension was used to achieve an almost scratch-free finish.

5.1.2 Microstructural Characterisation

Since the requirement of grain size on this material was between 10~20 μm, the billet was submerged in ice instead of liquid nitrogen (for ultra-fine grain size below 10 μm). The microstructure of the extrusion was characterised by EBSD as shown in figure 5.3a. The threshold misorientation angle to define a grain is 4°. The deformation twins might be caused by extrusion or polishing. The average grain size (by area fraction) of the as-extruded specimen was 19.8 μm (figure 5.3b). This extrusion sample was taken from the middle of the extruded wire, which was free from the extrusion defects at the ends. After rolling and waterjet cutting, the specimen was characterised again in the SEM as shown in figure 5.3c. It could be seen that the dimension of the specimen was approximately as desired, i.e. 0.3×0.3 mm^2.

The grain size of the specimen had just reached the target range (10~20 μm) and the dimension of the cut was as required. However, there were problems with EBSD characterisation on the as-cut specimen. Only a local area could be characterised by EBSD as shown in figure 5.4a

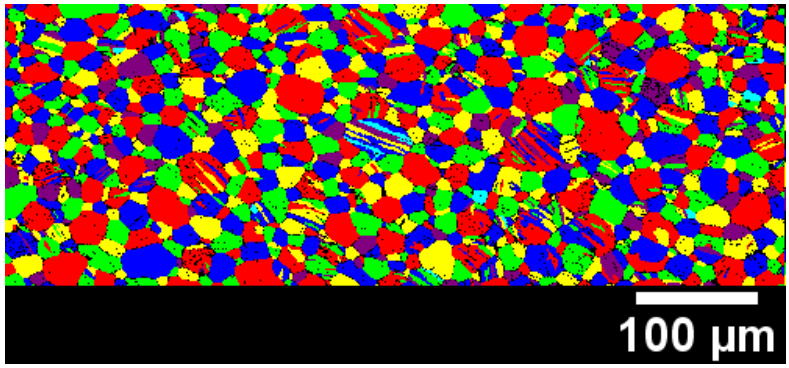

(a)

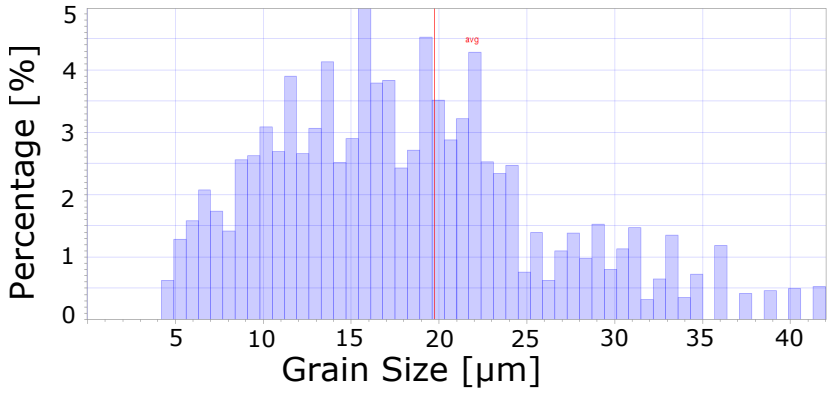

(b)

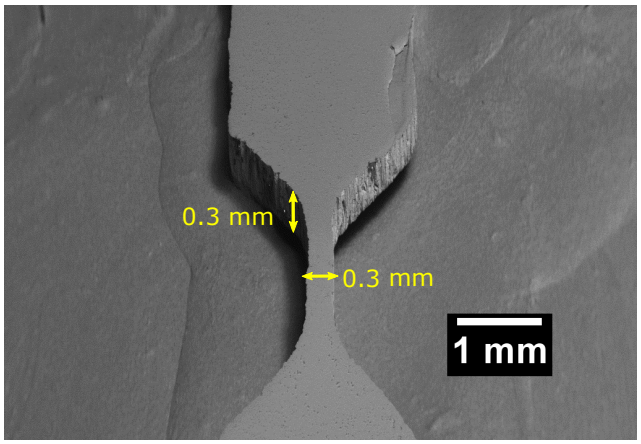

(c)

Figure 5.3: (a) EBSD analysis on the extrusion sample reveals a fine-grained microstructure. The colours were assigned randomly independent of the grain orientation. (b) Grain size distribution of the as-extruded sample. (c) The as-cut specimen in the SEM.

with a poor pattern quality. This is a grain misorientation average (MO average) map, which illustrated the average value of the orientation deviation from the average orientation for each grain. The relatively high MO values on the whole specimen indicated that it had a large amount of stored dislocation density, which was a result of rolling, waterjet cutting, polishing and even handling (due to its delicate size and low strength). In order to assess the suitability of the specimens for the synchrotron DCT experiment, they were tested on the laboratory DCT (LabDCT) equipment (refer to section 5.1.3.1). As shown in figure 5.4b, the diffraction spots were mostly along the radial direction. Those patterns could not be indexed unambiguously as the diffraction spots spanned across many orientations. This indicated the specimen was not ready for DCT due to its large mosaicity (orientation spread inside grains).

Therefore, annealing was required to reduce the intragranular plasticity. The specimens were annealed at 140°C for 60 minutes in a tube furnace with Argon inert atmosphere, before the EBSD characterisation. The MO average map after annealing (figure 5.4c) showed that intragranular disorientation had been significantly reduced. This was attributed to the annihilation of the dislocation structure during annealing. Similarly, the LabDCT diffraction spots after annealing were mostly along the tangential direction, which corresponds to only one orientation (figure 5.4d). This indicates that DCT would work better on the annealed specimen. EBSD on the as-annealed sample showed that the average grain size was 20.2 μm (from the Bruker software in figure 5.4e). The threshold angle to define grains was 4°, and there were few subgrains in the annealed specimens. The distribution histogram in figure 5.4f showed a large spread of grain sizes. The mean grain size was averaged from some grains that had grown to 40~50 μm, and many small grains of around 10 μm or below. This batch of specimens was used in the in-situ tensile tests coupled with DCT.

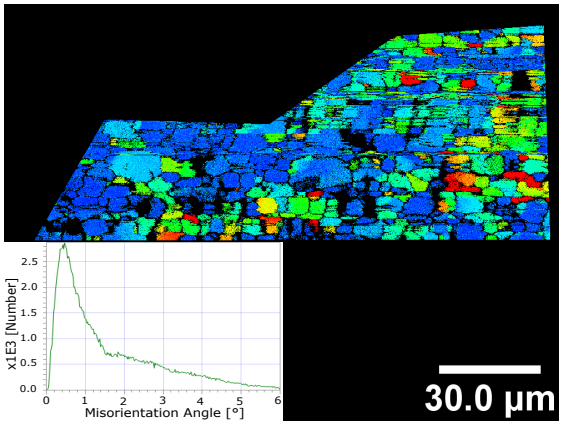

(a) Before Annealing

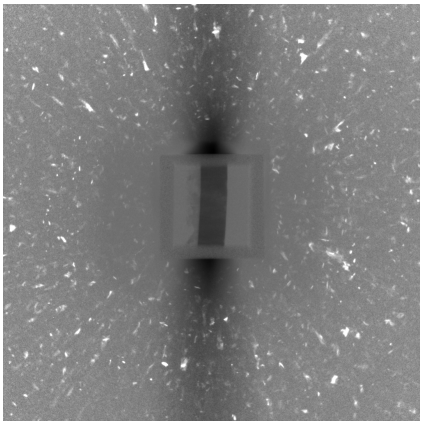

(b) Before Annealing

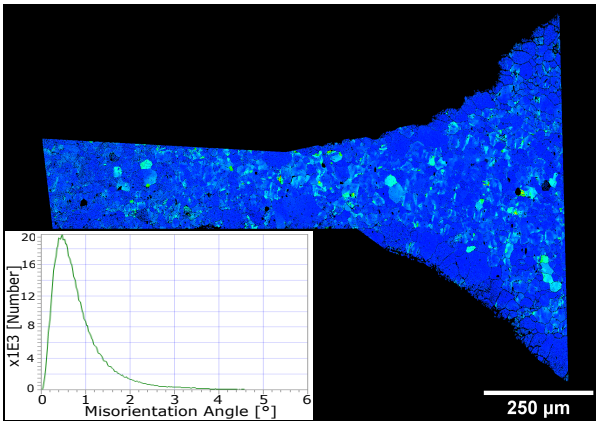

(c) After Annealing

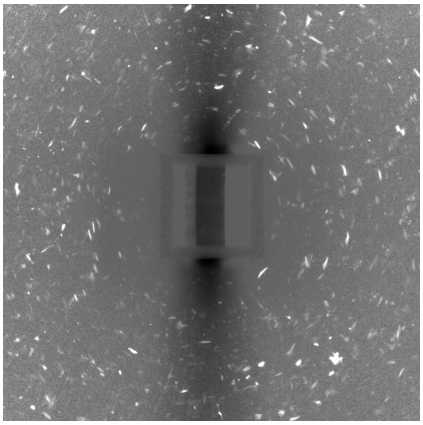

(d) After Annealing

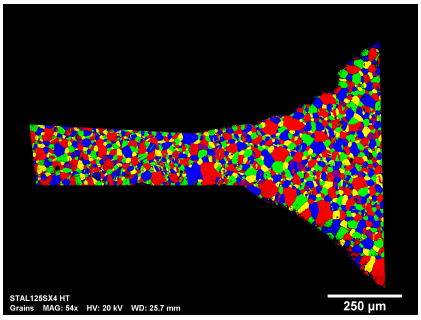

(e)

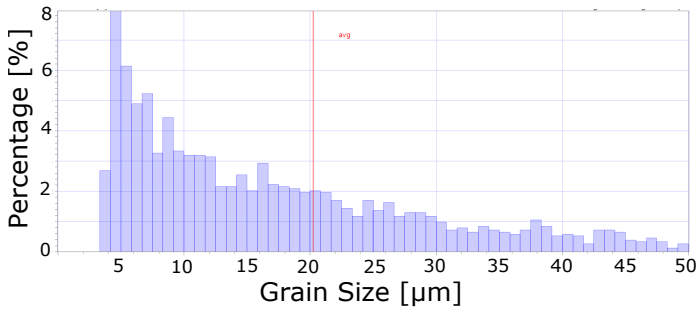

(f)

Figure 5.4: (a) Grain misorientation average (MO average) map of the as-cut dog-bone sample before annealing. (b) LabDCT diffraction spots of the specimen before annealing. (c) MO average map after annealing at 140°C for 60 minutes, showing a reduction in the intragranular disorientation. (d) LabDCT diffraction spots of the specimen after annealing. (e) EBSD map showing the grain structure after annealing. The colours are randomly allocated to the grains. (f) Grain size histogram of the annealed specimen shows an average grain size of 20 µm.

5.1.3 Diffraction Contrast Tomography (DCT)

The experimental apparatus and acquisition procedure used for DCT are similar to those for a conventional microtomographic imaging technique (figure 5.5a). The sample is irradiated by a parallel monochromatic synchrotron X-ray beam whose dimensions are defined by slits. The transmitted radiation beam illuminates the sample and forms an absorption contrast radiograph in the centre of the detector. As the sample rotates through 360° around an axis perpendicular to the incident beam, grains pass through alignments when the Bragg condition for diffraction is fulfilled. Therefore, some of the incoming intensity of the beam is diverted out of the direct beam into diffraction spots on the detector system. Provided that the intragranular orientation and strain gradients are small enough, the diffraction spots can be treated as parallel projections of the 3D grain volume. The diffraction spots of each grain usually appear in several consecutive images. There are a stack of 3600 diffraction images (0.1° angular step between patterns) which are analysed automatically through segmentation (from 3D diffraction volumes to 2D diffraction spots), pair matching (Friedel pairs), indexing (sorting out pairs belonging to the same grain) and grain reconstruction (projections into 3D grains) (figure 5.5b). Since the specimen rotates by 0.1° each time, the angle between the incident beam and a certain crystal plane of a grain keeps changing sinusoidally. Therefore, there are up to four times that this angle coincides with the Bragg angle [186]. A given set of lattice planes correspond to up to four diffraction spots, which could be matched into two pairs separated by 180° rotation. The diffraction angles can be calculated from the paired diffraction spots. Such pairs are termed Friedel pairs. Matching up Friedel pairs is crucial for accurate indexing of the diffraction spots. Based on the spatial and crystallographic criteria, the sets of diffraction spots are allocated to the grain that they belong to ("indexing") [183]. The scattering vectors can be determined from the grain position and diffraction spots, which are then used to calculate the crystallographic orientation of the grains.

Despite the remarkable advantages of the DCT technique, there are a few limitations to it. Firstly, there are only certain categories of polycrystalline mono (or dual) phase materials

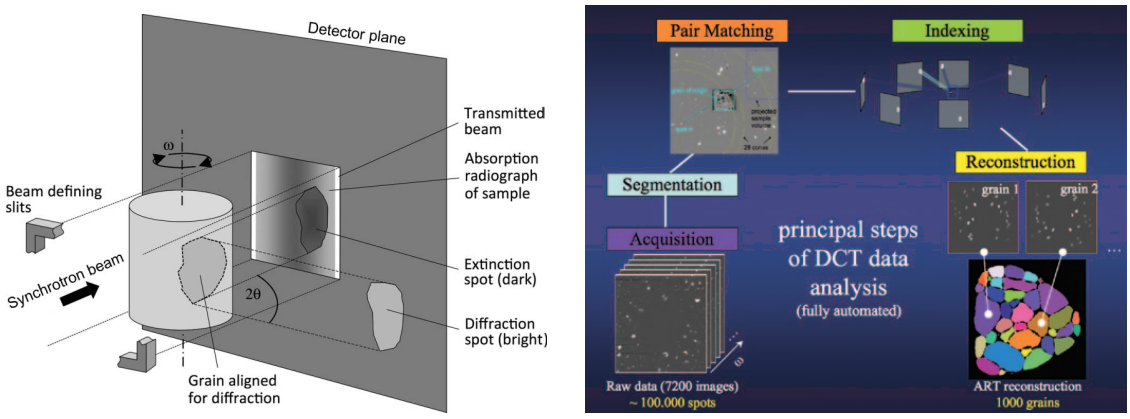

(a) After [179] (b) After [189]

Figure 5.5: Diffraction contrast tomography (DCT) experimental setup and data analysis. (a) The experimental apparatus of DCT is identical to a conventional microtomographic imaging setup, with the sample rotating through 360° around an axis perpendicular to the incident beam. The transmitted beam and diffracted beams from the sample are recorded on a high resolution detector placed within a close distance [179]. (b) Automated data analysis of the diffraction spots to reconstruct the 3D grain microstructure of the sample [189].

(metals and ceramics) that could be characterised by DCT technique [183]. Materials with high density and high atomic numbers (highly attenuating material), multiple (more than two) phases or subgrain structures are not possible for DCT. Secondly, the number of grains in the cross section and total sample volume is limited. In general, there should be only around 100 grains in each cross section and 1000 grains within the illuminated sample volume, in order to achieve accurate reconstruction of the diffraction data [181]. This is due to the limited spatial resolution of current X-ray imaging detector technology. The number of grains is also restricted by spot overlap that makes pair-matching and indexing difficult. Thirdly, there are strict requirements on the mosaicity and texture of the material. In other words, the material must exhibit a limited amount of intragranular misorientation spread [183]. The reconstruction of the 3D grain volume and orientation is only valid in the case of weak intragranular orientation gradients and elastic strain gradients. In addition, the reliability will degrade with increasing levels of plastic deformation of the sample [189]. This is because in significantly deformed polycrystals, the diffraction spots are no longer parallel projections of the 3D grain volume. Furthermore, the diffraction spots may overlap with each other.

5.1.3.1 Laboratory-based DCT

In preparation for the synchrotron beamtime, the specimens were first examined using Lab-DCT. Despite some differences between the synchrotron and laboratory-based DCT, the quality of diffraction patterns was a good indication of the suitability of the specimens for DCT. At a synchrotron light source, high flux, monochromatic X-ray beams could be used to provide high resolution DCT scans. However, due to the limited access to the synchrotron facilities, there were limited applications of the DCT technique to materials science research. With the recent development of X-ray microscopes based in laboratories, there have been optional LabDCT advanced imaging modules available to provide 3D grain crystallographic orientation information [190]. Supported by the reconstruction software, this powerful technique enables 3D crystallographic characterisation to be carried out routinely at the laboratory. More importantly, the enlarged cabinet design allows for the application of in-situ mechanical testing devices. In addition to the sufficient availability of the X-ray instrument, the LabDCT system provides insights into a "4D" (extended time evolution) in-situ experiment even across several days and weeks. This is a significant advantage over the synchrotron facility in terms of long-term characterisation of microstructural and crystallographic evolution of materials during deformation, such as stress corrosion cracking or superplasticity.

The LabDCT instrument is shown in figure 5.6a, which includes a DCT detector in the conventional X-ray microscope (Carl Zeiss Xradia 520 Versa 3D X-ray microscope). The principle of LabDCT is almost the same as the DCT technique based on a synchrotron facility except for the X-ray source. Instead of the parallel monochromatic beam used in a synchrotron, the Lab-DCT technique uses a polychromatic X-ray beam (a divergent beam with a wide wavelength spectrum) [191]. The experimental setup of LabDCT is illustrated in figure 5.6b. The source to sample and source to detector distances are around 23 mm and 577 mm, respectively [192]. The lens configuration of the microscope provides a spatial resolution of 0.7 μm [190]. The aperture determines the size of the direct X-ray beam, which forms an absorption contrast projection as shown in figure 5.6c. When a grain in the polycrystalline material diffracts the beam,

a diffraction spot is formed on the detector that is placed in the Laue focal plane. The focusing of the beam occurs in the diffraction plane and the polychromatic X-ray beam (with different energies and wavelengths) satisfies the Bragg diffraction condition at different positions over the entire volume of grain [191]. Therefore, the diffraction spot is in a narrow line shape. Furthermore, the length of the line-spot indicates the physical size of the grain along the plane perpendicular to the diffraction. Each diffraction spot corresponds to only one crystallographic lattice plane that fulfils the Bragg condition [191]. As shown in figure 5.6d to 5.6f, at the same X-ray flux and sample width, the diffraction spots decrease in length (size) as the average grain size of the samples changes from ~40, 35 to 20 μm, respectively. It could be seen that the diffraction spots of 20 μm grains are tiny and close to the resolution limit of LabDCT. The material with a 20 μm grain size was selected for the synchrotron DCT.

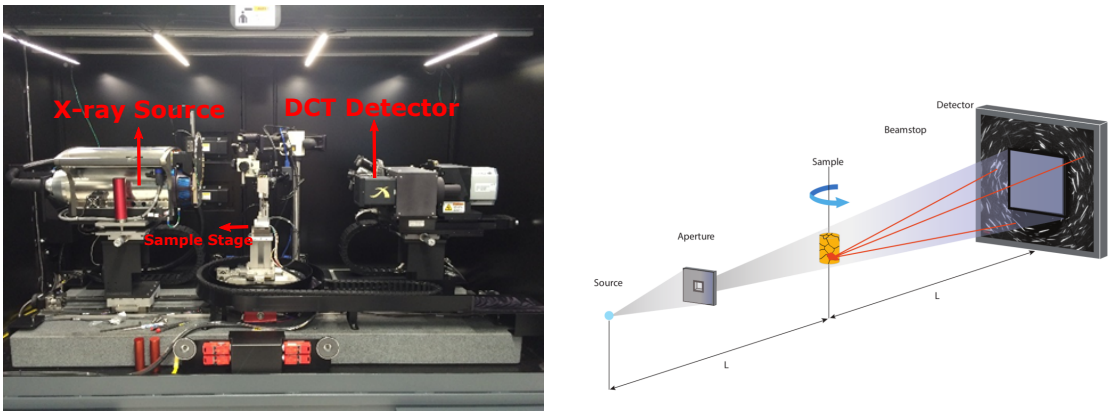

(a) (b)

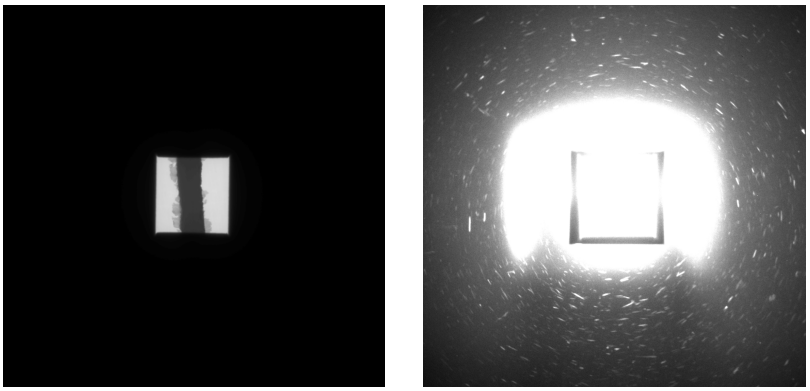

(c) (d)

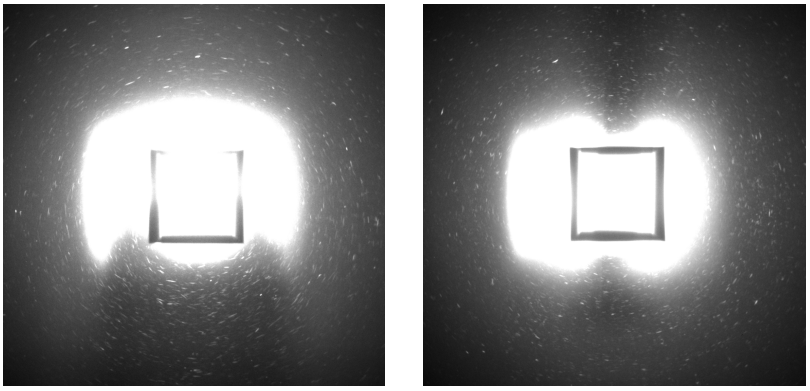

(e) (f)

Figure 5.6: (a) A Carl Zeiss Xradia 520 Versa X-ray Microscope integrated with a DCT detector [193]. (b) A schematic diagram of the LabDCT [191]. (c) An absorption contrast projection of the sample in the centre of the detector. (d) to (f) show the diffraction spots collected in the outer region of the detector (at a single rotation position). The specimens with different grain sizes, i.e. (d) - 40 μm, (e) - 35 μm and (f) - 20 μm, generate different sized diffraction spots.

5.1.3.2 Synchrotron-based DCT

A synchrotron provides a high energy and high flux monochromatic beam that can lead to high resolution and accuracy in reconstruction of diffraction patterns. For DCT scans, a synchrotron would enable smaller grains to be observed than the LabDCT. In-situ tensile tests coupled with DCT were carried out during a six-day beamtime. The experimental setup is illustrated in figure 5.7a. A monochromatic X-ray energy of 63.4 keV was sufficient to penetrate ~0.2 to 0.3 mm of tin. The sample was placed on the stage between the aperture and the high resolution DCT detector system. The stage allowed 360° rotation so that all the grains in the sample could fulfil the diffraction conditions. The sample to detector distance was around 6.7 mm, providing a spatial resolution of 0.75 μm. The spatial resolution was determined by the source size, detector resolution and sample position [192]. Depending on the level of deformation, the average distance between the actual grain boundary location and the reconstructed grain boundary location was around 1.5 to 3 times of the pixel size. When using a parallel beam, the ultimate spatial resolution was inherently limited by the conversion of X-rays to visible light and the optical imaging system of the detector [180]. The grain orientation resolution was around 0.1º. This resolution was limited by the angular step size used in the DCT scan (0.1º). There are a few other factors that can influence the accuracy of data processing, such as the indirect incidence of diffracted beams on the detector and the distorted diffraction spots resulting from the local changes in the scattering vector [183].

It has long been difficult to conduct mechanical tests coupled with near-field diffraction imaging techniques due to the severe space constraints. This is because the detectors, cameras and motorised sample stage all have to be around the sample. Near-field diffraction imaging requires the high-resolution X-ray detector screen to be positioned moderately close (a few millimetres) to the sample. Some testing device designs were developed for tomographic imaging during a load test ([194, 195]), but they were not suitable for DCT experiments which require the sample to be very close to the detector. The problem was not solved until a micro-mechanical testing device was designed to enable 3D grain mapping during interrupted load

tests [196]. This device was used in the DCT experiment for the current thesis. As shown in figure 5.7b, the micro-testing device could be placed very close to the DCT detector (would be even closer when a DCT scan was in progress). A beam stop made of platinum was placed in front of the DCT detector to protect it from overexposure and potential damage.

The cross section of the testing device is shown in figure 5.7c. The tensile specimen was fixed to the central steel shaft by two cylindrical pins through a quartz tube. Amorphous quartz was used as the material for the tube due to its weak diffraction of the X-ray beam. The outer diameter of the tube was around 5 mm, which made it easy to mount the specimen (dimension shown in figure 5.1a). This compact design allowed the DCT detector system to be as close as 2.6 mm to the centre of the specimen (minimum distance to the quartz tube being 0.1 mm) [196]. The shaft was integrated with a semiconductor strain gauge that measures the elastic strain of the shaft, which was converted to the load measurement. This customised load cell could measure a tensile load up to 500 N. The displacement of the shaft (and therefore the specimen) was controlled by ramping up the voltage of the piezoelectric actuator in increments of 1V (1V$\approx$3.33 μm) at a wide range of speeds. The greatest advantage of this device for an experiment on superplasticity was that it could provide strain rates as low as $10^{-7}/s$ (or even lower). However, the limitation of this device was that the maximum travel range was only 500 μm, i.e. the maximum voltage was 150V. Therefore, the maximum achievable strain for this particular sample design was only 33% (500 μm/1500 μm).

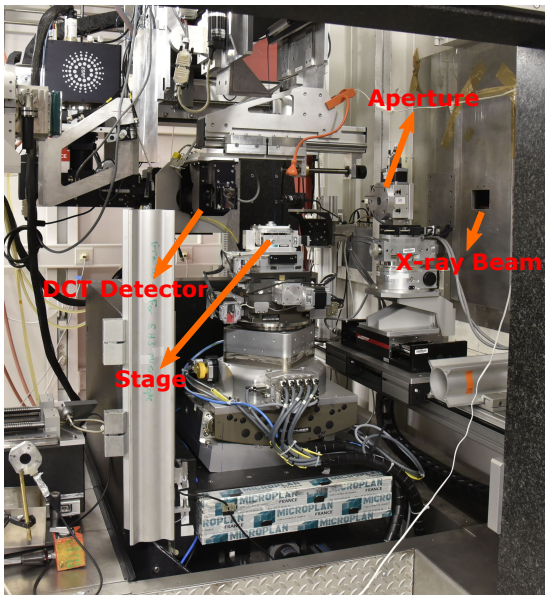

(a)

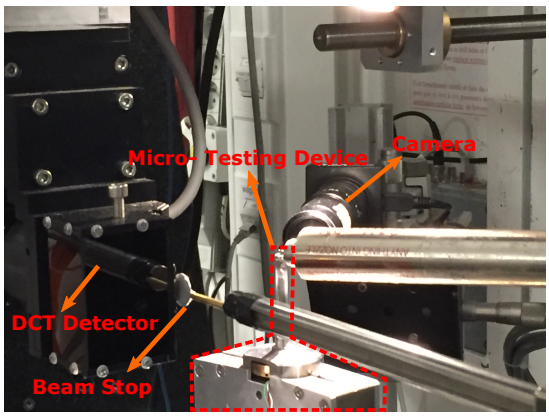

(b)

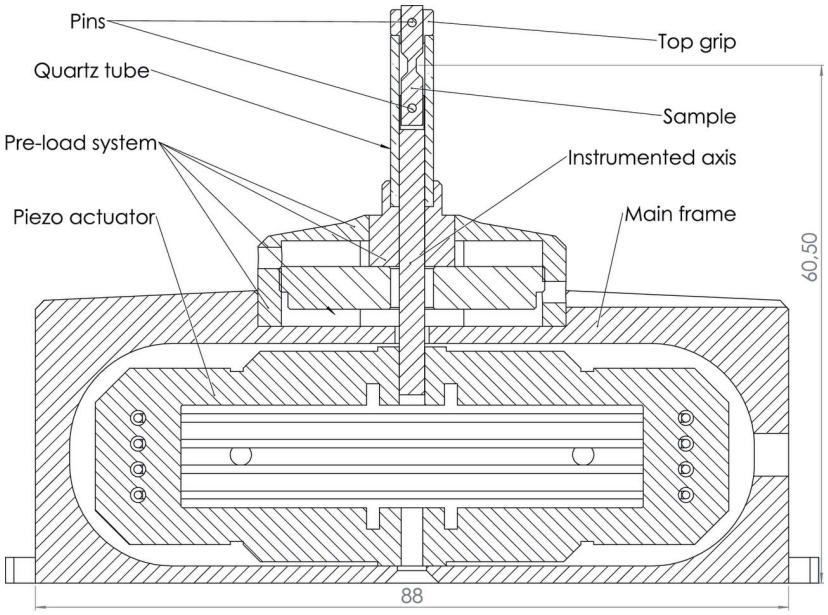

(c) After [196]

Figure 5.7: (a) Diffraction contrast tomography experimental setup at ESRF. (b) A new compact design of a micro-testing device was used for the in-situ tensile test. (c) Cross-sectional view of the in-situ testing rig with a piezoelectric actuator (the dimensions are in millimetres) [196].

Procedure to Take DCT & PCT Scans

After a decade of significant technical developments, the process of taking DCT scans has been highly automated. A command script was written to automatically move the specimen close to the DCT detector, open up and shut down the beam and aperture, rotate the specimen in equidistant intervals of 0.1° for DCT scans. The aperture size was adjusted for a suitable sample volume to be illuminated. First of all, the tensile specimen was carefully mounted onto the testing device. A DCT scan was then taken on a certain volume of the specimen without any loading. Considering the grain size as 20 μm as mentioned above, the aperture size was chosen to be 150 μm so that around 700 grains were analysed. Then a preload was applied to the specimen by ramping up the voltage of the piezo-actuator. X-ray radiographs were constantly taken on the whole specimen. Initially, the whole specimen was moving together because the top end of the specimen was not in good contact with the pin and shaft. The preload was complete as soon as the top end of the specimen stopped moving.

After the test started, it was important to keep track of the dimensional change of the specimen. Even though phase contrast tomography (PCT) could not reveal grain boundaries in a single phase material, it could be used to show the features and dimensions of the region of interest. Therefore, PCT scans were taken to monitor the change in the length and cross section uniformity with tensile deformation. The whole gauge length was illuminated in the PCT using the same X-ray energy of 63.4 keV as in the DCT. The same detector was used (in both PCT and DCT) and the sample to detector distance in the PCT was 56.7 mm. Each scan had 500 projection images with a pixel size of 0.75 μm. It was an automated process via a command script to take a PCT scan every 0.6% strain. There was no need to interrupt loading as it only took 12 minutes for each PCT scan.

Figure 5.8a is a slice from a PCT scan showing the cross section of the DCT sample volume. Subsequent scans were conducted as the specimen was loaded to 6%, 15% and 22% strains. The strains corresponding to the DCT scans are the overall strain of the whole specimen rather than the local strain unless specified. The local strains of the DCT sample volume were calcu-

lated from the PCT scans as will be described in section 5.2.2. In order to prevent relaxation during the DCT scans, the testing device was kept straining at a strain rate of $10^{-7}/s$, which was 10 times slower than the displacement rate of the rest of the test. There was around 0.1% strain over the time (~3 hours) of taking a DCT scan. After each DCT scan, the specimen was loaded up to the normal strain rate, i.e. $10^{-6}/s$.

Data Analysis

A typical DCT diffraction pattern collected from the detector is shown in figure 5.8b. The sample was illuminated in the absorption contrast radiograph in the centre. The diffraction spots spread out on the outer region of the detector, which are parallel projections of the grains. The diffraction spots were summed and segmented, matched to Friedel pairs that belong to the same grain, and finally indexed using the DCT analysis code (acknowledgements to Dr Ludwig at ESRF and Dr McDonald at the University of Manchester). The reconstructed map of a cross section of the specimen before loading is shown in figure 5.8c (without dilation by default, unless specified), which illustrated all the grains on that slice. The shapes and sizes of the grains were revealed. However, after some amount of deformation, the mosaicity of some grains increased and their diffraction spots started to overlap with each other, and so could not be indexed any more. As shown in figure 5.8d, there were slightly more non-indexed regions in this reconstructed map of the same slice after 6% strain. Despite this, almost all the grains were indexed at this amount of strain, which was not possible for the non-superplastic materials. With the dislocation mediated plasticity mechanism, DCT works up to only around 5% strain. This indicates the unique deformation mechanism of the superplastic material that mainly occurs on the grain boundaries.

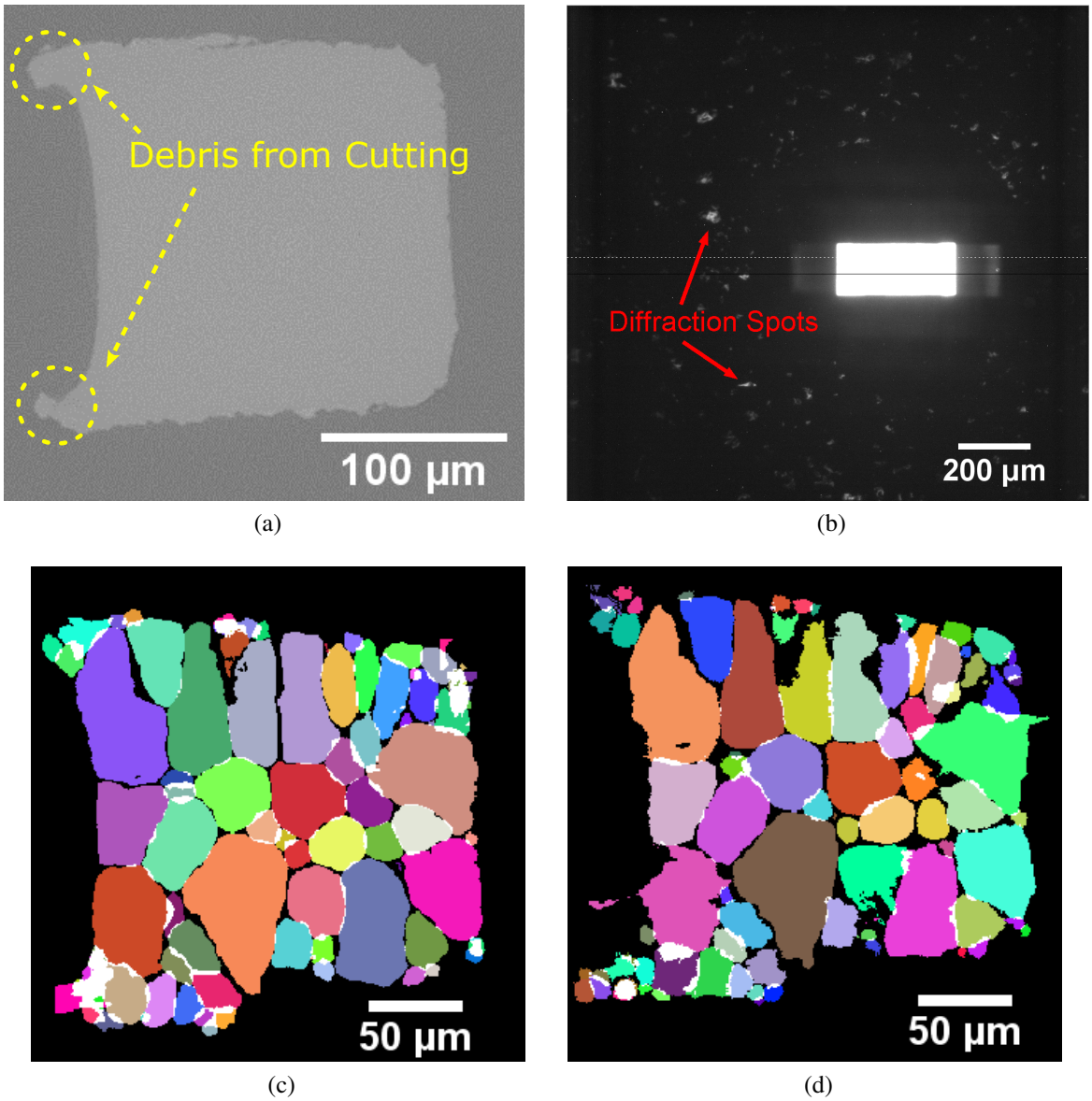

(a) (b)

(c) (d)

Figure 5.8: (a) A phase contrast tomography (PCT) image illustrating the features of the DCT sample volume before loading. (b) An example of DCT diffraction spots recorded on the detector. (c) A reconstructed DCT map of a cross section of the 0.2×0.2 mm^2 specimen before loading. The colours of the grains were randomly allocated. (d) A DCT grain map at 6% strain of the same slice as above, showing almost all the reconstructed grains as well as some non-indexed regions.

5.1.4 Preliminary Mechanical Tests

In order to investigate the suitability of the specimen's geometry and its superplastic properties, some tensile tests with various strain rates were carried out before the beamtime. Annealed samples with two different grain sizes were used. Therefore, the effect of two variables on the superplastic behaviour could be investigated: the strain rate and grain size. First of all, a coarser grained sample was tested at a few different displacement rates. The experimental procedure is described below as an illustration of the methodology used in the mechanical tests.

The microstructure is shown in figure 5.9a, with an average grain size of 35 μm (measured by EBSD with a threshold misorientation angle of 4°). Since twin boundaries are thought to be very difficult to slide, they were excluded for the grain size analysis. What is more, there were few subgrain structures found in this annealed specimen. The engineering tensile stress was calculated as load divided by the initial cross-sectional area of the gauge region. The displacement of the specimen was calculated from the voltage applied by the piezo-actuator. The engineering tensile strain was calculated using the change in gauge length divided by the initial gauge length. Some error analysis was carried out on the stress and strain data. There were four parameters in total. The load and displacement were outputs of the testing device. The load measurements had fluctuations due to the voltage ramping up in steps. The displacement data converted from the voltage were relatively accurate. However, the dimensions of the cross-sectional area and length of the gauge had large uncertainties. The area was measured from a series of cross-sectional slices of the PCT scan before loading. Due to the non-uniform cross-sectional area of the specimen, the uncertainty of stress measurements was relatively large - 6%. For the initial length of the gauge, since there were no clear points on the top and bottom ends of the gauge, a few measurements were taken and the average was used to measure the strain.

The engineering tensile stress was plotted against the engineering tensile strain for the strain rate jump test in figure 5.9b. An approximately stable stress was achieved before the displacement rate was changed (the changes are indicated by the red dashed lines). The slight drop in

stress was due to the stress relaxation when straining at $10^{-7}/s$ to simulate the process of a DCT scan. It could be seen that the stable stress at the plateau increases with the strain rate. Even though the specimen with a coarse grain size was not superplastic (low strain rate sensitivity of 0.28 as shown in the sub-figure on the bottom right corner), the series of tests confirmed the suitability of the testing device and specimen for the in-situ tests.

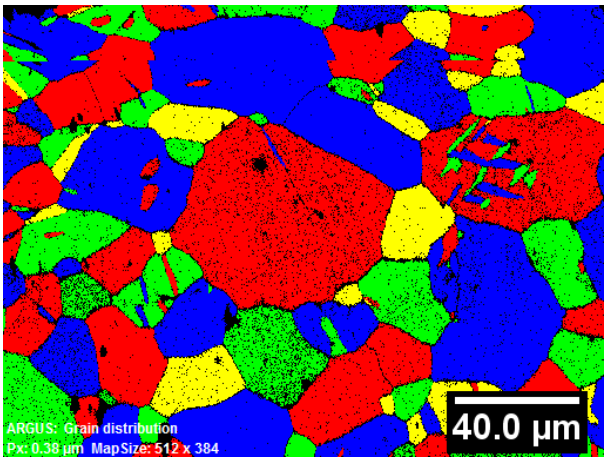

(a)

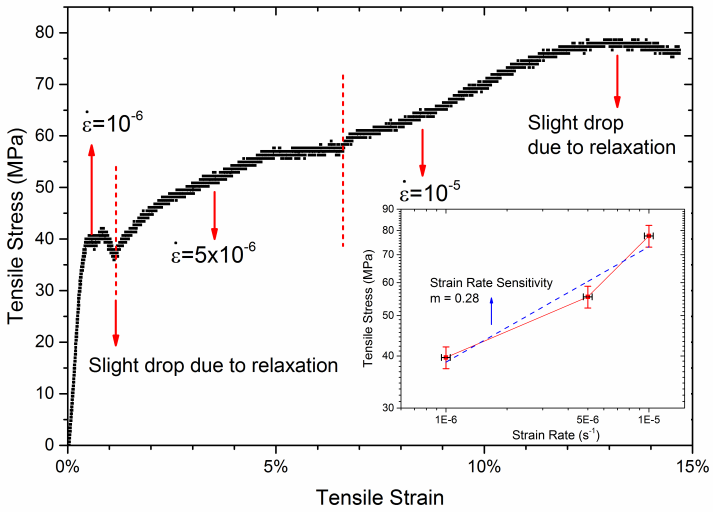

(b)

Figure 5.9: (a) EBSD map showing the coarse grains of the specimen used for the displacement/strain rate jump test. The threshold angle to define a grain was 4º. The colours were randomly assigned to grains independent of the grain orientation. (b) A plot of the tensile stress against strain for a test including several strain rates on the same specimen. A sub-figure on the bottom right corner illustrates a strain rate sensitivity of 0.28 for this microstructure.

5.2 Results: Synchrotron PCT and DCT with In-situ Tensile Tests

5.2.1 In-situ Mechanical Testing

5.2.1.1 Preliminary Tests on a Wider Specimen

For the in-situ tests with DCT scans, specimens with a 20 μm grain size were used, which had two gauge dimensions: 0.3 mm and 0.2 mm in width and thickness. The preliminary tests were carried out on the wider specimen of 0.3×0.3 mm^2 size at a strain rate of $10^{-5}/s$. All the stresses and strains are engineering stresses and strains unless otherwise specified. The tensile stress against strain curve of the 0.3 mm wide specimen is shown in figure 5.10. The stable tensile stress was around 20 MPa. The slight drop in stress in the middle of the test was due to the relaxation induced by taking a DCT scan with the sample deforming at a lower strain rate of $10^{-7}/s$. The DCT diffraction spots were highly overlapped, suggesting that there were too many grains for indexing and a large mosaicity inside the grains. Therefore, a 0.2×0.2 mm^2 sized specimen was used for the rest of the beamtime. The in-situ test was conducted at a lower strain rate of $10^{-6}/s$, which was a compromise between the optimum conditions for superplastic deformation and the limited beamtime.

5.2.1.2 Smaller Specimen and Lower Strain Rate

In order to reduce the number of grains in the DCT sample volume, another mechanical test was conducted on a smaller specimen – 0.2 mm wide in the gauge. Since the previous test at $10^{-5}/s$ induced too much intragranular plasticity for DCT to work, a much slower test was carried out at $10^{-6}/s$. The tensile stress is plotted against tensile strain in figure 5.11a. At the beginning of the test, it took 33 hours to reach 15% strain at such a low strain rate. The drop in stress (or load) corresponded to the interruption to the test while taking the DCT scan. At the beginning of the test up to 15% strain, the tensile stress was stable at around 18 MPa. Due

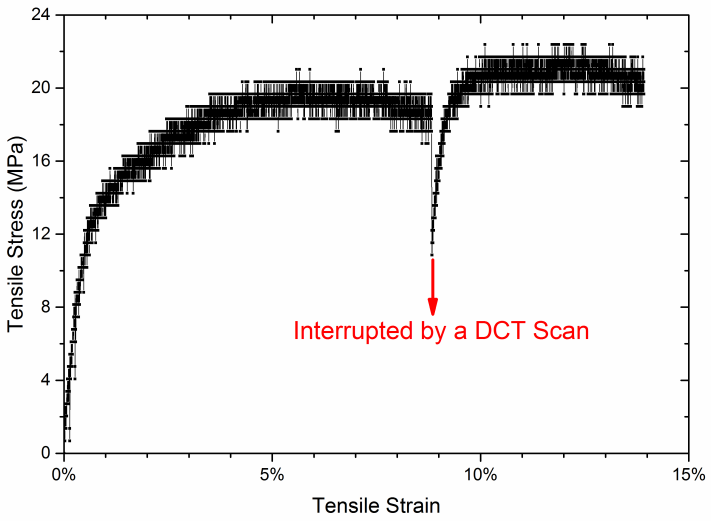

Figure 5.10: The tensile stress and strain data of the preliminary test on a specimen with a gauge width of 0.3 mm.

to the time constraints of the beamtime, the in-situ test had to be speeded up to $2 \times 10^{-6}/s$ and then $4 \times 10^{-6}/s$. Upon changing the strain rate, the stress increased to a certain point before dropping to a relatively stable stress. The strain rate sensitivity index was found to be 0.41. With the higher strain rates, the strain of the specimen was expected to reach 30% by the end of the beamtime. However, the radiograph in figure 5.11b has clearly shown that necking occurred towards the end of the test, which probably resulted from the increased strain rate. The necking region did not coincide with the region of interest where the DCT scans were taken.

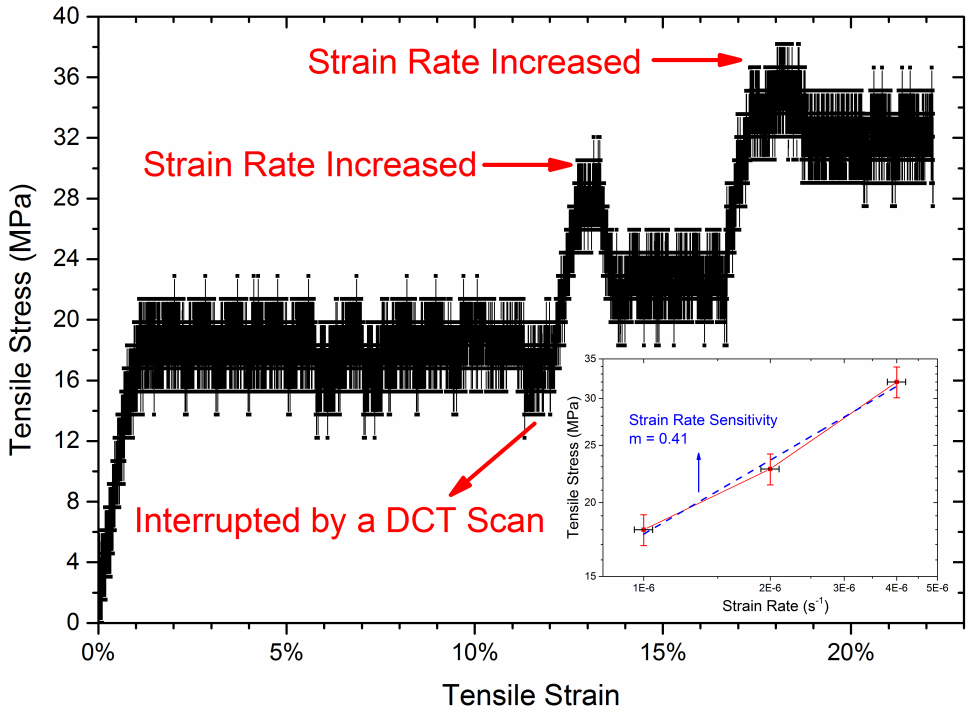

(a)

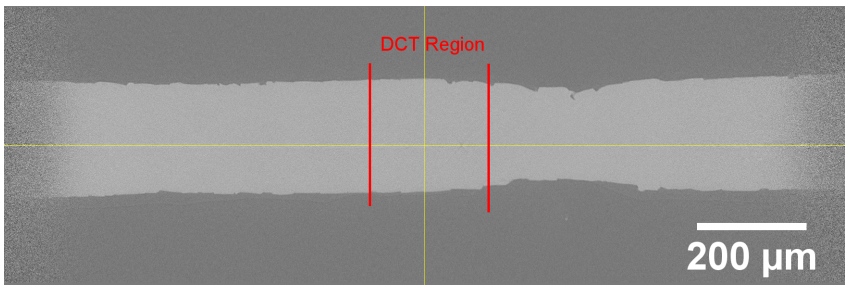

(b)

Figure 5.11: (a) The tensile stress and strain data of the fine-grained specimen with a smaller gauge used in the in-situ test. It was tested at a strain rate of $10^{-6}/s$ with slight changes towards the end of the test. The strain rate sensitivity index was obtained from the sub-figure on the bottom right corner. (b) A radiograph showing that necking has occurred towards the end of the test. The DCT scanned region was a little distance away from the necking segment.

5.2.2 PCT Scans

As mentioned in section 5.2.1, the engineering strain was measured for the whole specimen. However, this macroscopic strain could not represent the local strain of the region where DCT was taken. It is the local strain of the DCT sample volume that matters to the grains characterised by DCT. Therefore, the reconstructed phase contrast tomography (PCT) images were used to measure the actual local strain, which was calculated as the change in length divided by the original length of the DCT sample volume along the loading axis. The PCT data were batch processed using the routine analysis code at ESRF (acknowledgements to Dr Wolfgang Ludwig and Dr Samuel McDonald). The DCT sample volume was illuminated in the radiograph as shown in figure 5.12a. Two features were identified on the sample surface to follow the dimensional change. The initial length of the target sample volume was 153.66 μm. After loading, the reconstructed PCT images of the target sample volume are shown in figure 5.12b to 5.12d, corresponding to the subsequent three DCT datasets. The local strains calculated from the change in distance between the two features identified are 7%, 21% and 29% strain. It is noted that this region became thinner and elongated with the deformation. The dimensional change from figure 5.12c to 5.12d was quite small as most of the deformation occurred at the necking region. A 3D illustration of the sample volume at different strains are shown in figure 5.12e to 5.12g. Even though the PCT scans were designed to track the dimensional changes of the specimen, another important piece of information provided by PCT was that there were no voids forming in the whole sample volume with deformation.

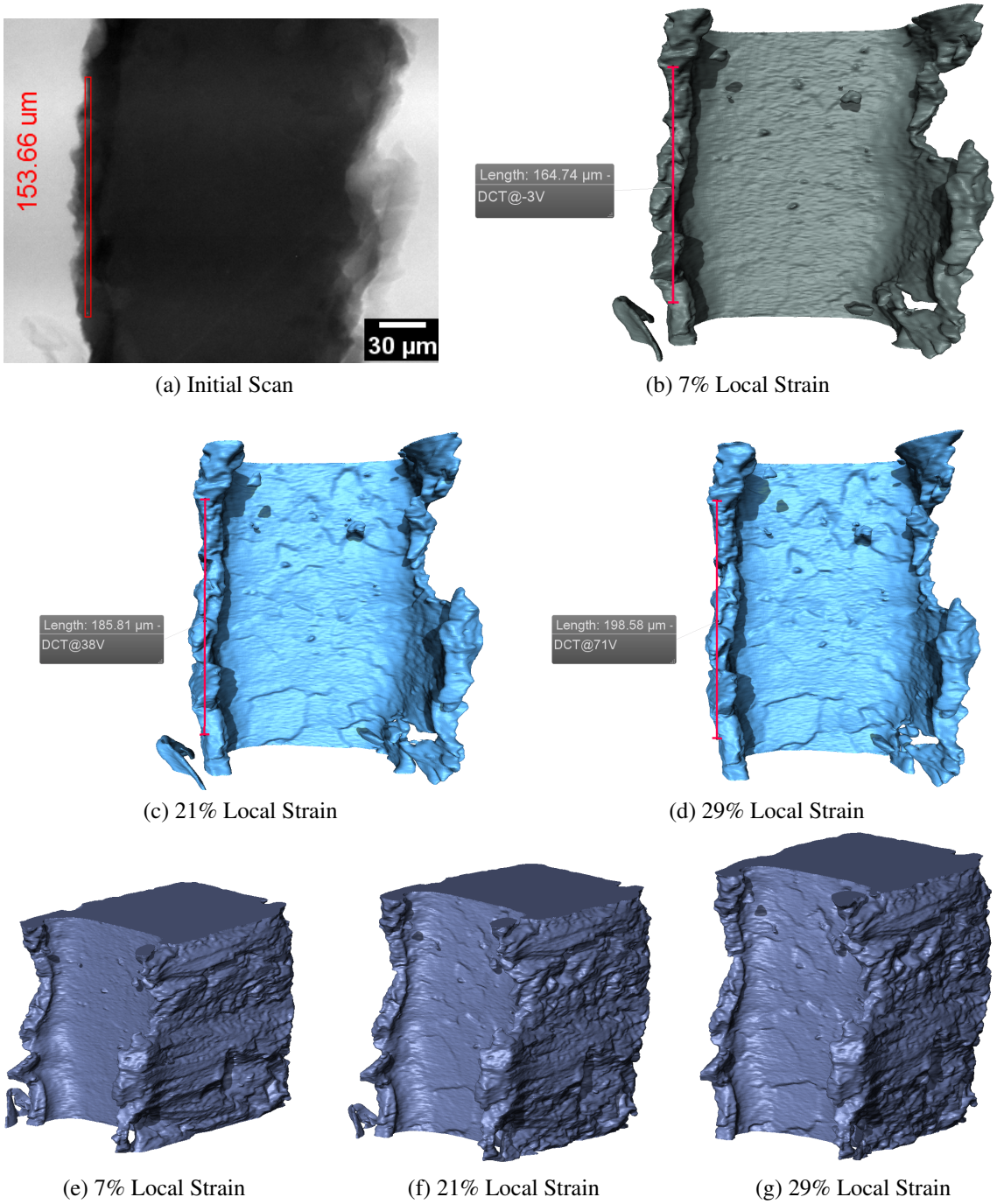

(a) Initial Scan

(b) 7% Local Strain

(c) 21% Local Strain

(d) 29% Local Strain

(e) 7% Local Strain

(f) 21% Local Strain

(g) 29% Local Strain

Figure 5.12: (a) A radiograph showing the sample volume where the DCT scans were taken. Two features were identified to measure the length of the DCT sample volume. (b), (c) and (d) are the reconstructed PCT images showing the sample volume for the three DCT scans taken at different strains. (e), (f) and (g) are the 3D images of the DCT sample volume corresponding to (b), (c) and (d), respectively.

5.2.3 DCT Scans

As mentioned in section 5.1.3.2, DCT scans were conducted before loading up the specimen, at 6%, 15% and 22% strains (overall strain for the whole specimen). The DCT dataset at 6% strain was not included in this section as it was quite similar to the initial one. The 2D slices of the DCT sample volume are stacked to a 3D grain map using the Avizo software (acknowledgements to Prof Marrow's research group). The reconstructed maps at 0, 15% and 22% strain are shown in figure 5.13a to 5.13c. The voxel size was 0.75 μm. The tensile loading axis was along the vertical direction (z axis). As for the last two DCT scans, the mosaicity inside the grains was so large that indexing of the diffraction patterns was difficult. This challenge was overcome by focusing on a smaller sample volume (by adjusting the aperture) to reduce the number of grains for analysis. Therefore, the last two scans had a reduction of 30% in the aperture size. Across the three scans, almost all the grains have been successfully indexed in the initial DCT dataset before loading. The last two DCT scans at larger strains were more likely to show grain neighbour switching events. Most of the grains were still able to be reconstructed even after as large a strain as 22%.

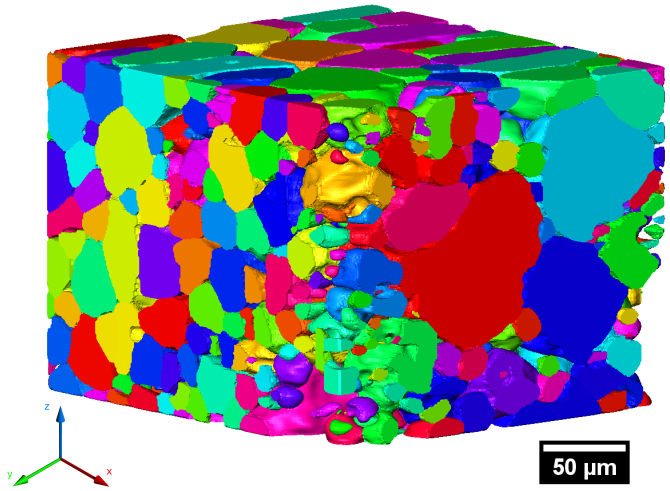

(a) Initial Scan

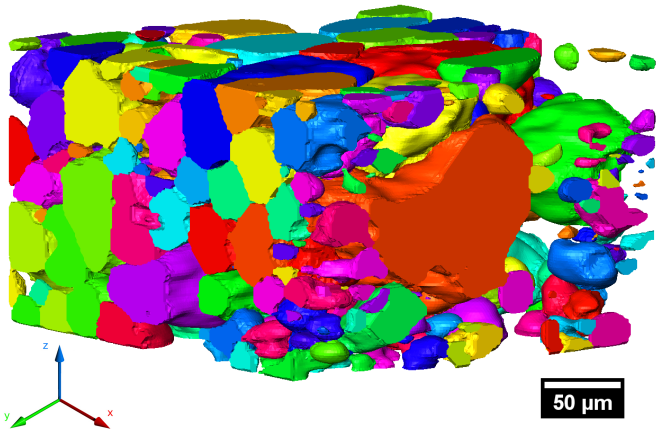

(b) 15% Strain

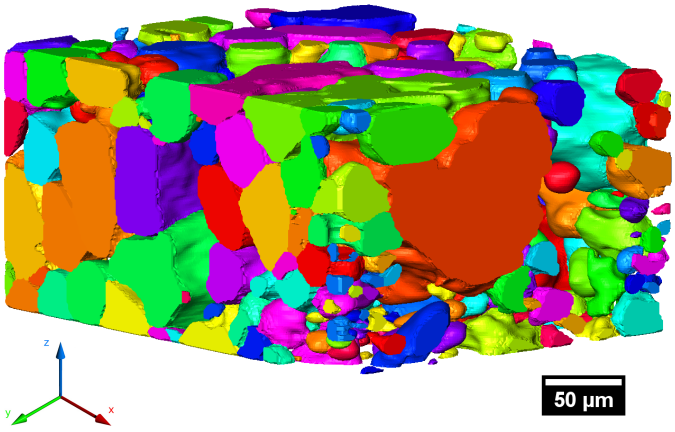

(c) 22% Strain

Figure 5.13: The reconstructed 3D grain maps for (a) the initial DCT scan before loading; (b) an intermediate scan at 15% strain; (c) a final scan at 22% strain at the end of the test. The loading direction was along the "z axis". The colours were randomly allocated to the grains and were not consistent across the three maps. (b) and (c) have a 30% shorter sample volume as the aperture was adjusted to focus on fewer grains.

5.2.3.1 Correlation of Grains in the Datasets

The total number of grains in the DCT sample volume was ~700 in the initial scan. There were fewer grains in the subsequent two scans probably due to the following three reasons (except for the reduction in aperture size): failure of indexing after large deformation, grain growth, or grains moving out of the analysed region as the specimen is strained. The following procedure was conducted to correlate the grains between the three datasets (at 0, 15% and 22% strain). Since the grain IDs were assigned independently in each dataset, a tool available at ESRF (acknowledgements to Dr Wolfgang Ludwig) was used to match the grain IDs across the datasets. However, there were still a small number of grains with unmatched IDs that required manual inspection. First of all, the grain size in each dataset was compared with each other. By assuming the grain as a regular sphere, the radius of the sphere/grain could be obtained. The grain size was represented by the equivalent grain (circle) diameter, which was twice of the radius. The equivalent circle diameter of the same grain obtained from the first and second dataset was compared in a scatter plot (figure 5.14a). Most of the points lay near the diagonal line going through the origin describing identical grain sizes in each scan, which indicates a good match of the IDs from the two datasets. The highlighted points in red were those identified as "mismatched grains". There were also many points lying along the two axes that corresponded to the grains only present in one dataset but absent in the other, for which a volume of zero was assigned.

Similarly, the equivalent grain diameters for all the three DCT scans were plotted in figure 5.14b, with most of the data points aligned near the identical size diagonal line. The highlighted grains lying on the axes were present in only one dataset but absent in the other two. It was not surprising that there were many grains only present in the first scan due to the aforementioned reasons. But the "new" grains only present in the second and third datasets (at high strains) provide strong evidence of grain emergence from other layers. The grains lying on the right side of the plot corresponded to those that reduced their volume in the higher strain scans, which was probably due to the incomplete indexing of the full grain volume. All the highlighted

grains were discarded for the grain size/volume analysis but were retrieved for other kinds of analyses on the grain centroid position and grain elongation.

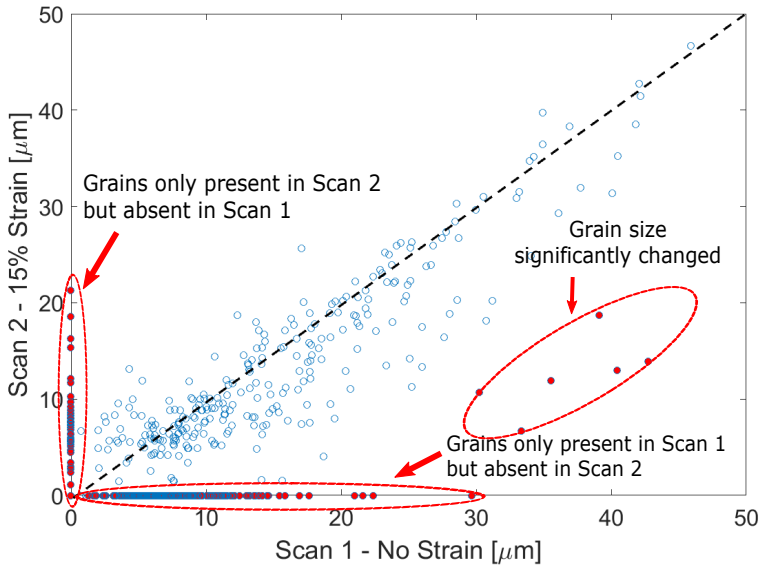

(a)

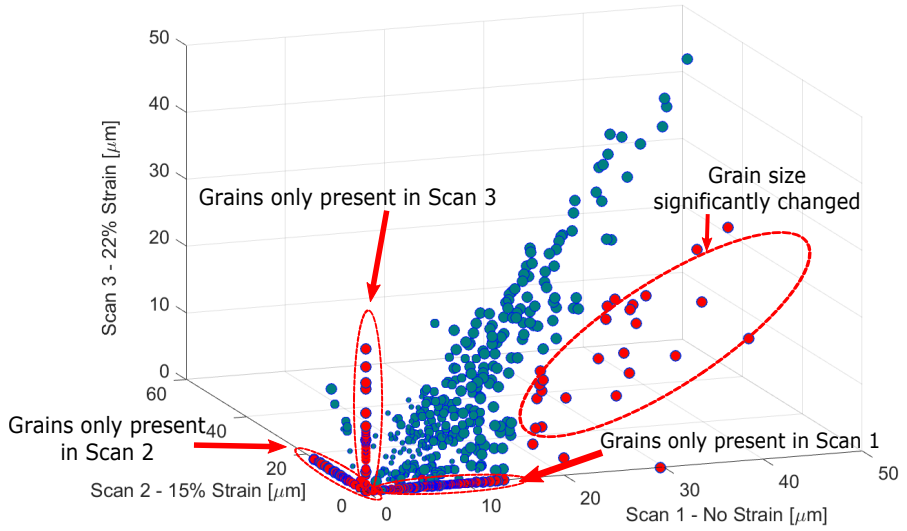

(b)

Figure 5.14: (a) A 2D scatter plot comparing the equivalent grain (circle) diameter from the first and second datasets. The dashed diagonal line represents that the grain has the same grain size in these two scans. (b) A 3D scatter plot comparing the equivalent grain (circle) diameter across three datasets.

5.2.3.2 Grain Volume

The grain volume was calculated by the sum of voxels inside each grain. A Matlab code was written to select and rule out the tiny grains (smaller than 3 μm diameter) and those that were only partially included in the DCT sample volume. In other words, only grains with their entire volume present in the DCT scanned region were considered. The grain size criterion was chosen as 3 μm based on the EBSD analysis that there were no grains smaller than 3 μm (figure 5.4f). The grains are dilated as shown in a 2D slice in figure 5.15a. The histogram distribution of equivalent grain diameter from the initial DCT scan is illustrated in figure 5.15b (in blue). It was calculated that more than half (45%) of the grains were smaller than 10 μm and more than 70% of the grains were smaller than 15 μm. The mean grain size was 16 μm, which confirmed the relatively fine microstructure of the material.

The grain size characterisations by EBSD and DCT are compared in figure 5.15b. The grain analysis using EBSD was based on the data from section 5.1.2 in figure 5.4f. There was no dilation in the EBSD data. The minimum pixel size to define a grain was 4 pixels. The threshold misorientation angle in the EBSD analysis was 4°. The mean grain size from EBSD analysis (18 μm) is slightly larger than DCT (16 μm). This comparison is on the contrary to the fact that DCT gives the full 3D grain volume, while EBSD gives the diameters of 2D sections that do not always cut through the centre of the grain volume. The discrepancy in grain size could be attributed to the difference in sample preparation for the two techniques. The grains on the surface of the specimen might by influenced by waterjet cutting. These grains remained in the DCT sample as it was not ground or polished due to its delicate size. However, the surface grains were mostly removed from the EBSD sample by polishing.

In order to investigate the microstructural evolution (e.g. grain growth) with deformation, the volume of each grain was compared across the three datasets (non-dilated). The total numbers of grains left in the three datasets were 345, 224 and 217 grains. The reduction in the number of grains resulted from the decrease in DCT sample volume and the failure to index some grains at higher strains. The volume or equivalent grain diameter of the common grains present in all

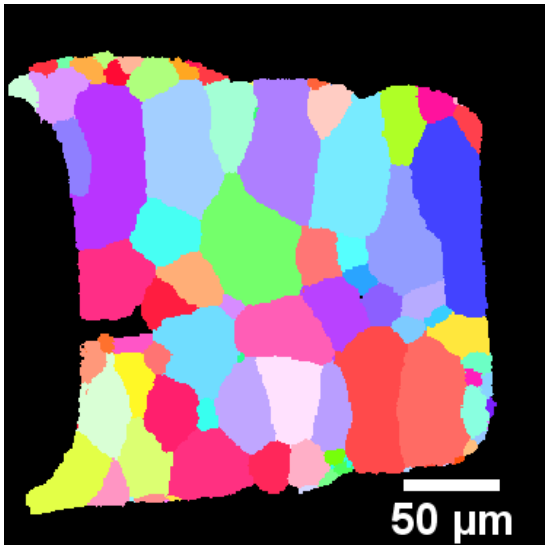

(a)

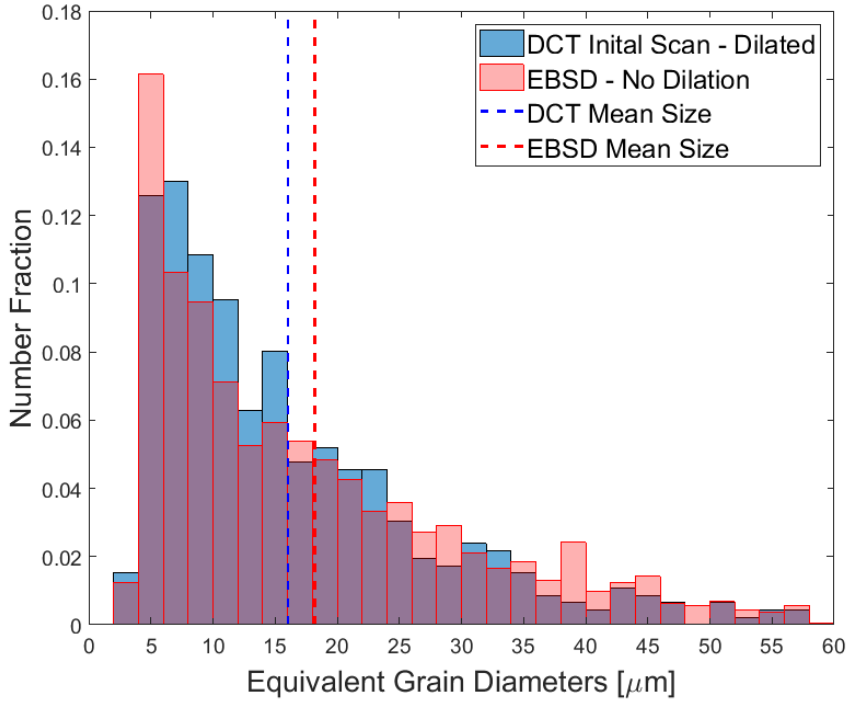

(b)

Figure 5.15: (a) A 2D slice of the initial DCT scan with dilation of the grains. (b) A histogram of the equivalent grain diameters of the same batch of material, characterised by DCT and EBSD, respectively.

the scans were compared as follows. It is worth noting all the grain sizes below are smaller than that obtained from EBSD characterisation. This is because the grains were not dilated in the reconstructed grain maps due to the presence of non-indexed regions.

Using the same analysis, the grain volumes in the subsequent DCT scans could be obtained as well, which were compared to each other in figure 5.16a. The histogram showed that the grain volume distributions were similar. There were 76% and 75% of the grains smaller than 15 μm for DCT scans at 15% and 22% strain, respectively. The mean grain sizes by number fraction were 11.5 μm, 11.9 μm and 12.1 μm for the 0, 15% and 22% datasets, respectively. The frequency of grains above 15 μm has stayed the same or slightly increased in the subsequent two DCT scans. The probability plots of the three datasets are compared in figure 5.16b. The reasonable approximation to a straight line suggests that the distributions were close to log-normal. The three curves almost overlapped with each other. The curve of the initial DCT scan (Scan 1) stayed slightly above the subsequent two scans for grains below 15 μm, while it was the opposite case for the grains above 15 μm. In general, the probability plots for grain volume are quite similar for the three datasets. The slight difference was mostly likely due to the failure to index the small grains in the strained datasets, rather than the possibility of grain growth during deformation.

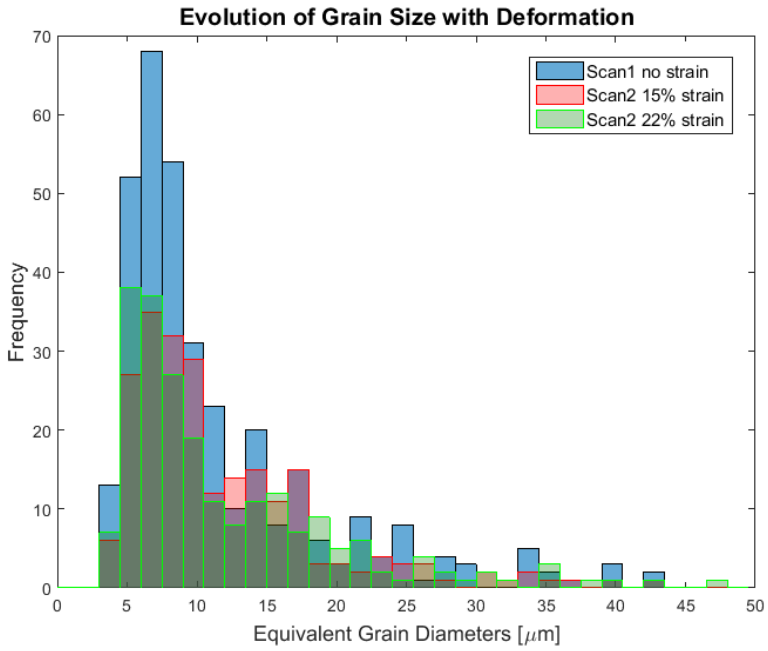

(a)

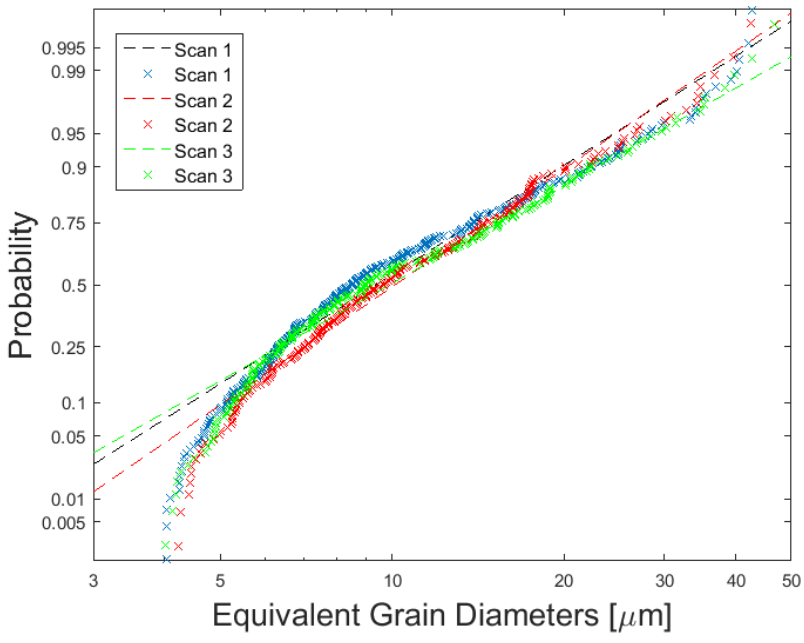

(b)

Figure 5.16: (a) A comparison of the histogram for scans at different strains. (b) A log-normal probability plot of the equivalent grain diameters for DCT scans taken at different strains.

5.2.3.3 Centroid Position (Centre of Mass)

Other than the evolution of grain volume, it is also interesting to investigate the changes to the grain positions during deformation. The position of a grain can be represented by the centre of mass or centroid position in 3D. A Matlab code was used to find the centroid of the 3D grains. Assuming that the grains didn't change too much in shape or position, the three coordinates (x, y, z) of a certain grain should be similar across all the three DCT datasets. An example is shown in figure 5.17a for the coordinate – x, where most grains show a good match with scatter points lying near the diagonal line. The red points deviate largely from the reference line, which is a result of either a notable change in the grain position or failure of indexing. The same approach was applied to the other two coordinates of the centroid positions. The final 3D scatter plot of the centroid position (x-coordinate) is shown in figure 5.17b. The highlighted points correspond to the grains that were only present in two of the scans (either Scan 1 and 2 or Scan 1 and 3). There were totally 150 grains consistently found in all three scans, which lay close to the diagonal line. The grains showing relatively large repositioning required further investigation as they were very likely to exhibit grain neighbour switching.

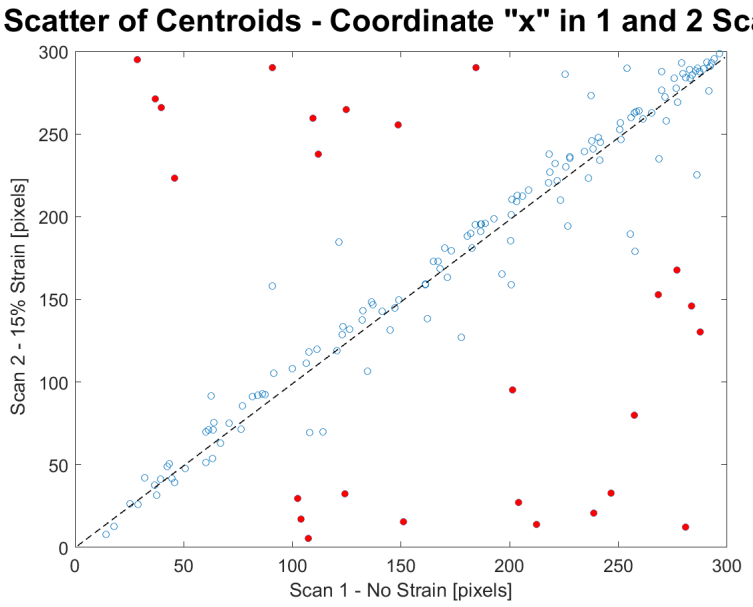

(a)

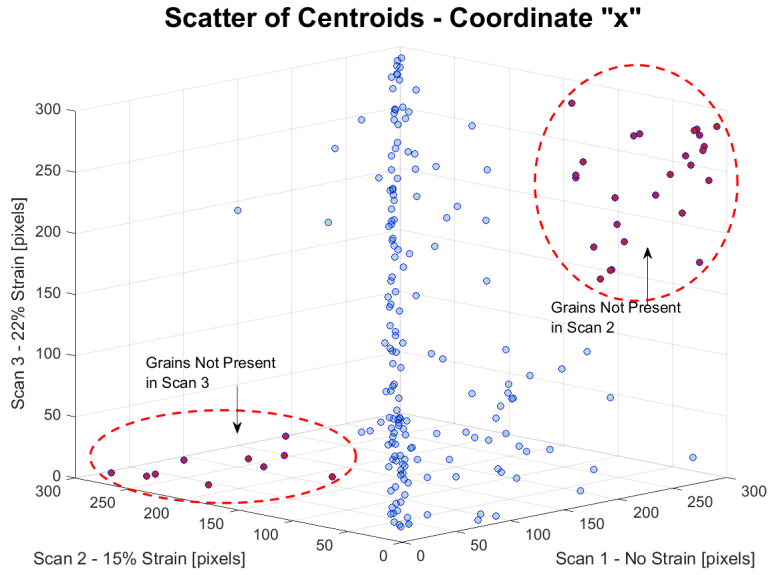

(b)

Figure 5.17: (a) A scatter plot of the centroid position (centre of mass) – x coordinates of the grains in the initial scan and scan at 15% strain. (b) A comparison of the centroid position – x coordinates in the three datasets. The grains that had large changes in the centroid position might be involved in grain neighbour switching events.

5.2.3.4 Grain Elongation

Often, under uniaxial tensile deformation, the grains tend to be elongated along the loading axis. Therefore, it is important to understand if the grains maintain or change their shapes under deformation. The dimension of the grain along the loading axis was calculated by the distance between the top and bottom slices that contain the target grain, which is shown in figure 5.18a. It could be seen that there was no significant difference in the dimension along the loading direction. Taking a closer look at the individual scatter plots in figure 5.18b and 5.18c, there was no clear trend of an increase in the grain dimension along the loading direction (z axis). Instead, most of the points lay below the line with a gradient indicating the strain (21% and 29%, respectively). Furthermore, the linear best fit (through the origin) of all the data points shows that the gradients (0.91 and 0.96, respectively) were much lower than 1.21 and 1.29, respectively. This indicates that the grains were not largely elongated along the loading axis, which was one of the main characteristics of superplastic deformation. It could be concluded that the change in centroid position was the best way to demonstrate the grain's deformation behaviour. Therefore, it was used in the next section to identify possible grain neighbour switching events.

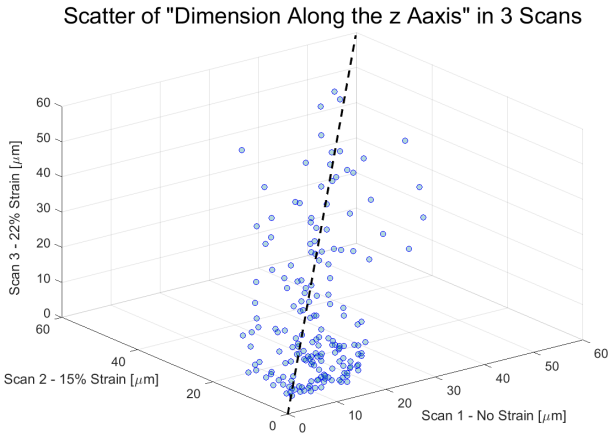

(a)

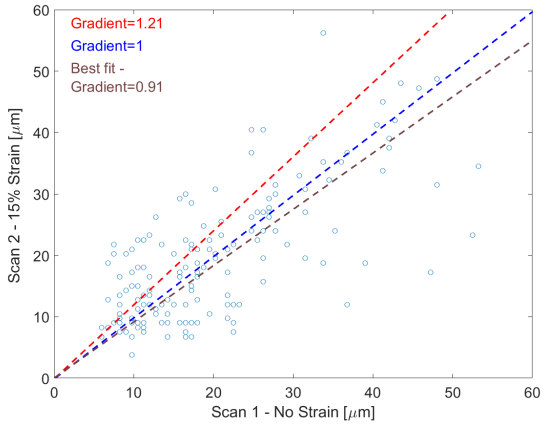

(b)

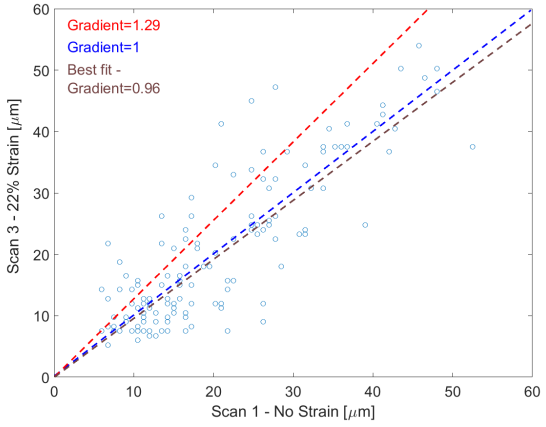

(c)

Figure 5.18: (a) A scatter plot of the dimension of the grains along the loading axis for three DCT scans taken at different strains. (b) and (c) are scatter plots of the grain's dimension along the loading direction for the scans at 21% and 29% local strain of the DCT sample volume, respectively, in comparison to the initial scan. Lines with gradients representing no strain and local strain are drawn, together with the linear best fit of all points.

5.2.3.5 Grain Neighbour Switching Phenomena

As mentioned in 5.2.3.3, the grains showing extraordinary changes in the centroid positions were most likely to have repositioned via grain boundary sliding. As a result, their neighbouring grains could have changed so regions containing these grains were inspected in 2D-slice images. When looking into a certain section of the sample volume, comparison was made on the 2D-slice images from different datasets corresponding to the same groups of grains. The images were compared grain by grain to identify possible neighbour switching events. In figure 5.19a, a group of grains were highlighted in the circle towards the bottom left corner. Grain 92 and 85 were separated by Grain 252 in the initial DCT scan (with the loading axis perpendicular to the page). After 21% local strain of the DCT sample volume, Grain 252 had apparently moved away and enabled Grain 92 and 85 to share a boundary with each other (figure 5.19b). Since the loading direction was perpendicular to the page, the grains tended to move out of the plane of the page. Therefore, in these 2D slices (such as the ones shown here), there were more likely to be grains becoming neighbours with each other and forming a new boundary.

The 2D images provided a preliminary hint of the location and IDs of the grains that have experienced neighbour switching. But the 2D slices could sometimes be misleading as they may have been in different positions across different datasets. Therefore, the 2D slices were stacked up to a 3D map using the Avizo software. A 3D visualisation of the individual group of grains is shown as follows. Figure 5.19c and 5.19e were taken from the initial scan, where the blue and purple grains were separated by the green and red ones. In figure 5.19c, the loading direction is along the vertical axis and the position of the 2D slice — figure 5.19a is also indicated. Grain 92, 85 and 252 are labelled in both 2D and 3D views. But the other grain (the green one in the 3D views) was not on the same 2D slice plane and therefore not labelled. After 21% local strain (at the DCT sample volume), the blue and purple grains were connected to each other forming a clear boundary, while the green and red ones became separated (figure 5.19d and 5.19f). The 3D visualisation images were reconstructed without dilation. Thus, there were blank areas between the grains.

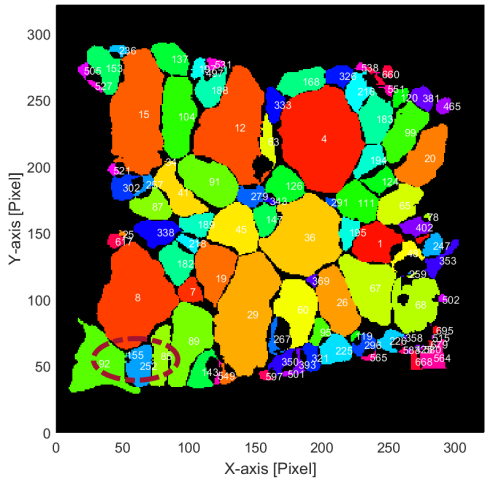

(a) Initial Scan

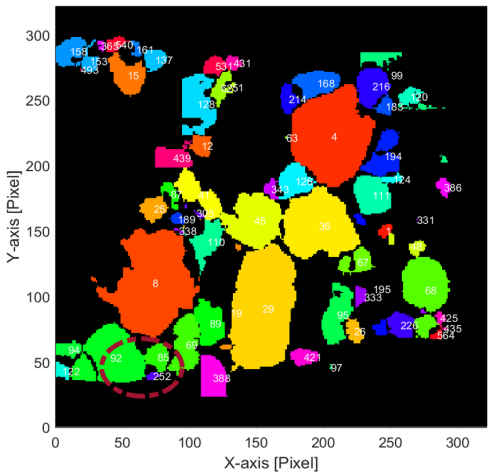

(b) 21% Strain

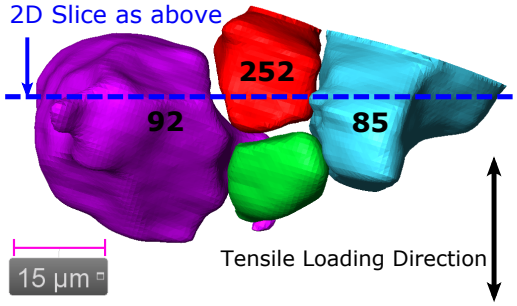

(c) Initial Scan

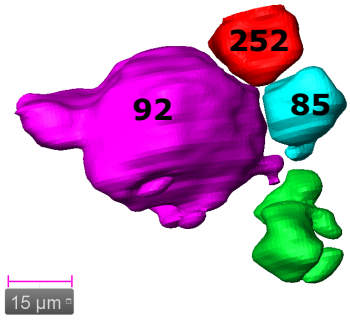

(d) 21% Strain

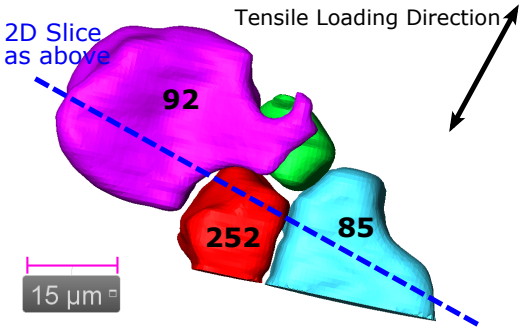

(e) Initial Scan

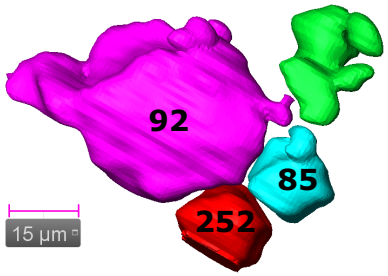

(f) 21% Strain

Figure 5.19: (a) and (b) A group of grains (circled towards the bottom left corner) changed their neighbours judging from the 2D slices at 0 and 21% local strain. (c) and (d) 3D illustration of the group of four grains that switched neighbours. (e) and (f) Another direction of view (rotated from (c) and (d)) showing the grain neighbour switching event.

Another example of grain neighbour switching is illustrated in figure 5.20a and 5.20b. The group of grains was circled in the middle of the images. Initially, Grain 36 and 343 were connected to each other, separating Grain 126 and 147. After 21% local strain, Grain 126 and 147 became neighbours while Grain 36 and 343 were separated. A 3D visualisation of this group of grains is shown in figure 5.20c to figure 5.20f. Figure 5.20c and 5.20d are viewed along the loading direction, i.e. the loading direction is perpendicular to the page. This viewing direction is the same as the 2D slices — figure 5.20a and 5.20b. The last row of images are views from another direction. These 3D views are carefully aligned so that the loading direction is along the vertical axis.

Figure 5.20c and 5.20e are taken from the initial scan, where the green and dark blue grains were separated by the light blue and red ones. After 21% local strain, the green and dark blue grains were connected to each other forming a clear boundary, while light blue and red ones became separated (figure 5.20d and 5.20f). Even though the axis along the centroids of Grain 36 and Grain 343 is not perfectly aligned with the loading direction, these two grains were still pulled apart by the tensile stress.

The third example of grain neighbour switching is illustrated in figure 5.21a and 5.21b. The loading direction is perpendicular to the page. A group of grains was circled towards the bottom right corner of the images. A 3D visualisation of this group of grains is shown in figure 5.21c to figure 5.21f. In all the four figures, the loading direction is along the vertical axis. Figure 5.21c and 5.21e are taken from the initial scan, where Grain 95 and 296 were separated from each other by Grain 26 and 119. The position of the 2D slice — figure 5.21a is also indicated. After 21% local strain, Grain 95 and 296 became neighbours while Grain 26 and 119 were separated (figure 5.21d and 5.21f).

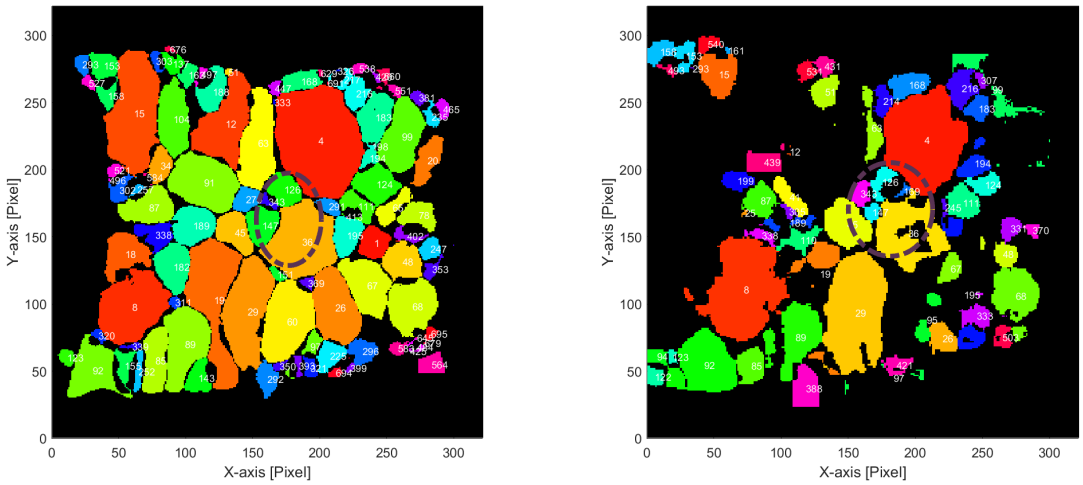

(a) Initial Scan (b) 21% Strain

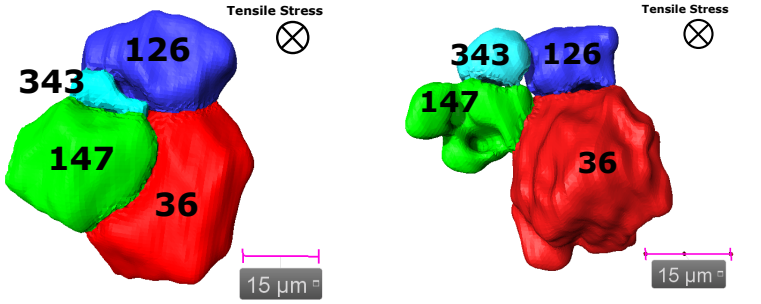

(c) Initial Scan (d) 21% Strain

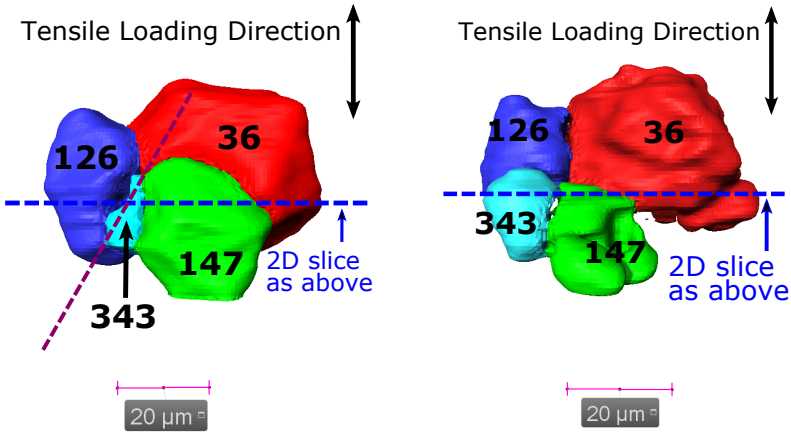

(e) Initial Scan (f) 21% Strain

Figure 5.20: 2D and 3D view of a group of grains showing neighbour switching. (a) and (b) are 2D slices showing a group of grains (circled in the middle) switched neighbours from 0 to 21% strain. (c) and (d) 3D illustration of the group of grains that switched neighbours viewed along the loading axis. (e) and (f) show the grain neighbour switching event from another direction that is perpendicular to the loading axis.

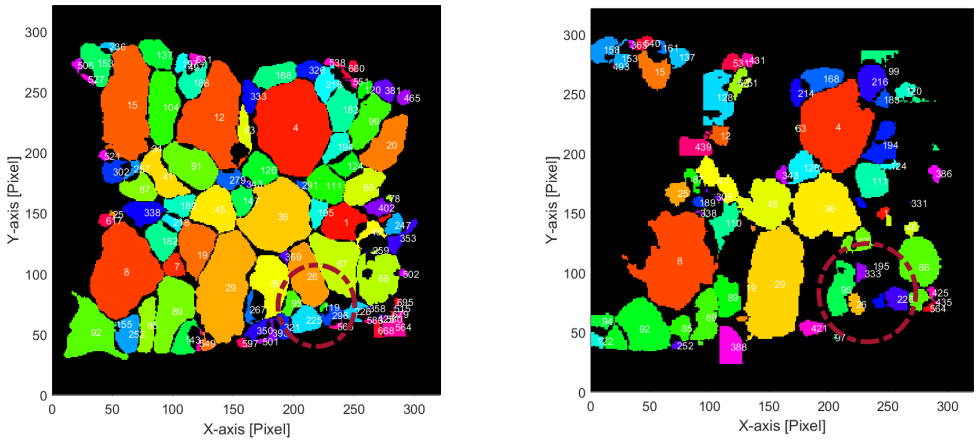

(a) Initial Scan (b) 21% Strain

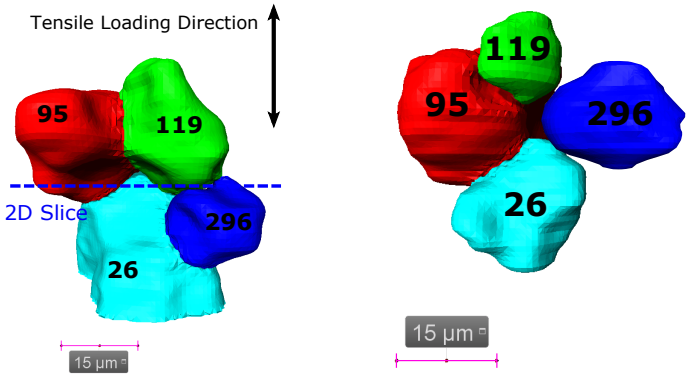

(c) Initial Scan (d) 21% Strain

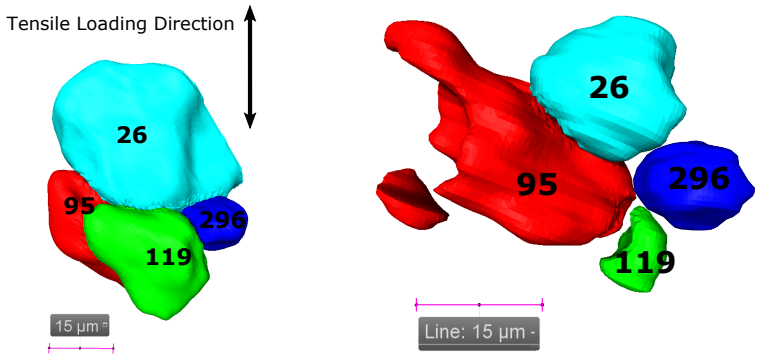

(e) Initial Scan (f) 21% Strain

Figure 5.21: 2D and 3D views of a group of grains showing neighbour switching. (a) and (b) are 2D slices showing a group of grains (circled towards the bottom right corner) that switched neighbours from 0 to 21% strain. (c) and (d) 3D illustration of the group of grains that switched neighbours. (e) and (f) Another direction of view (180° rotation from (c) and (d)) showing the grain neighbour switching event.

5.3 Discussion

5.3.1 Effective Stress-Strain Plot

In order to compare the tensile stress and strain (from the DCT in-situ tests) to the shear stress and strain (from the macro-mechanical tests in Chapter 3), all the stresses and strains were converted to effective stresses and strains. The so called invariant functions such as effective (or significant) stress and strain are frequently used to describe the plastic flow behaviour independent of the type of test [197]. The equations to calculate the effective stress and strain are given below:

$$\bar{\sigma} = \frac{1}{\sqrt{2}}\left[(\sigma_1-\sigma_2)^2+(\sigma_2-\sigma_3)^2+(\sigma_3-\sigma_1)^2\right]^{1/2} \tag{5.1}$$

$$\bar{\varepsilon} = \frac{\sqrt{2}}{3}\left[(\varepsilon_1-\varepsilon_2)^2+(\varepsilon_2-\varepsilon_3)^2+(\varepsilon_3-\varepsilon_1)^2\right]^{1/2} \tag{5.2}$$

It can be noted that the effective stress and strain reduce to normal stress and strain for a uniaxial tensile test. In the pure shear state in the macro-shear tests, the applied shear stress is τ and the shear strain is γ. The maximum shear stress is equal to the applied shear stress. The minimum and maximum normal stresses occur at 45° to the shear stresses, which are equal in magnitude to the shear stress, i.e. $\sigma_1 = \tau$ *and* $\sigma_3 = -\tau$. The principal strains are given by $\varepsilon_1 = \gamma/2$ and $\varepsilon_3 = -\gamma/2$ on a plane at 45° to the shear stress. This state of stress is identical to that when equal tensile and compressive stresses are applied in two axes. Therefore, the effective stress and strain for the pure shear state are calculated in equation 5.3 and 5.4. The effective strain rate is thus $\dot{\varepsilon}_e = \frac{1}{\sqrt{3}}\dot{\gamma}$. The simple shear stresses and strain rates are thus converted to the effective stress and strain rate as shown in figure 5.22. All the stresses of the tensile tests are above those of the shear tests for the same effective strain rate. This is because of the larger grain sizes used in the DCT experiments at ESRF. Despite this, the strain rate sensitivity is $m \approx 0.41$, which is

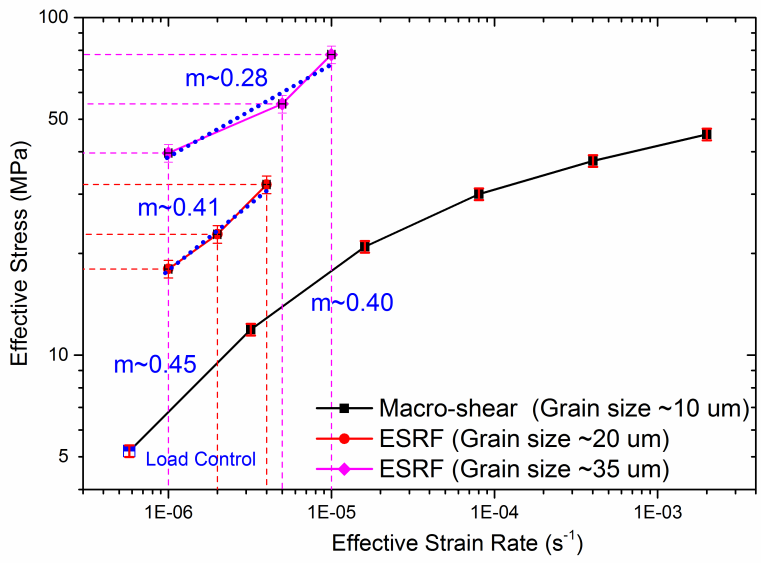

Figure 5.22: Comparison of the effective stresses and strain rates between the tensile and shear tests. The tensile stress and strain for the ESRF specimen remain the same as the effective stress and strain. The shear stress and strain for the macro-shear tests are converted to the effective stress and strain using equation 5.3 and 5.4.

at the top of Region II. Therefore, this material should have shown superplasticity during the in-situ test.

$$\sigma_e = \frac{1}{\sqrt{2}}(\tau^2 + \tau^2 + 4\tau^2)^{1/2} = \sqrt{3}\tau \tag{5.3}$$

$$\varepsilon_e = \frac{\sqrt{2}}{3}\left[\left(\frac{\gamma}{2}\right)^2 + \left(\frac{-\gamma}{2}\right)^2 + (-\gamma)^2\right]^{1/2} = \frac{1}{\sqrt{3}}\gamma \tag{5.4}$$

5.3.2 2D & 3D Grain Neighbour Switching

The conventional geometrical models of grain neighbour switching assume that the grains are in perfectly regular (hexagonal) shapes. These models predict that the minimum local true strain to achieve a full grain neighbour switching event is around 0.55 (or engineering strain of 73%) [1, 45, 177, 198]. It was found in the current study that individual groups of grains could change neighbours more quickly than the average. Three examples were presented in section

5.2.3.5 that the grains switched neighbours (in 3D) at a low local strain of 21%. Two examples of grain neighbour switching were from grains near or at the surface (figure 5.19 and 5.21). The findings are in agreement with the micro-creep tests on a Sn-Pb eutectic alloy that many surface grains tended to change neighbours several times [199]. However, in 2D surface studies, the identified grain neighbour switching could be misleading, because the 2D observation is from only one direction of view. These findings are usually based on grains showing separation or connection on the surface before and after deformation. But in reality, these grains could be in connection or separation beneath the surface without any change in neighbours. In 3D, while searching for grain neighbour switching events, a number of examples of these "pseudo" neighbour switching events were found, i.e. grain separation or connection from only certain direction(s) of view. The examples shown in section 5.2.3.5 are visualised in various angles, which demonstrates the inherent advantage of the 3D studies.

There was also one example of grain neighbour switching taking place right in the centre of the bulk (figure 5.20). The change in grains centroids is illustrated in figure 5.23a and 5.23b. The distance between the centroids of Grain 36 and 343 increased from 20.9 μm (no strain) to 26.5 μm at a true strain of 0.19 of the DCT sample volume (21% engineering strain). Calculated on the change in centroids, the true strain of this group of four grains was 0.24 (along the axis of Grain 36 and 343), which was much lower than the predicted true strain of 0.55 to achieve full neighbour switching [45, 46, 177]. This indicates the significant inhomogeneity of superplastic deformation, i.e. some groups of grains deform much faster than the average. Furthermore, in this specific example, the grain neighbour switching is producing strain in a sense different to the macroscopic strain of the specimen. This suggests that there must be grains around this group contributing to the macro-strain, which again illustrates the advantage and necessity of 3D studies.

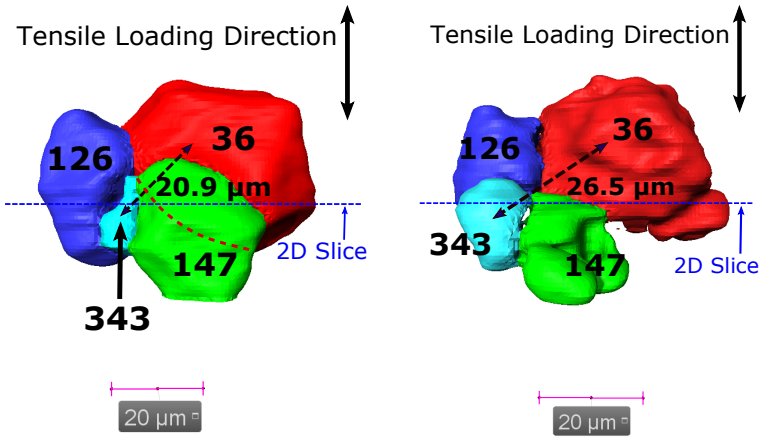

(a) Initial Scan (b) 21% Strain

Figure 5.23: 3D view of a group of grains showing neighbour switching from (a) 0 to (b) 21% local engineering strain. The distance between the centroids of Grain 36 and 343 has obviously increased.

5.3.3 Correlation to the Grain Boundary Sliding (GBS) Geometrical Models

From the results on the grain volume (section 5.2.3.2) and dimensional change along the loading axis (section 5.2.3.4), it was found that no significant grain growth or elongation had occurred on average. Furthermore, in the reconstructed grain maps at high strains, most grains were still able to be indexed. The non-indexed regions were possibly not participating in grain boundary sliding due to the inhomogeneity nature of superplasticity. Therefore, the mechanisms of grain boundary sliding in the current study do not involve widespread lattice dislocation activities. This is in agreement with the findings from the 2D surface studies of grain neighbour switching during superplasticity [1].

A few examples of grain neighbour switching have been found in the bulk and near the surface, which supported the following models: Lee's [46] model characterised by grain boundary sliding via grain boundary migration; Ashby and Verrall's [45] diffusion-accommodated grain boundary sliding model; Spingarn and Nix's diffusional flow model based on the normal tractions acting on the boundary; Gifkins' [177] model of grain emergence from other layers of grains. Lee's model, which has an intermediate process of grain boundary migration to achieve

full grain neighbour switching, was described in figure 2.10 on page 21 in the literature review. In a random polycrystal, during superplastic deformation, at a high enough macroscopic strain, there would presumably be groups of grains at all stages of the grain neighbour switching. But there was no direct experimental evidence to illustrate the intermediate stage featured by grain boundary migration. Therefore, the other three models are more likely to be appropriate as discussed below.

5.3.3.1 Ashby-Verrall Model of GBS with Migration

The Ashby-Verrall model was one of the first to describe and predict the grain boundary sliding behaviour. As shown in figure 5.24a, the grains remain thermodynamically identical (no grain elongation comparing the start with finish states) and switched neighbours after a local strain of 0.55. It was also pointed out that a smaller fraction of grains undergo neighbour switching at a lower strain than 0.55 in the specimen [45]. This is all in good agreement with the results from the current study. However, this model attributed the accommodation mechanism of grain boundary sliding to diffusion flux along and adjacent to the grain boundaries, predicting a linear relationship between stress and strain rate ($n = 1$). This is not in good agreement with most experimental data. The current 3D study has a stress dependence factor $n \approx 2.5$ (strain rate sensitivity $m \approx 0.41$).

The $n = 1$ stress dependence is based on the diffusion creep (Nabarro-Herring and Coble creep) models. Ashby-Verrall model also assumed that all the grains are in regular shapes and identical, which will all switch their neighbours after a true strain of 0.55. Ashby and Verrall suggested that at higher strains, dislocation creep is dominant and suggested an "interface reaction" effect. But this was not integrated to their model. In summary, the results of the current study is in accordance with the Ashby-Verrall model (in terms of geometry) that grain neighbour switching occurs without any net grain elongation. However, the kinetics of superplasticity proved to be more complicated than the diffusion creep model with the $n = 1$ stress dependence.

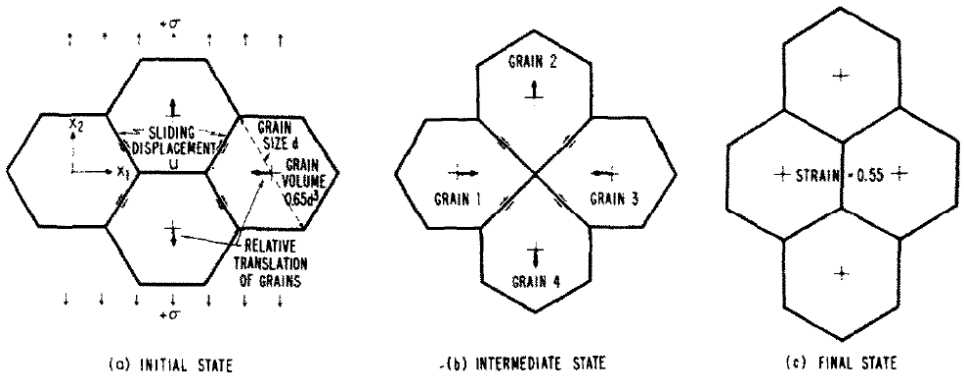

(a) After [45]

Figure 5.24: Ashby-Verrall model of grain boundary sliding accommodated by diffusion along and adjacent to the grain boundaries [45].

5.3.3.2 Gifkins Model of GBS with Grain Emergence

Another model proposed by Gifkins [177] explains the grain neighbour switching process by void formation (as illustrated in figure 5.25a) and "grain emergence" from the next layer of grains to fill the voids (figure 5.25b). However, there was no void formation in the current study based on the PCT results. Therefore, the model based on void formation is not consistent with the present study, but the grain emergence geometry is in agreement with the 3D findings of the DCT experiment. As mentioned in section 5.3.2, the grain neighbour switching events involve more than four grains and should be inspected from various directions in 3D. The grain emergence model is essentially consistent with the grain neighbour switching geometry, by viewing the group of grains at a rotation angle of 90°. In other words, the grain emergence is essentially the same as grains getting in connection to switch neighbours.

Gifkin's model not only considers the grain boundary sliding process in a 3D mode, but also takes into account of the increase in the surface area from grain neighbour switching. It is especially worth noting that the grain boundary sliding process is continuous and the characteristic pattern of grain emergence can be present at all strains. There are a few 2D surface studies that have observed grain emergence during grain boundary sliding [200, 201, 202, 203]. The current 3D study is a significant support of this model. Furthermore, as mentioned in section

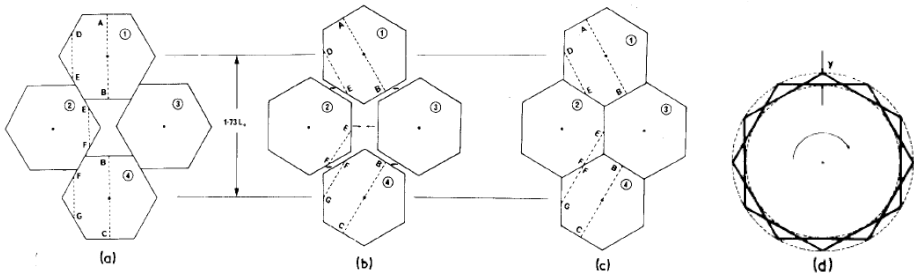

(a) After [177]

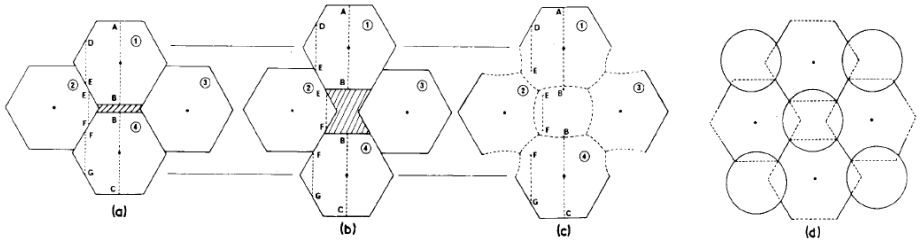

(b) After [177]

Figure 5.25: (a) Gifkin's model of grain boundary sliding via formation of voids. (b) Grain emerging from another layer to fill in the voids [177].

5.2.3.1, a strong evidence to support Gifkin's grain emergence model was that quite a number of grains were "new" as they were only present in the datasets at high strains while absent in the initial scan.

5.4 Conclusions

A novel experiment has been carried out on ID11, ESRF, using diffraction contrast tomography (DCT) to map in 3D the shapes and positions of the individual grains contained within a Sn-1%Bi alloy. It was coupled with in-situ tensile testing. Due to the strict requirements on the grain microstructure and strain rates of the mechanical tests, there was only a very small window for success of experiments. Despite this, there have been many exciting and novel outcomes as summarised below.

A fine-grained specimen was tested at a constant strain rate of ~$10^{-6}/s$ to an engineering strain of 22%. From the reconstructed PCT images, the local strain of the DCT sample volume was found to be higher than this (29%). The strain rate sensitivity index of this material was 0.41,

which was slightly lower than the maximum value measured from the macro-shear tests on specimens with a 10 μm grain size ($m \sim 0.45$). The stress was at the high end of Region II. Therefore, this material should show superplasticity.

Indexing diffraction spots of fine-grained material at large strains has long been a challenge. DCT generally works up to only 5% strain in most metallic materials. Superplastic materials have a unique advantage in this sense. This is because superplasticity occurs without intensive intragranular deformation. Using a superplastic Sn-Bi alloy, the current DCT study has expanded the strain to 29%. Due to the increased intragranular plasticity, fewer grains were indexed in the subsequent two scans at 21% and 29% strain. However, the histogram of the grain size evolution showed that the decreased number of grains was not due to grain growth. Instead, the grain size distribution of the different datasets was quite similar according to the log-normal probability plots. Therefore, grain growth was very limited during the superplastic deformation.

There was no clear trend of any increase in the grains' dimension along the loading axis. This indicated a limited amount of intragranular plasticity that would change the grain shape. Furthermore, the evolution of the grains' centroid positions was investigated. The grains showing large changes in the centroid position with deformation were candidates for searching for grain neighbour switching. By investigating the three datasets both in 2D and 3D, a few grain neighbour switching events were identified among individual groups of grains. The minimum true strain to achieve the full geometry change was calculated to be 0.55 for idealised models. But in reality, some grains switch neighbours sooner than average. Some examples have been found at a local true strain of 0.24. This finding in 3D in the bulk material is a valuable addition to the observation of grain neighbour switching in 2D [1].

Due to the limitation on the beamtime and the microstructure to be resolved by the DCT detector, the in-situ mechanical test was conducted at a low strain rate of ~$10^{-6}/s$. The low strain rate and available beamtime in the current study only allowed 22% strain (of the whole sample). Despite this, the evolution of grain size, centroid position and aspect ratio were studied. What

is more, there were some examples of grain neighbour switching given. The results of this 3D study revealed important information regarding the mechanisms of superplasticity. The findings have provided, for the first time, a full description of the evolution of grain trajectories during superplastic deformation to high creep strains, in 3D and in the bulk of samples.

Chapter 6

Overall Discussion

6.1 Micro- and Macro-tests

6.1.1 Stress against Strain Rate

In both macro- and micro-tests, a few displacement rates or strain rates were used to reach steady-state grain boundary sliding. The steady-state shear stresses for sliding could be compared between macro- and micro-tests for various strain rates. In order to convert displacement rates to strain rates for the micro-tests, an assumption is made that the deformation occurs only by grain boundary sliding. As shown in figure 6.1a, it was established in the literature review that the strain contributed by grain boundary sliding, ε_{gbs}, could be represented by $\varepsilon_{gbs} = \frac{\bar{u_l}}{\bar{L}}$, where $\bar{u_l}$ is the average value of the offset (due to sliding) along the loading axis and $\bar{L}$ is the mean linear intercept grain size [65]. The average grain size is assumed to be approximately 8.5 μm based on the microstructure of the material used in the macro-shear tests (Chapter 3). If the total strain of the specimen is attributed to grain boundary sliding, then the displacement of grain boundary sliding along the loading direction ($\bar{u_l}$) in the microcantilevers can be correlated to the macroscopic strain rate ($\dot{\varepsilon}$) when divided by the mean grain size ($\bar{L}$), i.e. $\dot{\varepsilon} \approx \dot{\varepsilon}_{gbs} = \frac{\dot{\bar{u}}_l}{\bar{L}}$. The stress against strain rate behaviour of micro-tests is compared to the macro-shear tests with logarithmic scales in figure 6.1b. The uncertainties of the stress originate from the dimen-

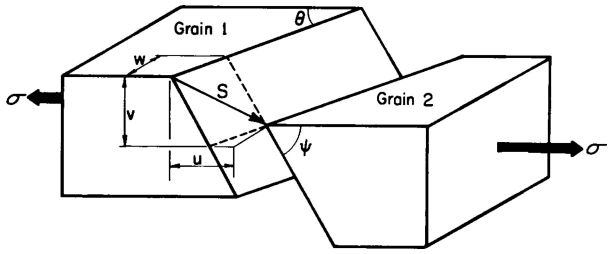

(a) After [34]

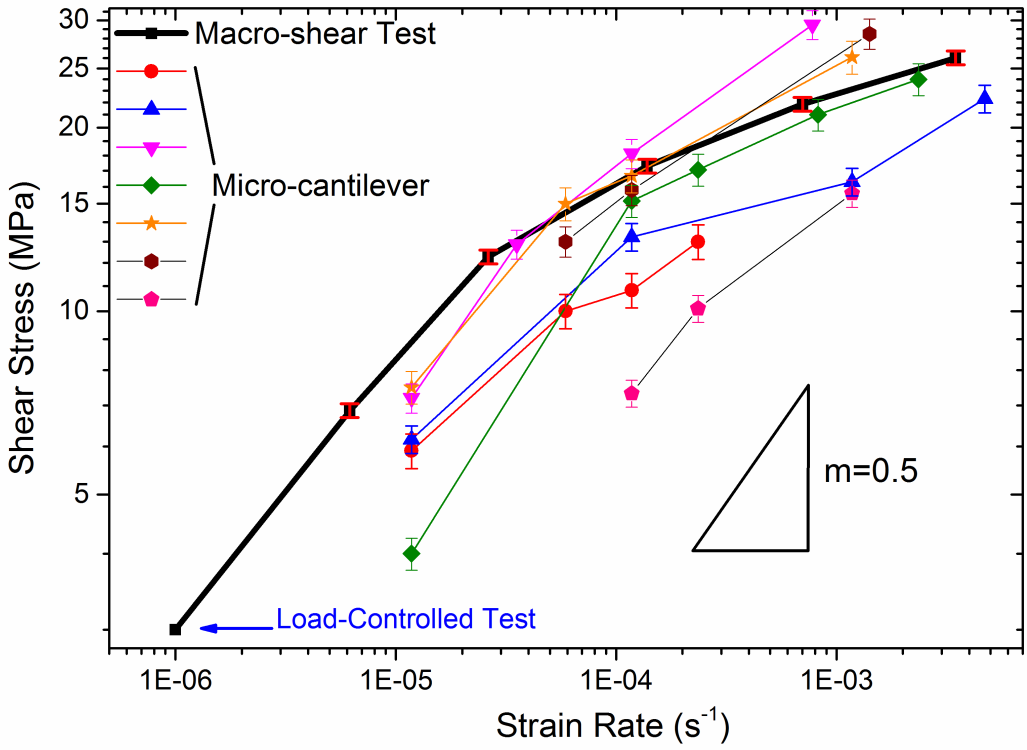

(b)

Figure 6.1: (a) Grain boundary sliding occurs between Grain 1 and 2 under an applied stress. The sliding vector *S*, can be resolved into three orthogonal components – *u*, *v* and *w*, where *u* is component along the loading axis [34]. (b) Shear stress – strain rate plots of a few microcantilevers tested at various displacement/strain rates, in comparison to the macro-shear test results.

sional measurements and the fluctuations in the steady-state stresses. The uncertainties of the displacement/strain rate are relatively small for both macro- and micro-tests. DIC was used to measure the actual displacement of the specimen in the macro-shear test. In the microcantilever tests, grain boundary sliding rates tend to be stable towards the end of the test. Therefore, the displacement rate is relatively accurate.

Despite some scatter in the micro-test data points, the overall shapes of the stress-strain rate curves are similar. The strain rate sensitivities of micro- and macro-tests follow similar trends, i.e. strain rate sensitivity index decreases as the strain rate increases. For the same strain rate, the steady-state shear stresses for the macro- and micro-tests are in the same order of magnitude. Generally, at the same or similar strain rate, the shear stress for the micro-tests is lower than that for the macro-test. This could be explained that the macro-tests have other types of deformation mechanisms such as diffusion and/or dislocation-mediated plasticity, therefore having a higher steady-state shear stress. The peak strain rate sensitivity indexes (the gradient of the line joining the first two data points of the stress-strain rate curve) are averaged to be 0.40 for the microcantilever tests, in comparison to 0.45 for the macro-shear tests.

6.1.2 Correlation to Literature Data

Using the method of stress conversion in section 5.3.1 of Chapter 5, the shear stress and strain rate measured in the macro-shear tests were converted to the effective/tensile stress and strain rate. Together with the tensile testing data from Chapter 5, they are plotted in figure 6.2a of tensile flow stress against strain rate from Alden's [167] studies on Sn-5wt% Bi alloy with various grain sizes. Another two sets of data on Sn-1wt% Bi from [141] (grain size of 1.8 μm) and [28] (grain size of 5 μm) are also included in the plot. All the data are reported as engineering stress and strain. It can be seen that the macro-shear testing results generated in the present thesis (Chapter 3) on 8.5 μm grain-sized Sn-1wt% Bi (in blue) fit in well with the overall stress-strain rate behaviour of other data points. For the same alloy composition — Sn-1wt% Bi, the grain size used in the present study is larger than that in [141] (1.8 μm) and [28] (5 μm), which shifts their curves to the left. For the ultrafine grained (1.2 μm and 1.8 μm) samples, the curves indicate that they are almost fully in Region II until $\sim 10^{-1} min^{-1}$. Compared with the Sn-5wt% Bi alloy, at low strain rates ($10^{-5} \sim 10^{-3} min^{-1}$), data from the present study (blue points) are between the 16 μm and 5.5 μm data points for Sn-5wt% Bi. However, when the strain rate is higher than $\sim 10^{-2} min^{-1}$, the stress of the 8.5 μm Sn-1wt%

Bi is slightly lower than that for the 5.5 μm Sn-5wt% Bi. One possible explanation is due to the different forms of deformation, i.e. tension and shear. In tension, at higher strain rates, the cross-section area of the specimen might have significantly changed, in comparison to the relatively constant area of the shear specimen. Another possibility lay on the differences in the chemical composition (1% and 5% Bi addition).

The DCT specimens with larger grain sizes of 20 and 35 μm could also be included in the plot without the need of stress conversion (as the tests were carried out in tension). The 35 μm data points lay well above those for all the grain sizes of Sn-5wt% Bi. The low strain rate sensitivity indicates that the 35 μm data are entirely in the plastic deformation regime, i.e. Region III. The 20 μm data points approximately overlap with the curve for the 16 μm grain-sized Sn-5wt% Bi, at the top of Region II.

The results from microcantilever tests could also be compared to those from the macro-tests on ultrafine grained Sn-1wt% Bi (figure 6.2b), by assuming that the deformation occurs entirely via grain boundary sliding in a 1.8 μm grain-sized sample (used in [141]). The shear stress and strain rate of the microcantilever tests were converted to the effective/tensile stress and strain rate. The strain rates of the micro-tests were obtained from the displacement rates divided by the assumed grain size of 1.8 μm. Both curves in figure 6.2b seem to reach Region III after a high strain rate of $\sim 10^{-1} min^{-1}$. Even though there were short of data at the lower strain rates for the micro-test to be compared to the 1.8 μm grain-sized sample, the overall trend was similar in both curves.

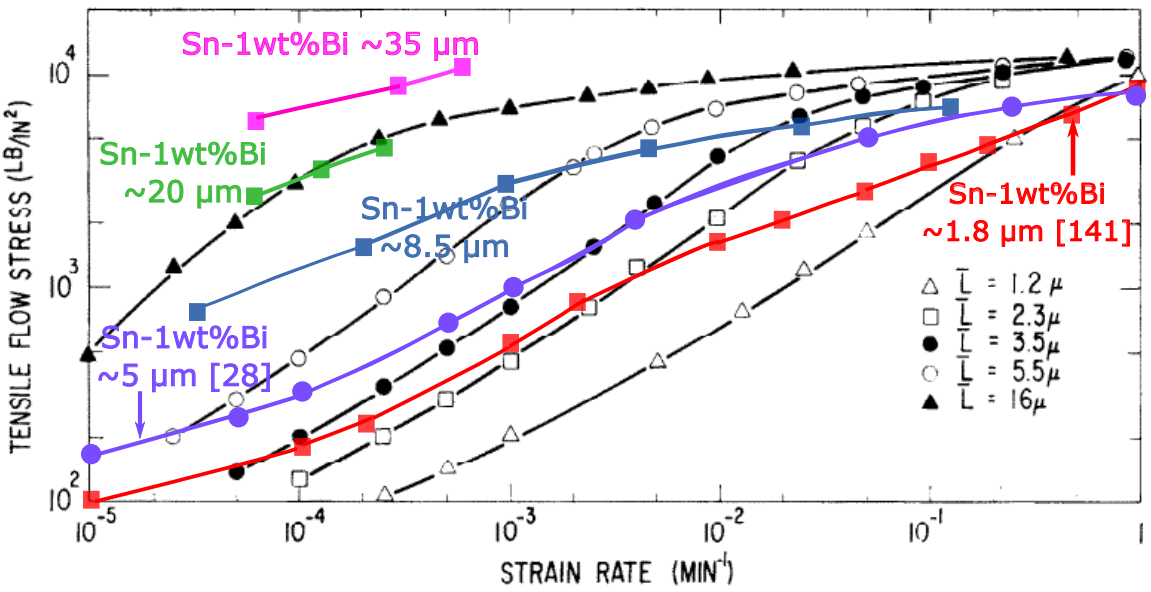

(a) Redrawn from [167]

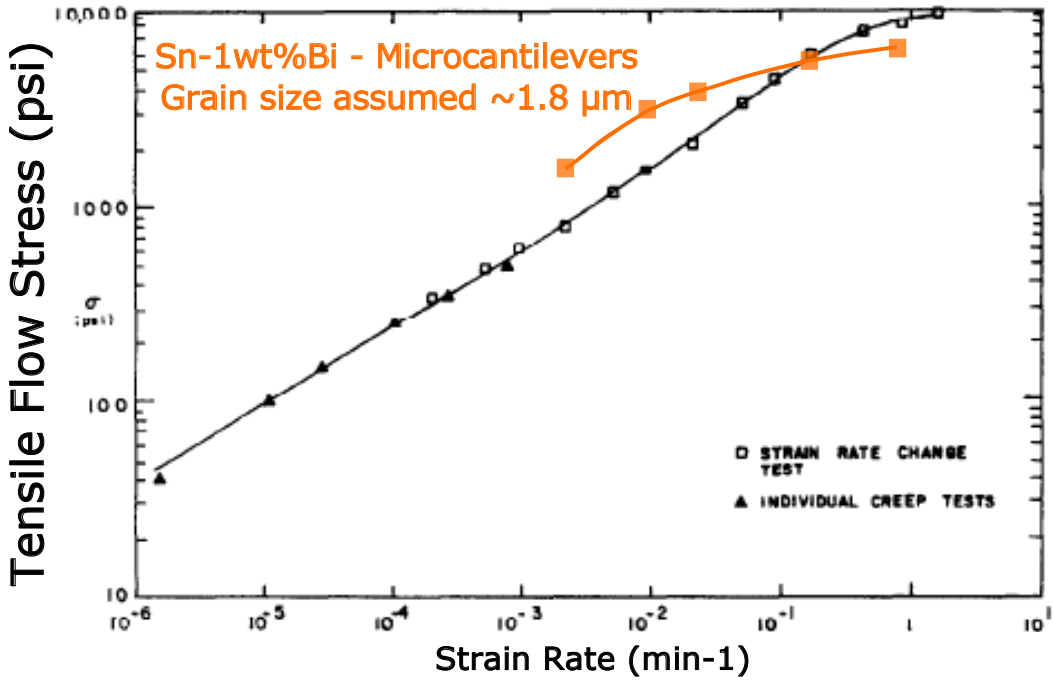

(b) Redrawn from [141]

Figure 6.2: (a) The stress-strain rate data from macroscopic tests of Sn-1wt% Bi alloy are plotted in comparison to those of the same alloy composition with 1.8 μm grain size [141] as well as 5 μm grain size [28], and Sn-5wt% Bi alloy with various grain sizes [167]. (b) Microcantilever test results are plotted in comparison to the ultrafine grained (1.8 μm) Sn-1wt% Bi [141] .

6.1.3 Grain Boundary Sliding of Low-Angle Boundaries

It was discussed in Chapter 3 on the in-situ macro-shear tests that low-angle boundaries below 4° do not slide. Unfortunately, no such grain boundary with this low misorientation angle was found in the well-annealed sample for the microcantilever tests. However, a "low-angle grain boundary" (Boundary 09: 12.4° [1 0 1] as shown in table 4.7) under the general definition (<15°) was tested using microcantilevers. There were six cantilevers made on that single grain boundary and they were repeatedly tested under nominally identical conditions. Stable sliding occurred in all those cantilevers. This finding was consistent with the results on Sn-based solder joints that boundaries with ~13° misorientations about a [1 1 0] axis were found to slide at room temperature [89]. However, this result was against the claim that low-angle grain boundaries (<15°) in zinc bicrystals were resistant to sliding owing to their low energy [148]. The contradiction indicates that the misorientation angle of a grain boundary by itself is not enough to determine its tendency to sliding. From the results in section 4.2.2 and 4.2.3 of Chapter 4, it was found that grain boundary rotation axis and grain boundary plane play important roles as well.

6.2 DCT and Macro-shear Tests

It was found in the DCT experiment that grain neighbour switching could happen at a true strain as low as 0.24, rather than 0.55 predicted by the classical models. This can be attributed to the inhomogeneity of superplasticity. This inhomogeneity was also found in the macro-shear tests discussed in Chapter 3, where some regions (containing a large fraction of low-angle boundaries) remained inactive after a large amount of strain in the whole sample. Similar to the DCT experiment, the observation from the in-situ surface studies also showed a few grain neighbour switching events up to 50% engineering shear strain. Some groups of grains switched neighbours faster than others. This inhomogeneity indicates the complexity of the process of grain boundary sliding and superplasticity, which could explain why the experimental results

are not well described by the classical models of diffusion creep or grain boundary sliding. The findings of the present research are compared to these models in the following section.

6.3 Models of Grain Boundary Sliding

6.3.1 Geometry

Based on the 2D and 3D observations, the grain neighbour switching geometry change is consistent with the Rachinger grain boundary sliding model (figure 2.5). Especially in 3D-DCT study, the reduction in the number of grains in the cross sections indicates an increase of number of grains along the tensile direction. The absence of obvious grain elongation also supports Rachinger sliding over Lifshitz sliding (grain elongation via diffusion creep). However, the deformation process was found to be much more complicated than the idealised Rachinger model. There were only limited number of groups of grains exhibiting grain neighbour switching, while many grains did not switch neighbours. This is in consistence with the so-called "cooperative grain boundary sliding" experimentally observed in many 2D studies [32, 160, 204, 205, 206]. The cooperative sliding is usually coupled with grain emergence as shown in figure 6.3 [207]. This geometry model proposed by Hazzledine and Newbury [207] is an extrapolation of Gifkin's 2D "grain emergence" model to the 3D cases. This model is supported by the present study in that quite a number of "new" grains were found in the subsequent datasets (at high strains) while absent in the initial DCT scan. This can be a result of "grain emergence" from other layers. This phenomenon was also indicated by the 2D slices of the DCT sample volume, where the grains were usually different on slices at similar positions in the sample between different scans. This model could also illustrate the limitations of surface observations of grain neighbour switching, because a group of more than four grains are usually required to be inspected in 3D.

Another geometry model proposed by Sotoudeh and Bate [208] is based on strain induced geometrical dynamic recrystallisation. As shown in figure 6.4a, the microstructure before de-

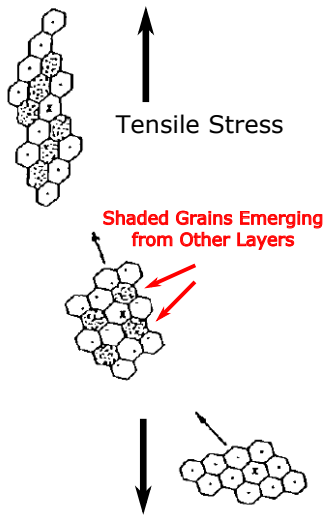

Figure 6.3: A schematic diagram showing a model of cooperative grain boundary sliding with grain emergence (After [207]).

formation is formed of banded structures (consisting of subgrains) elongated along the rolling direction. After testing, the grains become relatively equiaxed after dynamic recrystallisation (figure 6.4b). The present study on Sn-Bi is not consistent with this geometry model, because the grains maintained their integrity without much change in the grain size. In another commercial aluminium alloy with equiaxed microstructures, the superplastic behaviour was attributed to diffusion creep and Lifshitz sliding [208]. The present study does not support this model, based on the observation of grain neighbour switching in the bulk material (Rachinger sliding) and the absence of significant grain elongation (not Lifshitz sliding).

(a) Before Testing [208]

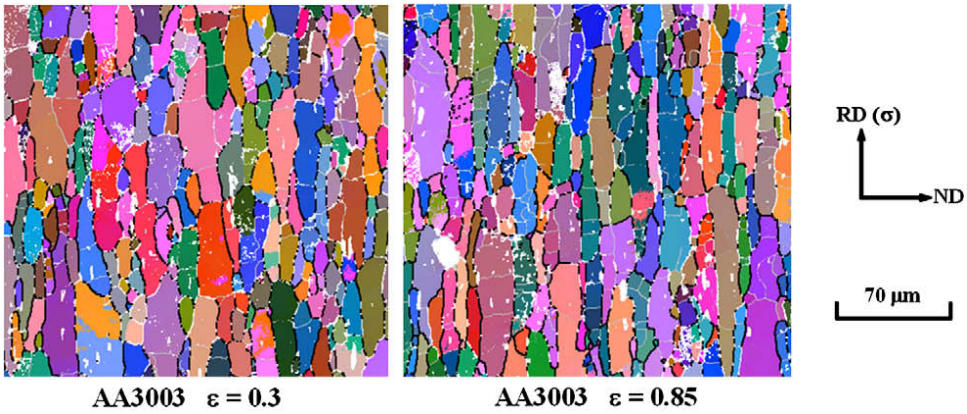

(b) After Testing [208]

Figure 6.4: (a) EBSD orientation image micrograph of the microstructure of an aluminium alloy – AA3003 prior to tensile testing. (b) The microstructure of the AA3003 alloy after tensile testing at 0.86 homologous temperature with a strain rate of $5 \times 10^{-4} s^{-1}$ [208].

6.3.2 Kinetics

The micro-tests investigate the rate of grain boundary sliding individually and separately from diffusion creep. It was found that at the same stress, the strain rate of grain boundary sliding is generally higher than the macroscopic strain rate (figure 6.1b). This indicates that there are other rate controlling processes in the macroscopic polycrystals, such as diffusional flow or dislocation motion. The results from the diffusion creep test (which separates diffusion creep from grain boundary sliding) indicate that diffusional flow of matter is rather slow at the grain boundary. This might be attributed to the "interface reaction" as the rate controlling process (i.e. creation or annihilation of vacancies at the grain boundary).

For the macro-tests, despite decades of experimental and theoretical research, the kinetics of superplasticity has never been satisfactorily explained. The classical diffusion creep models give a stress exponent $n \approx 1$, but in superplasticity the strain rate and stress relationship is typically $n \approx 2$. In the present study, the stress exponent was found to be $n \approx 2.2 \sim 2.5$, which was correlated to the two main mechanisms proposed to accommodate grain boundary sliding. The first type is based on diffusion flux along and adjacent to the grain boundaries. This mechanism is predominant in the models proposed by Ashby and Verrall [45], Spingarn and Nix [209]. When diffusion rate is controlled by the "interface reaction" rather than the diffusion rate of vacancies/atoms, these diffusion-based models could give $n > 1$. In summary, the macro-shear and in-situ DCT experiments were in consistence with these models in geometry as there were grain neighbour switching events, little grain elongation or grain growth, and limited dislocations activities. However, the kinetics of superplasticity is not satisfactorily explained by these models.

The second type of model is based on dislocation motion from the head of a pileup. This model was first proposed by Ball and Hutchinson [49] and modified by Mukherjee [210] and Gifkins [201]. As shown in figure 6.5a and 6.5b, grain boundary sliding is blocked at a triple point and the stress concentration is relieved by lattice dislocation motion in the blocking grain as a form of pileup at the opposite grain boundary [49]. The rate controlling process is therefore the climb of head dislocation along the grain boundary under the back stress, giving a stress component of $n \approx 2$ [211, 53]. Even though this model could potentially explain $n \approx 2$ in superplasticity, there is a lack of direct experimental evidence of dislocation pileup at the grain boundary. Another model based on intragranular dislocation activity was proposed by Bate and Humphreys [212], in which the crystallographic texture changes were attributed to intragranular slip as the dominant mechanism of superplasticity.

The in-situ 3D DCT experimental results of the present study do not support the dislocation pileup model [49, 210, 201] or Bate and Humphrey's intragranular slip model [212]. If these models were correct, there would have been extensive dislocation activities in the whole sample

and DCT would not have worked up to 29% strain. However, this was not the case in the current DCT study. Even though there were some non-indexed regions due to dislocation-mediated plasticity, the majority of the grains were still able to be indexed and reconstructed. Taking into account of the notable inhomogeneity seen in the macro-shear tests, the non-indexed regions were likely to be consisted of inactive grain boundaries, thereby undergoing dislocation-mediated plasticity. In contrast, the well-indexed regions of the DCT sample exhibited significant grain rearrangements via grain boundary sliding.

In summary, neither diffusion nor dislocation based mechanism could accommodate grain boundary sliding on its own. On the one hand, in order to maintain the integrity of grain structure after grain boundary sliding (to avoid formation of voids), it is essential to have diffusion flow of matter along grain boundaries and at triple points. On the other hand, diffusion creep proved to be slow in the long microcantilever creep tests. It is much slower than the rate predicted by the classical models (Coble creep). Therefore, grain boundary sliding accommodated exclusively by diffusion flow would be slower than the macroscopic strain rate in superplasticity. This indicates that there are some other accommodation mechanisms involved, such as dislocation activities.

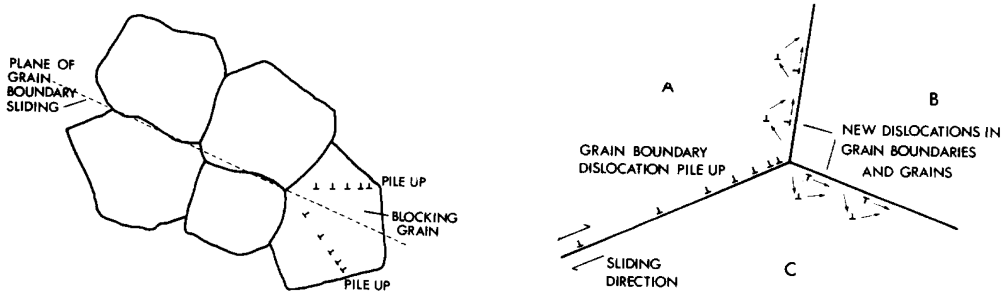

(a) After [49] (b) After [201]

Figure 6.5: (a) Dislocation pileup model proposed by Ball and Hutchinson [49]. (b) Similar pileup model modified by Gifkins [201].

Chapter 7

Conclusions and Future Work

Conclusion

In addition to the conclusions made at the end of the chapters, the following overall conclusions can be drawn:

- The in-house processed material (through casting, cold extrusion and rolling) proved to be superplastic at room temperature through a series of strain rate jump tests. The strain rate sensitivity index was found to be $m \approx 0.45$, which was slightly lower than the highest strain rate sensitivity ($m \approx 0.48$) reported for the Sn-1wt% Bi alloy [28]. Interestingly, $m \approx 0.48$ was found in this alloy with a grain size of 8.5 μm [28], but $m \approx 0.45$ was found for a grain size of 1.8 μm [141]. This indicates the complexity of the effect of grain size on superplasticity.

- In conventional mechanical tests on superplasticity in polycrystalline materials, grain boundary sliding and diffusion creep are always coupled with each other. Many mechanisms proposed by researchers are based on diffusion-accommodated grain boundary sliding, but the kinetics of both diffusion creep and grain boundary sliding is not well understood. The novel design of microcantilevers containing individual grain boundar-

ies has enabled grain boundary sliding and diffusion creep to be investigated separately by varying the stress conditions on the grain boundary.

- For tests on grain boundary sliding, short cantilevers (10 μm long) are used and the shear stress is more significant than the normal stresses, thereby exhibiting grain boundary sliding. For long cantilevers, the normal stresses are one to two orders of magnitude larger than the shear stress. So diffusion creep should be more favourable than grain boundary sliding.

- Diffusion flow at grain boundaries was found to be slower than that predicted by the classical models based on Coble creep.

- Grain boundary sliding is strongly dependent on the grain boundary structure, i.e. misorientation angle, rotation axis and grain boundary plane orientation.

- The tests proved to be reproducible through repeated tests on the same cantilevers and different cantilevers on the same boundary under nominally identical conditions. The steady-state shear stress for grain boundary sliding is in the same order of magnitude ($\sim 10\,MPa$) as the macro-shear tests.

- Grain boundary migration coupled with sliding was observed in both macro and micro-tests. It could potentially be explained by the grain boundary migration model associated with extrinsic secondary grain boundary dislocations motion.

- The in-situ tensile test coupled with DCT has revealed superplasticity in 3D for the first time. The grain size/volume was found to be relatively consistent across the datasets before and after loading. Little grain elongation was observed along the loading direction, i.e. there was little change in the grain shapes.

- Grain neighbour switching events were inspected in 3D in the bulk material, which was free from the artefacts associated with the conventional 2D surface studies.

- Significant inhomogeneity of superplastic deformation is also observed in 3D, where some groups of grains switch neighbours sooner than the average. They tend to switch neighbours at a true strain lower than the predicted strain (0.55) to achieve full grain neighbour switching according to the classical models of grain boundary sliding.

- Neither diffusion flow nor dislocation activities could accommodate grain boundary sliding alone. Diffusion flow is necessary to maintain the integrity of the grain structure after grain boundary sliding, while itself is too slow to match the macroscopic strain rate in superplasticity.

Future Work

Macro-tests

- For in-situ tests, the grain boundary characters (from EBSD) can be linked to their tendency to sliding (from SEM images). After testing, it would be feasible to make cantilevers on the grain boundaries that have not slid not as much or not at all. The results could be correlated to the findings in Chapter 4 on micro-mechanical tests.

- Digital Image Correlation (DIC) could be used on the in-situ SEM images to measure the amount of grain boundary sliding quantitatively.

- The in-situ test results on various grain-sized samples could be implemented in constitutive equations for numerical modelling techniques on grain boundary sliding.

Micro-tests

- It was found in the macro-shear tests that grain/subgrain boundaries below 4° were resistant to sliding. Therefore, it is worth making microcantilevers on the low-angle grain

boundaries below 4°. Individual grain boundary sliding tests will further investigate their tendency to sliding.

- The grain boundary sliding behaviour is strongly dependent on the grain boundary structure. Some visualisation software will be helpful to inspect the atomic arrangements at the grain boundary to be correlated to their tendency to sliding.

- Further investigation should be made on microscopic diffusion creep tests using long cantilevers. To achieve higher displacements, load controlled tests should be conducted and the displacement could be measured using SEM images after testing.

- The kinetics of superplasticity has suggested that dislocation motion could be one of the accommodation mechanisms of grain boundary sliding. Therefore, TEM characterisation could be conducted before and after microcantilever testing to investigate the role of dislocations in grain boundary sliding.

DCT

During the beam-time at ESRF, a far-field detector was also used together with the near-field DCT for quick in-situ measurements of grain reorientation during straining. The far-field diffraction data were collected every 0.6% strain without interruption to the straining of specimen. However, the far-field data has not been processed due to the time limit. On the one hand, the far-field detector has the best possible angular sensitivity if the diffraction spots are processed with the concept of Friedel pairs [186]. The data could provide more accurate information on the grain orientation than the DCT technique. On the other hand, the use of far-field detector would reduce the spatial resolution, which is the key to tracking the grain positions. Therefore, the near-field DCT technique combines good angular and spatial resolutions.

In the future, with the development of DCT detector and data processing techniques, the grain size of the specimen could be pushed towards 10 μm. The finer microstructure would enhance the superplastic mechanism, thereby enabling a faster strain rate to be used during straining

(~$10^{-5}/s$) and larger creep strains (~55%) to be attained. Such creep strains will allow grain neighbour switching and other aspects of grain trajectories to be observed more fully. In the near future, the X-ray flux will be increased by 10 to 100 times at ESRF by 2020. This will enable acquisition of 4D continuous observation (real-time videos) on the deforming microstructures.

As for the DCT scan techniques, the undeformed specimen could be scanned using the high-resolution detector as in the current experiment. Once the initial grain structure was fully observed, the subsequent DCT scans with in-situ loading could be conducted on a medium resolution, high-speed detector system. The data collection is about ten times faster than the high resolution detector. The greater efficiency of the medium resolution detector would acquire enough diffraction spots to determine changes in grain orientation within a shorter time. Since the strain was minimal during the time of a DCT scan, the in-situ loading process would not be interrupted. This ensures that no stress relaxation would occur during the entire loading process. In addition, with progress in the reconstruction algorithm, the diffraction spots at large strains could still be indexed.

In summary, future experiments should be aimed to extend the understanding from the current experiment to much larger creep strains (55% strain), thereby enabling the complete evolution of microstructural phenomena during superplastic deformation – grain boundary sliding, grain reorientation, grain rearrangement and neighbour switching – to be studied. This requires the following improvement to prevent the specimen from necking and ensure that grain boundary sliding is the dominant deformation mechanism:

1. With the improvement on the DCT detector and reconstruction algorithm, finer grain could be detected and indexed. This will promote superplasticity and enable observation of more grain neighbour switching events.

2. The contribution of superplasticity to the total deformation is dependent on the strain rate. In the current experiment conducted on samples with 20 μm grains, a strain rate of as low

as $10^{-6}/s$ was necessary to ensure superplasticity to occur. But even a slight increase in the strain rate led to the necking of the specimen. If finer-grained (10 μm) specimens were used, the tests could be much faster, which would achieve a larger strain as well. For a standard beamline time of four days, around ten DCT scans could be conducted without any interruption to the in-situ mechanical test (scans at 5% strain intervals up to 55%).

3. Another improvement to make is the surface finish. Electro-polishing could be conducted to achieve a smooth surface finish at the gauge of the specimen, which would effectively prevent necking from initiating at the rough surfaces.

Bibliography

[1] M. A. Rust and R. I. Todd. Surface studies of Region II superplasticity of AA5083 in shear: Confirmation of diffusion creep, grain neighbour switching and absence of dislocation activity. *Acta Materialia*, 59(13):5159–5170, 2011.

[2] Terence G. Langdon. Grain boundary sliding revisited: Developments in sliding over four decades. *Journal of Materials Science*, 41(3):597–609, 2006.

[3] K. D Sheffler and G. S Doble. Influence of creep damage on the low cycle thermal-mechanical fatigue behavior of two tantalum-base alloys. *Manager*, 1972.

[4] A. J. Barnes. Superplastic forming 40 years and still growing. *Journal of Materials Engineering and Performance*, 22(10):2935–2949, 2013.

[5] W A Rachinger. Relative grain translations in the plastic flow of aluminium. *J. Inst. Metals*, 1952.

[6] I M Lifshitz. On the theory of diffusion-viscous flow of polycrystalline bodies. *Soviet Physics JETP*, 1963.

[7] Terence G. Langdon. Grain boundary sliding as a deformation mechanism during creep. *Philosophical Magazine*, 22(178):689–700, 1970.

[8] J E Bird, A K Mukherjee, J E Dorn, and D G Brandon. Quantitative relation between properties and microstructure: proceedings of an international conference. Jerusalem, 1969. Israel Universities Press.

[9] M. F. Ashby. A first report on deformation-mechanism maps. *Acta Metallurgica*, 20(7):887–897, 1972.

[10] AH Chokshi and TG Langdon. Characteristics of creep deformation in ceramics. *Materials Science and Technology*, 1991.

[11] Wiliam. F Hosford. *Mechanical Behavior of Meterial*. 2005.

[12] F. R N Nabarro. Do we have an acceptable model of power-law creep? *Materials Science and Engineering: A*, 387-389(1-2 SPEC. ISS.):659664, 2004.

[13] J Harper;J.E Dorn. Viscous creep of aluminum near its melting temperature. *Acta Metallurgica*, 5(November), 1957.

[14] O. D. Sherby and P. M. Burke. Mechanical behavior of crystalline solids at elevated temperature. *Progress in Materials Science*, 13:323–390, 1968.

[15] Farghalli A. Mohamed and Terence G. Langdon. The transition from dislocation climb to viscous glide in creep of solid solution alloys. *Acta Metallurgica*, 22(6):779–788, 1974.

[16] M. E. Kassner. Harper-Dorn Creep. *Fundamentals of Creep in Metals and Alloys: Third Edition*, 23:109–128, 2015.

[17] Christopher Michael Sellars and A G Quarrell. High-Temperature Creep of Gold-Nickel Alloys. *Journal of the Institute of Metals*, 90(9):329, 1962.

[18] P. Yavari, F.A. Mohamed, Terence G. Langdon, Parviz Yavari, Farghalli A. Mohamed, Terence G. Langdon, P. Yavari, F.A. Mohamed, and Terence G. Langdon. Creep and substructure formation in an Al-5% Mg solid solution alloy. *Acta Metallurgica*, 29(8):1495–1507, 1981.

[19] Conyers Herring. Diffusional Viscosity of a Polycrystalline Solid. *Journal of Applied Physics*, 21(5):437, 1950.

[20] R. L. Coble. A model for boundary diffusion controlled creep in polycrystalline materials. *Journal of Applied Physics*, 34(6):1679–1682, 1963.

[21] X. Q. Shi, Z. P. Wang, Q. J. Yang, and H. L. J. Pang. Creep Behavior and Deformation Mechanism Map of Sn-Pb Eutectic Solder Alloy. *Journal of Engineering Materials and Technology*, 125(1):81, 2003.

[22] R N Stevens. Grain-boundary sliding in metals. *Metallurgical Reviews*, 1966.

[23] B. Cai, Q. P. Kong, P. Cui, L. Lu, and K. Lu. Creep behavior of cold-rolled nanocrystalline pure copper. *Scripta Materialia*, 45(12):14071413, 2001.

[24] X. Zhang, H. Wang, R. O. Scattergood, J. Narayan, C. C. Koch, A. V. Sergueeva, A. K. Mukherjee, J Narayan; C C Koch, A. V. Sergueeva, and A. K. Mukherjee. Studies of deformation mechanisms in ultra-fine-grained and nanostructured Zn. *Acta Materialia*, 50(19):48234830, 2002.

[25] C.E.Pearson. The viscous properties of extruded euteetic alloys of lead-tin and bismuth-tin. *Journal of Inst. Metals*, 54, 1934.

[26] O A Kaibyshev and Farid Z Utyashev. *Superplasticity : microstructural refinement and superplastic roll forming*. Number 3. Futurepast, Arlington, Va., 2005.

[27] G. J. Davies, J. W. Edington, C. P. Cutler, and K. A. Padmanabhan. Superplasticity: A review. *Journal of Materials Science*, 5(12):1091–1102, 1970.

[28] T.H. Alden. Superplastic behavior of a solid-solution Sn-1 pct Bi alloy. *TRANSACTIONS OF THE METALLURGICAL SOCIETY OF AIME.*, 236:1633, 1966.

[29] Amiya K. Mukherjee. An examination of the constitutive equation for elevated temperature plasticity. *Materials Science and Engineering A*, 322(1-2):1–22, 2002.

[30] N. A. Mara, A. V. Sergueeva, T. D. Mara, S. X. McFadden, and A. K. Mukherjee. Superplasticity and cooperative grain boundary sliding in nanocrystalline Ni3Al. *Materials Science and Engineering A*, 463(1-2):238–244, 2007.

[31] A. V. Sergueeva, N. A. Mara, R. Z. Valiev, and A. K. Mukherjee. Elevated temperature behavior of SePD materials: Superplasticity or enhanced ductility? *Materials Science and Engineering: A*, 410-411:413–416, 2005.

[32] A V Sergueeva, N A Mara, N A Krasilnikov, R Z Valiev, and A K Mukherjee. Cooperative grain boundary sliding in nanocrystalline materials. *Philosophical Magazine*, 86(36):5797–5804, 2006.

[33] W.R. Cannon, Roger W Cannon, and W.R. Cannon. The contribution of grain boundary sliding to axial strain during diffusion creep. *Philos. Mag*, 25(6):1489–97, 1972.

[34] Terence G. Langdon. Grain boundary sliding revisited: Developments in sliding over four decades. *Journal of Materials Science*, 41(3):597–609, 2006.

[35] Atul H. Chokshi. Role of diffusion creep in the superplastic deformation of 3 mol% yttria stabilized tetragonal zirconia. *Scripta Materialia*, 42(3):241–248, 2000.

[36] T G Langdon and R B Vastava. An evaluation of deformation models for grain boundary sliding. *Testing for Deformation Model*, 1982.

[37] X Y Pang, R Janisch, and A Hartmaier. Interplanar potential for tension-shear coupling at grain boundaries derived from ab initio calculations. *Modelling and Simulation in Materials Science and Engineering*, 24(1):015007, 2016.

[38] R. C. Gifkins. Diffusional Creep Mechanisms. *Journal of the American Ceramic Society*, 51(2):69–72, 1968.

[39] R. Raj and M. F. Ashby. On grain boundary sliding and diffusional creep. *Metallurgical Transactions*, 2(4):1113–1127, 1971.

[40] J. R. Spingarn and W. D. Nix. Diffusional Creep and Diffusionally Accommodated Grain Rearrangement. *Acta Metall.*, 26(9):1389–1398, 1978.

[41] R. C. Gifkins. Grain-boundary participation in high-temperature deformation: An historical review. *Materials Characterization*, 32(2):59–77, 1994.

[42] R S Gates. The role of grain boundary dislocations in grain boundary sliding. *Acta Metallurgica*, 1973.

[43] W. Bollmann. On the geometry of grain and phase boundaries. *Philosophical Magazine*, 16(140):383–399, 1967.

[44] R. C. Pond, D. A. Smith, and P. W. J. Southerden. On the role of grain boundary dislocations in high temperature creep. *Philosophical Magazine A*, 37(1):27–40, 1978.

[45] M. F. Ashby and R. A. Verrall. Diffusion-accommodated flow and superplasticity. *Acta Metallurgica*, 21(2):149–163, 1973.

[46] D Lee. Structural changes during the superplastic deformation. *Metallurgical and Materials Transactions B*, 1(January):1969–1971, 1970.

[47] Y Ishida and M. Henderson Brown. Dislocations in grain boundaries and grain boundary sliding. *Acta Metallurgica*, 15(May):857–860, 1967.

[48] T L Lin and D McLean. Changes produced by deformation in grains and grain boundaries of nickel. *Metal Science*, 1968.

[49] A. Ball and M.M. Hutchinson. Superplasticity in the aluminum-zinc eutectoid. *Metal Science Journal*, 3:1–7, 1969.

[50] Amiya K. Mukherjee. The rate controlling mechanism in superplasticity. *Materials Science and Engineering*, 8(2):83–89, 1971.

[51] F. W. Crossman and M. F. Ashby. The non-uniform flow of polycrystals by grain-boundary sliding accommodated by power-law creep. *Acta Metallurgica*, 23(4):425–440, 1975.

[52] O A Kaibyshev, R Z Valiev, and A K Emaletdinov. Deformation mechanisms and the theory of structural superplasticity of metals. *Physica Status Solidi (a)*, 90(1):197–206, 1985.

[53] R I Todd. Critical review of mechanism of superplastic deformation in fine grained metallic materials. *Materials Science and Technology*, 16(11-12):1287–1294, nov 2000.

[54] L.C.A. Samuelsson, K. N. Melton, and J. W. Edington. Dislocation structures in a superplastic Zn-40wt% Al alloy. *Acta Metallurgica*, 24(11):1017–1026, 1976.

[55] K N Melton and J W Edington. Superplasticity in Extruded Zn-40wt.-%Al and Zn-50wt.-% Al Alloys. *Metal Science Journal*, 7(1):172–175, jan 1973.

[56] K. Nuttall and R. B. Nicholson. Microstructure of superplastic alloys. *Philosophical Magazine*, 17(149):1087–1091, 1968.

[57] H. Naziri, R. Pearce, M. Menderson Brown, and K.F. Hale. In situ superplasticity experiments in the 1 million volt electron microscope. *In Situ*, 3(September 1952):519–520, 1973.

[58] R King, R W Cahn, and B Chalmers. Mechanical Behaviour of Crystal Boundaries in Metals. *Nature*, 161, 1948.

[59] K.E Puttick and R King. Boundary slip in bicrystals of tin. *Journal of the Institute of Metals*, 80(10):537, 1952.

[60] Brian Tuck. Grain Boundary Sliding in Bicrystals of Tin. *physica status solidi (b)*, 8(1):153–159, 1965.

[61] R L BELL and N B W THOMPSON. Grain-Boundary Sliding. *Nature*, 193(4813):363–364, jan 1962.

[62] W Rosenhain and D Ewen. Intercrystalline cohesion in metals. *Journal of the Institute of Metals*, 8:149–185, 1912.

[63] Herbert Fisher Moore, Bernard B Betty, and Curtis Walter Dollins. Creep and fracture of lead and lead alloys: a report. *University of Illinois at Urbana Champaign, College of Engineering. Engineering Experiment Station.*, 1935.

[64] R. L. Bell and T. G. Langdon. An investigation of grain-boundary sliding during creep. *Journal of Materials Science*, 2(4):313–323, 1967.

[65] Terence G. Langdon. An evaluation of the strain contributed by grain boundary sliding in superplasticity. *Materials Science and Engineering A*, 174(2):225–230, 1994.

[66] Terence G. Langdon. The role of grain boundaries in high temperature deformation. *Materials Science and Engineering: A*, 166(1-2):67–79, 1993.

[67] A P Sutton and R W Balluffi. Interfaces in crystalline materials. *Interfaces in crystalline materials*, 1995.

[68] J. W. Cahn. Transitions and Phase Equilibria among Grain Boundary Structures. *J. Phys. Colloques*, 43(C6):199–213, 1982.

[69] W. T. Read and W. Shockley. Dislocation models of crystal grain boundaries. *Physical Review*, 78(3):275–289, 1950.

[70] P Lejcek. Grain Boundaries : Description , Structure. *Grain boundary Segregation in Metals*, page 239, 2010.

[71] Orientation Maps. Generating Orientation Maps to Present EBSD Data. *Oxford Instruments*, pages 1–14, 2015.

[72] P Lagarde and M Biscondi. Fluage intergranulaire de bicristaux symétriques de flexion autour de <100> dans l'aluminium. *Canadian Metallurgical Quarterly*, 13(1):245–251, jan 1974.

[73] G R Kegg, C A P Horton, and J M Silcock. Grain boundary dislocations in aluminium bicrystals after high-temperature deformation. *Philosophical Magazine*, 27(5), 1973.

[74] N J M Horton, C A P; Silcock. Grain boundary dislocations and the mechanism of sliding in symmetrical [011] tilt Al bicrystals. *Journal of Microscopy*, 102(December), 1974.

[75] Tadao Watanabe and Peter W. Davies. Grain boundary sliding and intergranular fracture behaviour of copper bicrystals. *Philosophical Magazine A*, 37(January 2014):649–681, 1978.

[76] Hidetoshi Somekawa and Toshiji Mukai. Effect of grain boundary structures on grain boundary sliding in magnesium. *Materials Letters*, 76(April 2014):32–35, 2012.

[77] H. Watanabe, M. Fukusumi, H. Somekawa, and T. Mukai. Texture and mechanical properties of superplastically deformed magnesium alloy rod. *Materials Science and Engineering A*, 527(23):6350–6358, 2010.

[78] H Kokawa, T Watanabe, A Uehara, and S Karashima. Observations of grain boundary fine structures in zinc by transmission electron microscopy. *Scripta Metallurgica*, 12(4):357–359, apr 1978.

[79] Tadao Watanabe, Masayuki Yamada, Seiichi Karashima, and Seishi Shima. Misorientation dependence of grain boundary sliding in <1010> tilt zinc bicrystals. *Philosophical Magazine A*, 40(5):667–683, 1979.

[80] B. Michaut, A. Silvent, and G. Sainfort. Intergranular creep of stainless steel bicrystals. *Memoires Scientifiques de la Revue de Metallurgie*, 71(9):527–538, 1974.

[81] R C Pond and D A Smith. On the absorption of dislocations by grain boundaries. *Philosophical Magazine*, 36(2):353–366, 1977.

[82] Hiroyuki Kokawa, Tadao Watanabe, and Seiichi Karashima. Sliding behaviour and dislocation structures in aluminium grain boundaries. *Philosophical Magazine A*, 44(6):1239–1254, 1981.

[83] W Assassa, P Guiraldenq, L Beaunier, and M Froment. Les Joints Intergranulaires Dans Les Metaux Autodiffusion Intergranulaire Dans Des Bicristaux De Flexion D'Un Acier Inoxydable Austenitique, Desorientes Autour De L'Axe <100>. *Journal de Physique*, 36(4):225, 1975.

[84] D McLean. Dislocations, vacancies and solutes in grain boundaries. *Canadian Metallurgical Quarterly*, 13(1):145–153, jan 1974.

[85] Masaharu Kato and T Mori. Internal friction of copper bicrystals with [001] twist boundaries. *Philosophical Magazine A*, 8610(September 2011):37–41, 1993.

[86] T. Mori, H. Miura, T. Tokita, J. Haji, and M. Kato. Determination of the energies of [001] twist boundaries in Cu with the shape of boundary SiO2 particles. *Philosophical Magazine Letters*, 58(1):11–15, 1988.

[87] A U Telang and T R Bieler. The Orientation Imaging Microscopy of Lead-Free Sn-Ag Solder Joints. *JOM*, 57(June):44–49, 2005.

[88] S. Terashima, T. Kohno, A. Mizusawa, K. Arai, O. Okada, T. Wakabayashi, M. Tanaka, and K. Tatsumi. Improvement of thermal fatigue properties of Sn-Ag-Cu lead-free solder interconnects on casio's wafer-level packages based on morphology and grain boundary character. *Journal of Electronic Materials*, 38(1):33–38, 2009.

[89] A. U. Telang, T. R. Bieler, and M. A. Crimp. Grain boundary sliding on near 7, 14, and 22 degree special boundaries during thermomechanical cycling in surface-mount lead-free solder joint specimens. *Materials Science and Engineering: A*, 421(1-2):22–34, apr 2006.

[90] H Ljungcrantz, L Hultman, and J E Sundgren. Residual stresses and fracture properties of magnetron sputtered Ti films on Si microelements. *Journal of Vacuum Science & Technology A: Vacuum, Surfaces, and Films*, 11(3):543, 1993.

[91] T. P. Weihs, S. Hong, J. C. Bravman, and W. D. Nix. Mechanical deflection of cantilever microbeams: A new technique for testing the mechanical properties of thin films. *Journal of Materials Research*, 3(05):931–942, 1988.

[92] S Johansson, J Å Schweitz, and L Tenerz. Fracture testing of silicon microelements insitu in a scanning electron microscope. *Journal of Applied Physics*, 1988.

[93] Jan-Åke Å Schweitz. Mechanical characterization of thin films by micromechanical techniques. *MRS Bulletin*, 17(07):34–45, 1992.

[94] W Fang and J A Wickert. Comments on measuring thin-film stresses using bi-layer micromachined beams. *Journal of Micromechanics and Microengineering*, 5(4):276, 1995.

[95] A Gouldstone, N Chollacoop, M Dao, J Li, and A M Minor. Indentation across size scales and disciplines: Recent developments in experimentation and modeling. *Acta Materialia*, 2007.

[96] P Peralta, R Ledoux, M Hakik, and R Dickerson. Characterization of surface deformation around vickers indents in monocrystalline materials. *Metallurgical and Materials Transactions A*, 2004.

[97] J. McCarthy, Z. Pei, M. Becker, and D. Atteridge. FIB micromachined submicron thickness cantilevers for the study of thin film properties. *Thin Solid Films*, 358(1):146–151, 2000.

[98] D Di Maio and S G Roberts. Measuring fracture toughness of coatings using focused-ion-beam-machined microbeams. *Journal of Materials Research*, 20(02):299–302, 2005.

[99] D.E.J. Armstrong, A J Wilkinson, and S G Roberts. Measuring anisotropy in Young's modulus of copper using microcantilever testing. *Journal of Materials Research*, 24(11):3268–3276, 2009.

[100] Jicheng Gong and Angus J Wilkinson. Investigation of elastic properties of single-crystal alpha-Ti using microcantilever beams. *Philosophical Magazine Letters*, 90(7):503–512, 2010.

[101] E Demir, D Raabe, and F Roters. The mechanical size effect as a mean-field breakdown phenomenon: Example of microscale single crystal beam bending. *Acta Materialia*, 2010.

[102] C Motz, T Schöberl, and R Pippan. Mechanical properties of micro-sized copper bending beams machined by the focused ion beam technique. *Acta Materialia*, 2005.

[103] D Kiener, C Motz, T Schöberl, and M Jenko. Determination of mechanical properties of copper at the micron scale. *Advanced Engineering Materials*, 2006.

[104] Jicheng Gong and Angus J. Wilkinson. Anisotropy in the plastic flow properties of single-crystal alpha titanium determined from micro-cantilever beams. *Acta Materialia*, 57(19):5693–5705, 2009.

[105] D.E.J. Armstrong, M. E. Rogers, and S. G. Roberts. Micromechanical testing of stress corrosion cracking of individual grain boundaries. *Scripta Materialia*, 61(7):741–743, 2009.

[106] D Kiener, C Motz, W Grosinger, D Weygand, and R Pippan. Cyclic response of copper single crystal micro-beams. *Scripta Materialia*, 2010.

[107] A Stratulat and S G Roberts. Micromechanical testing of oxidised grain boundaries in Ni Alloy 600. *MRS Proceedings*, 2013.

[108] D.E.J. Armstrong, A J Wilkinson, and S G Roberts. Micro-mechanical measurements of fracture toughness of bismuth embrittled copper grain boundaries. *Philosophical Magazine Letters*, 91(6):394–400, 2011.

[109] Jicheng Gong and Angus J. Wilkinson. A microcantilever investigation of size effect, solid-solution strengthening and second-phase strengthening for <a> prism slip in alpha-Ti. *Acta Materialia*, 59(15):5970–5981, 2011.

[110] Jicheng Gong and Angus J. Wilkinson. Micro-cantilever testing of <a> prismatic slip in commercially pure Ti. *Philosophical Magazine*, 91(7-9):1137–1149, 2011.

[111] D.E.J. Armstrong, C.D. Hardie, J.S.K.L. Gibson, A.J. Bushby, P.D. Edmondson, and S.G. Roberts. Small-scale characterisation of irradiated nuclear materials: Part II nanoindentation and micro-cantilever testing of ion irradiated nuclear materials. *Journal of Nuclear Materials*, 462:374–381, 2015.

[112] D.E.J. Armstrong, A. S M A Haseeb, S. G. Roberts, A. J. Wilkinson, and K. Bade. Nanoindentation and micro-mechanical fracture toughness of electrodeposited nanocrystalline Ni-W alloy films. *Thin Solid Films*, 520(13):4369–4372, 2012.

[113] Guang hai Li, Xi jun Wu, Min Cai, Qiang Qiu, and Qi heng Tang. A fractocraphic study of bismuth embrittlement of tilt boundaries in a copper bicrystal. *Scripta Metallurgica et Materiala*, 24(11):2129–2134, 1990.

[114] Wang Jian-Sheng and P M Anderson. Fracture behavior of embrittled F.C.C. metal bicrystals. *Acta Metallurgica et Materialia*, 39(5):779–792, 1991.

[115] D. Kupka and E. T. Lilleodden. Mechanical Testing of Solid-Solid Interfaces at the Microscale. *Experimental Mechanics*, 52(6):649–658, 2012.

[116] D Kupka, N Huber, and E T Lilleodden. A combined experimental-numerical approach for elasto-plastic fracture of individual grain boundaries. *Journal of the Mechanics and Physics of Solids*, 64(1):455–467, 2014.

[117] M. D. Uchic. Sample Dimensions Influence Strength and Crystal Plasticity. *Science*, 305(5686):986–989, 2004.

[118] Michael D. Uchic and Dennis A M. Dimiduk. A methodology to investigate size scale effects in crystalline plasticity using uniaxial compression testing. *Materials Science and Engineering: A*, 400-401(1-2 SUPPL.):268278, 2005.

[119] Julia R. Greer, Warren C. Oliver, and William D. Nix. Size dependence of mechanical properties of gold at the micron scale in the absence of strain gradients. *Acta Materialia*, 53(6):1821–1830, 2005.

[120] Andrew T. Jennings, Michael J. Burek, and Julia R. Greer. Microstructure versus Size: Mechanical properties of electroplated single crystalline Cu nanopillars. *Physical Review Letters*, 104(13):1–4, 2010.

[121] Julia R. Greer, Christopher R. Weinberger, and Wei Cai. Comparing the strength of fcc and bcc sub-micrometer pillars: Compression experiments and dislocation dynamics simulations. *Materials Science and Engineering: A*, 493(1):21–25, 2008.

[122] Ju Young Kim and Julia R. Greer. Size-dependent mechanical properties of molybdenum nanopillars. *Applied Physics Letters*, 93(10):2006–2009, 2008.

[123] Ju Young Kim, Dongchan Jang, and Julia R. Greer. Tensile and compressive behavior of tungsten, molybdenum, tantalum and niobium at the nanoscale. *Acta Materialia*, 58(7):2355–2363, 2010.

[124] Gyuhyon Lee, Ju-Young Kim, Arief Suriadi Budiman, Nobumichi Tamura, Martin Kunz, Kai Chen, Michael J. Burek, Julia R. Greer, and Ting Y. Tsui. Fabrication, structure and mechanical properties of indium nanopillars. *Acta Materialia*, 58(4):1361–1368, 2010.

[125] Dennis M. Dimiduk, Chris Woodward, Richard LeSar, and Michael D. Uchic. Scale-free intermittent flow in crystal plasticity. *Science (New York, N.Y.)*, 312(5777):1188–1190, 2006.

[126] Bastian Philippi, Christoph Kirchlechner, Jean Sébastien Micha, and Gerhard Dehm. Size and orientation dependent mechanical behavior of body-centered tetragonal Sn at 0.6 of the melting temperature. *Acta Materialia*, 115:76–82, 2016.

[127] A. Lupinacci, J. Kacher, A. Eilenberg, A. A. Shapiro, P. Hosemann, and A. M. Minor. Cryogenic in situ microcompression testing of Sn. *Acta Materialia*, 78:56–64, 2014.

[128] J. W. Christian and S. Mahajan. Deformation twinning. *Progress in Materials Science*, 39(1-2):1–157, 1995.

[129] P Darbandi, T R Bieler, F Pourboghrat, and Tae-kyu Lee. Crystal Plasticity Finite-Element Analysis of Deformation Behavior in Multiple-Grained Lead-Free Solder Joints. *Journal of Electronic Materials*, 42(2):201–214, 2013.

[130] Masami Fujiwara and Tomoo Hirokawa. The Strength of Main Obstacles to Dislocation Motion in White Tin Crystals. *Journal of the Japan Institute of Metals*, 51(9):830–838, 1987.

[131] Thomas R. Bieler and Adwait U. Telang. Analysis of slip behavior in a single shear lap lead-free solder joint during simple shear at 25Â°C and 0.1/s. *Journal of Electronic Materials*, 38(12):2694–2701, 2009.

[132] C. Shashank Kaira, Sudhanshu S. Singh, Antony Kirubanandham, and Nikhilesh Chawla. Micro-scale deformation behavior of bicrystal boundaries in pure tin (Sn) using micropillar compression. *Acta Materialia*, 120:56–67, 2016.

[133] Peter J. Imrich, Christoph Kirchlechner, Christian Motz, and Gerhard Dehm. Differences in deformation behavior of bicrystalline Cu micropillars containing a twin boundary or a large-angle grain boundary. *Acta Materialia*, 73:240–250, 2014.

[134] Zachary H. Aitken, Dongchan Jang, Christopher R. Weinberger, and Julia R. Greer. Grain boundary sliding in aluminum nano-Bi-crystals deformed at room temperature. *Small*, 10(1):100–108, 2014.

[135] K.S. S Ng and A.H.W Ngan. Deformation of micron-sized aluminium bi-crystal pillars. *Philosophical Magazine*, 89(33):3013–3026, 2009.

[136] Allison Kunz, Siddhartha Pathak, Julia Greer R., Julia R. Greer, Julia Greer R., and Julia R. Greer. Size effects in Al nanopillars: Single crystalline vs. bicrystalline. *Acta Materialia*, 59(11):4416–4424, 2011.

[137] H Fukutomi and T Kamijo. Grain boundary sliding-migration of aluminum <110> sigma 11 {113} symmetric tilt coincidence grain boundary and its interpretation based on the motion of perfect DSC dislocations. *Scripta Metallurgica*, 19, 1985.

[138] S E Babcock and R W Balluffi. Grain boundary kinetics - In situ observations of coupled grain boundary dislocation motion, crystal translation and boundary displacement. *Acta Metallurgica*, 37, 1989.

[139] H. Fukutomi, T. Iseki, T. Endo, and T. Kamijo. Sliding behavior of coincidence grain boundaries deviating from ideal symmetric tilt relationship. *Acta Metallurgica et Materialia*, 39(7):1445–1448, 1991.

[140] Jicheng Gong and Angus J. Wilkinson. Sample size effects on grain boundary sliding. *Scripta Materialia*, 114:17–20, 2016.

[141] M. A. Clark and T. H. Alden. Deformation enhanced grain growth in a superplastic Sn-1% Bi alloy. *Acta Metallurgica*, 21(9):1195–1206, 1973.

[142] H. Okamoto. Bi-Sn (bismuth-tin). *Journal of Phase Equilibria and Diffusion*, 31(2):205, 2010.

[143] D. H. Bae and a. K. Ghosh. A planar simple shear test and flow behavior in a superplastic Al-Mg alloy. *Metallurgical and Materials Transactions A*, 34(November):2465–2471, 2003.

[144] E Alabort. *A Study of Superplasticity in Ti-6A-4V : Characterisation, Modelling and Applications*. PhD thesis, University of Oxford, 2015.

[145] E. Alabort, P. Kontis, D. Barba, K. Dragnevski, and R. C. Reed. On the mechanisms of superplasticity in Ti-6Al-4V. *Acta Materialia*, 105:449–463, 2016.

[146] Dantec Dynamics. 2D Least Squares Matching, 2017.

[147] LaVision DaVis. StrainMaster, 2017.

[148] Tadao Watanabe. Grain boundary design and control for high temperature materials. *Materials Science and Engineering A*, 166(1-2):11–28, 1993.

[149] Megumi Kawasaki and Terence G Langdon. Grain boundary sliding in a superplastic zinc-aluminum alloy processed using severe plastic deformation. 49(1):84–89, 2008.

[150] H. Watanabea, K. Kurimoto, T. Uesugi, Y. Takigawa, and K. Higashi. Isotropic superplastic flow in textured magnesium alloy. *Materials Science & Engineering A*, (558):656–662, 2012.

[151] F. Muktepavela, G. Bakradze, and V. Sursaeva. Micromechanical properties of grain boundaries and triple junctions in polycrystalline metal exhibiting grain-boundary sliding at 293 K. *Journal of Materials Science*, 43(11):3848–3854, 2008.

[152] Ningning Du, Yue Qi, Paul E. Krajewski, and Allan F. Bower. Aluminum R3 grain boundary sliding enhanced by vacancy diffusion. *Acta Materialia*, 58(12):4245–4252, 2010.

[153] Bite Zhou. *Characterization of Tin Crystal Orientation Evolution during Thermal Cycling in Lead-free Solder Joints*. Doctor of philosophy thesis, Michigan State University, 2012.

[154] N Saito, M Mabuchi, M Nakanishi, and M Nakamura. Control of grain boundary character distribution of commercial Al-Mg alloys by hot extrusion. *Journal of Materials Science Letters*, (18):41–45, 1999.

[155] Tadao Watanabe, Minoru Obata, and Seiichi Karashima. Intergranular fracture at migrating and sliding grain boundaries in an alpha iron - tin alloy. *Scripta Metallurgica*, 15(9):965–970, 1981.

[156] Tohru Takahashi and Ryo Horiuchi. Coupling of grain boundary migration and sliding in coincidence boundary of Zn bicrystal as an evidence of DSC dislocation method, 1984.

[157] Hiroshi Fukutomi, Hideo Takatori, and Ryo Horiuchi. Grain Boundary Sliding with and without Matrix Slip Deformation in Cadmium Bicrystals. *Transactions of the Japan Institute of Metals*, 23(10):579–584, 1982.

[158] Hiroshi Fukutomi, Mutsuto Tanaka, Taichi Kamijo, and Ryo Horiuchi. DSC Dislocation Mechanism of Grain Boundary Sliding in Aluminium. *Journal of the Japan Institute of Metals*, 48(12):1133–1137, 1984.

[159] A D Sheikh-Ali. Coupling of grain boundary sliding and migration within the range of boundary specialness. *Acta Materialia*, 58(19):6249–6255, 2010.

[160] M. G. Zelin, M. R. Dunlap, R. Rosen, and A. K. Mukherjee. The direct observation of cooperative grain-boundary sliding and migration during superplastic deformation of lead-tin eutectic in shear. *Journal of Applied Physics*, 74(8):4972–4982, 1993.

[161] R. L. Seliger, J. W. Ward, V. Wang, and R. L. Kubena. A high-intensity scanning ion probe with submicrometer spot size. *Applied Physics Letters*, 34(5):310–312, 1979.

[162] Agilent Technologies. Performance and Control of the Agilent Nano Indenter DCM. Technical report, 2010.

[163] Agilent Technologies. Agilent Technologies Nano Indenter G200 Compliant with ISO 14577. Technical report, 2009.

[164] G. Guillonneau, G. Kermouche, S. Bec, and J.-L. Loubet. Determination of mechanical properties by nanoindentation independently of indentation depth measurement. *Journal of Materials Research*, 27(19):2551–2560, 2012.

[165] W C Oliver and G M Pharr. An improved technique for determining hardness and elastic modulus using load and displacement sensing indentation experiments. *Journal of Materials Research*, 7(6):1564–1583, 1992.

[166] KLA-Tencor Corporation. MicroXAM - 100 3D Surface Profilometer, 2017.

[167] T H Alden. The origin of superplasticity in the Sn-5{%} Bi alloy. *Acta Metallurgica*, 15:469–480, 1967.

[168] K.E Puttick and B Tuck. Boundary sliding and migration in tin bicrystals. *Acta Metallurgica*, 13(10):1043–1048, 1965.

[169] J. H. Schneibel and P. M. Hazzledine. The role of Coble creep and interface control in superplastic Sn-Pb alloys. *Journal of Materials Science*, 18(2):562–570, 1983.

[170] Z P Wang and Q J Yang. Creep Behavior and Deformation Mechanism Map of Sn-Pb. 125(January 2003):81–88, 2003.

[171] Alan Atkinson. Grain-boundary diffusion: an historical perspective. *Journal of the Chemical Society, Faraday Transactions*, 86(8):1307–1310, 1990.

[172] R Monzen, Y Sumi, K Kitagawa, and T Mori. Nanometer grain boundary sliding in Cu-[011] symmetric tilt boundaries, misorientation dependence and anisotropy. *Acta Metallurgica et Materialia*, 38(12):2553–2560, 1990.

[173] W Lange and D Bergner. Messung der Korngrenzenselbstdiffusion in polykristallinem Zinn. *physica status solidi (b)*, 2(10):1410–1414, 1962.

[174] L. Holmes and W.C Winegard. Effect of Lead and Bismuth on Grain Growth in Zone-refined Tin. *Transactions of the Metallurgical Society of AIME*, 224, 1962.

[175] Peter Anker Thorsen. *The influence of the grain boundary structure on diffusional creep*. Risø National Laboratory, Roskilde, 1998.

[176] D S Wilkinson and C H Cáceres. An evaluation of available data for strain-enhanced grain growth during superplastic flow. *Journal of Materials Science Letters*, 3(5):395–399, 1984.

[177] R. C. Gifkins. Grain rearrangements during superplastic deformation. *Journal of Materials Science*, 13(9):1926–1936, 1978.

[178] V.V. V Astanin, O.A. A Kaibyshev, and S.N. N Faizova. The role of deformation localization in superplastic flow. *Acta Metallurgica et Materialia*, 42(8):2617–2622, aug 1994.

[179] Peter Reischig, Andrew King, Laura Nervo, Nicola Vigano, Yoann Guilhem, Willem Jan Palenstijn, K. Joost Batenburg, Michael Preuss, and Wolfgang Ludwig. Advances in X-ray diffraction contrast tomography: Flexibility in the setup geometry and application to multiphase materials. *Journal of Applied Crystallography*, 46(2):297–311, 2013.

[180] A. King, M. Herbig, W. Ludwig, P. Reischig, E. M. Lauridsen, T. Marrow, and J. Y. Buffière. Non-destructive analysis of micro texture and grain boundary character from X-ray diffraction contrast tomography. *Nuclear Instruments and Methods in Physics Research, Section B: Beam Interactions with Materials and Atoms*, 268(3-4):291–296, 2010.

[181] Greg Johnson, Andrew King, Marcelo Goncalves Honnicke, J. Marrow, and Wolfgang Ludwig. X-ray diffraction contrast tomography: A novel technique for three-dimensional grain mapping of polycrystals. II. The combined case. *Journal of Applied Crystallography*, 41(2):310–318, 2008.

[182] Melanie Syha, Andreas Trenkle, Barbara Lodermann, Andreas Graff, Wolfgang Ludwig, Daniel Weygand, and Peter Gumbsch. Validation of three-dimensional diffraction contrast tomography reconstructions by means of electron backscatter diffraction characterization. *Journal of Applied Crystallography*, 46(4):1145–1150, 2013.

[183] W. Ludwig, A. King, P. Reischig, M. Herbig, E. M. Lauridsen, S. Schmidt, H. Proudhon, S. Forest, P. Cloetens, S. Rolland du Roscoat, J. Y. Buffière, T. J. Marrow, and H. F. Poulsen. New opportunities for 3D materials science of polycrystalline materials at the micrometre lengthscale by combined use of X-ray diffraction and X-ray imaging. *Materials Science and Engineering A*, 524(1-2):69–76, 2009.

[184] A. King, G. Johnson, D. Engelberg, W. Ludwig, and J. Marrow. Observations of intergranular stress corrosion cracking in a grain-mapped polycrystal. *Science*, 321(5887):382–385, 2008.

[185] Michael Herbig, Andrew King, Péter Reischig, Henry Proudhon, Erik M. Lauridsen, James Marrow, Jean Yves Buffire, and Wolfgang Ludwig. 3-D growth of a short fatigue crack within a polycrystalline microstructure studied using combined diffraction and phase-contrast X-ray tomography. *Acta Materialia*, 59(2):590–601, 2011.

[186] W. Ludwig, P. Reischig, A. King, M. Herbig, E. M. Lauridsen, G. Johnson, T. J. Marrow, and J. Y. Buffîre. Three-dimensional grain mapping by x-ray diffraction contrast tomography and the use of Friedel pairs in diffraction data analysis. *Review of Scientific Instruments*, 80(3), 2009.

[187] Laura Nervo, Andrew King, Arnas Fitzner, Wolfgang Ludwig, and Michael Preuss. A study of deformation twinning in a titanium alloy by X-ray diffraction contrast tomography. *Acta Materialia*, 105:417–428, 2016.

[188] Hongchang Wang, Sebastien Berujon, Julia Herzen, Robert Atwood, David Laundy, Alexander Hipp, and Kawal Sawhney. X-ray phase contrast tomography by tracking near field speckle. *Scientific Reports*, 5:8762, 2015.

[189] Wolfgang Ludwig, Andrew King, Michael Herbig, Péter Reischig, James Marrow, Laurent Babout, Erik Mejdal Lauridsen, Henry Proudhon, and Jean-Yves Buffière. Characterization of polycrystalline materials using synchrotron X-ray imaging and diffraction techniques. *The Journal of The Minerals, Metals & Materials Society (TMS)*, 62(December):22–28, 2010.

[190] Carl-Zeiss. Laboratory Diffraction Contrast Tomography on Zeiss Xradia 520 Versa, 2017.

[191] S A Mcdonald, P Reischig, C Holzner, E M Lauridsen, P J Withers, and A P Merkle. Non-destructive mapping of grain orientations in 3D by laboratory X-ray microscopy. *Nature Publishing Group*, pages 1–11, 2016.

[192] A. King, P. Reischig, J. Adrien, and W. Ludwig. First laboratory X-ray diffraction contrast tomography for grain mapping of polycrystals. *Journal of Applied Crystallography*, 46(6):1734–1740, 2013.

[193] University of Manchester. Zeiss Xradia 520 Versa with DCT, 2017.

[194] J.-Y Buffière, E Maire, P Cloetens, G Lormand, and R Fougères. Characterization of internal damage in a MMCp using X-ray synchrotron phase contrast microtomography. *Acta Materialia*, 47(5):1613–1625, 1999.

[195] Paul A Shade, Basil Blank, Jay C Schuren, Todd J Turner, Peter Kenesei, Kurt Goetze, Robert M Suter, Joel V Bernier, Shiu Fai Li, Jonathan Lind, Ulrich Lienert, and Jonathan Almer. A rotational and axial motion system load frame insert for in situ high energy x-ray studies. *Review of Scientific Instruments*, 86(9):93902, sep 2015.

[196] N. Gueninchault, H. Proudhon, and W. Ludwig. Nanox: A miniature mechanical stress rig designed for near-field X-ray diffraction imaging techniques. *Journal of Synchrotron Radiation*, 23(6):1474–1483, 2016.

[197] G E Dieter and D Bacon. Mechanical metallurgy. *Mechanical metallurgy*, 1986.

[198] T D Langdon. The Significance of Grain-Boundary Sliding in Creep and Superplasticity. *Metals forum*, 4(1-2):14, 1981.

[199] G Rai and Nicholas J Grant. Observations of grain boundary sliding during superplastic deformation. *Metallurgical Transactions A*, 14(7):1451–1458, 1983.

[200] H Naziri, R Pearce, M.Henderson Brown, and K F Hale. Microstructural-mechanism relationship in the zinc/ aluminium eutectoid superplastic alloy. *Acta Metallurgica*, 23(4):489–496, 1975.

[201] R C Gifkins. Grain-boundary sliding and its accommodation during creep and superplasticity. *Metallurgical Transactions A*, 7(8):1225–1232, 1976.

[202] R C Gifkins. The effect of grain size and stress upon grain-boundary sliding. *Metallurgical Transactions A*, 8(10):1507–1516, 1977.

[203] K Matsuki, H Morita, M Yamada, and Y Murakami. Relative motion of grains during superplastic flow in an Al-9Zn-1 wt.%Mg alloy. *Metal Science*, 11(5):156–163, may 1977.

[204] D J Dingley. Trends in Physics, 1973.

[205] M. G. Zelin and A. K. Mukherjee. Cooperative phenomena at grain boundaries during superplastic flow. *Acta Metallurgica Et Materialia*, 43(6):2359–2372, 1995.

[206] N. A. Mara, A. V. Sergueeva, T. D. Mara, S. X. McFadden, and A. K. Mukherjee. Superplasticity and cooperative grain boundary sliding in nanocrystalline Ni3Al. *Materials Science and Engineering A*, 463(1-2):238–244, 2007.

[207] P M Hazzledine and D E Newbury. 7. Role of Grain Boundaries in Superplasticity. *Grain boundary structure and properties*, page 235, 1976.

[208] K Sotoudeh and P S Bate. Diffusion creep and superplasticity in aluminium alloys. *Acta Materialia*, 58(6):1909–1920, 2010.

[209] J. R. Spingarn and W. D. Nix. Diffusional creep and diffusionally accommodated grain rearrangement. *Acta Metallurgica*, 26(9):1389–1398, 1978.

[210] Amiya K. Mukherjee. The rate controlling mechanism in superplasticity. *Materials Science and Engineering*, 8(2):83–89, 1971.

[211] J.W Edington, K.N Melton, and C.P Cutler. Superplasticity. *Progress in Materials Science*, 21(1-2):61–170, 1976.

[212] P. S. Bate, F. J. Humphreys, N. Ridley, and B. Zhang. Microstructure and texture evolution in the tension of superplastic Al-6Cu-0.4Zr. *Acta Materialia*, 53(10):3059–3069, 2005.